ResearchOnline@JCU

JAMES COOK UNIVERSITY AUSTRALIA

This file is part of the following work:

Bertelli, Martina (2007) ***Hydrothermal processes in barren and mineralized systems: insights using fluid inclusion microanalysis and geochemical modelling.*** **PhD Thesis, James Cook University.**

Access to this file is available from:

https://doi.org/10.25903/rb06%2Dxq02

Copyright © 2007 Martina Bertelli

The author has certified to JCU that they have made a reasonable effort to gain permission and acknowledge the owners of any third party copyright material included in this document. If you believe that this is not the case, please email researchonline@jcu.edu.au

Hydrothermal processes in barren and mineralized systems

Insights using fluid inclusion microanalysis and geochemical modelling

Thesis Submitted by Martina Bertelli B.Sc. (Hons), Padova

in March 2007

for the degree of Doctor of Philosophy

in the School of Earth and Environmental Sciences

James Cook University

STATEMENT OF ACCESS

I, the undersigned, author of this work, understand that James Cook University will make this thesis available for use within the University Library and, via the Australian Digital Theses network, for use elsewhere.

I understand that, as an unpublished work, a thesis has significant protection under the Copyright Act and;

I wish this work to be embargoed until: March 31st, 2008

All users consulting this thesis will have to sign the following statement: "In consulting this thesis I agree not to copy or closely paraphrase it in whole or in part without the written consent of the author; and to make proper public written acknowledgment for any assistance that I have obtained from it.

_____ _____

STATEMENT OF SOURCES

DECLARATION

I declare that this thesis is my own work and has not been submitted in any form for another degree or diploma at any university or other institution of tertiary education. Information derived from the published or unpublished work of others has been acknowledged in the text and a list of references is given.

_____ _____

ELECTRONIC COPY

I, the undersigned, the author of this work, declare that the electronic copy of this thesis provided to the James Cook University Library is an accurate copy of the print thesis submitted, within the limits of the technology available.

_____ _____

STATEMENT OF CONTRIBUTIONS

Fees, stipend support and project cost contributions included:

- James Cook University Postgraduate Research Scholarships (JCUPRS)
- International Postgraduate Research Scholarships (IPRS)
- Pmd*CRC Top-up Scholarship
- Pmd*CRC educational and training fund

Contributions of others included:

- Dr. T. Baker - supervision throughout the entire project including help in designing the PhD project, discussions and revision of all chapters
- Dr. J. Cleverley - supervision included help in designing the PhD project, assistance in the field, discussions and review of Chapters 3 and 8.
- Prof. N.H.S. Oliver - supervision included help in designing the PhD project and fieldwork assistance
- Dr. D. R. W. Foster – fieldwork assistance, discussions in relation to the geology of Mt Isa Inlier
- Dr. K. L. Blake - assistance during microprobe and cathodoluminescence analyses (Chapters 3, 4 and 5) at the Advanced Analytical Centre, James Cook University, Townsville
- Dr. T. P. Mernagh – Laser Raman analyses (Chapter 5) at Geoscience Australia, Canberra.
- Dr. D.A. Banks, Prof. B. W. D. Yardley, Dr. M.M. Allan, Mrs L. Forbes - assistance during LA ICP MS fluid inclusion analyses (Chapters 5 and 6) analyses at the School of Earth and Environment, University of Leeds, Leeds, UK
- Dr. D.A. Banks - Bulk crush leach analyses (Chapter 5) at the School of Earth and Environment, University of Leeds, Leeds, UK
- Dr. T. Ulrich – LA ICP MS fluid inclusion analyses (Chapter 8) at Department of Earth & Marine Sciences, Australian National University, Canberra
- D. Gillen (PhD candidate at JCU) – introduction to microthermometric analysis (chapter 4).

ACKNOWLEDGEMENTS

I am grateful to Dr. Tim Baker for his constant support and his patience particularly during the revision of drafts. Dr. Damien Foster and Dr. James Cleverley are thanked for several discussions that helped improving numerous aspects of the thesis. I also acknowledge Prof. Nick Oliver for his help in designing the project and for dragging me in to the breccia world.

I also acknowledge Dr. K. L. Blake for his help during microprobe analysis at JCU, Dr. D.A. Banks, Prof. B. W. D. Yardley, Dr. M.M. Allan and Mrs Linda Forbes for their assistance during LAICPMS analysis at Leeds University, Dr. D.A. Banks for crush leach analysis at Leeds University, Dr T.P. Mernagh for laser raman analysis at Geoscience Australia and Dr. T. Ulrich for LA ICP MS analysis at ANU. I would like to thank David Gillen for his help. This project was sponsored by an International Post Graduate Award, and a pmd*CRC top-up scholarship.

I am grateful to my parents Angelo and Graziella for their love and support during this time far away from home. Thanks to my sister Roberta for the long night calls and for making me always laugh. Thanks to Micaela, Barbara and all the Baccaglini clan for being like a second family for me. I would like to acknowledge Isabella, Gianni and Susanna Feltrin for their support. I am indebted to Leonardo for his constant encouragement, his infinite patience and above all for believing in me. None of this would have been possible without you.

ABSTRACT

The study of fluid inclusions in this thesis was used as a research tool to characterize fluids associated with specific types of deposits and related hydrothermal systems and to investigate ore deposition processes with the ultimate aim of addressing key questions relating to ore genesis. Two magmatic-hydrothermal systems were investigated. The first part of the thesis focuses on the study of the Suicide Ridge Barren Breccia Pipe (SRBP; ~ 1527 ± 4 Ma), located in the Snake Creek area, in the Cloncurry district, Australia. The pipe is one of numerous breccia systems that characterize the Cloncurry District and is temporally and spatially associated with a granite that outcrops at its southwestern boundary and which is ascribed to the Williams and Naraku magmatic event (ca 1550-1500 Ma). The breccia is characterized by clasts of variable dimensions, degree of rounding and composition that includes dominant calc-silicate clasts of the Corella Formation that underlie rocks of the Soldiers Cap Group that host the pipe. This indicates a dominant upward transport of the fragments. Other breccia fragments include granite bodies characterized by albite-quartz rocks that have textures typical of the magmatic-hydrothermal transition. These rocks likely formed in a fractionated carapace of a granite during the exsolution of volatiles associated with the cooling magma. Two dominant types of inclusions have been identified in these textures and include early primary and pseudosecondary CO_2-rich and secondary sodic-calcic brine inclusions. The CO_2-rich fluid inclusions represent fluid released from the crystallizing magma and variable homogenization temperatures in the primary and pseudosecondary inclusions indicate that they were trapped under different pressure conditions. Pressures estimated from the primary CO_2 fluid inclusions suggest that they were trapped at 4.2 kbar, at least 1 kbar above the inferred lithostatic

pressure. This likely represents the overpressuring produced by release of CO_2-rich volatiles during the crystallization of magma and which ultimately caused the subsequent brecciation. Sodic-calcic fluid inclusions represent a later influx of fluids in the breccia system that produced widespread albitization. Bulk crush leach analysis suggests that the carbonic fluid inclusions in the granite clasts have either a magmatic origin or formed from the dissolution of evaporites (or mixing of the two), whereas the sodic-calcic inclusions may have been sourced from bittern brines.

The study also included LA ICP MS analysis of fluid inclusions from the SRBP and the Eloise Cu-Au deposit in order to address the key differences between barren and mineralized hydrothermal systems in the Cloncurry district. The major difference between the barren breccia pipe and IOCG deposits is the absence in the former of multisolid high salinity, high temperature fluid inclusions, suggesting that these were critical for the formation of IOCG deposits. Fluid mixing was a key deposition mechanism at Eloise as indicated by the general abundance of Ba in multisolid fluid inclusions, that possibly suggests S-poor fluid, the variable chemistry of fluid inclusions consistent with a mixing trend and the significant lower of salinity that characterize later fluids compared to the ore forming fluid that can not be attributed to precipitation of Cl-bearing phases. The preferred model for ore deposition at Eloise is fluid mixing between hot, ultrasaline Cu-bearing, S-poor fluid, evolving as the result of cooling and wall rock reaction as it migrated in a northern direction and a S-bearing fluid cooler fluid. Possible sources of sulphur include the later halite-bearing fluid inclusions and CO_2-rich fluid inclusions.

The second part of the study focused on the base metal-rich, high-temperature, carbonate-replacement Bismark deposit in northern Mexico. Previous fluid inclusion studies based on microthermometry and PIXE showed that the Zn-rich, Pb-poor

Bismark deposit formed from a moderate salinity magmatic fluid but the exact precipitation mechanisms were unclear. Furthermore, PIXE data suggested that Pb and Zn concentrations were comparable and inconsistent with the Zn-rich nature of the ore. In this study LA ICP MS analysis of the same fluid inclusion populations was carried out to compare with the PIXE data and the new results were used to model possible ore deposition mechanisms. The new laser ablation data revealed overall lower concentrations of Pb in the ore fluid (average value ~336ppm) than previously indicated by PIXE analysis (average value ~713ppm). Chemical modeling using this new data tested the following processes: 1) cooling; 2) fluid-rock reaction at constant temperature; 3) cooling and simultaneous fluid-rock interaction. Modeling results show that the gangue and ore minerals observed at Bismark are best reproduced by fluid-rock interaction with simultaneous cooling. Results from the simulations strongly indicate that ore deposition was mainly driven by a pH increase due to the neutralization of the acidic ore fluid (pH = 3.9) through reaction with the limestone.

Table of contents

STATEMENT OF ACCESS i

STATEMENT OF SOURCES DECLARATION ii

ELECTRONIC COPY iii

STATEMENT OF CONTRIBUTIONS iv

ACKNOWLEDGEMENTS v

ABSTRACT vi

Chapter 1 – Introduction

1.1. General introduction 1.1

1.2. Thesis aims 1.3

1.3. Methodology 1.5

1.4. Thesis outline 1.6

1.5. General background 1.9

Chapter 2 – Regional Geology of the Mt Isa Inlier

2.1. Introduction 2.1

2.2. Regional geology 2.2

2.2.1. Stratigraphy and structural evolution 2.2

2.2.2. Metamorphism 2.5

2.2.3. Magmatism 2.6

2.2.4. Metasomatism 2.8

2.2.4.1. Sodic (-calcic) metasomatism 2.8

2.2.4.2. K-Fe alteration 2.10

2.2.5. Mineralization 2.11

2.2.6. Brecciation 2.15

Chapter 3 – Geology and petrography of the Suicide Ridge Breccia Pipe

3.1. Introduction 3.1

3.2. Local Geology & Field Relationships 3.1

3.3. Sample petrography 3.8

3.3.1. Description of breccia clasts and groundmass 3.8

3.3.2. Description of granite and pegmatite breccia clasts and their alteration 3.13

3.3.2.1. Mineralogy and textures 3.13

3.3.2.2. Alteration 3.16

3.3.3. Magnetite-hematite-rich rocks 3.20

3.3.3.1. Discussion on the origin of magnetite-hematite-rich rock.....3.24

3.4. Summary and discussion 3.26

Chapter 4 - Fluid chemistry and conditions of the Suicide Ridge Breccia Pipe (I): Fluid inclusion paragenesis, classification and microthermometry

4.1 Introduction 4.1

4.2 Sample selection and paragenesis 4.1

4.3 Paragenesis and classification of fluid inclusions 4.3

4.3.1 Type I – Carbonic fluid inclusions 4.4

4.3.2 Type II - Mixed brine-carbonic fluid inclusions 4.6

4.3.3 Type III – Liquid rich – brine inclusions 4.11

4.3.4 Type IV – Liquid - rich brine inclusions 4.11

4.3.5 Type V - Liquid rich fluid inclusions 4.16

4.4 Microthermometry 4.19

4.4.1 Thermometric analysis of Type I fluid inclusions 4.19

4.4.2 Thermometric analysis of Type II fluid inclusions.....4.22

4.4.3 Thermometric analysis of Type III fluid inclusions 4.29

4.4.4 Thermometric analysis of Type IV fluid inclusions 4.33

4.4.5 Thermometric analysis of Type V fluid inclusions 4.36

4.5 Laser Raman Analysis 4.38

4.6 Estimation of Pressure and Trapping Conditions 4.38

4.6.1 Estimation of Density and Pressure of Type Ia and Ib – CO_2 rich inclusions 4.38

4.6.2 Type III – Liquid rich inclusions 4.46

4.7 Summary.....4.50

Chapter 5 – Fluid Chemistry and Conditions of the Suicide Ridge Breccia Pipe (II): Microanalytical, Bulk and Microprobe Analysis

5.1 Introduction.....5.1

5.2 LA ICP MS analysis of fluid inclusions 5.1

5.2.1 Methodology.....5.1

5.2.2 Sample and fluid inclusion selection 5.5

5.2.3 Results.....5.6

5.3 Crush Leach Analysis 5.20

5.3.1 Methodology.....5.20

5.3.2 Results.....5.21

5.4 Apatite chemistry 5.26

5.4.1 Introduction and Methodology 5.26

5.4.2 Results.....5.27

5.5 Summary 5.31

Chapter 6 – A comparison of hydrothermal fluids related to the Eloise Cu-Au deposit and to the Suicide Ridge Breccia Pipe

6.1. Introduction.....6.1

6.2. The Eloise Cu-Au Deposit 6.2

6.2.1. Background Geology 6.2

6.2.2. Summary of fluid inclusions studies.....6.6

6.2.3. Fluid evolution and genetic model for the Eloise Cu-Au deposit.....6.8

6.3. LA ICP MS analysis of fluid inclusions from the Cu-Au Eloise Deposit 6.9

6.3.1. Methodology and sample and fluid inclusion selection.....6.9

6.3.2. Results and Discussion 6.14

6.4. Comparison of fluids from Eloise deposit with fluids associated to the Suicide Ridge barren breccia pipe 6.23

6.5. Summary 6.30

Chapter 7 - Part I Discussion

7.1. Introduction.....7.1

7.2. Genesis of the Suicide Ridge Breccia Pipe.....7.1

7.3. Fluid geochemistry insights into the evolution and formation of the Eloise Cu-Au deposit 7.13

7.4. Regional vs IOCG fluids – Implication for formation of IOCG.....7.25

7.4.1. Comparison of fluids from the Suicide Ridge Breccia Pipe with other regional fluids 7.25

7.4.2. Comparison of fluids associated with IOCG deposits, granites and barren regional systems.....7.30

Chapter 8 - Geochemical modelling of a Zn-Pb skarn: constraints from LA-ICP-MS Analysis of Fluid Inclusions

Abstract.....8.1

8.1. Introduction.....8.2

8.2. Background Geology & Summary of Previous Studies 8.4

8.3. LA ICP MS analysis of fluid inclusions 8.10

8.4. Comparison of LA ICP MS and PIXE data 8.13

8.5. Geochemical modelling 8.17

8.5.1. Overview of the method 8.17

8.5.2. Fluid composition 8.18

8.5.3. Process modeling 8.20

8.6. Results.....8.21

8.6.1. Temperature decrease 8.21

8.6.2. Host rock reaction 8.23

8.6.3. Host rock reaction and cooling 8.26

8.7. Discussion of modelling results and comparison with the Bismark ore stage minerals assemblage 8.28

8.8. Conclusions.....8.30

Chapter 9 - Conclusions

9.1. Genesis of the Suicide Ridge Breccia Pipe and implication for the formation of sodic (-calcic) alteration in the Cloncurry district 9.1

9.2. Fluid geochemistry insights into the evolution and formation of the Eloise Cu-Au deposit 9.3

9.3. Regional vs IOCG fluids – Implication for formation of IOCG.....9.4

9.4. Testing ore-forming processes for the origin of the Zn-Pb Bismark deposit: constraints from geochemical modelling and LA-ICP-MS analysis of fluid inclusions 9.5

9.5. Future work.....9.6

References.....R1-R26

Appendices

Appendix 3.1 Mineral abbreviation used in the thesis A.1

Appendix 3.1 Sample List..... A.2

Appendices 4.1-4.9 Fluid inclusion thermometric data A.4

Appendices 4.10 Laser Raman data A.15

Appendices 5.1 LA ICP MS data on fluid inclusions from the Suicide Ridge Breccia Pipe..... A.16

Appendices 5.2 Micropobe data..... A.18

Appendices 6.1 LA ICP MS data on fluid inclusions from Eloise A.20

List of Figures

Chapter 2 – Regional Geology of the Mt Isa Inlier

Figure 2.1 Simplified geology of the Eastern Fold Belt. 2.4

Figure 2.2 Summary of tectonic, metamorphic, magmatic, alteration and mineralization events in the Cloncurry district. 2.7

Chapter 3 – Geology and petrography of the Suicide Ridge Breccia Pipe

Figure 3.1 Map of the Snake Creek Anticline. 3.3

Figure 3.2 Map of the breccia locality showing the SRBP and its relationship with the host rock and the granitoid that outcrop in the southwestern part of the area..3.4

Figure 3.3 Diagram representing microprobe analysis on primary and secondary albite.....3.21

Figure 3.4 Diagram illustrating the paragenetic evolution of the SRBP 3.28

Chapter 4 - Fluid chemistry and conditions of the Suicide Ridge Breccia Pipe (I): Fluid inclusion paragenesis, classification and microthermometry

Figure 4.1 Thermometric results for type Ia and Ib fluid inclusions. 4.21

Figure 4.2 Thermometric results for type IIa fluid inclusions. 4.24

Figure 4.3 Thermometric results for type IIb fluid inclusions. 4.25

Figure 4.4 Histogram displaying salinity estimates of types II, III, IV and V fluid inclusions. 4.26

Figure 4.5 Pressure-Temperature diagrams for fluids in the H_2O-NaCl- $CaCl_2$

system.. ..... 4.28

Figure 4.6 Thermometric results from type III fluid inclusions.. ..... 4.32

Figure 4.7 Ternary diagram for the NaCl - $CaCl_2$ - H_2O system displaying the composition of type III fluid inclusions..... 4.34

Figure 4.8 Thermometric results for type IV fluid inclusions. 4.35

Figure 4.9 Thermometric results for type V fluid inclusions. 4.37

Figure 4.10 Pressure-temperatures diagram for type I fluid inclusions (I)…..……....4.43

Figure 4.11 Pressure-temperatures diagram for type I fluid inclusions (II)…….4.44

Figure 4.12 Pressure-temperatures diagram for type I fluid inclusions (III)…...4.45

Figure 4.13 Diagram illustrating the relationship between the P-T formation conditions and the mode of homogenization of H_20-NaCI fluid inclusions with a salinity of 40 wt%.. .....4.48

Figure 4.14 Pressure-temperatures diagram for type IIIa fluid inclusions. 4.49

Chapter 5 – Fluid Chemistry and Conditions of the Suicide Ridge Breccia Pipe (II): Microanalytical, Bulk and Microprobe Analysis

Figure 5.1 Picture of type III fluid inclusions before (A) and after (B) ablation. ..5.4

Figure 5.2 LA ICP MS signals obtained from ablation of type III fluid inclusions for the first (A) and the second (B) suite of analyzed elements. 5.4

Figure 5.3 Diagram displaying minimum, maximum and average concentrations of major and trace elements of fluid inclusions for each sample determined from LA ICP MS analysis.....5.14

Figure 5.4 Diagram displaying minimum, maximum and average concentrations of major and trace elements of type III and IV fluid inclusions 5.15

Figure 5.5 Average fluid inclusion composition for each sample determined using LA-ICP-MS. 5.15

Figure 5.6 Plots of the concentrations of major and trace elements in fluid inclusions from the SRBP……..…… 5.16

Figure 5.7 Average fluid inclusion composition for granite clast and ironstone samples determined using LA-ICP-MS. 5.19

Figure 5.8 Bivariate plots displaying the relationships and relative abundances of anions measured with crush leach analysis..... 5.22

Figure 5.9 Br/Cl ($x10^3$) mol ratios versus SO_4/Cl mol ratios obtained from crush leach analysis. 5.24

Chapter 6 – A comparison of hydrothermal fluids related to the Eloise Cu-Au deposit and to the Suicide Ridge Breccia Pipe

Figure 6.1 Regional geological setting of the Eloise deposit. 6.4

Figure 6.2 Geology and alteration map of the Eloise deposit..... 6.5

Figure 6.3 Paragenesis of alteration and veins at the Eloise deposit. 6.6

Figure 6.4 Picture of halite-bearing fluid inclusion before (A) and after (B) ablation. 6.12

Figure 6.5 LA ICP MS signals obtained from Eloise fluid inclusions for the first (A) and the fifth (B) suite of analyzed elements. 6.12

Figure 6.6 Diagram displaying minimum, maximum and average concentrations of major and trace elements for multisolid (A) and halite-bearing (B) fluid inclusions determined from LA ICP MS analysis.. .....6.19

Figure 6.7 Average composition of multisolid and halite-bearing fluid inclusions from the Eloise deposit determined using LA-ICP-MS analysis..... 6.20

Figure 6.8 Plots of the concentrations of major and trace elements in fluid inclusions from the Eloise deposit. 6.21

Figure 6.9 Comparison between average fluid inclusion composition of fluid inclusions from the Eloise deposit and from the SRBP determined from LA-ICP-MS analysis. 6.27

Figure 6.10 Plots of the concentrations of major and trace elements in fluid inclusions from the Eloise deposit and from the SRBP. 6.29

Chapter 7 - Part I Discussion

Figure 7.1 Proposed model for the formation of the SRBP……..7.11

Figure 7.2 Simplified map of the Eastern Fold Belt showing sample locations for previous fluid inclusions studies. 7.12

Figure 7.3 Figure illustrating the possible relationships between multisolid and halite-bearing fluid inclusions and implication for ore deposition at the Eloise Cu-Au deposit. 7.14

Figure 7.4 Isocon diagrams illustrating rock geochemistry variations related to the major alteration stages at the Eloise Cu-Au deposit. 7.17

Figure 7.5 Average composition of multisolid and halite-bearing fluid inclusions for each sample determined from LA ICP Ms analysis. 7.22

Figure 7.6 Selected plots comparing the chemistry of multisolid and halite-bearing fluid inclusions…….7.23

Chapter 8 - Geochemical modelling of a Zn-Pb skarn: constraints from LA-ICP-MS Analysis of Fluid Inclusions

Figure 8.1 Location map and geology of the Bismark deposits, Chihuahua. 8.7

Figure 8.2 Diagram showing the paragenesis of alteration within the limestone at the Bismark deposit. 8.8

Figure 8.3 Element concentrations determined by LA ICP MS and PIXE.. ..... 8.11

Figure 8.4 Scatter plot illustrating the interelement ratio variation between PIXE and LA ICP MS……8.16

Figure 8.5 Mineral assemblages, composition of the aqueous phase and gases resulting from cooling the ore fluid from 350°C to 100°C..... 8.22

Figure 8.6 Results of reaction of the ore fluid with host rock at constant temperature (350°C)…….8.25

Figure8.7 Results of ore fluid- host rock interaction and cooling of the system from 350°C to 100°C. ……..8.27

List of Tables

Chapter 2 – Regional Geology of the Mt Isa Inlier

Table 2. 1 Summary and characteristics of major sodic (-calcic) alteration events in the Eastern Fold Belt..... 2.9

Table 2.2 Characteristics of IOCG deposits in the Eastern Fold Belt……..……2.12

Chapter 3 – Geology and petrography of the Suicide Ridge Breccia Pipe

Table 3.1 Summary and description of samples collected for petrographic and fluid inclusion studies.....3.10

Chapter 4 - Fluid chemistry and conditions of the Suicide Ridge Breccia Pipe (I): Fluid inclusion paragenesis, classification and microthermometry

Table 4.1 Description of samples selected for the fluid inclusion study and of analysis undertaken for each samples……..…….. 4.2

Table 4.2 Summary and classification of the types of fluid inclusions observed associated with the barren SRBP. 4.5

Table 4.3 Relative abundance of each fluid inclusion type in the different samples.....4.5

Table 4.4 Summary of microthermometry data obtained from type I and II fluid inclusions……. 4.20

Table 4.5 Bulk fluid properties of type IIa fluid inclusions.....4.27

Table 4.6 Summary of microthermometry measurements for type III, IV and V fluid inclusions…… 4.31

Chapter 5 – Fluid Chemistry and Conditions of the Suicide Ridge Breccia Pipe (II): Microanalytical, Bulk and Microprobe Analysis

Table 5.1 LA ICP MS results for type III and IV fluid inclusions ……..5.8

Table 5.2 Average, maximum and minimum composition of type III and IV fluid inclusions determined using LA ICP MS analysis. 5.13

Table 5.3 Average, maximum and minimum composition of type III fluid inclusions in granite clast and ironstone samples determined using LA ICP MS analysis..... 5.19

Table 5.4 Summary of results obtained from crush leach analysis. 5.22

Table 5.5 Microprobe data on apatites from granite clasts and ironstones found within the breccia pipe…….…….5.30

Chapter 6 – A comparison of hydrothermal fluids related to the Eloise Cu-Au deposit and to the Suicide Ridge Breccia Pipe

Table 6.1 Summary of fluid inclusion characteristics from the Eloise deposit. 6.8

Table 6.2 Summary of samples selected for fluid inclusion LA ICP MS analysis..... 6.10

Table 6.3 Chemistry of fluid inclusions from the Eloise deposit determined with LA ICP MS analysis…….6.16

Table 6.4 Comparison of the main fluid inclusion features from the Eloise deposit and the SRBP…….. 6.25

Table 6.5 Average, minimum and maximum composition of fluid inclusions from the Eloise deposit and from the SRBP…….6.28

Chapter 8 - Geochemical modelling of a Zn-Pb skarn: constraints from LA-ICP-MS Analysis of Fluid Inclusions

Table 8.1 Summary of fluid inclusions characteristics from the Bismark deposit.. ..... 8.8

Table 8.2 PIXE analysis of ore stage low-salinity fluid inclusions from the Bismark deposit…… 8.9

Table 8.3 LA ICP MS analysis of ore stage low-salinity fluid inclusions from the Bismark deposit……... 8.12

Table 8.4 Input data used to constrain the initial fluid composition of the fluid used for simulation of ore-forming processes. 8.20

List of Plates

Chapter 3 – Geology and petrography of the Suicide Ridge Breccia Pipe

Plate 3.1 Photographs of rock types observed in outcrop at the SRBP 3.7

Plate 3.2 Field and thin section pictures illustrating characteristics of the breccia.....3.12

Plate 3.3 Representative pictures of textures and mineralogy of granite clasts....3.15

Plate 3.4 Representative pictures of alteration in granite clasts 3.18

Plate 3.5 Photographs showing key characteristics of Fe oxide-rich rocks……..3.23

Chapter 4 - Fluid chemistry and conditions of the Suicide Ridge Breccia Pipe (I): Fluid inclusion paragenesis, classification and microthermometry

Plate 4. 1 Type I fluid inclusions 4.8

Plate 4. 2 Type I and II fluid inclusions 4.10

Plate 4.3 Type III and VI fluid inclusions 4.13

Plate 4.4 Relationship between albite alteration and type III fluid inclusions 4.15

Plate 4. 5 Type V fluid inclusions..... 4.18

Chapter 1

Chapter 1 - Introduction

1.1. General introduction

The large number of works published each year on fluid inclusion studies applied to ore deposit research illustrates the importance of this topic. Fluid inclusions represent a direct sample of ore forming fluids and thus provide a valuable source of information about the chemistry and conditions of such fluids and ore forming processes. The study of fluid inclusions in this thesis was used as a research tool to characterize fluids associated with specific types of deposits and related hydrothermal systems and to investigate ore deposition processes with the ultimate aim of addressing key questions relating to ore genesis. Two systems were investigated: the barren Suicide Ridge Breccia Pipe (SRBP), located in the Snake Creek Anticline of the Cloncurry district, Queensland, Australia and the Bismark Zn skarn deposit, situated in northern Chihuahua, Mexico. The first part of the project focuses on the study of the barren SRBP, one of numerous breccia occurrences in the Eastern Fold Belt (Marshall, 2003; Oliver et al., 2006) and illustrates how information from a number of different fluid inclusion techniques can be integrated in order to draw conclusions about ore-forming processes and ore deposit models. Interest in breccia systems in the Cloncurry district is related to their possible link with iron oxide copper-gold deposits. Much of the fluid inclusion research in the district has focused on fluids associated with ore deposits (Adshead, 1996; Baker, 1998; Rotherham et al., 1998; Williams et al., 2001; Mustard et al., 2004; Williams, personal communication), while few studies have dealt with

regional fluids (Fu et al., 2003; Fu et al., 2004a; Fu et al., 2004b) and in particular barren breccia systems (de Jong and Williams, 1995; Marshall, 2003; Oliver et al., 2006). Therefore, the aims of this part of the project are primarily to determine the fluid characteristics associated with the barren SRBP and to compare them with fluids linked to ore deposits in order to understand the key differences between barren and mineralized systems. Research tools include conventional methods such as fluid inclusion petrography and microthermometry combined with more cutting-edge techniques such as Laser Ablation Inductively Coupled Plasma Mass Spectrometry (LA ICP MS). The study has important implications for the genesis of breccia pipes in the Cloncurry district, particularly in relation to the role played by fluids during brecciation, and for the nature and origin of fluids that produced widespread sodic (-calcic) alteration in the district. The research also offers new insights into the nature of fluids associated with IOCG deposits and into processes involved in the formation of Cu-Au mineralization in the Cloncurry district. The second part of the project illustrates how data obtained from fluid inclusions can be applied to geochemical modeling simulations of ore-forming processes. The system chosen for this application is the Zn Bismark deposit, one of several base metal-rich high-temperature, carbonate-replacement deposits hosted in northern Mexico. The Bismark deposit was chosen because of its well constrained geology and fluid inclusion data (Baker and Lang, 2003; Baker et al., 2004). Results from the modelling, and in particular the close reproduction of ore stage minerals of the Bismark deposit, support the application of fluid inclusion data to modelling in order to test ore genesis hypothesis.

1.2. **Thesis aims**

1. **Define the chemistry of fluids associated with the SRBP using a combination of conventional and cutting-edge analytical techniques**

The thesis reports a detailed study of the physical-chemical properties of the fluids associated with the SRBP. Information was gathered employing an innovative approach that combines the application of several analytical techniques. In addition to conventional fluid inclusion petrography and microthermometry, the study included cathodoluminescence analysis, laser Raman spectroscopy (LRS), bulk crush-leach, microprobe analysis and laser ablation inductively coupled mass spectrometry (LA ICP MS). A review of fluid inclusion analytical techniques is reported in Section 1.5.

New fluid chemistry data combined with geological and petrographic evidence and with the integration of existing published data are used to define a model for the genesis of the SRBP.

2. **Identify key differences characterizing barren and mineralized systems in the Cloncurry district**

For this purpose was carried out a detailed comparison of fluids associated with the SRBP and fluids from the Eloise Cu- Au deposit. New quantitative microanalysis of fluids from the Eloise deposits by LA ICP MS has been presented and provided the basis of a refined model for the genesis of the deposit. Comparison of barren and mineralized hydrothermal fluids was also expanded to major IOCG deposits and regional barren systems in the Eastern Fold Belt.

3. Application of fluid inclusion data to geochemical modelling of ore deposition processes

Geochemical modelling is a powerful tool that can be used to quickly test hypotheses about ore genesis. Previous geochemical modelling simulations of fluid-rock interactions utilized a model fluid whose composition was generally estimated equilibrium reaction with a model rock prior to entering the system (e.g. Komninou and Sverjensky, 1995; Komninou and Sverjensky, 1996) due to the inability of analytical techniques to accurately determine the ore fluid chemistry. In this thesis, new microanalytical fluid inclusions data provided the basis for geochemical modelling simulations of ore forming processes. For the modelling, ideally, it would have been best to utilize the IOCG data from the Eloise Cu-Au deposit. However, IOCG deposits in the Cloncurry district are very complex systems whose genesis and particularly fluid nature and ore-forming processes are still subject of debate and controversy. In particular, fluid inclusions regarded as the ore-forming fluid have very high salinity (40-60 wt% NaCl equiv.) and contain several (3 to 5) daughter phases indicating a complex aqueous system. Current thermodynamic models are unable to model such complex fluids. Therefore, as an alternative the Zn-rich Bismark skarn deposit was selected for the modeling test due to its well constrained geology and fluid inclusion data. In addition, it was felt that the geochemical modelling section of the thesis represents a standalone scientific paper. Therefore, it is presented in a journal submission format. It is, however, an integral part of the thesis as it presents a new approach in the investigation of hydrothermal and mineralizing processes based on microanalytical fluid inclusion analysis.

1.3. **Methodology**

Geological mapping of the SRBP was conducted between 2004 and 2005 and included the documentation on the nature of breccia groundmass and clasts, the nature of the host rock and alteration affecting the pipe (Chapter 3). The fieldwork also included the collection of samples for petrography and fluid inclusions studies (Chapters 3, 4, 5 and Appendix 3.1). The composition of the breccia and ironstones were determined through the observations of hand specimen, polished thin sections and microprobe analysis (Chapter 3).

A detailed fluid inclusion study was conducted to characterize the fluids associated with the SRBP. The research study integrated the use of several different techniques including a paragenetic study, microthermometry, cathodoluminescence analysis, LA ICP MS, bulk crush-leach, laser raman analysis and microprobe analysis of apatites (Chapter 4 and 5). In addition the LA ICP MS study included fluid inclusions from the Eloise Cu-Au deposit (Chapter 6) and from the Zn Bismark skarn deposit (Chapter 8). Details and analytical procedures of each technique are reported in the appropriate chapters together with the presentation of analytical results.

Geochemical modelling was used to simulate ore-forming processes for Zn Bismark deposit utilizing data from fluid inclusion analysis (Chapter 8). Geochemical modeling simulations were performed using The Geochemists Workbench (GWB) software package (Bethke, 1996; Bethke, 2002). The thermodynamic dataset for the simulations was specifically created for this case (Cleverley and Bastrakov, 2005) and details are reported in Chapter 8.

1.4. **Thesis outline**

The thesis is subdivided into two parts for a total of 9 chapters. Chapters 1 and 9 are general introduction and conclusions respectively. Part I includes chapters 2 to 7 and focuses on the first of the two systems studied, the SRBP. Part II contains Chapter 8 and focuses on the Bismark Zn skarn deposit. The structure of the thesis and content of each chapter are outlined below.

Chapter 1 – Introduction

This chapter presents the general aims and structure of the thesis as well as the methodology applied in the research. The chapter concludes with a brief review of previous fluid inclusion research and geochemical modelling studies applied to ore deposits.

Part I: Geology and genesis of the barren Suicide Ridge Breccia Pipe, Snake Creek Anticline - Implications for IOCG formation in the Cloncurry district

Chapter 2 - Regional Geology of the Mt Isa Inlier

This chapter introduces the study of the SRBP, describes the regional geological context in which the breccia pipe formed and summarizes previous research on regional hydrothermal systems and IOCG deposits.

Chapter 3 - Geology and petrography of the Suicide Ridge Breccia Pipe

Chapter 3 focuses on the geology and petrography of the SRBP and associated rocks. In particular, the chapter presents detailed descriptions of the geometry and the field relationships of the breccia pipe, the distribution of breccia fragments, petrographic characteristics of the breccia and ironstone bodies found within and around the breccia pipe. The different types of alteration that affect the breccia and host rocks are also documented, and their relative timing.

Chapter 4 - Fluid chemistry and conditions of the Suicide Ridge Breccia Pipe (I): Fluid inclusion paragenesis, classification and microthermometry

Chapter 4 is the first of two chapters dedicated to the study of fluid inclusions. This chapter in particular focuses on the classification of fluid inclusion types and their temperature, pressure and density through the study of the fluid inclusion paragenesis, microthermometric and laser Raman analysis.

Chapter 5 - Fluid chemistry and conditions of the Suicide Ridge Breccia Pipe (II): microanalytical, bulk and microprobe analysis

This chapter focuses on the investigation of the chemistry of the fluids associated the SRBP using several analytical techniques that include LA ICP MS, bulk crush-leach and microprobe analysis.

Chapter 6 – A comparison of hydrothermal fluids related to the Eloise Cu-Au deposit and to the Suicide Ridge Breccia Pipe

In this chapter results from LA ICP MS analysis of fluid inclusions from the Eloise Cu-Au deposit are presented and discussed. This study aims to expand the

knowledge of the chemistry of fluids associated with IOCG deposits in the Cloncurry district and provide new insights into ore-forming processes. The chapter also addresses the issue of the formation of barren versus mineralized systems and for this purpose the fluid inclusions associated with the Eloise deposit are compared to fluid inclusions related to the Suicide Ridge Barren Breccia Pipe.

Chapter 7 - Discussion

The main results of the study of the first part of the project are here presented and discussed. The chapter is subdivided into three main sections. In the first section the genesis and evolution of SRBP are discussed with particular attention to the fluids involved in the pipe formation and albite alteration. In the second section the nature and origin of fluids from the Eloise Cu-Au deposit are discussed together with possible models for the genesis of the deposit. The final section focuses on a comparison between fluids associated with IOCG deposits, intrusion-related hydrothermal systems and regional barren environments in the Cloncurry district that aims to determine possible differences between barren and mineralized systems.

Part II

Chapter 8 - Geochemical modelling of a Zn-Pb skarn: constraints from LA ICP MS analysis of fluid inclusions

The second part of the thesis focuses on the Bismark Zn skarn deposit. This study represents an attempt to apply fluid inclusion data obtained from LA ICP MS analysis to constrain the initial composition of the ore-forming fluid in geochemical modelling simulations of possible ore-forming processes.

Chapter 9 - Conclusions

This chapter summarizes and highlights the major findings of the research project and broader implications for magmatic-hydrothermal processes.

1.5. **General background**

The potential of fluid inclusion research for unveiling the nature of mineralizing fluids and ore-forming processes was first recognized by Sorby (1858) almost 150 years ago. Since then the study of fluid inclusions in general, and associated to ore deposits in particular, has developed significantly thanks to the work of many researchers, in particular Roedder from the 60's onward, and benefiting, especially in the last few decades, from technological advances that allowed the development of innovative analytical methods and the improvement of existing techniques (Roedder, 1967; Roedder, 1984; Shepherd et al., 1985; Lattanzi, 1991; Boiron and Dubessy, 1994; Lattanzi, 1994; Roedder and Bodnar, 1997; Shepherd and Rankin, 1998; Wilkinson, 2001). The information that can be obtained from fluid inclusions includes temperature, pressure, density and composition. This information can be used to improve the knowledge and understanding of the nature and origin of mineralizing fluids, conditions of metal transport as well as to identify processes, particularly those that may have led to ore deposition. Temperature, pressure, density, salinity as well as major salt and volatile composition are routinely obtained from microthermometric measurements. Determination of the detailed chemistry of the fluids was for many years restricted to microthermometry and bulk methods (e.g. Shepherd and Rankin, 1998) which provided qualitative or at best semi-quantitative analysis. Nowadays there are a large number of

techniques available for fluid inclusions analysis, spanning from the bulk methods to the recently developed single inclusion microanalytical techniques including high sensitivity analytical methods such as ICP MS and microbeam technologies.

The analytical procedure of bulk methods generally include three steps: opening the inclusions, releasing the inclusion content and analyzing the extract (Roedder and Bodnar, 1997). There are several variations of the above procedure mainly relating to the way the inclusion content is released (i.e. crushing, thermal decrepitation) and the instrument used for the analysis (i.e. ion chromatography, ICP) (Roedder, 1990; Roedder and Bodnar, 1997; Shepherd and Rankin, 1998; Gleeson, 2003). The major advantages of bulk methods include the capability of analyze anions, the capacity to analyze fluid inclusions too small for single inclusions analysis and to generate data rapidly and cheaply for a large number of inclusions (Shepherd and Rankin, 1998; Gleeson, 2003). On the other hand, bulk methods suffer particularly from problems related to sample contamination, especially when the material is very fine grained, and of loss of material during the preparation and extraction of the sample (Roedder, 1990; Roedder and Bodnar, 1997; Shepherd and Rankin, 1998; Gleeson, 2003). Furthermore, since the techniques provide an average composition of the fluid contained in the sample, the analyzed samples should contain only one or at least a dominant generation of inclusions (Roedder, 1990; Roedder and Bodnar, 1997; Shepherd and Rankin, 1998; Gleeson; 2003). In these cases to avoid such inconvenience the use of single inclusion techniques is more appropriate.

Among the most widely used single inclusion methods are the non destructive laser Raman spectroscopy (LRS), proton induced X-ray emission (PIXE), synchrotron X-ray fluorescence microanalysis (SXFMA) and destructive laser ablation (LA). Details and overviews of LRS methodology can be found in recent reviews by Turrell and

Corset (1996), McCreery (2000), Burke (2001) and Burruss (2003). In fluid inclusion analysis LRS is particularly used for the determination of gas species and also for the identification of certain daughter phases. The method is based on the inelastic scattering produced by the vibration of molecular bonds when illuminated with monochromatic light. The inelastic scattering produces a shift in frequency of a small portion of the incident light (10^{-8} % of the incident intensity), the Raman scattering, that is characteristic of the molecular species that cause the scattering (Burke, 2001; Burruss, 2003). One of the weaknesses of this method is the inability to identify mono-atomic ions in solutions because the Raman scattering is produced by molecular vibrations (Burke, 2001; Burruss, 2003). Determination of aqueous species is restricted to polyatomic anions. The technique is particularly useful for the identification of daughter minerals characterized by strong oxygen bonds such as oxides, carbonates and sulphates, whereas minerals with ionic bonds (e.g., halite, sylvite) are usually non-detectable (Burke, 2001).

PIXE analysis is non-destructive and utilizes a proton beam to irradiate the sample that produces characteristic secondary X-rays. Quantification of PIXE analysis requires modelling of the fluid inclusion geometry and estimation of depth and thickness (Ryan et al., 1991; Heinrich et al., 1992; Ryan et al., 1993), that may result in significant errors (up to 30 %; Heinrich et al., 1992). The estimation of the inclusion depth is particularly critical influencing the determination of concentrations of light elements due to absorption of low-energy X-rays (K lines for $Z < 21$ and L lines for $Z < 50$) producing, for example, errors of more than 50 percent in Cl concentrations for depth uncertainty of ±1.5μm (Heinrich et al., 1992). Additional sources of error are related to heterogeneities in the inclusion, such as the presence of vapour and/or daughter phases, due to variations in X-ray absorption and variations in beam intensity

for different vapour bubble and/or crystal position (Heinrich et al., 1992; Ryan et al., 1991). Detection limits vary significantly depending on the inclusion size, depth, nature of the matrix and atomic mass (Z) of the analyzed elements. PIXE is commonly combined with proton induced gamma-ray emission (PIGE) used for the determination of lighter elements (Z<14).

SXFMA analysis is non-destructive and utilizes an X-ray beam to irradiate the sample that generates characteristic secondary X-rays. Detail on the method and application to fluid inclusion studies can be found in the review by Vanko and Mavrogenes (1998) and in several other publications (Frantz et al., 1988; Rankin et al., 1992; Vanko et al., 1993; Mavrogenes et al., 1995; Philippot et al., 1998; Buhn and Rankin, 1999; Philippot et al., 2000; Menez et al., 2001; Philippot et al., 2001; Menez et al., 2002; Cauzid et al., 2004; Rickers et al., 2004; Cauzid et al., 2006). The quantification of SXFMA analysis requires fluorescence adsorption corrections related to the depth and thickness of the single fluid inclusion similar to PIXE (Vanko and Mavrogenes, 1998). Detection limits vary significantly depending on the host mineral, analyzed element and geometry-related factors (e.g. size and depth of the inclusion) (Mavrogenes et al., 1995; Vanko and Mavrogenes, 1998). In general, detection limit vary from around 25 ppm for Mn to around 1000 ppm for Cl (Vanko and Mavrogenes, 1998). Relative error is estimated in the range between 10 and 40% depending on the analyzed element (Vanko and Mavrogenes, 1998).

Laser ablation is a destructive technique in which the fluid inclusion is opened by a laser, the content volatilized and transported and analyzed in a spectrometer. Variations of the methods are related to the choice of the employed laser and method of detection (ion mass spectrometry or photon emission spectrometry). In this thesis inductively coupled plasma mass spectrometry (LA ICP MS) was used to analyze fluid

inclusions from the SRBP, from the Eloise Cu-Au deposit and the Bismark Zn-Pb skarn deposit. Detection limits vary significantly and must be determined for each element in each inclusion being a function of the mass of the element, the size and shape of the inclusion and the number of elements measured from a single inclusion (Heinrich et al., 2003). Standard detection limits for fluid inclusions of 25μm are in the μg range. Imperfect sampling of inclusions, particularly of inclusions containing daughter crystals, is one of the primary source of uncertainties (Heinrich et al., 2003). LA ICP MS do not suffer depth-related or inclusion size and geometry problems as much as PIXE and SXFMA (Heinrich et al., 2003; Allan et al., 2005).

Each microanalytical technique has its own strength and weaknesses so that the choice of the method to employ depends on the type of problem to solve and the fluid inclusion material to analyze. One of the innovations described in this thesis is the use of combined technique in order to obtain data analysis as detailed and complete as possible. This approach was applied to characterize the fluids associated with the Suicide Ridge barren breccia pipe, focus of the first part of the thesis.

A further new development utilized in this thesis is the application of fluid inclusion data to geochemical modelling. Natural geological processes are often not observable and computer simulations of geochemical processes offer the undoubted advantage to test potential models of ore-forming processes relatively quickly and inexpensively. Results from modelling can be readily compared with the natural system and thus enable hypothesis testing about ore deposition. Geochemical modelling has been inevitably linked to the development of computers. Nonetheless, the first geochemical calculations in the sixties were computed by hand (Garrels and Thompson, 1962; Garrels and Mackenzie, 1967) and the first computerized geochemical simulation was run by Helgeson (1968). This first code was followed by a number of software

packages for geochemical modelling such as SOLMNEQ (Kharaka and Barnes, 1973), WATEQ (Truesdell and Jones, 1974), SOLVEQ and CHILLER (Reed, 1982) and EQ3/EQ6 (Wolery and Jarek, 2003). Nowadays, there is a large number of software packages for geochemical modelling available commercially or that can be downloaded directly from the web, including some updated versions of the above mentioned computer software (i.e. EQ3/EQ6; Wolery and Jarek, 2003). The quality of modelling results depends on the quality and completeness of the data applied and of the dataset used.

In the past the composition of the model fluid in geochemical modelling studies of fluid-rock interaction was commonly reconstructed assuming equilibrium with a model rock prior to entering the system (Sverjensky, 1987; Heinrich, 1990; Lu et al., 1992; Komninou and Sverjensky, 1995; Komninou and Sverjensky, 1996). The recent progresses in fluid inclusion analysis discussed above now allow the determination of a large number of elements with high level of accuracy and precision, providing the basis for modeling of geochemical processes. However, there are still very few examples of this type of application in the literature. Heinrich et al. (2004) and Heinrich (2005) utilized LA ICP MS fluid inclusion results to model the ascent and relative chemical-physical changes of hydrothermal fluids from a magmatic source to the near-surface environment in order to investigate the conditions for gold transport and deposition in porphyry and epithermal systems. Mark et al. (2004) used LA ICP MS fluid inclusions results from Ernest Henry Cu-Au deposit to predict the geochemical characteristics of the outflow zones of the deposit.

The solution of geochemical problems requires the knowledge of the standard molal thermodynamic properties of all the various species involved in the modelled process over the temperature and pressure range of interest. Theories and equations for

the calculation of these properties were developed along with experimental data through the contributions of several researchers including Helgeson and Kirkham (1974a; 1974b), Helgeson et al. (1981), Shock and Helgeson (1988; 1990), Tanger and Helgeson (1988), Shock et al. (1989), Johnson and Norton (1991) and Sverjensky et al. (1997). In some cases the data were organized in software such as SUPCRT92 (Johnson et al., 1992) and UNITHERM (Shvarov and Bastrakov, 1999) capable of storing and calculating thermodynamic properties at various T-P conditions. In other cases data were incorporated in datasets accompanying modelling software packages. Geochemical modeling simulations in this study were carried out using The Geochemists Workbench (GWB) software package (Bethke, 1996; Bethke, 2002) using a thermodynamic dataset specifically created for this case study to fit the T-P conditions (Cleverley and Bastrakov, 2005; Chapter 8). The modeling test required a system characterized by relatively low complexity starting from the geological setting, through to fluid inclusion properties, to the genesis of the deposits. IOCG deposits in the Cloncurry district are very complex systems characterized by highly saline complex fluids (40-60 wt% NaCl equiv.) that commonly contain several (3 to 5) daughter phases. For all of these reasons IOCG deposits were not chosen for the modeling test. The deposit selected for this application is the Zn-rich Bismark skarn deposit due to its well constrained geology and fluid inclusion data (Baker and Lang, 2003; Baker et al., 2004).

Part I: Geology and genesis of the barren Suicide Ridge Breccia Pipe, Snake Creek Anticline - Implications for IOCG formation in the Cloncurry district

Chapter 2

Chapter 2 – Regional Geology of the Mt Isa Inlier

2.1. Introduction

The occurrence of breccia in close association with a wide variety of hydrothermal ore deposit has been well documented in several studies (Sillitoe and Sawkins, 1971; Meinert, 1982; Scherkenbach et al., 1985; Sillitoe, 1985; Meinert et al., 2003). Breccia commonly occurs as host for the mineralization, but it also plays an important role as a pathway for mineralizing fluids. In the Cloncurry district brecciation is widespread particularly in the proximity of the Cloncurry fault and is developed predominantly within calc-silicate rocks of the Corella Formation (Marshall, 2003). These breccia systems are commonly associated with extensive regional Na (-Ca) and later (K-) Fe alteration and have been interpreted as conduits for these metasomatic fluids (de Jong and Williams, 1995; Marshall, 2003). The aim of this chapter is to describe the Mt Isa Inlier, the regional geological context of the Suicide Ridge Breccia Pipe (SRBP), and to summarize and the review previous research on breccias in the Cloncurry district.

2.2. Regional geology

2.2.1. Stratigraphy and structural evolution

The Mount Isa Inlier is a large Proterozoic terrain in northwest Queensland, Australia. The Inlier has been subdivided into three tectonostratigraphic blocks, the Western Fold Belt, the Kalkadoon-Leichardt Belt and the Eastern Fold Belt (EFB) (Blake, 1987). Foster and Austin (2007) recently revised the chronostratigraphic history of the EFB (Figure 2.1) and identified four major periods of magmatism and sedimentary accumulation: 1890-1850 Ma, 1800-1725 Ma, 1710-1690 Ma, and 1680-1610 Ma. The older sequence comprises sedimentary and volcanic rocks that predate and were deformed by the Barramundi Orogeny (1900-1870 Ma; Blake, 1987) and now form the basement of the Mt Isa Inlier and felsic volcanic rocks of Cover Sequence 1 of Blake (1987) that are restricted to Kalkadoon-Leichardt Belt (Foster and Austin, 2007). In the EFB basement rocks are represented by the Plum Mountain Gneiss and the Kurbayia Migmatite (Foster and Austin, 2007). The second period of sedimentation (1800-1725 Ma) broadly corresponds to Cover Sequence 2 of Blake (1987). In the EFB the lowest stratigraphic unit ascribed to Cover Sequence 2 is the Argylla Formation 1781±3 Ma (1781±3 Ma, Page, 1998), which consists of felsic volcanic rocks (Derrick, 1980; Betts et al., 2006). The Argylla Formation in the Cloncurry district is overlain by the mafic volcanics of the Marraba Volcanics. These rocks are overlain by rocks of the Mary Kathleen Group that include calc-silicate dominated rocks of the Doherty (1725± 3 Ma; Page and Sun, 1998) and Corella Formation (1738±2 Ma; Foster and Austin, 2007; Page, Geoscience Australia Ozchron database), sandstone and quartzite of the Mitakoodi Quartzite (Betts et al., 2006; Potma and Betts, 2006) and limestone and argillite of the Overhang Jaspilite (Loosveld, 1989; Foster and Austin, 2007). The Mary

Kathleen Group also comprises the stratigraphically equivalent rocks of the Ballara Quartzite (1755±3 Ma) and the Mitakoodi Quartzite occurring in the Cloncurry district and in the Mary Kathleen Fold Belt respectively (Foster and Austin, 2007). In the Western Succession this period corresponds with deposition of rocks of the Leichhardt Superbasin (ca 1790-1730 Ma) (Jackson et al., 2000; Betts et al., 2006; Foster and Austin, 2007). Between 1710-1690 Ma sedimentation was mostly restricted to the Western Fold Belt with the deposition of rocks of the Calvert Superbasin (Jackson et al., 2000; Betts et al., 2006; Foster and Austin, 2007). The last period of accumulation is represented in the EFB by rocks of the Soldiers Cap Group, the Young Australia Group, the Tommy Creek Block (1630-1610 Ma) and likely the Mount Albert Group that correspond to Cover Sequence 3 of Blake (1987) (Foster and Austin, 2007). The Soldiers Cap Group include rocks of the Kuridala Formation (<1676 ± 5 Ma; previously assigned to the Mary Kathleen Group), turbitic pelite of the Llewellyn Formation (<1666 ± 14 Ma), psammopelites, pelites and metavolcanics of the Mount Norna Quarzite (1654 ± 4 Ma, <1693 ± 5 Ma) and metavolcanics, quartzite, carbonaceous pelite and iron-formation of the Toole Creek Volcanics (1658 ± 8 Ma) (Page, 1998; Page and Sun, 1998; Giles and Nutman, 2003; Hatton and Davidson, 2004; Betts et al., 2006; Foster and Austin, 2007). The Young Australia Group (1675-1610 Ma) comprises rocks of the Answer Slate, the Staveley Formation, the Marimo Slate and the Agate Downs Siltstone previously included in the Mary Kathleen Group (Foster and Austin, 2007). These units correlate with rocks of the Isa Superbasin in the Western Succession (Scott et al., 2000; Betts et al., 2006; Foster and Austin, 2007).

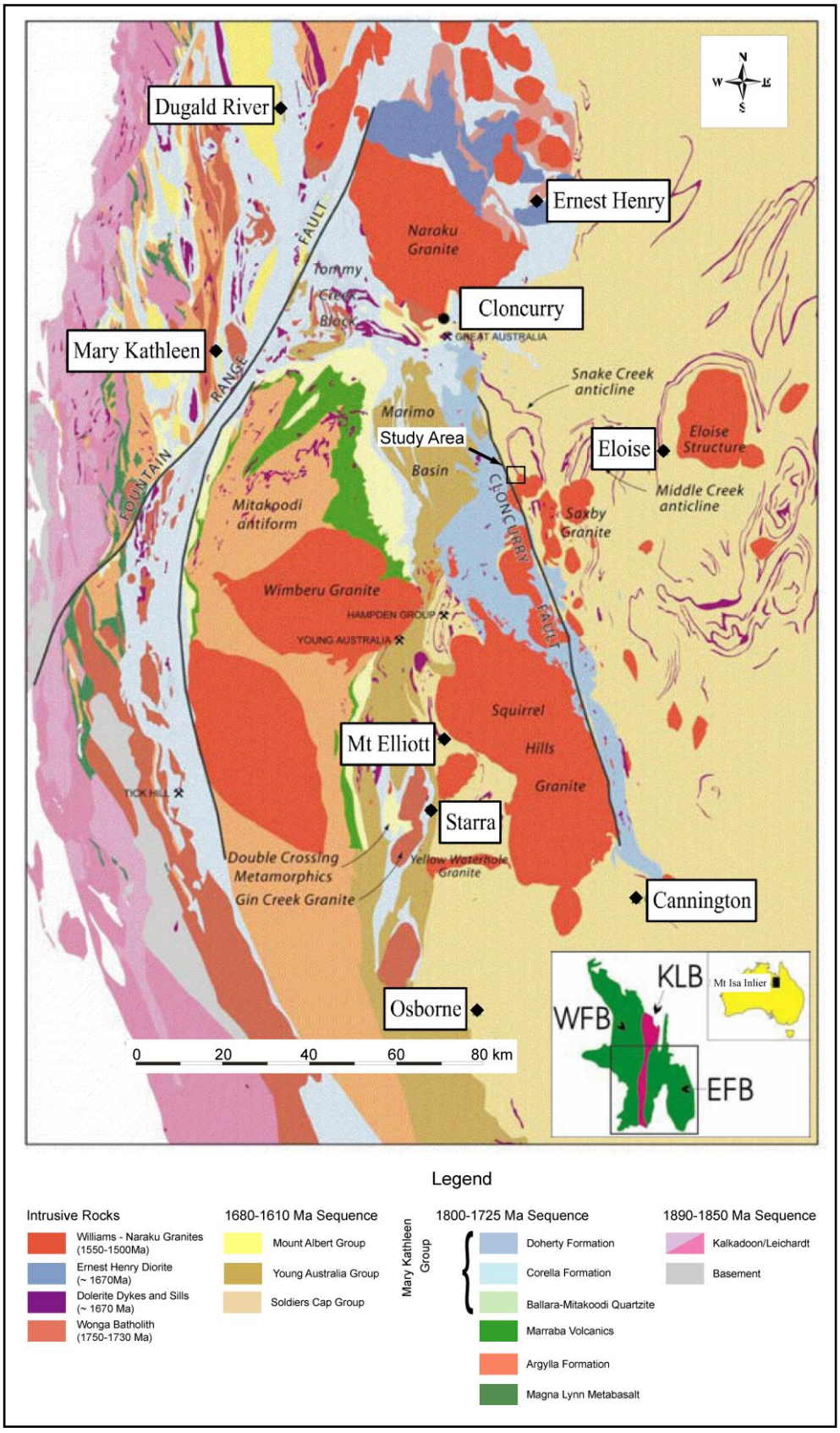

Figure 2.1 Simplified geology of the Eastern Fold Belt. Modified after Foster and Austin (2007)

Deposition was interrupted by the ca 1600-1500 Ma Isan Orogeny (Blake and Stewart, 1992; Page and Sun, 1998; Foster and Austin, 2007), which comprises three major stages (Bell, 1983): D_1 was a north-south compression event that produced east-west thrusting and folding; D_2 was an east-west compressive event that generated large-scale upright north-south-orientated folds; and D_3 was an east-west compressive event resulting in NNE-trending faulting and folding.

2.2.2. Metamorphism

The Isan Orogeny was accompanied by low pressure high temperature metamorphism with variable metamorphic grade from lower greenschist to upper amphibolite facies (Foster and Rubenach, 2006). Amphibolite and greenschist facies form alternate north-south oriented belts (Foster and Rubenach, 2006). The amphibolite facies belts are also generally wider towards the south and are observed in the Sybella Belt, west of Mt Isa, in the Mary Kathleen Fold Belt and south of Cloncurry (Foster and Rubenach, 2006). The peak of metamorphism in the Mt Isa Inlier is inferred to have occurred between 1595 and 1580 Ma and to have reached P-T conditions between 4 and 5 kbar and >650°C (Foster and Rubenach, 2006; Rubenach et al., 2007). In the Cloncurry district the peak of metamorphism reached a maximum of ~ 670°C and 4 to 5 kbar at the Cannington and Osborne mines (Foster and Rubenach, 2006; Rubenach et al., 2007).

2.2.3. Magmatism

The Mt Isa Inlier exhibits a protracted history of igneous activity (Blake, 1987; Wyborn et al., 1988; Pollard et al., 1998; Wyborn, 1998; Mark, 1999; Mark, 2001) (Figure 2.2). The earliest major episode of magmatism occurred between 1880 and 1840 Ma and generated felsic volcanic and granite emplacement (Wyborn et al., 1988). Additional igneous activity at around 1780 Ma produced rhyolitic to dacitic volcanic rocks (Blake, 1987).

Between 1750 and 1730 Ma the Inlier underwent a period of extension, the Wonga extensional event, when the Wonga Batholith was emplaced within rocks of the Mary Kathleen Fold Belt and of the Kalkadoon–Leichhardt Belt (Pearson et al., 1992; Page and Sun, 1998). The batholith is composed of tholeiitic gabbros and dolerite rocks and granites (Pearson et al., 1992; Oliver et al., 1994; Williams, 1998b). The emplacement of the Wonga batholith produced scapolitization, sodic (-calcic) alteration and formation of skarns (Oliver et al., 1994; Oliver, 1995). Granitoids of similar age in the Cloncurry district such as the Levian granite, ascribed to the Williams–Naraku event based on their location, are now inferred to belong to the Wonga magmatic event based on their older ages (Davis et al., 2001).

The Sybella Batholith was emplaced around 1670 Ma within rocks of the basement and of Cover Sequence 2 (Wyborn et al., 1988; Hoadley et al., 2001). These plutonic rocks are restricted to the Western Succession and are dominantly composed of granodiorite and alkali-feldspar granite (Wyborn et al., 1988).

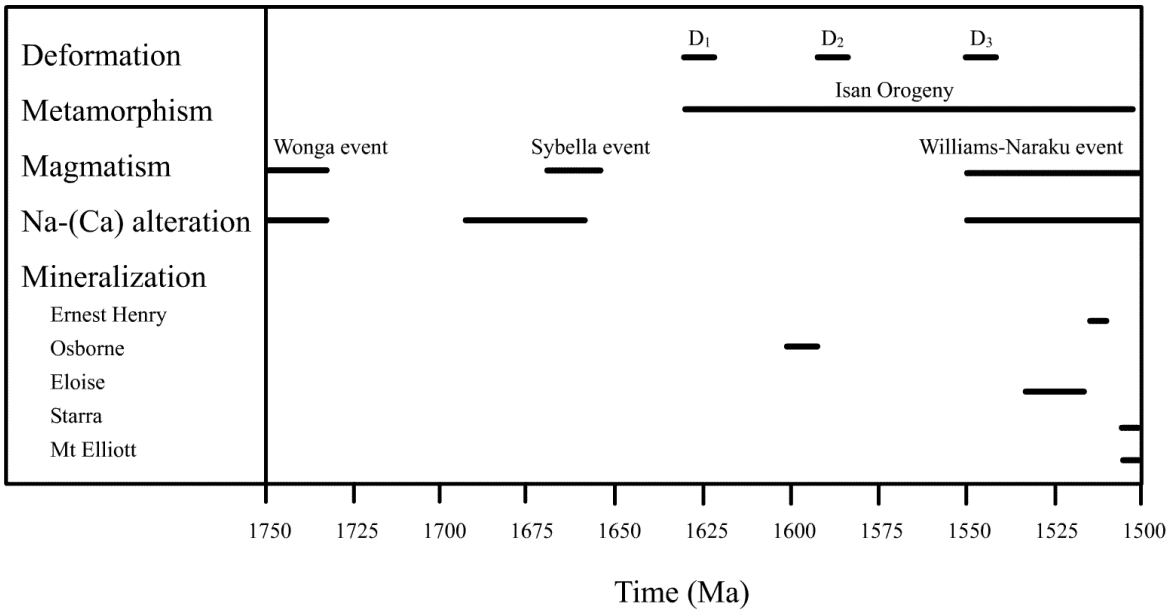

Figure 2.2 Summary of tectonic, metamorphic, magmatic, alteration and mineralization events in the Cloncurry district. The Sybella event is restricted to the Western Succession. References: Oliver (1995); Little (1997); Rotherham et al. (1998); Twyerould, (1997); Page and Sun (1998); Baker et al. (2001); Gauthier et al. (2001); Hoadley et al., (2001); Rubenach et al. (2001); Foster and Rubenach (2006); Foster and Austin (2007); Rubenach et al. (2007)

The latest major magmatic episode occurred during the Isan Orogeny after the metamorphic peak dominantly within rocks of the EFB and produced the Williams-Naraku Batholiths (ca 1550-1500 Ma) (Page and Sun, 1998; Wyborn, 1998). These rocks and in particular the younger (<1530 Ma) (Page and Sun, 1998) intrusions outcropping in the EFB were subdivided by Pollard et al. (1998) into two groups, the Cloncurry Supersuite and the Eureka Supersuite, based on distinct geochemical properties. The Cloncurry Supersuite dominantly consists of subalkaline granites and granodiorite and include the Saxby Granite, the Wiley Igneous Complex and likely part of the Malakoff Granite and Capsize granodiorite (Pollard et al., 1998). The Eureka Supersuite is characterized by mafic, intermediate and felsic intrusions and include the Mount Angeley Igneous Complex and likely the Squirrel Hills and Wimberu Granite

(Pollard et al., 1998). The Eureka Supersuite is spatially and temporally linked to sodic (-calcic) alteration in the Cloncurry district (Pollard et al., 1998).

2.2.4. Metasomatism

2.2.4.1. Sodic (-calcic) metasomatism

The EFB is characterized by several episodes of sodic-(calcic) alteration, summarized in Table 2.1. The earliest episode of hydrothermal alteration occurred in the Mary Kathleen Fold Belt and was related to fluid circulation associated with the extensional phase related to the emplacement of the Wonga Batholith (1750-1730) (Oliver et al., 1994; Oliver, 1995). During extension mafic and felsic magma intruded the sedimentary sequence that consisted of carbonate and evaporite rocks of the Corella Formation (Oliver et al., 1994). The fluid circulation associated with the emplacement of the intrusions caused scapolitic alteration and formation of skarns (Oliver et al., 1994; Oliver, 1995). Alteration is inferred to have formed at high temperature (500-700 °C) from a dominantly magmatic fluid (Oliver et al., 1994; Oliver, 1995).

In the Cloncurry district early, pre- Williams-Naraku magmatism albitization (1640-1690 Ma; Rubenach et al., 2007) has been observed in the Snake Creek Anticline and at the Osborne mine (Adshead et al., 1998; Rubenach and Barker, 1998; Rubenach et al., 2001; Rubenach and Lewthwaite, 2002; Rubenach et al., 2007). Albitites in the Snake Creek Anticline are commonly spatially related to mafic sill bodies (gabbro/dolerite/trondjemite) and local shear zones (Rubenach et al., 2007). Rubenach et al. (2007) suggested that the formation of these early albitites is related to fluid circulation associated with the emplacement of the mafic sill bodies.

Table 2.1 Summary and characteristics of major sodic (-calcic) alteration events in the Eastern Fold Belt. Mineral abbreviations after Kretz (1983; Appendix 2.1). Also Amph = amphibole.

	Timing	**T-P conditions**	**Alteration assemblage**	**References**
Mary Kathleen Fold Belt	1750-1730 Ma	500 - 700 °C 1.5 - 2 kbar	Cpx-Grt-Scp skarn, Scp-Ab shear zones, Scp-Amph alteration in mafic rocks	Oliver et al., 1994; Oliver, 1995
Eastern Fold Belt (Snake Creek Anticline and at the Osborne mine)	1640-1690 Ma	500 - 650°C 3 - 4.5 kbar	Ab-Rt ± Qtz-Bt-Kfs-Crd-St-Ged	Adshead et al., 1998; Rubenach and Barker, 1998; Rubenach et al., 2001; Rubenach and Lewthwaite, 2002; Rubenach et al., 2007
Eastern Fold Belt	< 1550 Ma	400 - 600 °C 2 - 4.5 kbar	Ab-Ttn-Amph-Cpx-bt-Ap-Ep-Mag-Hem-Rt-Qtz-Py	Mark, 1998; de Jong and Williams, 1995; Oliver, 1995; Mark, 1998; Mark and Foster, 2000; Marshall, 2003; Oliver et al., 2004

Extensive sodic (-calcic) alteration also developed in spatial and temporal association with the emplacement of the Williams Batholith (de Jong and Williams, 1995; Mark, 1998; Pollard et al., 1998; Mark and Foster, 2000; Perring et al., 2000; Pollard, 2001; Oliver et al., 2004) and is usually found within or close to brittle/ductile structures (Pollard, 2001; Oliver et al., 2004) such as large-scale faults, breccias, veins and shear zones (de Jong and Williams, 1995; Oliver, 1995; Baker and Laing, 1998; Mark, 1998; Marshall, 2003; Oliver et al., 2004). Sodic (-calcic) alteration is characterized by variable mineralogy (mostly albite with or without actinolite, titanite, apatite, diopside, quartz, rutile, biotite, magnetite, hematite, pyrite; Oliver et al. 2004

and references therein) that likely reflects local control (e.g. host rock) on the alteration mineralogy. Many studies report temperatures of formation of sodic (-calcic) alteration mostly between 400 and 600 °C and pressures between 2 and 4.5 kbar (de Jong and Williams, 1995; Oliver, 1995; Mark, 1998; Mark and Foster, 2000; Marshall, 2003; Oliver et al., 2004). The origin of fluids producing sodic (-calcic) alteration is controversial and proposed models include a dominant magmatic source (Mark, 1998; Mark and Foster, 2000; Perring et al., 2000; Pollard, 2001) and a crustal evaporitic and/or halite dissolution origin for the these fluids (Barton and Johnson, 1996; Kendrick et al., 2007a).

Sodic (-calcic) alteration has been described in host rocks of all major Cu-Au occurrences in the Cloncurry district and generally predate the main mineralization stage (Little, 1997; Rotherham, 1997; Adshead et al., 1998; Baker, 1998; Mark et al., 2000; Wang and Williams, 2001).

2.2.4.2. K-Fe alteration

Sodic-(calcic) alteration is commonly overprinted by later K-Fe metasomatism which is usually more localized than the former albitic alteration (Williams, 1998b). K-Fe metasomatism produces mineral assemblages of variable composition that in general include magnetite, hematite, quartz, K-feldspar, biotite amphibole and calcite. In some cases these assemblages host the mineralization (e.g., Starra; Rotherham, 1997).

2.2.5. Mineralization

The EFB hosts several mineral deposits that can be broadly subdivided in three groups: 1) ±Cu±Au±Ag±Co and; 2) ±Pb±Zn±Ag 3) U-REE (Williams, 1998b). The Cloncurry district is dominated by ±Cu±Au±Ag±Co occurrences the most significant including Ernest Henry Cu-Au, Osborne Cu-Au, Eloise Cu-Au, Mt Elliott Cu-Au and Starra Au-Cu deposits (Figure 2.1, Table 2.2). The deposits are characterized by many common features that include evidence of structural control on ore deposition, similar style and paragenesis of alteration, association with Fe-oxide rocks and hot ultrasaline fluids and generally similar ages of formation that postdated the peak of metamorphism in the region and coincided with the emplacement of the Williams-Naraku Batholiths (Adshead, 1996; Little, 1997; Rotherham, 1997; Twyerould, 1997; Adshead et al., 1998; Adshead-Bell, 1998; Baker, 1998; Baker and Laing, 1998; Perkins and Wyborn, 1998; Rotherham et al., 1998; Mark et al., 2000; Williams and Skirrow, 2000; Baker et al., 2001; Gauthier et al., 2001; Rubenach et al., 2001; Wang and Williams, 2001; Mark et al., 2006b). The deposits also display some important differences including variable Cu/Au ratios, host rocks, oxidation state and in the case of Osborne a different age of formation. Recent U-Pb dating on titanite from the skarn alteration halo around the ore and Re-Os on molybdenite from the ore at Osborne indicate ages of ca 1600-1590 Ma (Gauthier et al., 2001; Rubenach et al., 2001; Williams and Pollard, 2001) that suggest the deposit is older than other IOCG deposits in the district and formed broadly synchronous with early albitization.

Table 2.2 Characteristics of IOCG deposits in the Eastern Fold Belt. Mineral abbreviations after Kretz (1983). Also Amph = amphibole.

Deposit	Size and Grade	Age (Ma)	Host Rock	Ore and alteration mineralogy	Fluid inclusion types	References
Ernest Henry	166 Mt @ 1.1% Cu, 0.54 g/t Au	1510	Mary Kathleen Group brecciated and strongly altered felsic to mafic metavolcanics	Ccp, Py, Mag ore; Mag, Bt, Kfs, Grt, Py, Hem, Brt, Ms alteration	1) Hypersaline, multisolid (33–55 wt % NaCl equiv) 2) CO_2-rich 3) L+V±H (20 wt% NaCl equiv.)	Twyerould, 1997; Mark et al., 2000 and 2006b
Osborne	15.2 Mt @ 3.0% Cu, 1.05 g/t Au	1600–1590	Soldiers Cap Group feldspathic to pelitic schists, amphibolite and ironstones	Ccp, Py ± Hem or Po ore; Mag, Bt, Ab, Ms, Ab, Qtz, Py, Po, Hem, Amph, Cal alteration	1) Hypersaline, multisolid 603–70 wt % NaCl equiv) 2) CO_2-CH_4 3) L+V±H (20-37 wt% NaCl equiv.)	Adshead, 1998; Rubenach et al. 2001; Gauthier et al., 2001
Eloise	3.1 Mt @ 5.5% Cu, 1.4 g/t Au, and 16 g/t Ag	1530-1514	Soldiers Cap Group meta-arkose, quartz-biotite schists and amphibolite	Po, Ccp, Py ore; Po, Ccp, Chl, Act, Py, Mag, Ms, Qtz alteration	1) Hypersaline, multisolid (29–60 wt % NaCl equiv) 2) CO_2-rich 3) L+V±H (18-39 wt% NaCl equiv.)	Baker, 1998; Baker and Laing, 1998; Baker et al., 2001
Starra	7.4 Mt @ 1.9% Cu, 3.8 g/t Au	1505	Mary Kathleen Group magnetite-hematite ironstones and biotite-rich schists	Ccp, Py, Hem ore; Mag, Hem, Brt, Ab, Bt, Cal, Py, Act, Scp alteration	1) Hypersaline, multisolid (29–52 wt % NaCl equiv) 2) CO_2-rich 3) L+V±H (8-38 wt% NaCl equiv.)	Rotherham, 1997; Rotherham et al., 1998; Williams et al., 2001
Mt Elliott	3.3 Mt @ 3.6% Cu, 1.8 g/t Au	1505	Soldiers Cap Group amphibolite and carbonaceous schists	Py, Po, Ccp ore; Dio, Scp, Mag, Py, Po, Ccp alteration	1) Hypersaline, multisolid 2) CO_2-rich	Little, 1997; Wang and Williams (2001)

Host rocks for IOCG deposits in the Cloncurry district include brecciated and strongly altered felsic to mafic metavolcanics at Ernest Henry (Twyerould, 1997; Mark et al., 2000; Mark et al., 2006b), magnetite-hematite ironstones at Starra (Rotherham, 1997), meta-arkose, quartz-biotite schists and amphibolite of the Soldiers Cap Group at Eloise (Baker, 1998; Baker and Laing, 1998), amphibolite and pegmatite at Osborne (Adshead et al., 1998) and amphibolite and carbonaceous schists at Mt Elliott (Little, 1997; Wang and Williams, 2001). The Cu/Au ratio appears to be related to the nature of Fe-phase stable during mineralization, which reflects the temperature, oxygen and sulfur fugacity of the system (Williams and Pollard, 2001). In particular, the lowest Cu/Au ratios occur in hematite-rich ores (e.g. Starra; Rotherham, 1997) whereas the highest Cu/Au ratios are associated with pyrrhotite-rich deposits (e.g. Eloise; Baker, 1998) (Williams and Pollard, 2001). Fluid inclusion studies indicate that the ore-forming fluids were hot (>300-500°C), hypersaline (26-70 wt% NaCl equiv.) and CO_2-bearing (Adshead, 1995; Adshead, 1996; Baker, 1998; Rotherham et al., 1998; Mark et al., 2001; Williams et al., 2001). The genesis of these deposits is controversial, particularly in relation to the origin of the mineralizing fluids and the role played by granitoids in the mineralization process. A magmatic origin for the mineralizing fluids in IOCG deposits in the Cloncurry district has been favored by many authors based on the temporal association with magmatism and on stable isotope, fluid inclusion and geochemical data (Rotherham et al., 1998; Mark et al., 2000; Williams and Skirrow, 2000; Baker et al., 2001; Pollard, 2001; Mark et al., 2006a). Barton and Johnson (1996; 2000) proposed an alternative model for IOCG deposits globally invoking an evaporitic source for the mineralizing fluids with igneous rock contributions restricted to alteration and element abundances. Recently, the involvement of an external crustal fluid has been proposed for the formation of Cu-Au mineralization at Eloise and Osborne based on

halogen and noble gas data (Fisher et al., 2005; Kendrick et al., 2006). Recent genetic models inferred origins due to mixing between fluids of different source (Williams et al., 2001; Mark et al., 2006b; Kendrick et al., 2007b).

Pb±Zn±Ag occurrences include Cannington, Dugald River, Pegmont, Maramungee and Maronan (Williams, 1998b). These deposits, with the exception of Dugald River, occur in the southestern part of the district within high grade metamorphosed siliciclastic rocks (Williams, 1998b). The genesis of these deposits includes several possible models of formation such as syngenetic, syndiagenetic and syntectonic origins (Vaughan and Stanton, 1986; Newberry et al., 1993; Williams and Heinemann, 1993; Dixon and Davidson, 1996; Xu, 1997; Bodon, 1998; Chapman and Williams, 1998; Walters and Bailey, 1998; Williams, 1998a; Williams et al., 1998; Xu, 1998).

U-REE mineralization is represented in the district by the Mary Kathleen deposit located approximately 50 km west of Cloncurry within calcsilicates and marbles of the Mary Kathleen Group and in close association with a Wonga–age granite (Derrick, 1977; Page, 1983; Williams, 1998b). The mineralization is hosted within a garnet pyroxene skarn that replaced the Mary Kathleen Group rocks (Derrick, 1977; Williams, 1998b). Age dating revealed that the mineralization is considerably younger than the granite and associated skarn, but synchronous with regional deformation and metamorphism (Page, 1983; Maas et al., 1987). Oliver (1995) inferred that the skarn may have acted as a chemical trap for regional metamorphic fluids.

2.2.6. Brecciation

Previous research on regional breccia in the Cloncurry district includes studies by Tunks (1987), Ryburn et al. (1988a; 1988b), Oliver et al. (1990), de Jong and Williams (1995) and more recently works by Oliver et al. (2001; 2006), Marshall (2003) and Marshall and Oliver (2006). Ryburn et al. (1988a; 1988b) subdivided the breccias into two categories, the Corella breccias and the Gilded Rose breccias, and proposed for the latter a hydrothermal intrusive origin associated with the emplacement and crystallization of magmatic bodies.

Tunks (1987) worked on brecciated rocks of the Corella Formation and identified two genetically distinct groups of breccias. The Early Breccias are collapse breccias that formed in response to dissolution of evaporitic horizons, whereas the Late Breccias are hydrothermal breccias that formed in response to second boiling processes associated with the emplacement and cooling of granitoids (Tunks, 1987; Marshall 2003).

De Jong and Williams (1995) described the distribution and evolution of metasomatism in the proximity of the Cloncurry fault and found that the alteration was associated with breccia systems, providing evidence that the latter acted as conduits and traps for metasomatic fluids. De Jong and Williams (1995) also provided insight into the chemistry of metasomatic fluids. Fluid inclusion analysis in altered rocks revealed the involvement of high salinity fluids in both sodic (-calcic) and K-Fe alteration.

Oliver et al. (1990; 2001) attributed the cause of brecciation in the Mary Kathleen Fold Belt to the heterogeneous nature of the rocks. The different competency of strong metagranite bodies and weak calc-silicate rocks of the Corella Formation likely resulted in a localization of the stress at the boundaries between the two

lithologies with formation of fractures that may have driven large fluid circulation that in turn may have triggered the brecciation (Oliver et al., 2001).

The contribution of Marshall (2003) represents the most comprehensive work on breccias in the Cloncurry district to date. In his PhD thesis, he described the distribution of brecciation and metasomatic alteration within the Corella Formation, and focused in particular on mechanical aspects of breccia formation and the role of brecciation in channeling metasomatic fluids. He proposed that brecciation occurred in part in a ductile regime, due to retrograde buckle folding, and in part was related to the emplacement of granitoids, which generated high fluid pressure and strain rates that, in combination with low temperatures during the late stages of deformation, favored rock fracturing. Brecciation was associated with widespread sodic (-calcic) alteration that formed from hot metasomatic fluid (400-600°C) of inferred magmatic origin (Marshall, 2003; Marshall and Oliver, 2006).

Oliver et al. (2006) proposed a magmatic-hydrothermal origin for breccia dikes and pipes in the Cloncurry district related to fluid overpressuring generated at the top of magmatic bodies in response to cooling and crystallization. The study suggested that the overpressuring needed for the brecciation was generated at depths of ~ 10 km by separation and volume expansion of a CO_2-rich phase from the magma, similar to processes that leads to formation of kimberlite pipes and diatremes (Wilson and Head, 2004).

Other research on breccias included those associated with ore deposits in the Cloncurry district (Pollard et al., 1997; Rotherham, 1997; Baker, 1998; Baker et al., 2001; Mark et al., 2006b). Brecciation at Eloise developed mainly during the mineralization stage, when gangue and ore phases replaced and brecciated earlier alteration (Baker, 1998; Baker et al., 2001). Rotherham (1997) inferred that brecciation

and shearing associated with Fe-metasomatism of previously Na-metasomatised rocks produced massive ironstone bodies, main host of the mineralization, at Starra. The breccias consist of quartz-albite clasts with a matrix of K-Fe minerals (biotite-magnetite) and sulphides (Rotherham, 1997). A breccia pipe body consisting of dominant felsic volcanic rocks is the main host for Cu-Au mineralization at Ernest Henry (Mark et al., 2000; Mark et al., 2006a; Mark et al., 2006b).

Chapter 3

Chapter 3 – Geology and petrography of the Suicide Ridge Breccia Pipe

3.1. Introduction

This chapter focuses on the geology and petrography of the Suicide Ridge Breccia Pipe (SRBP) in the Snake Creek Anticline and associated rocks. In particular, the chapter addresses the following points: (1) detailed description of the geometry and the field relationships of the breccia pipe; (2) description of the distribution and petrographic characteristics of the breccia including granite clasts and ironstone bodies found within and around the breccia pipe (the term ironstone throughout this thesis refers to Fe-rich rocks); (3) description of the different types of alteration that affect the breccia and host rocks and their relative timing.

3.2. Local Geology & Field Relationships

The area of study is located in the Snake Creek Anticline (Figure 3.1), approximately 30 km southeast of Cloncurry. Lithologies in the area comprise the Mary Kathleen Group and the Soldiers Cap Group that outcrop respectively on the western and eastern side of the Cloncurry fault (Figure 3.1). The Mary Kathleen Group in the Snake

Creek Anticline predominantly consists of extensively brecciated calc-silicate and marbles of the Corella Formation. Calc-silicate rocks contain calcite, scapolite, K-feldspar, biotite magnetite and titanite (Marshall, 2003). The Soldiers Cap Group in the Snake Creek Anticline includes two lithostatigraphic units, the Llewellyn Creek Formation and the Mount Norna Quartzite. The Llewellyn Creek Formation consists of interbedded layers of metamorphosed quartz-mica arenites and pelites. The Mount Norna Quartzite contains metamorphosed arenites and pelites, quartzites and amphibolites. The Saxby granite (1527 ± 4 Ma, Rubenach et al., 2007) outcrops in the southern part of the Snake Creek Anticline and was emplaced during a protracted period of magmatism that produced the Williams and Naraku batholiths. The area is characterized by extensive brecciation that developed predominantly within the calc-silicate rocks of the Corella Formation (Marshall, 2003). Bodies of breccia of different sizes and shapes are commonly widespread around and along the Cloncurry Fault and appear to be closely associated with 1550-1500 Ma granitoids (Oliver et al., 2006).

The SRBP crops out within schists and quartzites of the Mount Norna Quartzite (Figure 3.2). The breccia forms a pipe-like body about 1000m long and 25m wide and strikes SW-NE, cutting the foliation of the schist almost perpendicularly. The foliation of the schist corresponds to the regional S_2 and the crosscutting relationship implies that brecciation post-dates the D_2 event. The contact between the breccia and the host rock is sharp (Plate 3.1A). The pipe is found in close proximity to, and extends from, a granitic intrusion located at its southwestern end. The intrusion is surrounded by a carapace of breccia that in its eastern side joins together with the pipe. The granite in some cases displays lobate and truncated margins (Plate 3.1B) suggesting that the brecciation was broadly simultaneous with emplacement of the granitoid.

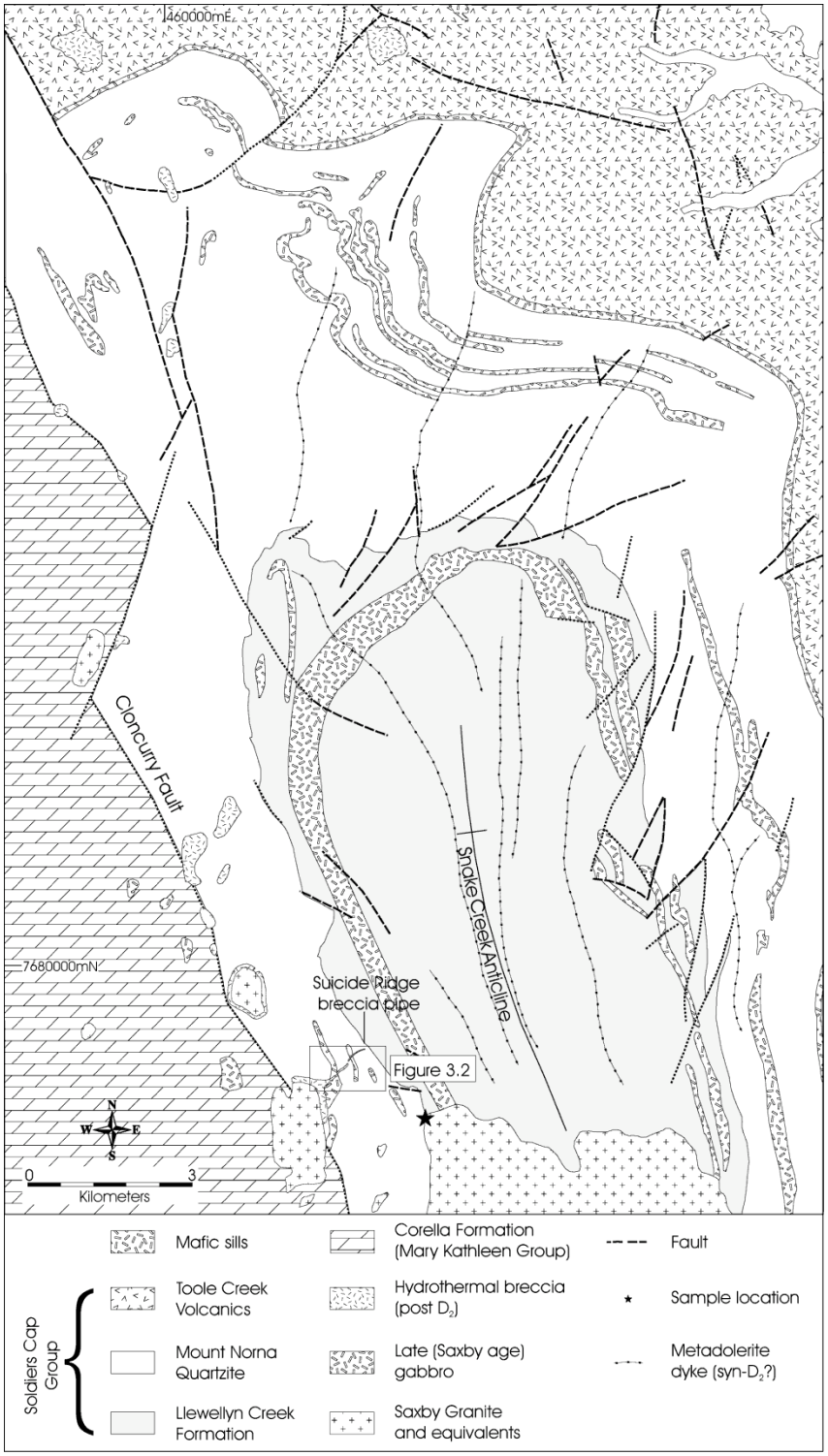

Figure 3.1 Map of the Snake Creek Anticline. The star indicates the location of the sample used by Rubenach et al. (2007) for the determination of temperature and pressure conditions of the Saxby Granite that are used in Chapter 4 as an independent constraint for the estimate of pressure. Modified after Rubenach et al. (2007).

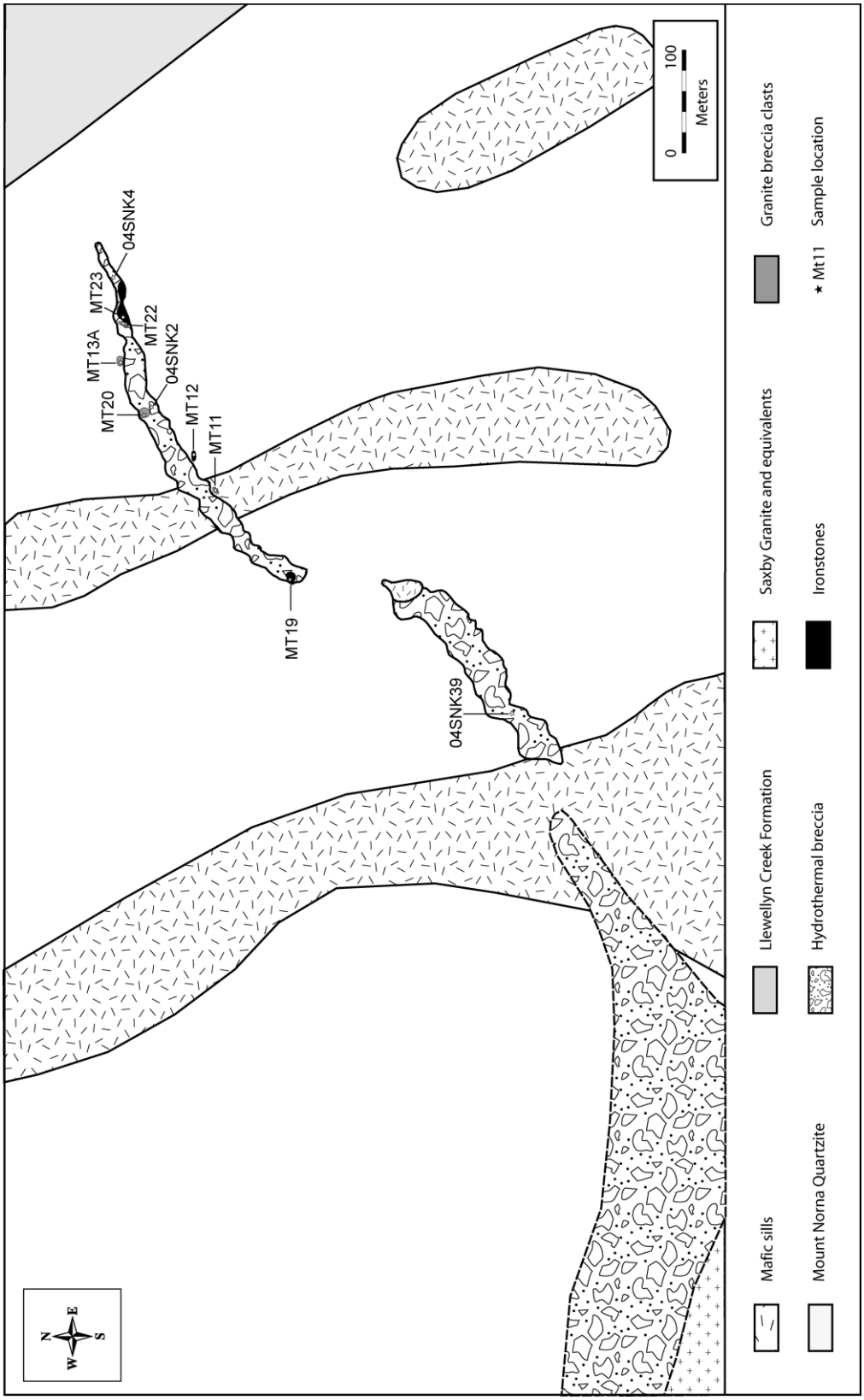

Figure 3.2 Map of the breccia locality showing the breccia pipe and its relationship with the Soldiers Cap Group and the granitoids that outcrop in the southwestern part of the area. The map also shows small granites and ironstones within or immediately outside the pipe and the location of the

The intrusion is part of the Saxby granite and consists of a medium-grained granite mainly composed of K-feldspar, quartz and plagioclase with less hornblende, biotite and magnetite and accessory apatite.

The composition of the breccia clasts is dominated by calc-silicate rocks of the Corella Formation (Plate 3.1C). Fragments of the Soldiers Cap Group, the immediate host of the breccia, are rare. This observation suggests that brecciation probably took place at depth and implies a significant vertical transport of the fragments because the Corella Formation lies structurally and stratigraphically beneath the Soldiers Cap Group. These observations are supported by results of previous studies on this and other similar occurrences in the proximity of the Cloncurry fault (Marshall, 2003; Oliver et al., 2006). Other clast types include several granitic (up to 10m in size) and rare mafic intrusive bodies (Figure 3.2 and Plate 3.1D). The granite clasts occur dominantly as oval and circular bodies, and more rarely as irregularly shaped-bodies. They contain very intense albite alteration which affects breccia throughout the whole pipe and host rocks adjacent to the pipe.

The pipe contains several magnetite-hematite-rich rocks that change in character through the pipe. The south-western and central part of the pipe is characterized by massive magnetite-dominated bodies (up to 10m in size) that are black to brownish red in outcrop (Figure 3.2 and Plate 3.1E). Towards the north-eastern end of the pipe the ironstones are hematite-dominated and occur as intense quartz-hematite ± magnetite rich veins cutting the breccia (Plate 3.1F). This branch of the pipe is also characterized by quartz veining that crosscuts the quartz-hematite ± magnetite rich veins (Plate 3.1D, F). The veins are normally thin (<3cm) and consisting exclusively of quartz (Plate 3.1D, F).

Plate 3.1

(A) Field picture representing albite alteration developed at the contact between schists of the Soldiers Cap Group and the breccia.

(B) Granite intruding the breccia and being incorporated in the breccia, suggesting synchronous breccia-granite development.

(C) Field picture of breccia showing the dominant calc-silicate nature of the clasts.

(D) Granite clast outcropping in the north-eastern branch of the pipe cut by later quartz veins.

(E) Small outcrop of Fe oxide-rich rocks in the middle section of the pipe.

(F) Hematite-quartz-rich vein cutting and replacing the breccia at the northeastern end of the pipe.

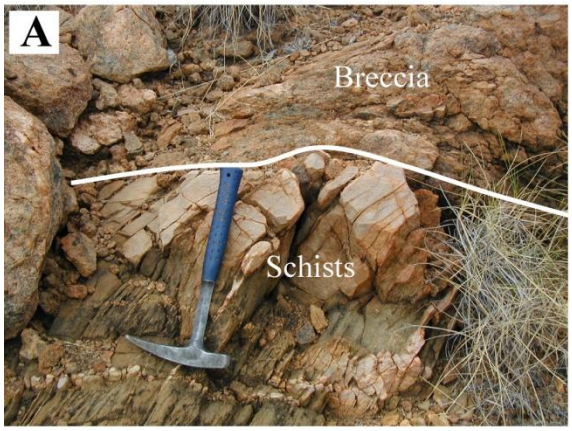
A
Breccia
Schists

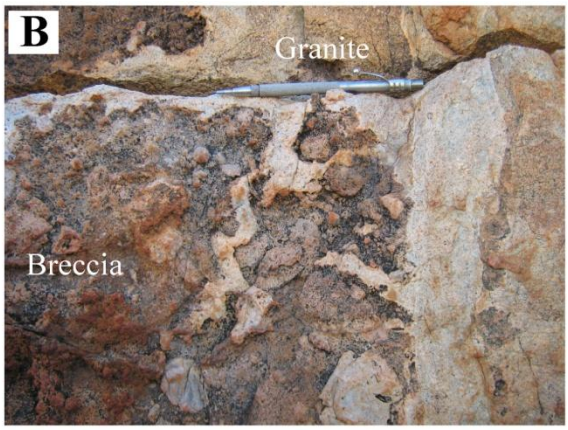
B
Granite
Breccia

C
Calcsilicate clast

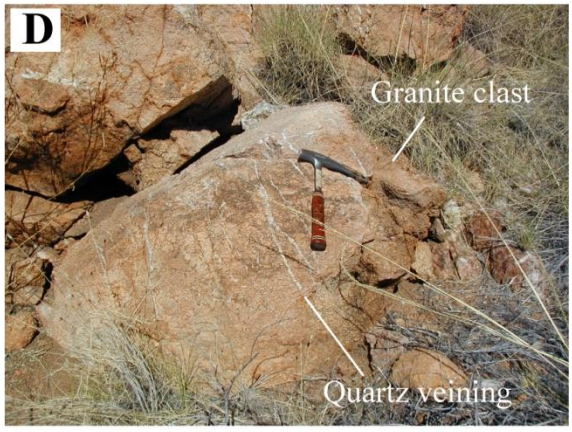
D
Granite clast
Quartz veining

E
Fe oxide-rich rock

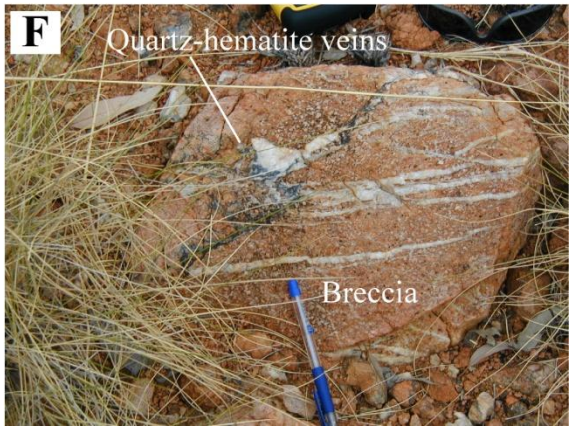
F
Quartz-hematite veins
Breccia

3.3. Sample petrography

Samples collected to characterize the breccia and magnetite-hematite-rich rocks are described in this section and their locations are shown in Figure 3.2 (Table 3.1 and Appendix 3.1). The characteristics of the breccia are described into two separate sections: the first focuses on the description of breccia fragments and groundmass; the second deals with the description of the granite breccia clasts and their alteration. Great attention has been dedicated to these granite clasts as they are interpreted to represent samples of the crystallizing magma introduced in the pipe during the brecciation and contain abundant fluid inclusions, unlike the remaining breccia material. Data obtained from these fluid inclusions have provided valuable information about the composition and P-T conditions of hydrothermal fluid related to the formation of the breccia pipe (Chapters 4, 5 and 7). Their origin is discussed in section 3.4 and in Chapter 7. The origin of magnetite-hematite-rich rocks is discussed in Section 3.3.1.1 and they are described separately from the breccia.

3.3.1. Description of breccia clasts and groundmass

Breccia clasts display variable composition and include dominant calc-silicate of the Corella Formation (Plate 3.1.C), and less abundant albite (Plate 3.2A) and granite clasts (Plate 3.1D; Section 3.3.2). Fragments are rarely angular and dominantly sub-rounded to rounded in shape with variable dimensions that range from millimetre to metre-scale, with

the most common dimension centimetre to tens of centimeter scale. The clasts do not show particular distributions or sorting of size and type within the pipe.

The groundmass comprises albite, titanite, actinolite, magnetite and lesser hematite, quartz, apatite and calcite (Plate 3.2B-E) and represents up to 70% of the breccia volume. The term groundmass is preferred here because it is free of genetic implication and it useful in cases where it is difficult to establish whether minerals represent matrix, infill or alteration phases. Albite is ubiquitous and is present in clasts and as the dominant phase in the groundmass mainly occurring as alteration (Plate 3.2A-E). Titanite, actinolite and magnetite crystals appear extensively altered by later albite and calcite alteration, and it is difficult to infer if they are matrix or infill material (Plate 3.2B-D). In fact, these phases may predate the brecciation event and be the result of mechanical and chemical alteration associated with the brecciation or they may postdate the brecciation event and be precipitated in void as infill material (in some crystals euhedral shapes are still recognizable) that was subsequently altered. The size of these minerals ranges from around 1 to 1.5 mm for actinolite, from around 0.5 to 2mm for titanite and from around 0.1 to 1.3mm for magnetite. Apatite (Plate 3.2C) and quartz are interpreted as infill due to their occurrence as euhedral crystals. Alteration phases include albite overprinted by later calcite-hematite-quartz alteration (Plate 3.2B-E). Albite alteration typically occurs as subhedral to anhedral crystals that display variable dimensions that range from tens of microns up to a few millimeters. Calcite-hematite-quartz alteration overprints, and therefore postdates, actinolite-titanite-magnetite-apatite matrix/infill material of the breccia and the albite alteration (Plate 3.2B-E). Calcite crystals are usually subhedral to anhedral and mostly fine-grained (<0.5 mm). Quartz is mostly anhedral whereas hematite occurs in euhedral tabular crystals up to around 500μm long and 100 μm wide (Plate 3.2E).

Table 3.1 Summary and description of samples collected for petrographic and fluid inclusion studies

Sample	Rock Type	Mineralogy
MT11	Clast of granite pegmatite	Albite and quartz with hematite-magnetite-biotite alteration
MT13A	Clast of granite pegmatite	Albite and quartz cut by actinolite-titanite-apatite alteration and altered by later albite
MT20	Clast of granite pegmatite	Albite and quartz with accessory apatite and zircon cut by hematite-magnetite-biotite-titanite alteration
MT22	Clast of granite pegmatite	Albite, quartz, magnetite, hematite and apatite.
MT12	Ironstone	Magnetite-quartz-hematite
MT19	Ironstone	Magnetite-quartz-hematite
04Snk02	Breccia	Albite clasts; actinolite, titanite, magnetite, apatite, quartz groundmass; albite, calcite± hematite±quartz alteration
04Snk 04	Breccia	Albite clasts; actinolite, titanite, magnetite, apatite, quartz groundmass; albite, calcite± hematite±quartz alteration
04Snk39	Breccia	Actinolite, titanite, magnetite, apatite, quartz groundmass; albite, calcite± hematite±quartz alteration

Plate 3.2 Field and thin section pictures illustrating characteristics of the breccia. Sample 04SNK2.

(A) Hand specimen of breccia characterized by albite clasts and surrounded by idiomorphic actinolite; albite is also present as a matix/infill and an alteration phase.

(B) Actinolite, magnetite and titanite crystals overprinted by albite and later calcite-hematite-quartz alteration.

(C) Euhedral apatite crystals.

(D) and (E) Calcite-hematite alteration overprinting actinolite-magnetite-titanite assemblage and albite alteration. Sample 04SNK2.

Mineral abbreviations after Kretz (1983).

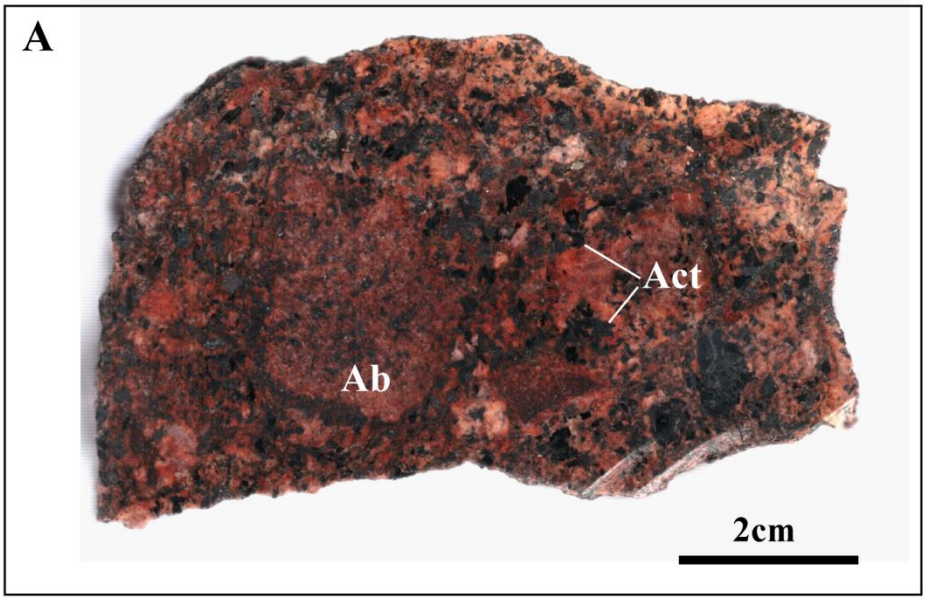
A
Act
Ab
2cm

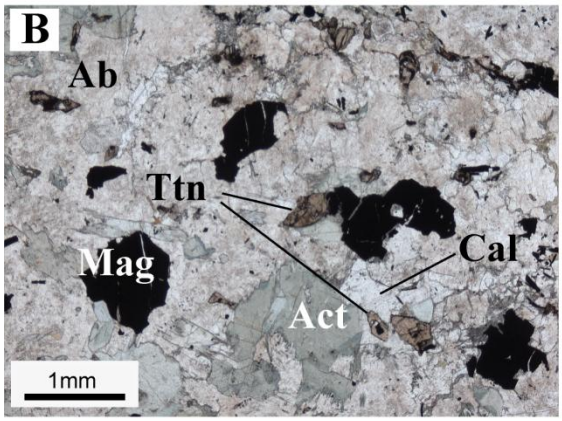
B
Ab
Ttn
Mag
Cal
Act
1mm

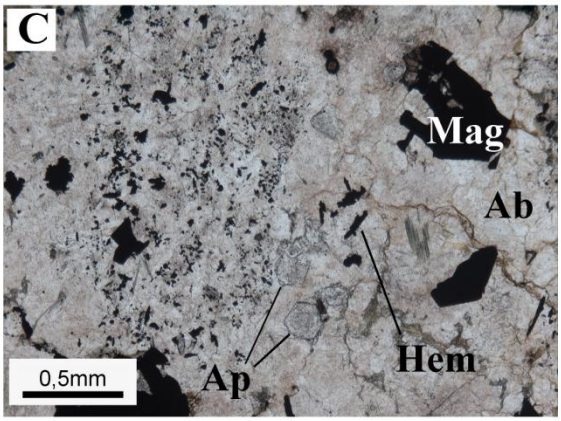
C
Mag
Ab
Hem
Ap
0,5mm

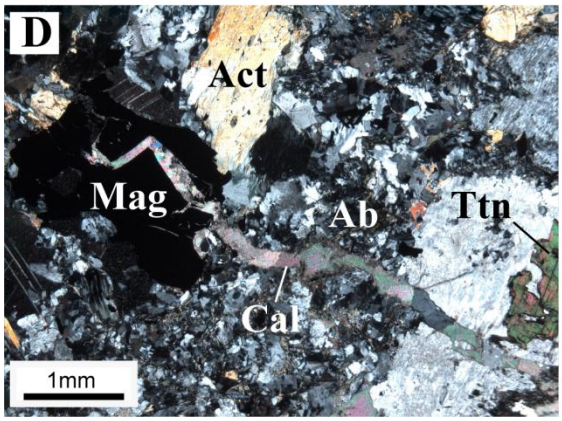
D
Act
Mag
Ab
Ttn
Cal
1mm

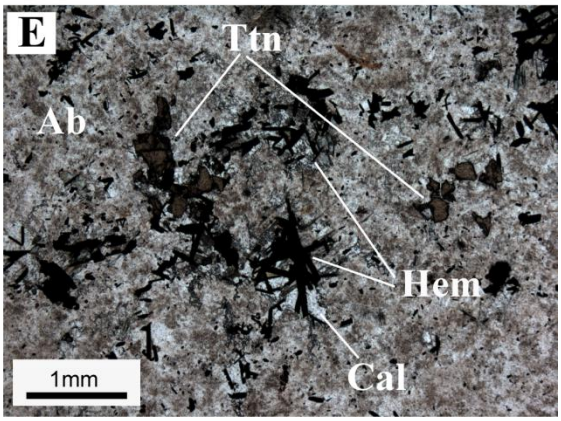
E
Ttn
Ab
Hem
Cal
1mm

3.3.2. Description of granite and pegmatite breccia clasts and their alteration

3.3.2.1. Mineralogy and textures

Granite clast samples collected in this study (Figure 3.2) consist primarily of albite and quartz in approximately equal proportions. Accessory minerals comprise apatite and zircon and more rarely magnetite. The opaque content of these rocks is restricted to alteration assemblages, with the exception of sample MT22 which contains primary hematite and magnetite. The granites display a variety of textures that include equigranular, granophyric quartz-albite intergrowths, graphic granite and layered quartz-albite bodies. Textures for each sample are described in detail as it follows.

Sample MT11 comprises two distinct textural components: 1) a fine-grained (up to few millimeters) broadly equigranular albite-rich component; and 2) a fine- to medium-grained monomineralic quartz component (Plate 3.3A). These two components form rhythmic alternated layers of different thickness: the albite-rich layers are about 2 to 2.5cm thick while the thickness of the quartz layers commonly ranges from 0.1 to 0.5 cm (Plate 3.3A). Albite is the dominant mineral of the albite-rich layer and normally occurs as anhedral crystals; these layers also contain patches of quartz displaying dendritic shapes. The quartz layer is commonly subhedral to anhedral with crystal dimensions ranging from 0.5mm to up to a few centimeters.

Sample MT20 displays dominant medium- to fine-grained (crystal diameters up to few millimeters) equigranular texture and consists of euhedral to subhedral albite and typically anhedral quartz both up a few millimeters in size (Plate 3.3B). The sample also displays granophyric quartz-albite intergrowth similar to sample MT13A.

Plate 3.3 Representative pictures of textures and mineralogy of granite clasts

(A) Photographs of hand specimen of sample MT11 showing alternate quartz-rich and albite-rich layers.

(B) Photomicrograph of sample MT20 displaying medium- to fine-grained equigranular texture.

(C) and (D) Thin section scan and photomicrograph (crossed polars) of sample MT13A showing quartz-albite granophyric intergrowth.

(E) Hand specimen of sample MT22 showing graphic granite textures; rods of quartz are clearly visible in the albite host.

(F). Scan of thin section of sample MT22 showing the parallel alignment of quartz rods; also the association of Fe oxide phases, dominantly hematite and lesser magnetite, exclusively with the quartz rods.

Mineral abbreviations after Kretz (1983).

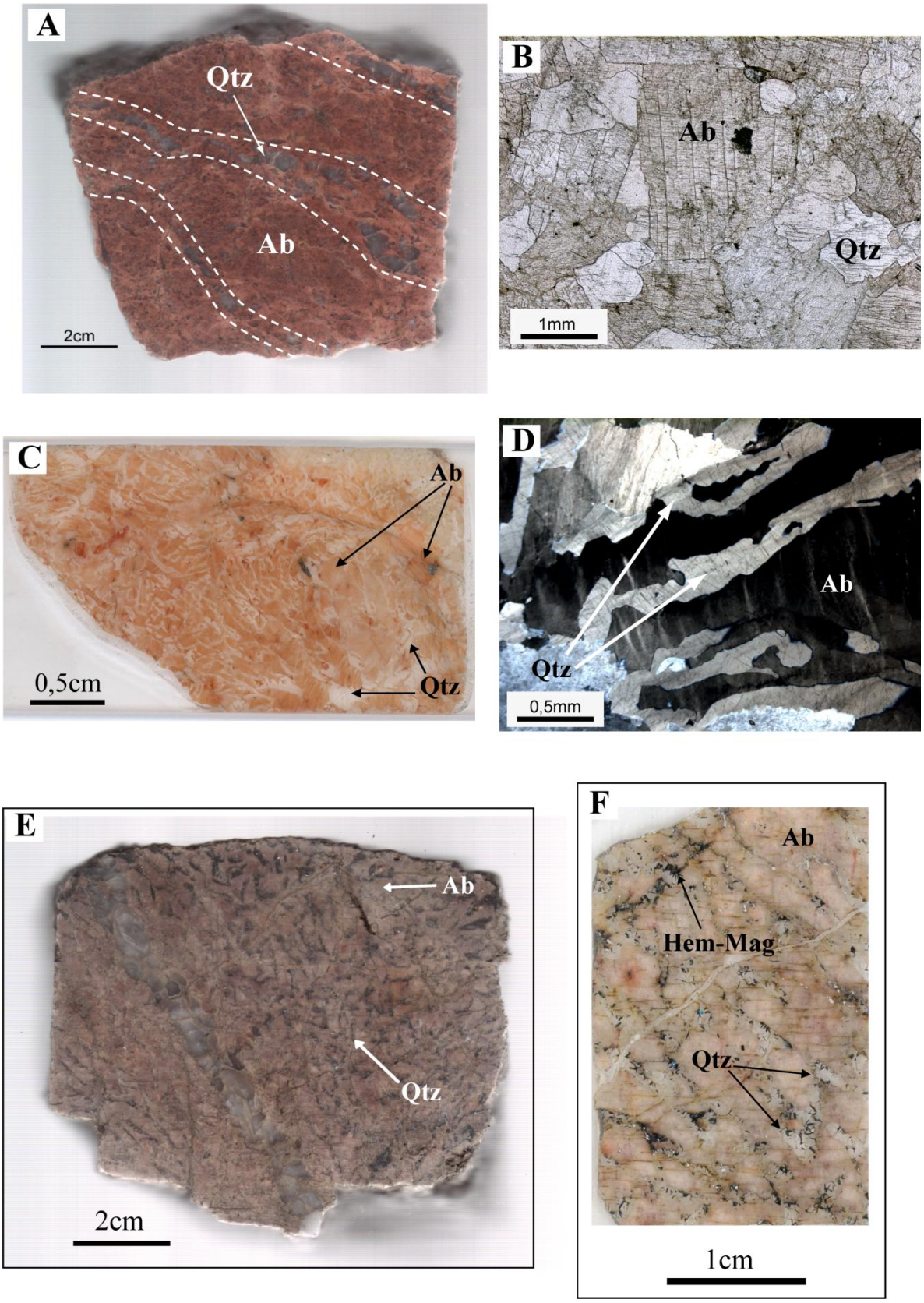
A
Qtz
Ab
2cm
B
Ab
Qtz
1mm
C
Ab
Qtz
0,5cm
D
Ab
Qtz
0,5mm
E
Ab
Qtz
2cm
F
Ab
Hem-Mag
Qtz
1cm

Sample MT13A displays granophyric quartz-albite intergrowths (Barker, 1970). Quartz crystals exhibit morphologies that vary from cuneiform to more complex vermicular-shaped approximately up to 5mm long and up to 0.3 mm wide and are characterized by optical continuity (Plate 3.3C, D). Albite as well forms crystals displaying cuneiform and more complex irregular intergrowths whose dimensions vary from a few mm to up 5mm (Plate 3.3C, D).

Sample MT22 has a graphic granite texture consisting of intergrown quartz and albite (cf Barker, 1970; Plate 3.3E). Quartz rods are characteristically cuneiform and display parallel elongation (Plate 3.3F); the thickness of the rods varies from 0.5 mm to few mm. Quartz within the rods is typically euhedral, rarely subhedral, and fine-to medium-grained with dimensions of the crystals ranging from 0.5mm up to 3 mm. Primary minerals also comprise abundant hematite and rarer magnetite that are restricted to the quartz layers (Plate 3.3F). Hematite occurs as crystals with a tabular habit, while magnetite occurs in euhedral crystals that characteristically exhibit martitization replacement by hematite.

3.3.2.2. Alteration

Observed alteration phases in the granite clasts include fracture-controlled localized amphibole-titanite-apatite±magnetite±hematite alteration, pervasive albite alteration, magnetite-hematite-quartz±biotite±titanite alteration and chloritization of actinolite and biotite (Plate 3.4). Albite and magnetite-hematite-quartz-±biotite±titanite alterations are the most volumetrically significant.

Plate 3.4

(A) Hand specimen of sample MT13A showing the alteration assemblage developed as a fracture infill; coarse crystals of amphibole are easily recognizable.

(B) Idiomorphic actinolite crystal enclosing apatite. Sample MT13A.

(C) Back-scattered electron (BSE) image of idiomorphic titanite showing replacement by rutile; locally rutile is replaced by ilmenite. Sample MT13A.

(D) Back-scattered electron (BSE) image showing secondary albite overprinting actinolite. Sample MT13A.

(E) Cathodoluminescence image of sample MT13A showing secondary luminescent albite (Ab II) cutting primary quartz and non luminescent albite (Ab I).

(F) Photomicrograph of K- Fe alteration in granite sample. The alteration assemblage comprises hematite, quartz, biotite and subordinate magnetite and titanite; chlorite is present as product of alteration of biotite. Sample MT20.

Mineral abbreviations after Kretz (1983).

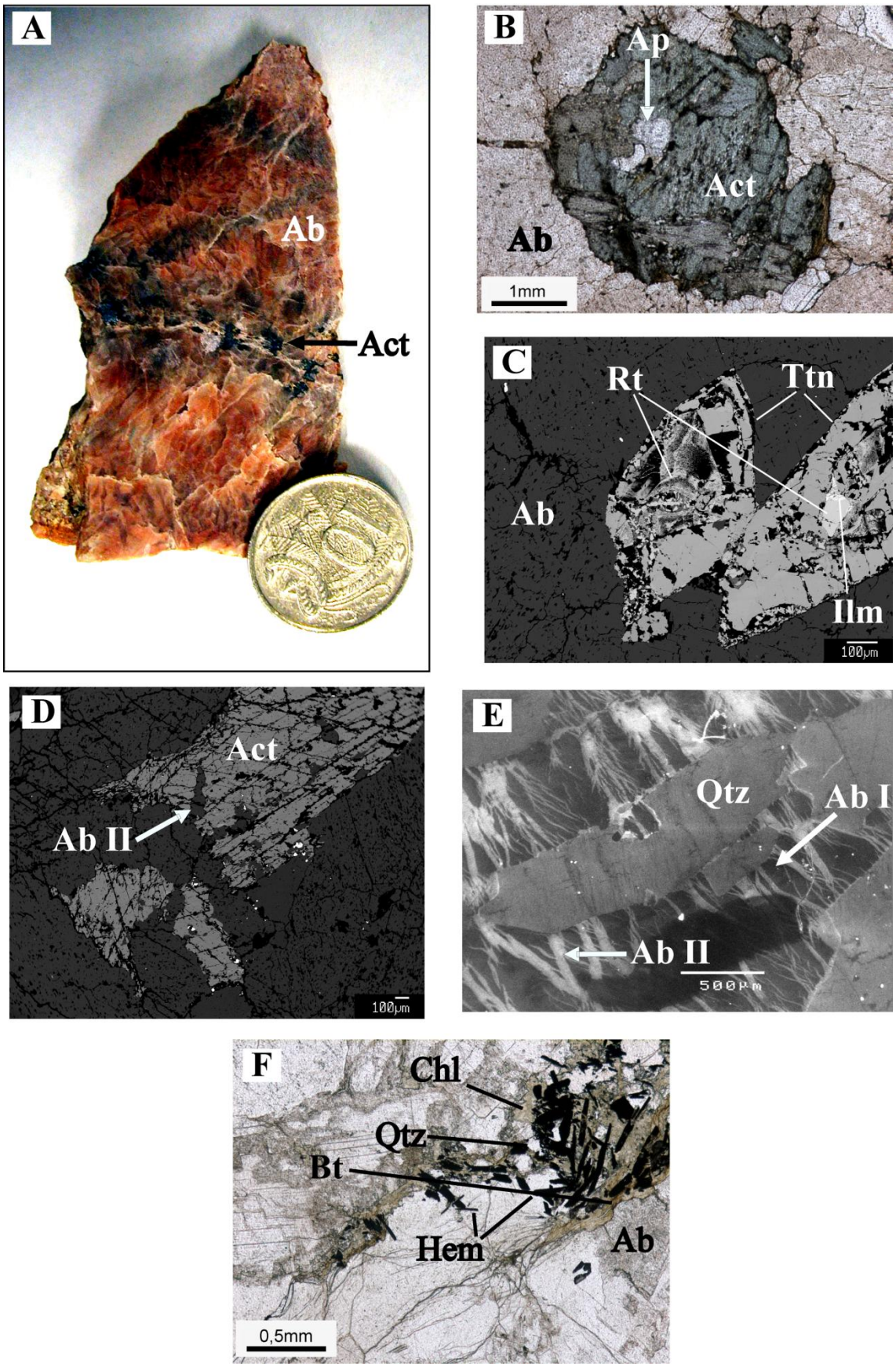
A
Ab
Act
B
Ap
Act
Ab
1mm
C
Rt
Ttn
Ab
Ilm
100µm
D
Act
Ab II
100µm
E
Qtz
Ab I
Ab II
500µm
F
Chl
Qtz
Bt
Hem
Ab
0,5mm

Amphibole-titanite-apatite±magnetite±hematite alteration was observed in two samples of granite breccia clasts and is localized in centimeter-scale fractures (Plate 3.4A). Actinolite occurs in euhedral to subhedral medium-grained crystals with dimensions in the range of 3 to 4 mm (Plate 3.4B). Titanite is intimately associated with amphibole and occurs as euhedral crystals whose dimensions vary from 0.5 to 1mm (Plate 3.4C). Observations in reflective light and back scattered electron imaging (BSE) revealed a series of rutile-rich fractures in titanite, and that rutile is sometimes replaced by ilmenite (Plate 3.4C). Apatite occurs in subeuhedreal to anhedral crystals of dimensions between 0.1 and 0.6 mm (Plate 3.4B). Hematite and magnetite are less abundant than the previous minerals and occur as fine-grained crystals. The same assemblage was observed as matrix/infill material in the breccia (Section 3.3.1 and Plate 3.2)

Albite alteration is pervasive and overprints the primary mineral assemblages and the amphibole-titanite-apatite alteration of the granite breccia clasts (Plate 3.4D). In hand specimen the albite alteration is pink-red in colour, but it is difficult to recognize petrographically because it overprints earlier albite and has perthite-like texture. Nonetheless, its presence is easily identified by cathodoluminescence analysis because this second generation of albite is luminescent (700 nm) in contrast with the primary albite which is not luminescent (Plate 3.4E). Microprobe analysis on the two types of albite revealed that the luminescent albite has higher iron content (Figure 3.3).

Magnetite-hematite-quartz±biotite±titanite alteration was also observed in granite breccia samples as centimeter scale fracture infill dominated by hematite and quartz and lesser magnetite and is part of the alteration that produced at least some of the ironstones observed within and in close proximity to the pipe described in Section 3.3.3. Hematite occurs in crystals displaying tabular shapes up to 500μm long and 100 μm wide (Plate

3.4F). Quartz is mostly anhedral. Magnetite occurs in euhedral crystals and is often replaced by hematite as shown by typical martitization textures. These phases are sometimes accompanied by biotite and titanite. Biotite is present as crystal aggregates and appears extensively altered by later chlorite; however, in some areas it is still recognizable with its distinct interference color (Plate 3.4F). Titanite occurs in rare euhedral crystals. Chlorite occurs dominantly as replacement of biotite and actinolite, between grain boundaries and less frequently in thin veins (Plate 3.4F).

3.3.3. Magnetite-hematite-rich rocks

The magnetite-hematite-rich rocks can be subdivided into magnetite-rich, found in the middle section of the breccia pipe, and hematite-rich, that outcrop towards the northeastern end of the pipe (Figure 3.2). Samples MT12 and MT19 were collected inside and immediately outside the breccia pipe respectively in its middle section (Figure 3.2). Both samples occur in massive ironstone bodies ranging up to ten meters in size (Figure 3.2 and Plate 3.1E). In hand specimen, the samples exhibit a black to brownish colour, do not display any noticeable banding and are cut by later quartz veins (Plate 3.5A). Both samples are fine-grained rock primarily composed of quartz and magnetite (Plate 3.5B-C). In sample MT19 magnetite occurs in small euhedral crystals (average size approximately 100μm), while in sample MT12 magnetite forms aggregates (Plate 3.5B-C). Quartz is present as subeudral to anhedral crystals. Magnetite is frequently replaced by hematite as shown by typical martitization replacement textures (Plate 3.5D).

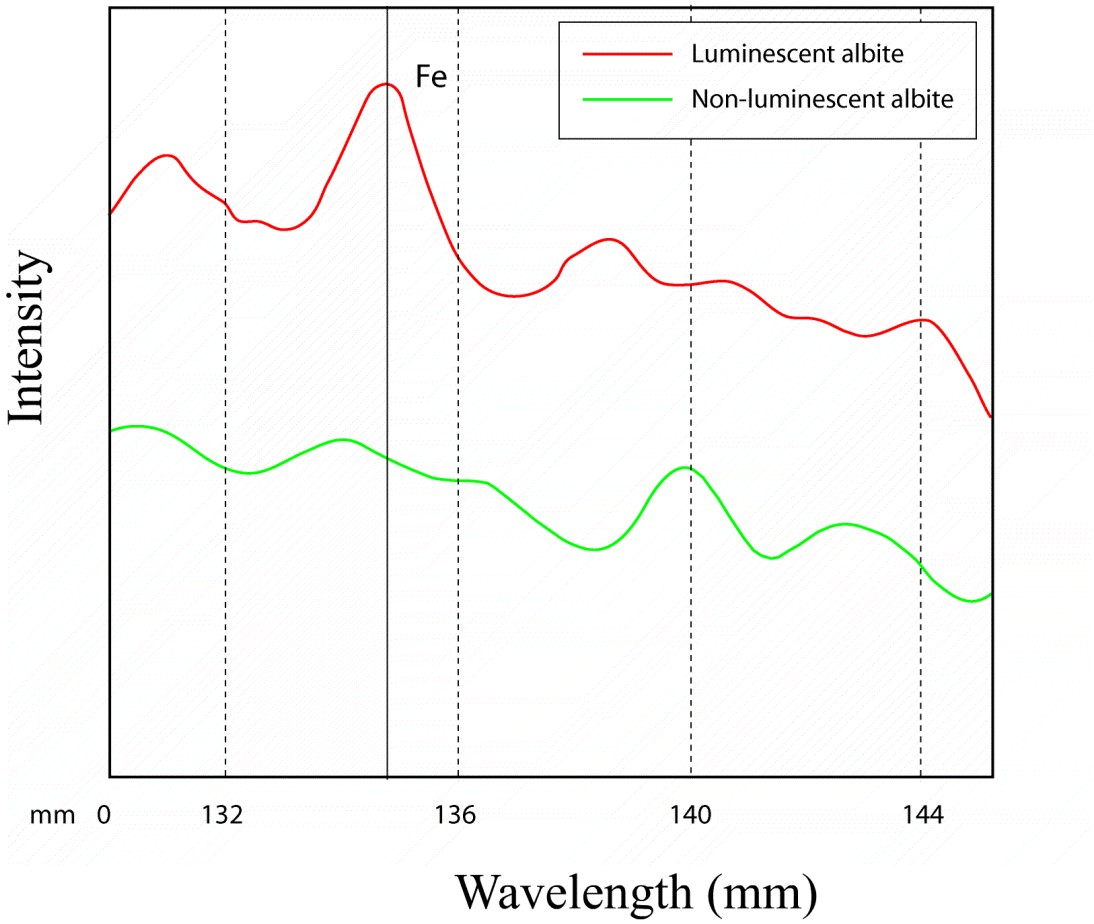

Figure 3.3 The diagram represents microprobe analysis on primary and secondary albite. Primary albite and secondary luminescent albite are represented by a green and a red line respectively. The two scan differ for the pronounced peak, that correspond to Fe, displayed by the luminescent albite suggesting that has a higher Fe content than non luminescent albite.

Plate 3.5 Photographs showing key characteristics of Fe oxide-rich rocks.

(A) Hand specimens of samples MT12 black in color, but more often typically brownish to reddish due to weathering of Fe oxide minerals; both samples are cut by later quartz-veins.

(B) and (C) photomicrographs illustrating the textures of samples MT12 and MT19 respectively: in sample MT12 magnetite occurs mostly in aggregates, while in samples MT19 magnetite occurs in small euhedral crystals.

(D) Replacement martitization textures in magnetite from sample MT12 (reflected light).

(E) Photomicrograph in reflected light of sample MT19 illustrating pyrite affected by goethite alteration.

(F) Hand specimen of sample MT23 exhibiting a black to reddish colour, the latter due to Fe-oxide weathering, and cut by later quartz veins.

(G) Photomicrograph showing the texture of sample MT23 consisting of euhedral quartz crystals and idiomorphic tabular crystals of hematite.

Mineral abbreviations after Kretz (1983).

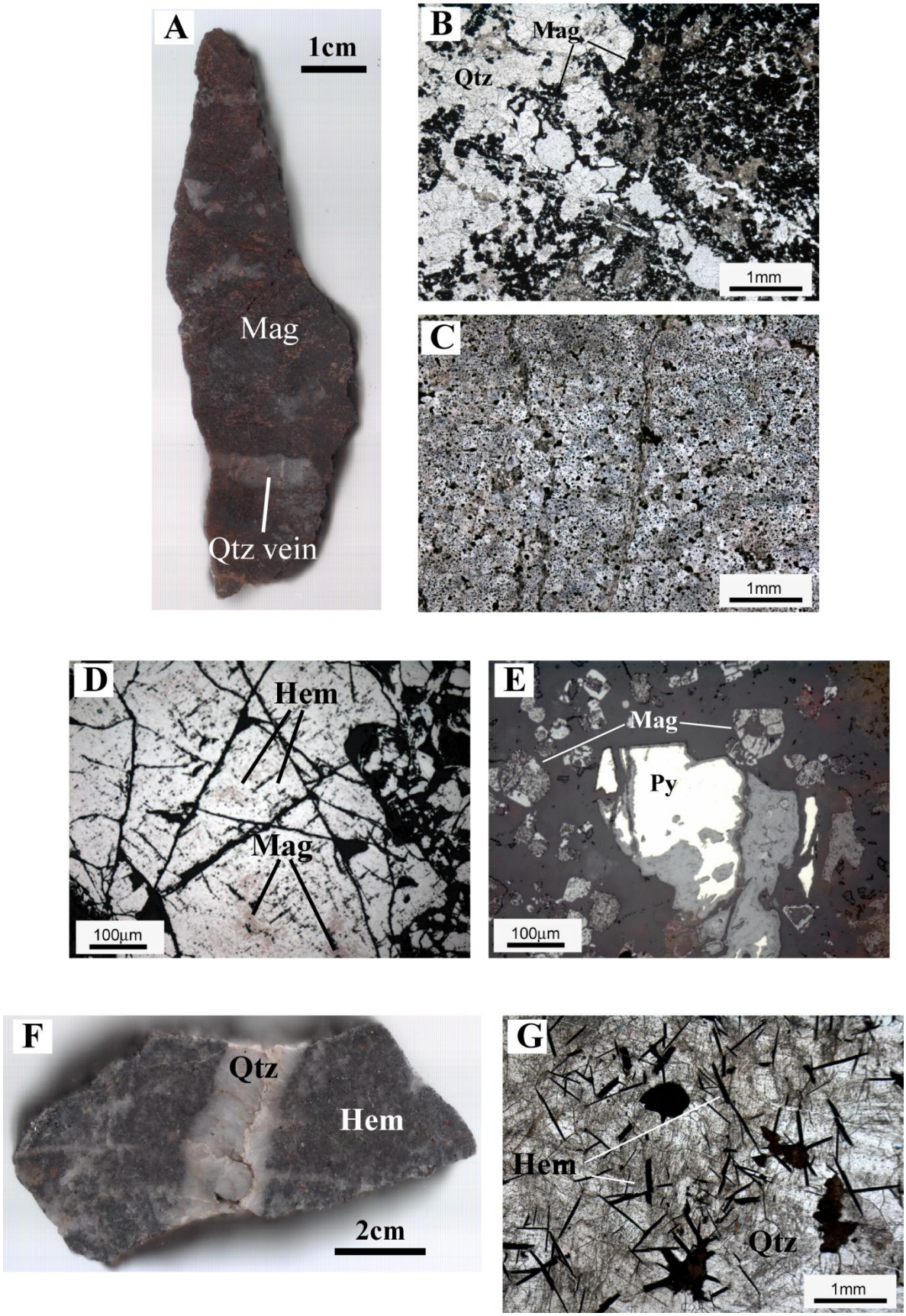
A
1cm
Mag
Qtz vein
B
Mag
Qtz
1mm
C
1mm
D
Hem
Mag
100µm
E
Mag
Py
100µm
F
Qtz
Hem
2cm
G
Hem
Qtz
1mm

Minor phases in MT19 include apatite, actinolite and rare titanite, while none of these phases were observed in sample MT12. Sample MT19 also contains small amounts of pyrite, the only occurrence of sulphide within rocks of the pipe (Plate 3.5E). Alteration phases include abundant chlorite, later crosscutting quartz veins and goethite as late weathering product of hematite and magnetite.

Sample MT23 comprises hematite-quartz veins that cut the breccia at its northeastern end (Figure 3.2 and Plate 3.1F). The veins are up to 10cm thick and mainly composed of quartz and hematite and lesser magnetite (Plates 3.1F and 3.5F). Both quartz and hematite occur as well-formed idiomorphic grains with quartz sometimes displaying evident growth zones (Plate 3.5G). Alteration phases include biotite and chlorite (chlorite developed as a late overprint of biotite) that occurred as fracture infill and in intergranular spaces and later quartz veins (Plate 3.1F). Goethite is present as a product of weathering of hematite and magnetite.

3.3.3.1. Discussion on the origin of magnetite-hematite-rich rock

Iron-rich rocks may form from a variety of processes that include orthomagmatic, transitional magmatic-hydrothermal and hydrothermal. Hydrothermal processes are responsible at least for the formation of ironstones occurring in the northeastern end of the pipe. The hydrothermal nature of these ironstones is supported by their occurrence in veins that cut granite and breccia, and their replacement of the original mineralogy of these rocks. The origin of Fe-rich rock in the middle part of the pipe is less certain due to the lack of

field relationships similar to those at the end of the pipe. However, an orthomagmatic or transitional magmatic-hydrothermal origin for Fe-rich rocks in the middle section of the pipe is very unlikely due to the lack of typical textures that characterize these two processes, namely cumulus-intercumulus and globular-spherulitic textures (e.g. Wager et al., 1960). Alternatively, these rocks may have been part of the sedimentary sequence and have been transported upward during the brecciation event. Both the Corella Formation and the Mt Norna Quartzite contain Fe-rich rocks. The basal units of Corella Formation reportedly display general iron enrichment (magnetite-hematite) and magnetite-rich "pods" (Stewart, 1994). These Fe-rich bodies are characterized by the presence of peak metamorphic minerals, in particular hornblende, intimately associated with magnetite (Stewart, 1994). The Mt Norna Quartzite contains two distinct levels of Fe-rich rocks namely the Mt Norna iron formation at the contact between the Mt Norna Quartzite and the Llewellyn Formation and the Weatherly Creek iron formation which occur in the middle of the Mt Norna Quartzite (Hatton and Davidson, 2004). The term iron formation is indicative of the banded-laminated nature of these units (Gross, 1965; Hatton and Davidson, 2004). The Mt Norna iron formation comprises thinly laminated to massive bodies composed of hematite-magnetite ± quartz ± garnet and hematite-magnetite assemblages, while the Weatherly Creek iron formation consists of alternating dominant garnet-quartz-apatite ± stilpnomelane laminae and magnetite-hematite-quartz ± grunerite laminae (Hatton and Davidson, 2004). The Fe oxide-rich rocks in the middle section of the pipe are significantly different from the iron-formation described above, lacking any type of banding or orientation of minerals and displaying a much simpler mineralogy consisting dominantly of magnetite, hematite and quartz with subordinated actinolite and apatite. Furthermore, these ironstones hosted in the pipe lack albitic alteration which is widespread in rock within the

breccia pipe and the host rocks. These observations suggest that these ironstones are unrelated to the underlying Fe-rich rock of the Corella Formation and Mt Norna Quartzite and that their formation post-dated the widespread albitic alteration. The Fe-rich rocks are most likely hydrothermal in origin and the transition from magnetite- to hematite-rich ironstones may reflect a vertical variation due to different depths of formation with magnetite occurring in deeper more reduced environments and hematite dominating in shallower more oxidized parts, as observed in many IOCG deposits (Hitzman et al., 1992).

3.4. Summary and discussion

The breccia in this study shares many characteristics with breccia described in previous studies in the Cloncurry district (Marshall, 2003; Marshall and Oliver, 2006; Oliver et al., 2006). In particular, the breccia in this study is similar to the Gilded Rose breccia described by Marshall (2003) and Marshall and Oliver (2006). Both breccia types are characterized by subrounded to rounded fragments, variable fragment size and variable composition of the clasts, although dominated by calc-silicate of the Corella Formation and groundmass material consisting of actinolite-titanite-magnetite and albite. Furthermore, clasts of the Soldiers Cap Group that are the host rock to the pipe and overlie the Corella Formation are rare indicating a general upward movement of the clasts (Marshall, 2003; Oliver et al., 2006). The breccia pipe outcrops within rocks of the Soldiers Cap Group cutting the S_2 foliation of the schist almost perpendicularly. The crosscutting relationship implies that brecciation post-dates the D_2 event and temporal and spatial relationships with

the granite suggest syn-emplacement of the Williams-Naraku Batholith (Figure 3.1). The genesis of the pipe is thoroughly discussed in Chapter 7. However, some points of the discussion are briefly described in this section. There are several lines of evidence for a direct involvement of a crystallizing magma in the formation of the pipe. Firstly, the pipe is spatially and temporally associated with the granite that outcrops in its southwestern boundary. Other evidence of the direct involvement of the magma is the presence of several granitic bodies as breccia clasts. The granite clasts locally display fragmentation plus brecciated and lobate margins, as also reported by Marshall (2003) and Oliver et al. (2006). This latter observation suggesting that the magma was introduced in the pipe when it was not completely solidified and infers that the formation of the granite was broadly synchronous with the brecciation event. These granite clasts are characterized by a very simple mineralogy that consists almost exclusively of albite and quartz and by magmatic-hydrothermal textures similar to other occurrences reported in previous studies in the Cloncurry district (Tolman, 1998; Mark and Foster, 2000; Perring et al., 2000; Marshall, 2003). These textures can be interpreted as evidence of a magma crystallizing in volatile-saturated conditions and likely indicate accumulation of volatiles towards the top of the crystallizing magma, as also proposed by Mark and Foster (2000). These data therefore support the hypothesis of brecciation in response to fluid overpressuring generated by cooling and crystallization of the magmatic body (cf. Burnham, 1985). This hypothesis is further discussed in Chapter 7.

Breccia and host rocks in the proximity of the pipe are commonly intensely altered by sodic (-calcic) alteration. An early actinolite-apatite-titanite assemblage is developed in granite clasts and is similar to assemblages found in the breccia groundmass together with albite. Both these assemblages are overprinted by later albitic alteration. Albite occurs also

as clasts in the breccia. These observations suggests a prolonged period of sodic (-calcic) alteration with albite likely developing before brecciation as supported by the presence of albite as clasts and within the breccia matrix, and continuing during and after the brecciation event as proven by the presence of sodic (-calcic) assemblages as infill and alteration in the breccia.

The ironstones change in character throughout the pipe from magnetite-dominated in the western and middle section of the pipe to hematite-dominated in its northern branch. The ironstones are interpreted to have metasomatic origin and post-date the sodic (- calcic) alteration. The final stages of the pipe evolution are characterized by the development of quartz veining.

The paragenetic evolution of the SRBP is illustrated in Figure 3.4.

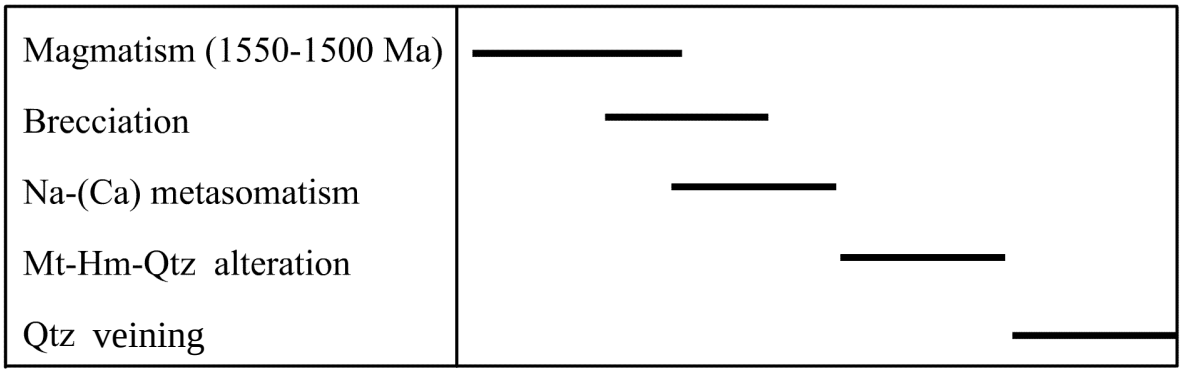

Figure 3.4 Diagram illustrating the paragenetic evolution of the SRBP.

Chapter 4

Chapter 4 - Fluid chemistry and conditions of the Suicide Ridge Breccia Pipe (I): Fluid inclusion paragenesis, classification and microthermometry

4.1 Introduction

A fluid inclusion study was undertaken to characterize the fluids associated with the Suicide Ridge Breccia Pipe (SRBP) described in Chapter 3. Samples were selected to represent the different paragenetic stages of the evolution of the breccia pipe. The study includes paragenesis and classification of the inclusions, microthermometric analysis and laser Raman. The chemistry of the fluids associated with the barren breccia pipe is further investigated in Chapter 5 where results are presented from several analytical techniques including LA ICP MS, bulk crush-leach and microprobe analysis.

4.2 Sample selection and paragenesis

Samples selected for the fluid inclusion are summarized in Table 4.1. Samples of granite found as clasts in the breccia were selected to determine the fluid characteristics of the early stages of breccia formation. The samples dominantly consist of albite and quartz and display textures that collectively have been interpreted as characteristic of the magmatic-hydrothermal transition (Chapter 3).

Table 4.1 Description of samples selected for the fluid inclusion study and of analysis undertaken for each samples.

Sample	Rock Type	Mineralogy	Fluid inclusion Host Mineral	Fluid inclusion paragenesis and classification	Microther-mometry	Laser Raman	LA ICP MS	Bulk Crush Leach
MT11	Clast of granite pegmatite	Albite and quartz with hematite-magnetite-biotite alteration	Quartz	√	√		√	√
MT13A	Clast of granite pegmatite	Albite and quartz cut by actinolite-titanite-apatite alteration and altered by later albite	Quartz	√	√		√	√
MT20	Clast of granite pegmatite	Albite and quartz with accessory apatite and zircon cut by hematite-magnetite-biotite-titanite alteration	Quartz	√	√	√	√	√
MT22	Clast of granite pegmatite	Albite, quartz, magnetite, hematite and apatite.	Quartz					√
MT22v	Quartz vein cutting sample MT22	Quartz	Quartz					√
MT12	Ironstone	Magnetite-quartz-hematite	Quartz	√	√		√	√
MT19	Ironstone	Magnetite-quartz-hematite	Quartz	√	√		√	√

Classification and microthermometry of fluid inclusions in samples MT22 and MT22v were not carried out due to their small size (<5μm)

Quartz in these samples contains several clusters and trails of fluid inclusions that represent different stages of the fluid evolution in the breccia pipe (see below). The matrix and infill component of the breccia were also examined for fluid inclusions, in particular infill minerals such as quartz and apatite that potentially represented samples that trapped fluid circulating during the brecciation event, but fluid inclusions were scarce and too small to be analyzed. Samples of ironstone interpreted to have formed as the result of Fe metasomatism (Chapter 3) were also selected for the fluid inclusion study with the aim of determining the nature and composition of fluids related to their formation. Samples of ironstones MT12 and MT19 contain trails of fluid inclusions hosted in quartz.

4.3 Paragenesis and classification of fluid inclusions

Fluid inclusions were classified using the criteria defined by Roedder (1984) for primary, pseudosecondary and secondary inclusions. Primary inclusions formed during the growth of the host crystal and generally occur parallel to growth zones or randomly within the host mineral as single inclusions or three-dimensional groups of inclusions. Secondary inclusions formed through the healing of fractures after the growth of the host crystal is complete; these inclusions normally crosscut the boundaries of the host grain. Pseudosecondary inclusions also formed as result of healing of fractures but before the growth of the host mineral had terminated; this type of inclusion does not crosscut the host crystal boundaries. Inclusions were further subdivided based on the nature of the fluid and the phases present at room temperature. Five main types of

inclusions have been identified from the study of polished thin sections and fluid inclusion sections (Table 4.2 and Table 4.3).

4.3.1 Type I – Carbonic fluid inclusions

Type I fluid inclusions are monophase CO_2-rich fluid inclusions containing only liquid at room temperature, with a vapour bubble developing upon cooling. These inclusions were observed only in granite clast samples MT20 and MT11 and occur within quartz related to transitional magmatic-hydrothermal textures (Chapter 3; Plate 4.1A). These inclusions were further subdivided into type Ia and Ib based on their origin. Type Ia inclusions are primary fluid inclusions occurring in three dimensional clusters normally consisting of a large number of inclusions randomly distributed within the quartz host (Plate 4.1B). The clusters generally consist exclusively of type Ia fluid inclusions, however, in few cases type Ia inclusions were observed associated with type II. Type Ib inclusions occur in trails that do not crosscut the host crystal boundaries and are therefore interpreted as pseudosecondary (Plate 4.1C). Both inclusions types are normally ≤15μm and mostly ovoid or square-shaped.

Table 4.2 Summary and classification of the types of fluid inclusions observed associated with the barren pipe. The composition of the CO_2 phase was determined by microthermometric observations (a vapour bubble developing upon cooling). Distinction between type III and IV inclusions is based on eutectic temperatures determined from microthermometry. Distinction between type IIIb, VIb and V is based on eutectic temperatures determined from microthermometry. Abbreviations: P = primary; PS = pseudosecondary; S = secondary; L = liquid; V = vapor; H = halite.

Type		Phases	Origin	Size (μm)	Fluid Inclusion
Type I - Carbonic	**Type Ia**	CO_2(L)	P	<5-15	
	Type Ib	CO_2(L)	PS	<5-15	
Type II - Mixed Aqueous-Carbonic and Mixed Brine-Carbonic	**Type IIa**	CO_2 (L)+H_2O (L)	P?	⩽ 10	
	Type IIb	CO_2 (L)+H_2O (L)+H	P?	⩽ 10	
Type III - Liquid-rich or halite bearing	**Type IIIa**	L+V+H	S	<5-20	
	Type IIIb	L+V	S	<5-20	
Type IV - Liquid-rich or halite bearing	**Type IVa**	L+V+H	S	<5-20	
	Type IVb	L+V	S	<5-20	
Type V -Liquid-rich		L+V	S	⩽ 10	

Table 4.3 The table summarizes the relative abundance of each fluid inclusion type in the different samples.

	Type Ia	Type Ib	Type IIa	Type IIb	Type III	Type IV	Type V
Pegmatite clast - MT11	abundant	rare	common	rare	abundant	common / rare	common / rare
Pegmatite clast - MT13A	?	?	?	?	abundant	–	common / rare
Pegmatite clast - MT20	abundant	common	common	rare	abundant	common / rare	common / rare
Ironstone - MT12	–	–	–	–	abundant	common	common
Ironstone - MT19	–	–	–	–	abundant	–	common / rare

4.3.2 Type II - Mixed brine-carbonic fluid inclusions

Type II fluid inclusions are mixed brine-carbonic fluid inclusions and they can be further subdivided into type IIa and IIb based on the presence or absence respectively of halite as a daughter phase. Type IIa fluid inclusions at room temperature contain an aqueous phase and liquid CO_2 (a vapour bubble of CO_2 develops upon cooling). They display variable degree of filling ranging from 0.3 to 0.85. This type of inclusion is common and is exclusively observed in pegmatite clast samples MT20 and MT11 (Chapter 3). They are normally found in association with type Ia and type IIb inclusions in three dimensional groups of inclusions occurring in random positions within the host quartz crystals (Plate 4A-C). Most of these inclusions are ≤ 10μm in size and they display variable shapes including ovoidal, square and irregular (Plate 4.2C). Their origin is unclear, although their association with type Ia may suggest a primary origin.

Type IIb fluid inclusions are rare and, like type IIa inclusions, were found exclusively in granite clast samples MT20 and MT11 (Chapter 3). They occur in association with type Ia and IIa fluid inclusions and form three-dimensional clusters that are generally located in random positions within the quartz host (Plate 4.2A-D). At room temperature these inclusions contain an aqueous phase, liquid CO_2 (a vapour bubble of CO_2 develops upon cooling) and a small daughter solid phase, identified as halite (Plate 4.2C and D). The size of the inclusions varies between 5μm and 10μm and they are mostly irregular in shape. Similar to type IIa inclusions their origin is unclear, but their association with type Ia may suggest a primary origin.

Plate 4. 1

(A) Hand specimen of sample MT11 showing primary transitional magmatic-hydrothermal textures in which primary type Ia and pseudosecondary type Ib fluid inclusions were observed.

(B) Photomicrograph showing clusters of primary type Ia CO_2 - rich monophase fluid inclusions. Sample of pegmatite clast MT20.

(C) Photomicrograph showing pseudosecondary trails of type Ib CO_2 - rich monophase fluid inclusions. Sample of pegmatite clast MT20.

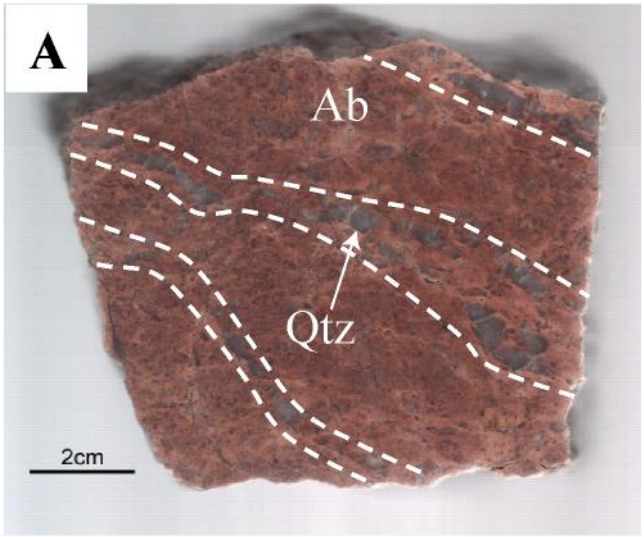
A
Ab
Qtz
2cm

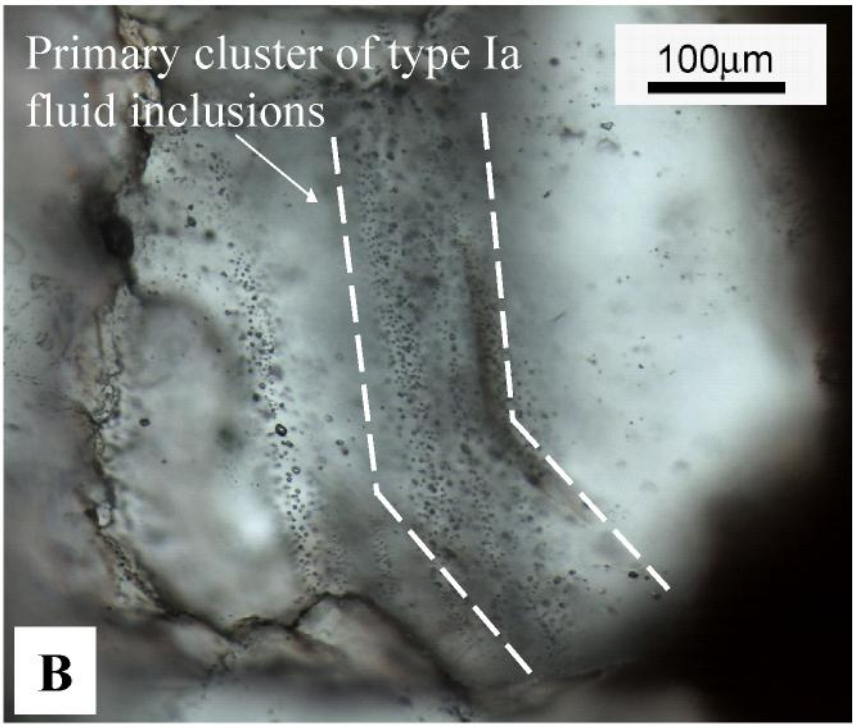
Primary cluster of type Ia fluid inclusions
100µm
B

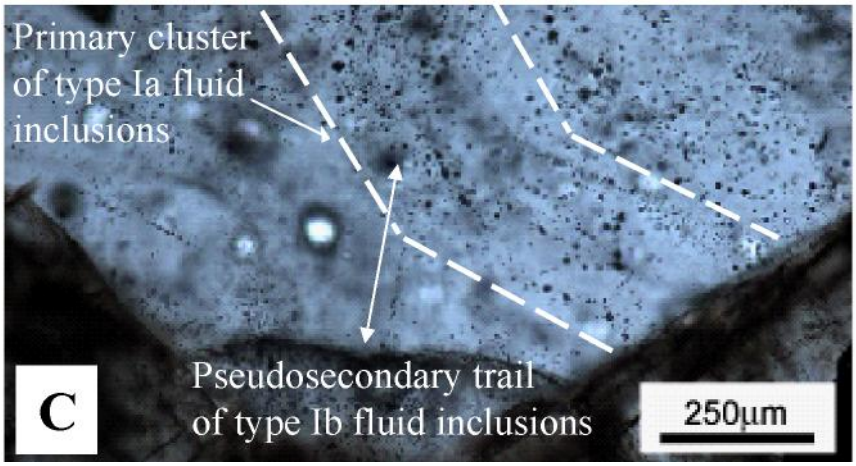
Primary cluster of type Ia fluid inclusions
Pseudosecondary trail of type Ib fluid inclusions
C
250µm

Plate 4. 2

(A) and (B) Photomicrograph showing clusters consisting of primary type Ia CO_2 - rich monophase fluid inclusions, type Ic mixed aqueous-carbonic fluid inclusions, type II mixed brine - carbonic fluid inclusions and type III brine inclusions. Sample of pegmatite clast MT20.

Enlargement of plates 4.3A and B showing (C) type Ic and II fluid inclusions and (D) type Ia and II fluid inclusions. Sample of pegmatite clast MT20.

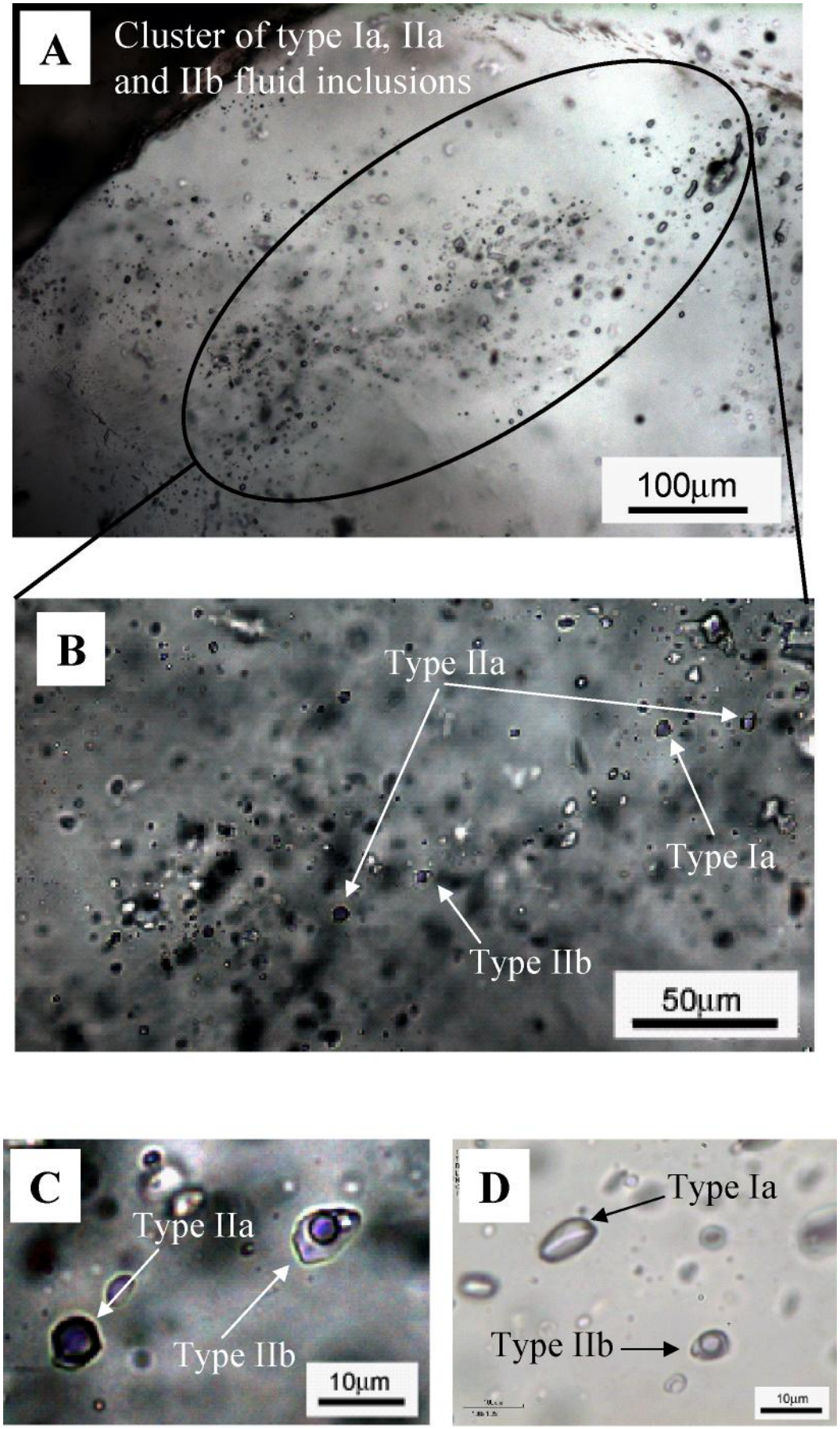
A
Cluster of type Ia, IIa
and IIb fluid inclusions
100µm
B
Type IIa
Type Ia
Type IIb
50µm
C
Type IIa
Type IIb
10µm
D
Type Ia
Type IIb
10µm

4.3.3 Type III – Liquid rich – brine inclusions

Type III inclusions are the most abundant inclusions and occur in every sample considered in the study. Type III fluid inclusions have been subdivided into type IIIa, three phase liquid-rich inclusions with a vapour bubble and a small halite crystal, and type IIIb, two-phase liquid-rich inclusions without daughter phases (Plate 4.3A-E), where the two types occur together type IIIa is the dominant inclusion. Both inclusion types are up to 20μm in size (Plate 4.3A-E). They were observed as single inclusions, in groups of several inclusions occurring randomly within quartz and finally and most commonly in trails that crosscut the quartz host (Plate 4.3A-B). These inclusions are interpreted to be secondary and in particular are linked to albite alteration that affects rock within and adjacent to the pipe (Plate 4.4A-B). This alteration was recognized by cathodoluminescence analysis in quartz - albite intergrowths of sample MT13A where a second generation of luminescent albite was observed cutting non-luminescent primary albite. Type III fluid inclusion trails were observed cutting the quartz and lining up with the luminescent albite (Plate 4.4).

4.3.4 Type IV – Liquid - rich brine inclusions

Type IV inclusions are similar to type III inclusions and the distinction between the two types is based on their different eutectic temperatures that imply different compositions as determined by microthermometry (see section 4.4.4 and 4.4.5).

Plate 4.3

(A) Photomicrograph showing trails of type III and IV fluid inclusions. Ironstone sample MT12.

(B) and (C) Secondary trails of type III halite - bearing and liquid-rich fluid inclusions. Granite clast sample MT11.

(D) Type IIIa three phase halite – bearing and IIIb two phase liquid – rich fluid inclusions. Granite clast sample MT11.

(E) Type IIIa halite – bearing fluid inclusions. Granite clast sample MT11.

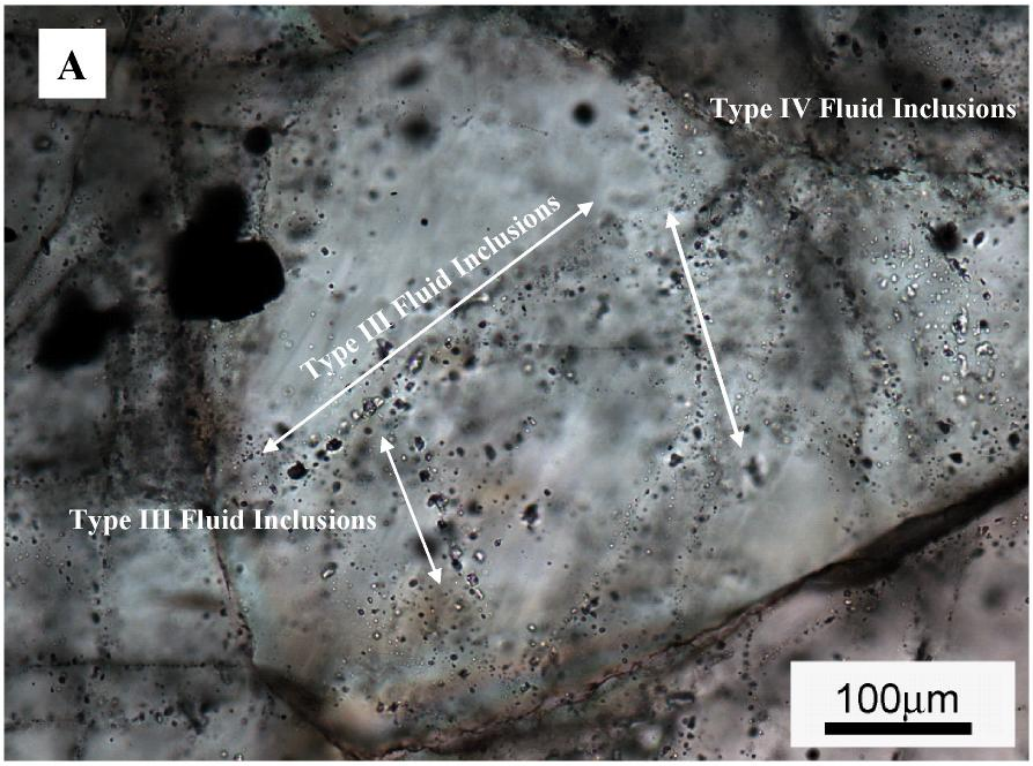
A
Type IV Fluid Inclusions
Type III Fluid Inclusions
Type III Fluid Inclusions
100µm

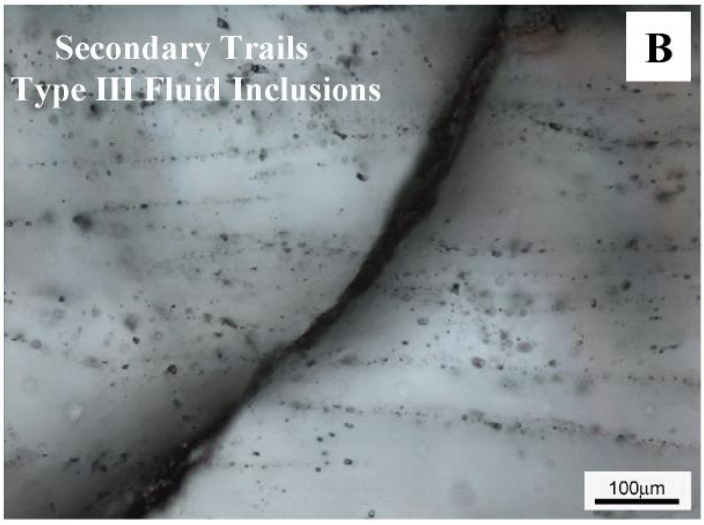
Secondary Trails
Type III Fluid Inclusions
B
100µm

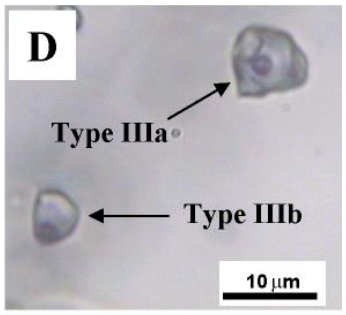
D
Type IIIa
Type IIIb
10 µm

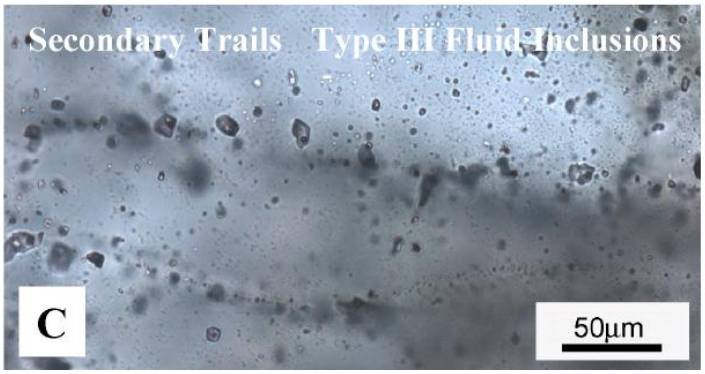
Secondary Trails
Type III Fluid Inclusions
C
50µm

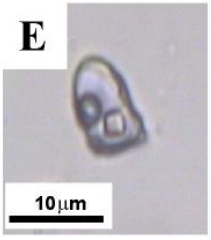
E
10µm

Plate 4.4

(A) Cathodoluminescence image of pegmatite clast MT13A showing secondary luminescent albite cutting primary quartz and non luminescent albite. Secondary fluid inclusion trails can be traced cutting through the quartz layers and linking to the bands in the albite-rich layers.

(B) Photomicrograph of the area shown in plate 4.1A with secondary fluid inclusions trails.

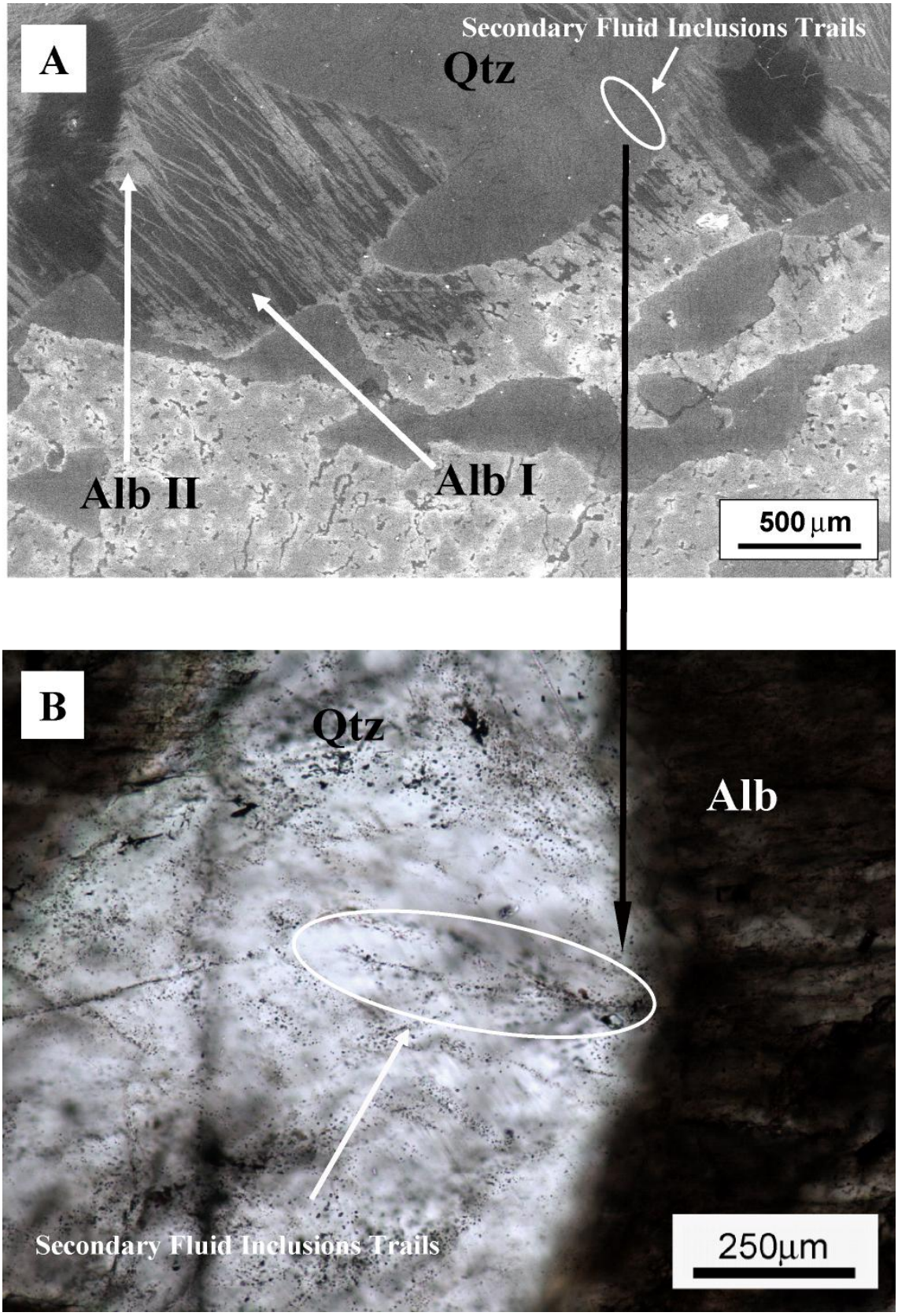
A
Secondary Fluid Inclusions Trails
Qtz
Alb II
Alb I
500 µm
B
Qtz
Alb
Secondary Fluid Inclusions Trails
250µm

Type IV inclusions are less abundant than type III and only occur in samples MT11 and MT12. Type IV fluid inclusions have been subdivided in type IVa and IVb based on the presence or absence respectively of halite as a daughter phase. Where the two types occur together type IVa is the dominant type; the inclusions for both types are up to 20μm in size (Plate 4.3A). They were observed in groups of several inclusions occurring randomly within quartz but mostly in trails (Plate 4.3A). These inclusions are interpreted to be secondary.

4.3.5 Type V - Liquid rich fluid inclusions

Type V inclusions are two phase, liquid-rich and small (<10μm) in size. They are common although not abundant and occur in trails that crosscut the grain boundaries. These inclusions are interpreted as secondary (Plate 4.5A-C). Type V fluid inclusions are commonly smaller than type IIIb and IVb fluid inclusions and are characterized by lower eutectic temperatures and salinities (Table 4.6).

Plate 4. 5

(A) Photomicrograph showing secondary trails of liquid-rich type V fluid inclusions. Ironstone sample MT12.

(B) and (C) Type V fluid inclusions consisting of small vapor bubble and liquid. Ironstone sample MT12.

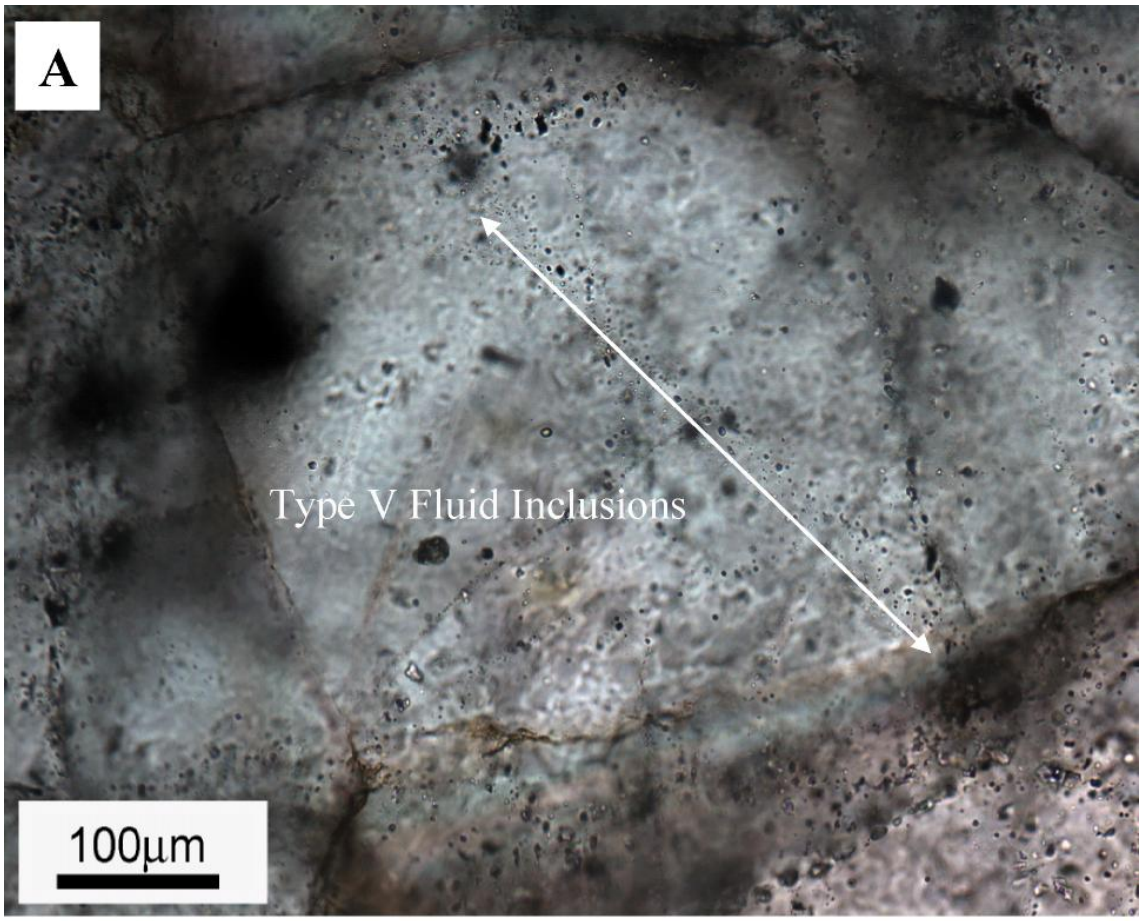
A
Type V Fluid Inclusions
100µm

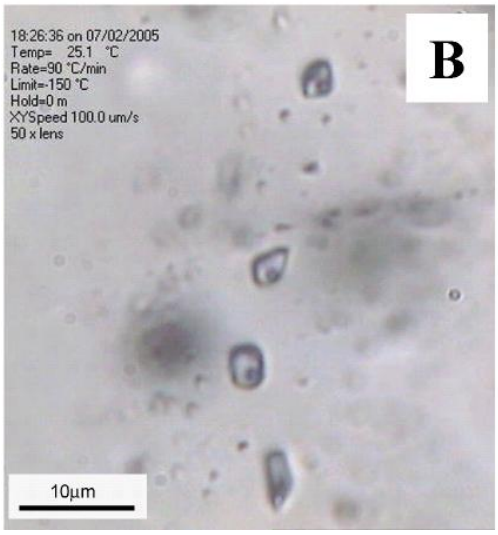
18:26:36 on 07/02/2005
Temp= 25.1 °C
Rate=90 °C/min
Limit=-150 °C
Hold=0 m
XYSpeed 100.0 um/s
50 x lens
B
10µm

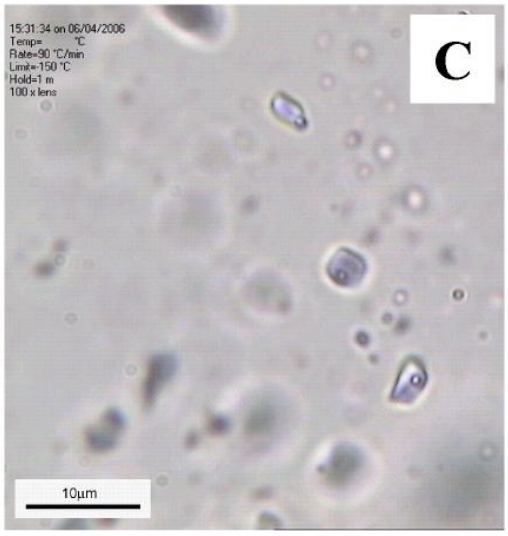
15:31:34 on 06/04/2006
Temp= °C
Rate=90 °C/min
Limit=-150 °C
Hold=1 m
100 x lens
C
10µm

4.4 Microthermometry

Microthermometric analysis of fluid inclusions was undertaken on fluid inclusion wafers using a Linkam MDS600 heating/freezing stage at the School of Earth and Environmental Sciences, James Cook University, coupled to a BX51 Olympus polarizing microscope, with liquid nitrogen as the cooling medium. The stage was calibrated using synthetic fluid inclusions standards consisting of H_2O and H_2O-CO_2. Reproducibility of the melting temperatures of both solid CO_2 and ice below 0°C was better than ± 0.1°C at heating rates of 0.5°C/minute. In total, 149 inclusions of type I-V were analyzed. Data are tabulated in Appendix 4.

4.4.1 Thermometric analysis of Type I fluid inclusions

Type Ia inclusions display CO_2 melting temperatures that vary from -57.7 to -56.7°C (Figure 4.1A, Table 4.4 and Appendix 4.1). The inclusions homogenized by disappearance of the vapour into the liquid phase and homogenization temperatures ranged from -17.5 to -0.5°C (Figure 4.1B, Table 4.4 and Appendix 4.1).

Type Ib inclusions have CO_2 melting temperatures ranging from -57.3 to -56.1°C (Figure 4.1A, Table 4.4 and Appendix 4.2). The inclusion homogenized by disappearance of the vapour into the liquid phase between -1.1 and 30.5°C (Figure 4.1B, Table 4.4 and Appendix 4.2).

Table 4.4 Summary of microthermometry data obtained from type I and II fluid inclusions. Abbreviations: $TmCO_2$ = CO_2 melting temperature; Tfm = temperature of first melting; Thm = temperature of hydrohalite melting; Tm Cla = temperature of clathrate melting; $ThCO_2$ = CO_2 homogenization temperature; TsNaCl = halite dissolution temperature; Th = total homogenization temperature; Tdec = decrepitation temperature; Sal = salinity; Df= degree of filling. Temperature in degree Celcius. The numbers in brackets refer to the total number of inclusions analyzed. However, not all the phase transitions were recorded for each inclusion type (see Appendices 4.1-4.4). For example, a total of 12 Type IIa fluid inclusions were analyzed but complete homogenization was observed for just one inclusion (Appendix 4.3).

Fluid inclusion type		$TmCO_2$	Tfm	Thm	TmCla	$ThCO_2$	TsNaCl	Th	Tdec	Sal (wt% NaCl eq)	D_F	CO_2 Density (gr/cm^3)	Bulk Density (gr/cm^3)
Type I- Carbonic	**Type Ia (n=24)**	–57.7 to −56.7				–17.5 to −0.5					–	0.93 to 1.02	
	Type Ib (n= 10)	–57.3 to −56.1				–1.1 to 30.5					–	0.57 to 0.94	
Type II - Mixed Aqueous-Carbonic and Mixed Brine-Carbonic	**Type IIa (n=12)**	–57.8 to –56.2	– 57.3 to –54.1		–12.9 to –3.6	–9.1 to –25.4		276.4	248.9 to 462.1	22.4 to 29	0.3 to 0.96	0.71 to 0.98	0.84 to 0.96
	Type IIb (n=4)	–57.7 to −56.2	–56.6/ −32.4	11.4 to 14.4	–12.3 to −11.6	–0.7 to −21.3	186.3 to 307		255 to 315.4	31.2 to 38.7	–		

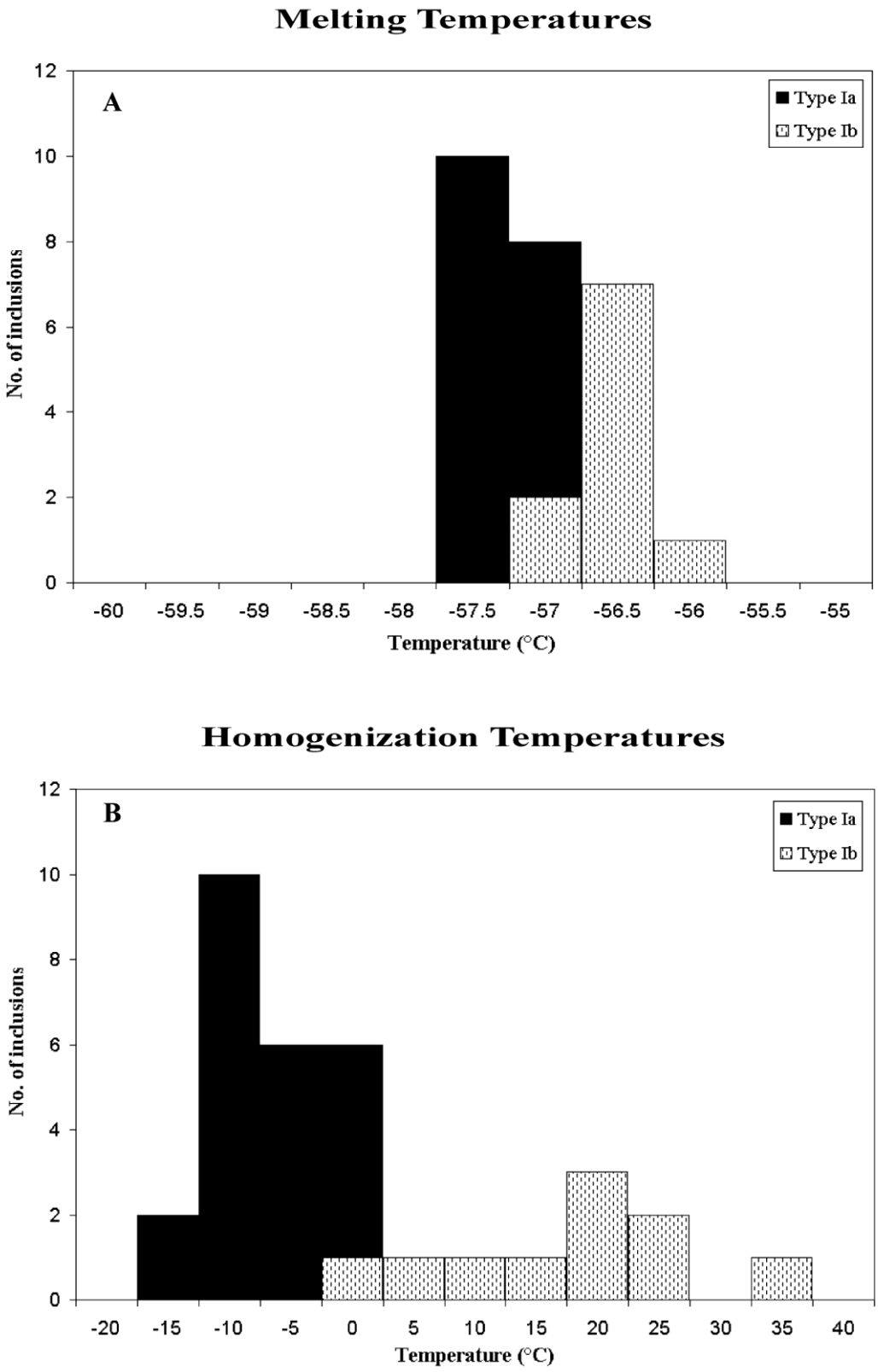

Figure 4.1 Histograms showing temperatures of CO_2 melting (A) and CO_2 homogenization temperatures (B) of type Ia and Ib fluid inclusions.

4.4.2 Thermometric analysis of Type II fluid inclusions

CO_2 in type IIa fluid inclusions melted between -57.8 and -56.2°C (Figure 4.2A, Table 4.4 and Appendix 4.3). Temperature of first melting of the aqueous phase ranged from -57.3 to -54.1°C. CO_2-clathrate melted from -12.9 to -3.6°C (Figure 4.2A, Table 4.4 and Appendix 4.3). CO_2 homogenized through vapour disappearance into the liquid phase at temperatures between -9.1 and 25.4°C (Figure 4.2B, Table 4.4 and Appendix 4.3). Most of the inclusions decrepitated before total homogenization and only one homogenization temperature was recorded at 276.4°C into liquid carbonic phase. Decrepitation temperatures ranged between 256 and 462.1°C (Figure 4.2C, Table 4.4 and Appendix 4.3).

Type IIb fluid inclusions are very rare and here data are reported for 4 fluid inclusions only. CO_2 melted between -57.7 and -56.2°C. Temperature of first melting was observed on only two occasions and the recorded values are -56.6°C and -32.4°C; temperature of CO_2-clathrate melting ranged between -12.3 and -11.6°C (Figure 4.3A, Table 4.4 and Appendix 4.4). All the inclusions displayed metastable hydrohalite melting at temperatures spanning from 11.4 to 14.4°C (Figure 4.3A, Table 4.4 and Appendix 4.4). Homogenization of CO_2 occurred via disappearance of the vapour into the liquid phase and range from -0.7 to 21.3°C (Figure 4.3B, Table 4.4 and Appendix 4.4). Halite dissolution temperatures are 186.3, 255.7 and 307°C (Figure 4.3C, Table 4.4 and Appendix 4.4). All the inclusions decrepitated before total homogenization and decrepitation temperatures ranged from 250 to 315°C (Figure 4.3C, Table 4.4 and Appendix 4.4).

Salinities for type IIa inclusions were estimated from CO_2-clathrate melting temperatures using the software Q_2 (Bakker, 1997; Bakker and Brown, 2003) for a H_2O-

CO_2-NaCl system using equations by Duan et al (1992a; 1992b). However, clathrates melted for most inclusions below -10°C, a temperature that represents the lower limit of the clathrate stability field for fluids in the H_2O-CO_2-NaCl system. Such low clathrate melting temperatures may be associated with the presence of salts other than NaCl in the aqueous phase. The addition of salts to a H_2O-CO_2 fluid has the effect of depressing the clathrate stability and the depression is greater when salts of strongly charged cations such as Ca^{2+}, $Fe^{2+}$and Mg^{2+} are present (Diamond, 2003). Low eutectic temperatures observed for these inclusions indicate the presence of $CaCl_2$ in the aqueous phase (Shepherd et al., 1985). For those inclusions displaying clathrate melting below -10°C only a minimum estimate of the salinity is possible: the calculated salinity is 29 wt % NaCl equivalent that correspond to a clathrate melting temperature of -10°C (Figure 4.4, Table 4.4 and Appendix 4.3). Calculated salinities for the remaining inclusions are 22.4 and 25.7 wt % NaCl equivalent (Figure 4.4, Table 4.4 and Appendix 4.3). The software Q_2 determines the salinities of inclusions based on clathrate melting temperatures. For type IIb inclusions that contain a halite crystal using Q_2 would have lead to an underestimate of the salinities and therefore.was not used. Salinities of type IIb fluid inclusions were calculated based on halite dissolution temperatures using the equation of Sterner et al. (1988). The equation is valid for evaluation of salinities of halite-bearing inclusions in the H_2O-NaCl system. Type IIb inclusions do not represent a simple H_2O-NaCl fluid since the measured eutectic temperature indicates the presence of $CaCl_2$ in the fluid (Shepherd et al., 1985). Nonetheless, this method provides a guide to salinity and it is useful for comparing different types of inclusions. Estimated salinities are 31.2, 35 and 38.7 wt % NaCl equivalent (Figure 4.4, Table 4.4 and Appendix 4.4).

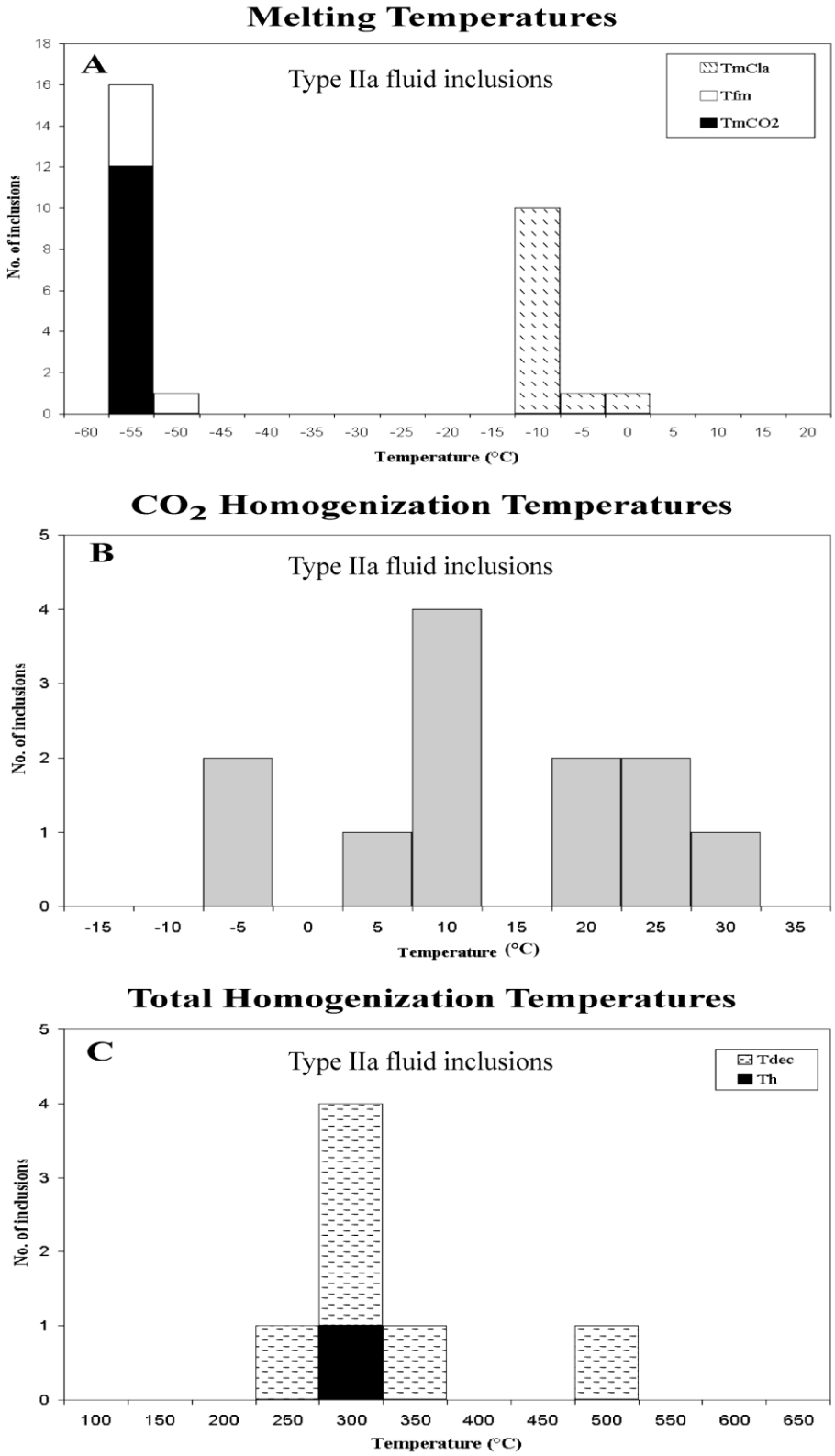

Figure 4.2 Histogram showing (A) temperatures of melting (CO_2 melting, first melting and final ice melting), (B) CO_2 homogenization temperatures and (C) total and decrepitation temperatures of type IIa fluid inclusions. $TmCO_2$ = CO_2 melting temperature; Tfm = temperature of first melting; TmCla = temperature of clathrate melting; Th = total homogenization temperature; Tdec = decrepitation temperature.

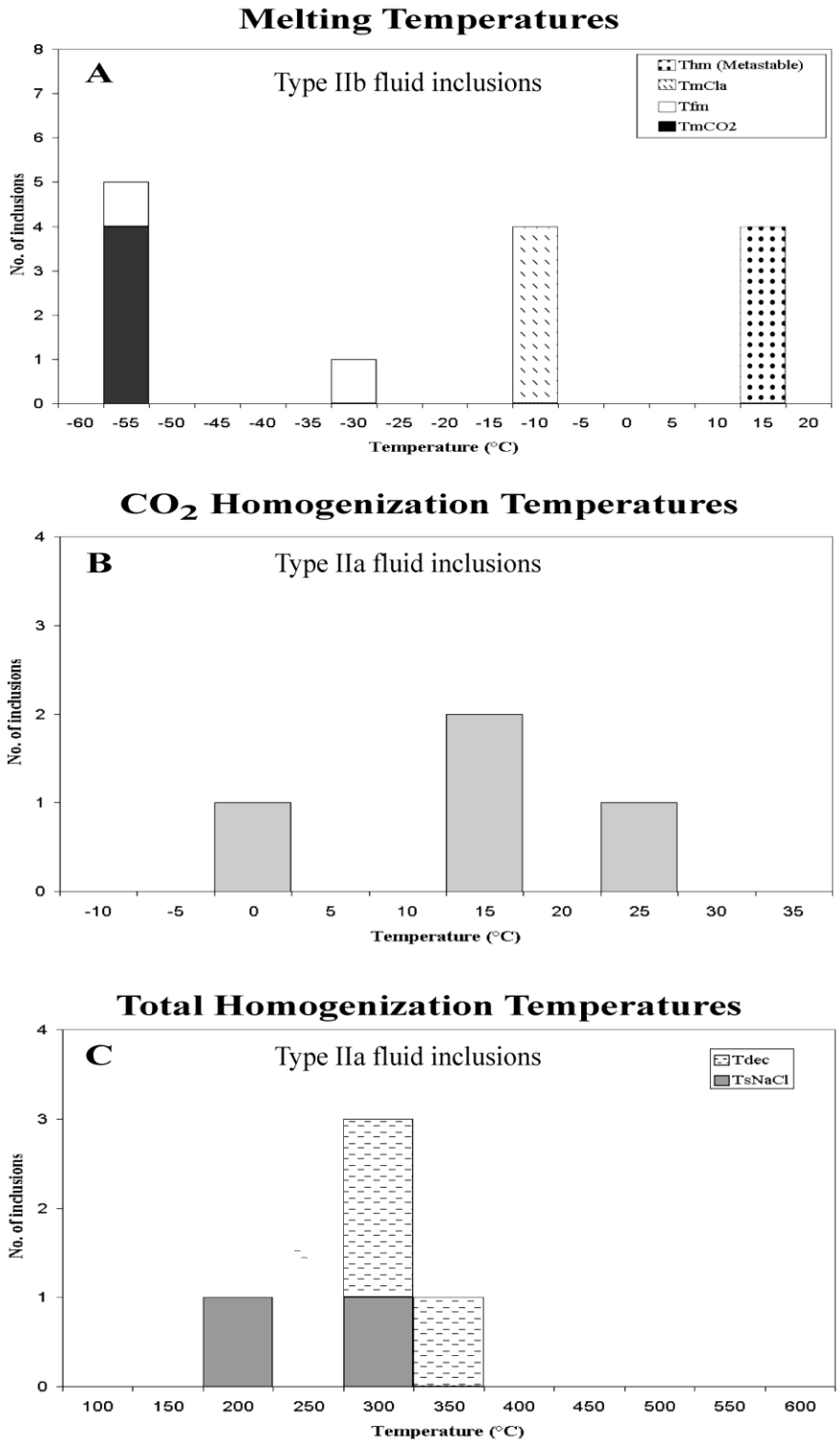

Figure 4.3 Histograms displaying (A) temperatures of melting (CO_2 melting, first melting, final ice melting and final hydrohalite melting), (B) temperatures of CO_2 homogenization and (C) temperatures of halite dissolution and decrepitation of type IIb fluid inclusions. $TmCO_2$ = CO_2 melting temperature; Tfm = temperature of first melting; TmCla = temperature of clathrate melting; Thm = temperature of hydrohalite melting; Tdec = decrepitation temperature; Ts NaCl = halite dissolution temperature.

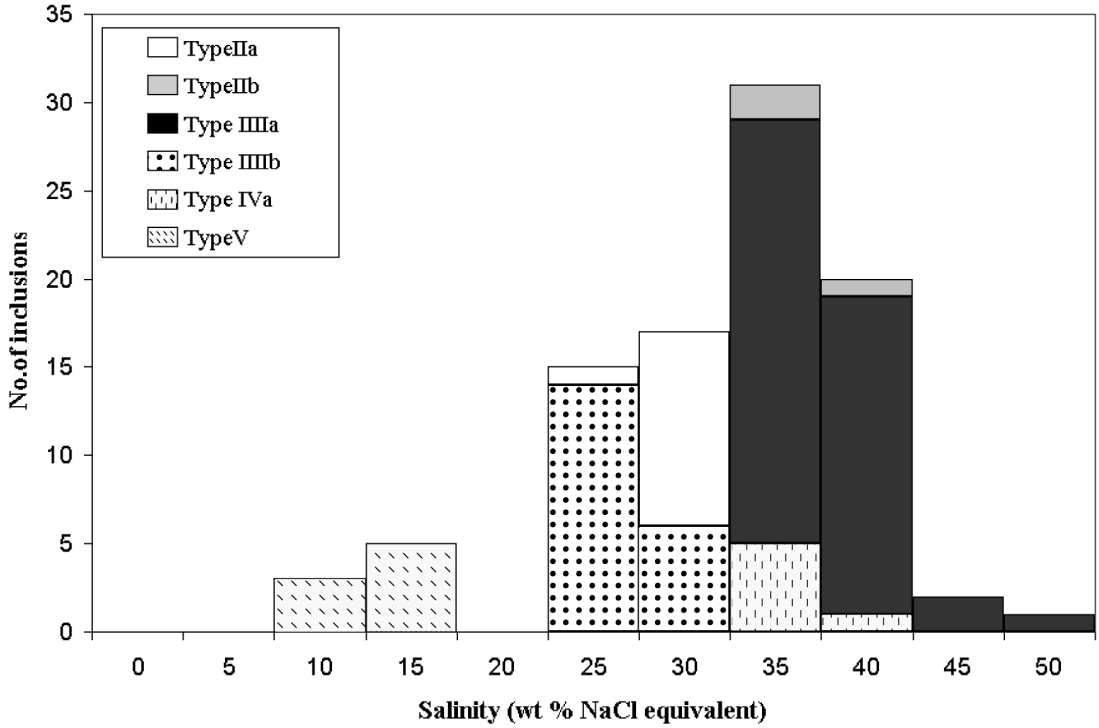

Figure 4. 4 Histogram displaying salinity estimates of types II, III, IV and V fluid inclusions. Values of salinity for type III inclusions are reported in NaCl + $CaCl_2$ wt% equivalent. For the remaining inclusion types values are intended in NaCl wt% equivalent.

The composition of type IIa inclusions was estimated using Q_2 (Bakker, 1997; Bakker and Brown, 2003) and is reported in Table 4.5 and Appendix 4.3. Unfortunately isochores for these inclusions could not be calculated since homogenization temperatures were not observed (all fluid inclusions but one decrepitated before complete homogenization). An attempt was made to model type IIb fluid inclusions with the program BULK (Bakker, 2003; Bakker and Brown, 2003), but these inclusions exceed the eutectic composition of a H_2O-NaCl system. The presence of other salts in solution (i.e. $CaCl_2$) is confirmed by the low eutectic temperatures displayed by these inclusions. The modeling of these inclusions in the H_2O-NaCl- $CaCl_2$ system requires the knowledge of the Na/Ca ratios that, however, cannot be determine since final ice

melting was not observed (both ice melting and halite dissolution temperatures are needed for the calculation of Na/Ca ratio; see Section 4.4.3). Therefore no compositional data is presented for type IIb fluid inclusions.

Table 4. 5 Bulk fluid properties of type IIa fluid inclusions obtained with the software Q_2 (Bakker, 1997; Bakker and Brown, 2003)

Sample	Ref. No	fi_id	Sal (TmCla)	D CO_2	Bulk Density	x(H_2O)	x(CO_2)	x(NaCl)
MT20	MT20_f3	f3_33	29.0	0.903	0.912	0.640	0.199	0.161
MT20	MT20_f3	f3_34	29.0	0.881	0.905	0.652	0.183	0.165
MT20	MT20_f3	f3_35	22.4	0.803	0.879	0.655	0.228	0.117
MT20	MT20_f3	f3_36	25.7	0.704	0.848	0.692	0.160	0.148
MT20	MT20_f3	f3_37	29.0	0.883	0.909	0.697	0.127	0.176
MT20	MT20_f3	f3_17	29.0	0.795	0.844	0.520	0.348	0.131
MT20	MT20_f8	f8_2	29.0	0.962	0.958	0.470	0.412	0.118
MT20	MT20_f8	f8_3	29.0	0.760	0.893	0.739	0.075	0.186
MT20	MT20_f8	f8_4	29.0	0.878	0.929	0.671	0.160	0.169
MT20	MT20_f8	f8_5	29.0	0.761	0.856	0.645	0.192	0.163
MT20	MT20_f8	f8_6	29.0	0.884	0.897	0.494	0.381	0.125
MT20	MT20_f8	f8_8	29.0	0.978	0.960	0.398	0.502	0.100

Compositional data of type IIa fluid inclusions are interpreted by comparison with experimental work on synthetic fluid inclusions in the H_2O-CO_2-NaCl system by Schmidt and Bodnar (2000). In their paper they presented several isoplethic diagrams in the P-T space, for temperatures between 300°C and 800°C and pressures between 1000 and 5000 bar, for a range a fluid inclusion compositions. P-T diagrams constructed by Schmidt and Bodnar (2000) for fluid inclusion compositions closest to type IIa inclusion composition are shown in Figure 4.5. The diagrams show the high-pressure portions of the solvus and lines of equal homogenization temperatures for constant

composition for fluid inclusions containing 20 wt% NaCl and 20 mol% CO_2 (Figure 4.5A) and 40 wt% NaCl and 10 mol% CO_2 both relative to water (Figure 4.5B). Type IIa fluid inclusions have salinity (~ 30 wt% NaCl equiv.) intermediate between the two composition studied by Schmidt and Bodnar (2000) and display generally higher CO_2 concentrations (Table 4.5). Most of type IIa fluid inclusions have CO_2 concentrations around 20 mol% but quite a few contain CO_2 concentrations ≥ 35 mol% and up to 50 mol% (Table 4.5).

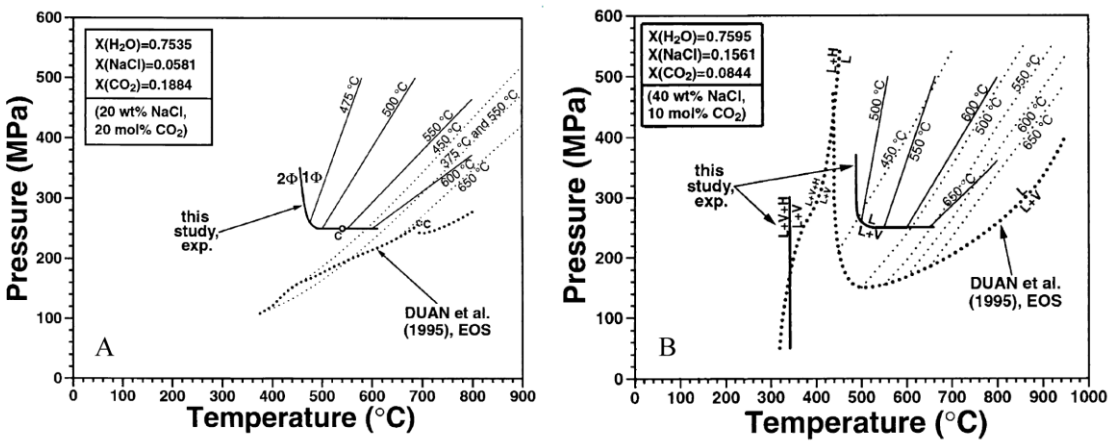

Figure 4.5 (A) High-pressure portions of the solvus, critical points, and lines of equal homogenization temperature for a fluid containing H2O + 20 wt.% NaCl + 20 mol% CO2. 1Φ = one-phase field; 2Φ = coexisting liquid and vapor; C = critical point. (B) Liquidi, high-pressure portions of the solvus, and lines of equal homogenization temperature for a fluid containing H2O + 40 wt.% NaCl + 10 mol% CO2. L = liquid field, L(40) = liquid containing 40 wt.% NaCl, L + V = coexisting liquid and vapor field, L + H = coexisting liquid and halite field, L + V 1+ H = field of coexisting liquid, vapor, and halite. Heavy lines refer to phase equilibria; thin lines refer to lines of equal homogenization temperature in the one-phase field, labeled with the corresponding homogenization temperature. The experimental data are from Schmidt and Bodnar (2000) and reference therein. Modified after Schmidt and Bodnar (2000).

Schmidt and Bodnar (2000) showed that the addition of NaCl or CO_2 or both causes a shift of the critical point and the solvus towards higher temperatures and pressures resulting in immiscibility over a wide range of PTX conditions, even in deeper crustal rocks. For example, for fluid composition shown in Figure 4.5A (20 wt% NaCl and 20 mol% CO_2) and 4.5B (40 wt% NaCl and 10 mol% CO_2) immiscibility occurs for temperatures and pressures below approximately 450°C and 2500 bar and

below 500°C and 2500 bar respectively. Type IIa fluid inclusions have higher salinities and generally higher CO_2 concentrations than the fluid represented in Figure 4.5A and lower salinities but consistently higher CO_2 contents than the fluid shown in Figure 4.5B. Therefore, immiscibility for type IIa fluid inclusions is expected to occur at higher temperature and pressure conditions compared to fluids in Figure 4.5. These considerations are further developed Section 7.2 where the origin of type II fluid inclusions is discussed, particularly in relation to the genesis of the SRBP.

4.4.3 Thermometric analysis of Type III fluid inclusions

First melting for type IIIa fluid inclusions spanned a wide range of temperatures from -67.2 to -44.2°C (Figure 4.6A, Table 4.6 and Appendix 4.5). These inclusions displayed brown colour and granular appearance during cooling which combined with the low eutectic temperatures indicate the presence of $CaCl_2$ in the fluid (Shepherd et al., 1985). Ice melting for these inclusions ranged from -29.4 to -21.7°C (Figure 4.6A, Table 4.6 and Appendix 4.5). Hydrohalite melting in most cases was metastable and ranged between 0.2 and 32.2°; only two inclusions displayed hydrohalite melting below 0°C (-11.6°C and -1.1°C; Figure 4.6A, Table 4.6 and Appendix 4.5). Upon heating the vapor bubble normally disappeared before dissolution of halite at temperatures between 106.8 and 198.3°C, while halite dissolved at temperatures ranging from 147.5 and 360°C. One inclusion homogenized via vapor disappearance with halite dissolving at 204.9°C and the vapor bubble disappearing at 238.2°C (Figure 4.6B, Table 4.6 and Appendix 4.5). Total homogenization temperatures ranged between 147.5°C and 360°C (Figure 4.6C, Table 4.6 and Appendix 4.5).

Type IIIb have eutectic temperatures between -69.7 and -50.4°C and displayed freezing behavior similar to type IIIa (Figure 4.6A, Table 4.6 and Appendix 4.6). Ice melted between -33.7 and -20.0°C (Figure 4.6A, Table 4.6 and Appendix 4.6). Hydrohalite melted at temperatures ranging from -42.4 and -3.7°C, although commonly the melting was metastable and occurred at temperatures spanning from 2.8 to 25°C (Figure 4.6A, Table 4.6 and Appendix 4.6). Type IIIb inclusions homogenize between 109.2 and 183.5°C (Figure 4.6B and C, Table 4.6 and Appendix 4.6).

Salinities of these inclusions were estimated using the program Calcicbrine designed for fluids in the H_2O-NaCl-$CaCl_2$ system (Naden, 1996). Salinities for halite-bearing fluid inclusions are calculated using both ice melting and halite dissolution temperatures. Calculation of salinities for two-phase fluid inclusions requires both temperatures of ice and hydrohalite melting (Naden, 1996). Salinities for two-phase fluid inclusions displaying metastable melting of hydrohalite were not determined. The program return salinity values as the sum of the NaCl and $CaCl_2$ concentration in the fluid expressed as NaCl + $CaCl_2$ equivalent. Calculated salinities range from 30.3 to 45.4 and from 22.4 to 28.1 NaCl + $CaCl_2$ wt% equivalent for type IIIa and IIIb fluid inclusions respectively (Figure 4.4, Table 4.5, Appendix 4.5 and 4.6). The software also allows the calculation of the NaCl and $CaCl_2$ contents. Type IIIa inclusions have concentrations of NaCl ranging from 20 to 43 wt% equiv. and $CaCl_2$ from 1.5 to 13 wt. % equiv. with NaCl/NaCl+$CaCl_2$ between 0.6 and 1 but consistently around 0.7 for most of the inclusions. Type IIIb fluid inclusions display variable NaCl and $CaCl_2$ content ranging from 2.1 and 20.7 and from 5.2 to 24.2 wt. % equiv respectively, mirrored by variable NaCl/NaCl+$CaCl_2$ spanning from 0.1 to 0.8 (Figure 4.7, Appendix 4.6).

Table 4.6 Summary of microthermometry measurements for type III, IV and V fluid inclusions. Tfm = temperature of first melting; Thm = temperature of hydrohalite melting; Tm = final melting temperature of ice; Thv = temperature of vapor disappearance; TsNaCl = halite dissolution temperature; Th = total homogenization temperature; Sal = salinity. Temperature in degree Celcius. The numbers in brackets refer to the total number of inclusions analyzed. However, not all the phase transitions were recorded for each inclusion type (see Appendices 4.5-4.9).

Fluid inclusion type		Tfm	Thm	Tm	Thv	TsNaCl	Th	Sal (wt% NaCl eq)	Sal (wt% NaCl +CaCl2 equiv.)	Bulk Density (gr/cm^3)	D_F
Type III - Liquid-rich or halite bearing	**Type IIIa (n=69)**	–67.2 to – 44.2	–11.6 to 32.2	–29.4 to – 21.7	106.8 to 238.2	147.5 to 360	147.5 to 360		30.3 to 45.4	0.94 to 1.17	
	Type IIIb (n=32)	–69.7 to – 50.4	–42.4 to 25	–33.7 to – 20	109.2 to 183.5		109.2 to 183.5		22.4 to 28.1	1.08 to 1.11	0.26 to 0.93
Type IV - Liquid-rich or halite bearing	**Type IVa (n=11)**	–36.6 to – 27.1	5.1 to 15	–24.4 to – 19.1	118.1 to 255.9	203.6 to 256.7	203.6 to 256.7	32.1 to 35.1		1.11 to 1.19	
	Type IVb (n=6)	–33.3 to – 29	9 to 14.6	–25.1 to – 21.6	166.3 to 184.7		166.3 to 184.7			1.07 to 1.07	0.53 to 0.84
Type V -Liquid-rich	**Type V (n=9)**	– 27.2 to – 24	– 24.9 to – 20.5	– 9 to – 5.7	144 to 245.4		144 to 245.4	8.8 to 12.8		0.91 to 0.99	0.22 to 0.95

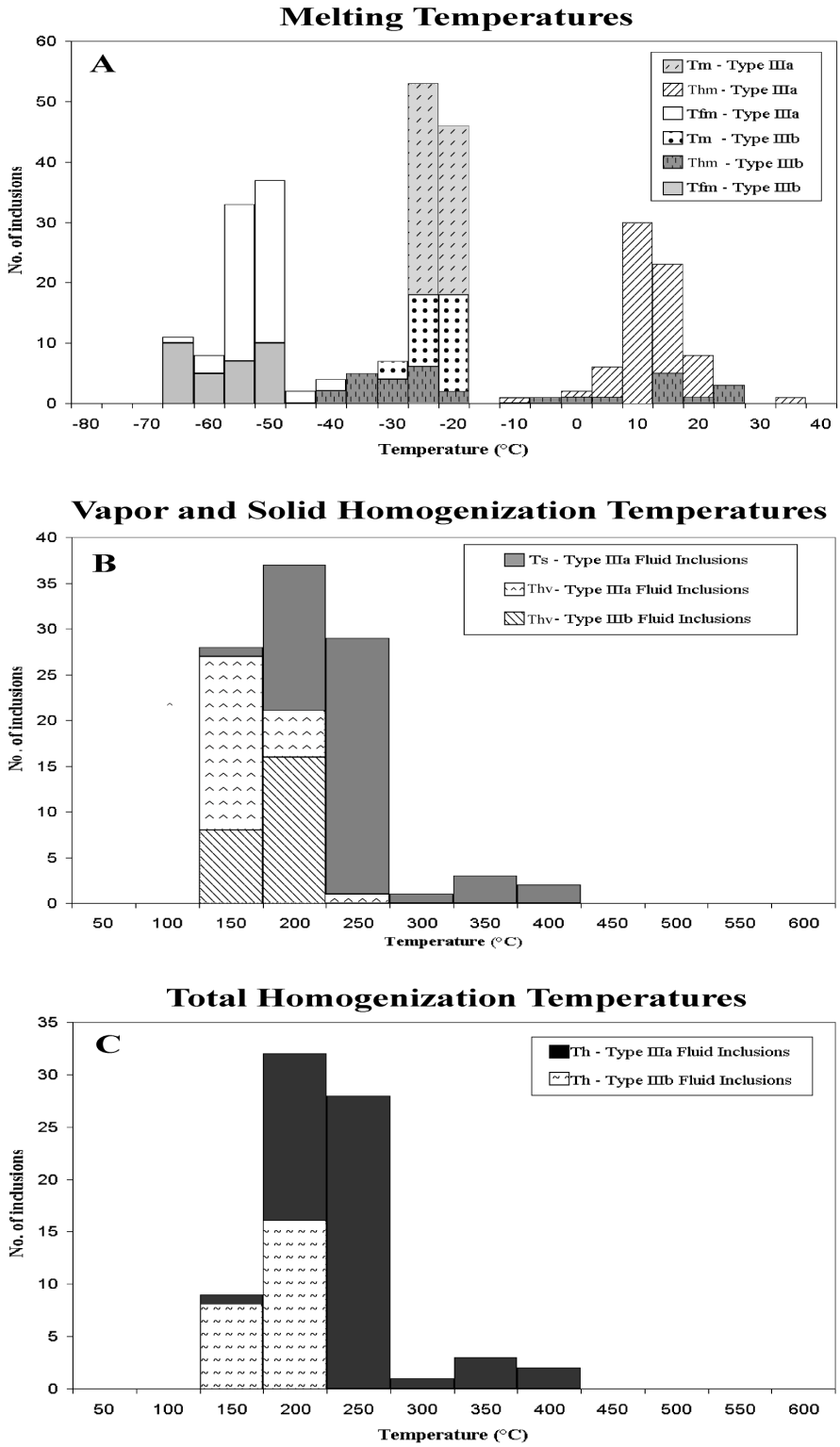

Figure 4.6 Histograms showing (A) melting temperatures (first melting, final ice melting and final hydrohalite melting), (B) vapor and solid phase homogenization temperatures and (C) total homogenization temperatures of type III fluid inclusions. Tfm = temperature of first melting; Thm = temperature of hydrohalite melting; Tm = final melting temperature of ice; Thv = temperature of vapor disappearance; TsNaCl = halite dissolution temperature; Th = total homogenization temperature.

4.4.4 Thermometric analysis of Type IV fluid inclusions

Temperatures of first melting for type IVa fluid inclusions span from -36.6 to -27.1 °C (Figure 4.8A, Table 4.6 and Appendix 4.7) and indicate the presence of other salts (i.e. $MgCl_2$ and $FeCl_2$) in addition to NaCl (Shepherd et al., 1985). Ice melted between -25.1 and -19.1°C, while hydrohalite melting was metastable between 5.1 and 15°C (Figure 4.8A, Table 4.6 and Appendix 4.7). These inclusions displayed homogenization behavior similar to type IIIa inclusions with the vapor bubble disappearing first upon heating, at temperatures between 118.1 and 255.9°C, followed by halite dissolution at temperatures between 203.6 and 256.7°C (Figure 4.8B, Table 4.6 and Appendix 4.7). One inclusion homogenized via vapor disappearance at 256.7°C with halite dissolving first at 246.3°C (Figure 4.8B and Appendix 4.7). Total homogenization occurred at temperatures in the range from 203.6 to 256.7°C (Figure 4.8C, Table 4.6 and Appendix 4.7).

Type IVb displayed eutectic temperatures in the range between -33.3 and -29°C, ice melting from -25.1 to -21.6°C and metastable hydrohalite melting between 9 and 14.6°C (Figure 4.8A, Table 4.5 and Appendix 4.8). The inclusions homogenized at temperatures spanning from 166.3 to 184.7°C (Figure 4.8B and C, Table 4.6 and Appendix 4.8).

Temperatures of first melting indicate a fluid with composition more complex than a H_2O-NaCl fluid and that likely includes KCl-$MgCl_2$-$FeCl_2$ components (Shepherd et al., 1985). Salinities were determined based on halite dissolution using the equation of Sterner et al. (1988) derived for evaluation of salinities of halite-bearing inclusions in the H_2O-NaCl system. This method was employed despite eutectic temperatures that indicate the fluid has a more complex composition than a simple H_2O-

NaCl fluid for reasons similar to those mentioned for the estimation of salinity of type II inclusions. Salinity was not estimated for two-phase inclusions due to the metastabilty of the hydrohalite. However, a salinity estimate for type IVb can be derived from the upper stability limit of hydrohalite (0.1°C). The calculated value is 26.3 wt%NaCl equiv. and represents a maximum salinity estimate. Calculated salinities for type IVa range from 32.1 to 35.1 wt % NaCl equivalent (Figure 4.4, Table 4.6 and Appendix 4.7).

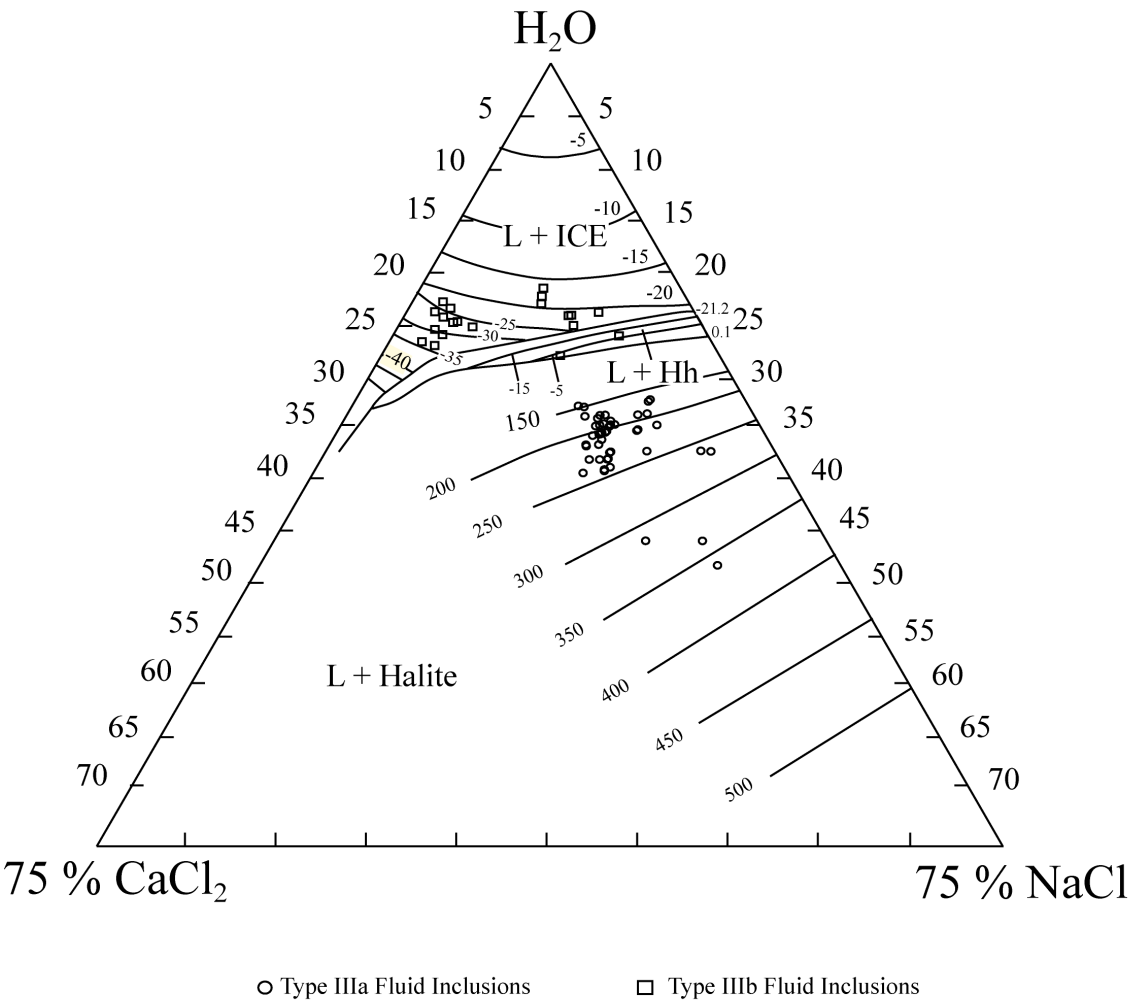

Figure 4.7 Ternary diagram for the NaCl - $CaCl_2$ - H_2O system displaying the composition of type III fluid inclusions (modified from Vanko et al. 1988).

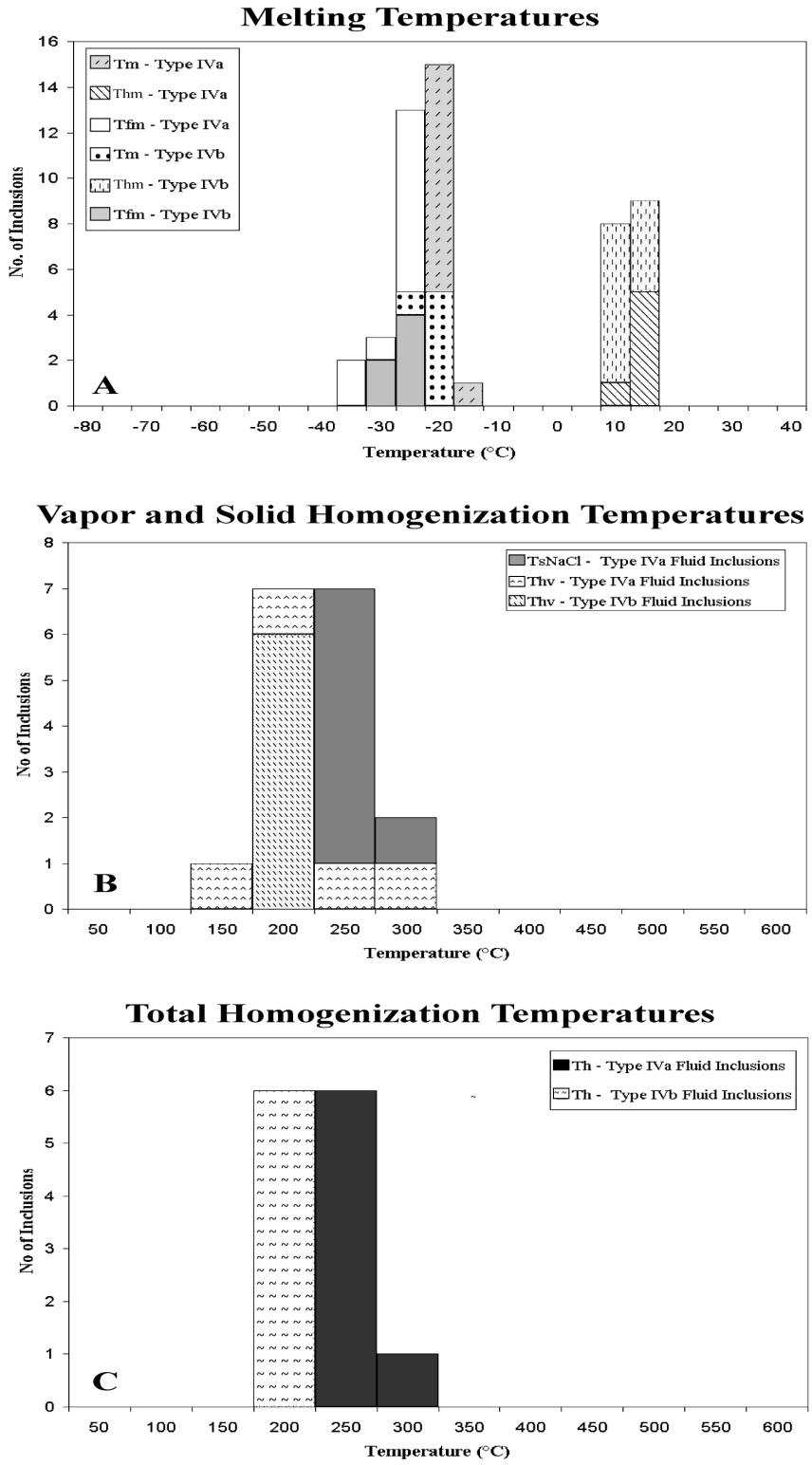

Figure 4.8 Histograms showing (A) melting temperatures (first melting, final ice melting and final hydrohalite melting), (B) vapor and solid phase homogenization temperatures and (C) total homogenization temperatures of type IV fluid inclusions. Tfm = temperature of first melting; Thm = temperature of hydrohalite melting; Tm = final melting temperature of ice; Thv = temperature of vapor disappearance; TsNaCl = halite dissolution temperature; Th = total homogenization temperature.

4.4.5 Thermometric analysis of Type V fluid inclusions

Eutectic temperatures ranged from -37.2 to -24°C (Figure 4.9A, Table 4.6 and Appendix 4.9). These temperatures are lower than eutectic temperatures for a fluid with H_2O-NaCl and indicate the presence of other salts in the fluid (i.e. $MgCl_2$, $FeCl_2$ and KCl). Hydrohalite melted between -24.9 and -20.5°C and ice between -9 and -5.7°C (Figure 4.9A, Table 4.6 and Appendix 4.9). In some cases hydrohalite melting was not observed. The inclusions homogenize by vapour disappearance into the liquid phase and homogenization temperatures range from 144°C to 245.4°C (Figure 4.9B, Table 4.6 and Appendix 4.9). Salinities were determined based on ice melting temperatures using the equation of Bodnar (1993), although eutectic temperatures may indicate the presence of other salts in solution. Nonetheless, this method provides a guide to salinity and it is useful for comparing different types of inclusions. Calculated salinities range from 8.8 to 12.8 wt % NaCl equivalent (Figure 4.4, Table 4.6 and Appendix 4.9).

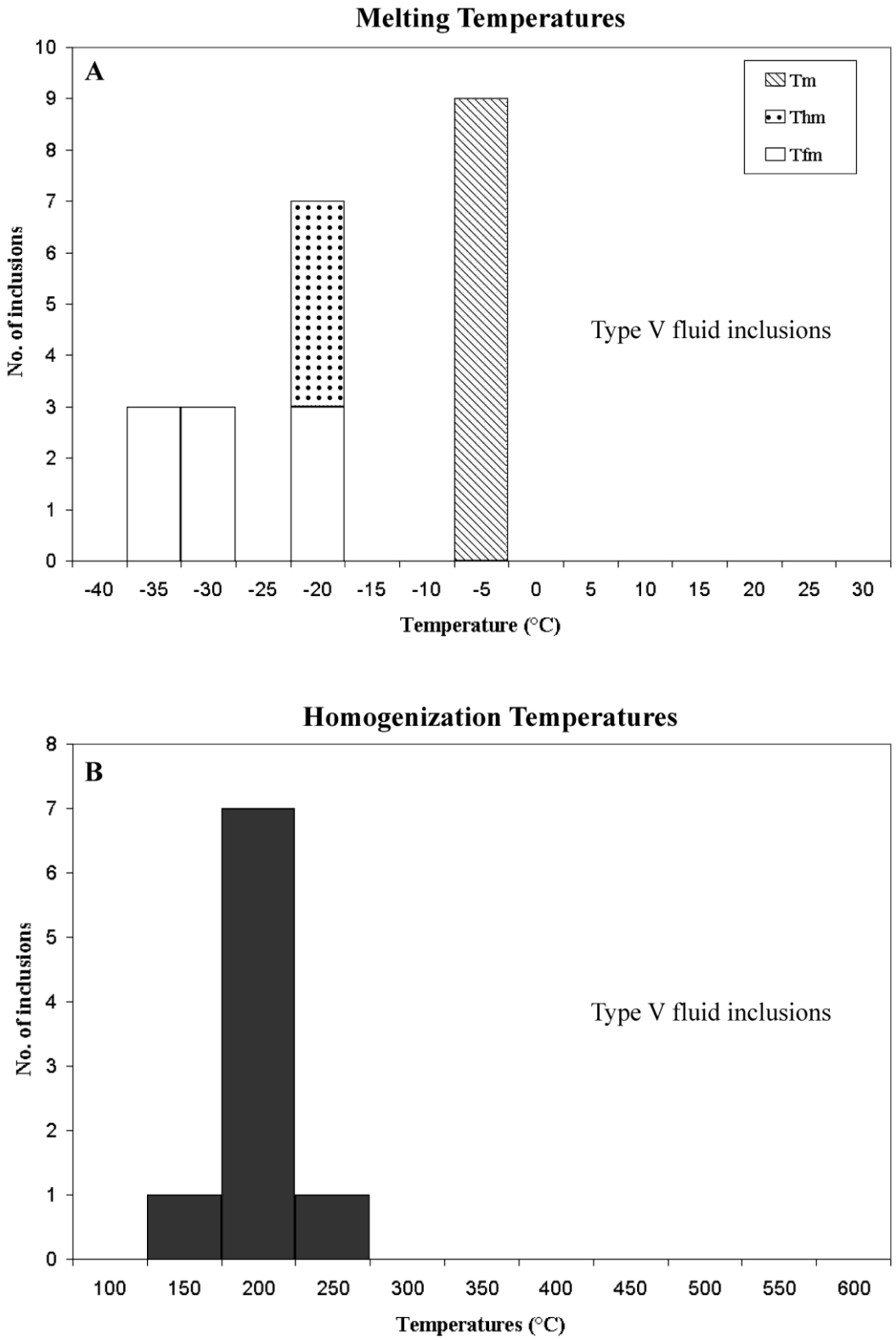

Figure 4.9 Histograms showing (A) melting temperatures (first melting, final ice melting and final hydrohalite melting), (B) and total homogenization temperatures of type V fluid inclusions. Tfm = temperature of first melting; Thm = temperature of hydrohalite melting; Tm = final melting temperature of ice.

4.5 Laser Raman Analysis

Laser Raman Spectroscopic (LRS) analyses were performed on twelve type I and II fluid inclusions to identify the composition and relative concentration of the gas phases. The analysis was carried out at Geoscience Australia in Canberra, Australia, using a DILOR MICRODIL-28® Laser Raman spectrometer. Information about principles and the application of LRS to fluid inclusion studies can be found in a number of publications (Burruss, 1981; Roedder, 1984; Pasteris et al., 1988; Dubessy et al., 1989; Burke, 2001). LRS analyses were conducted at 40 mW on a 514.5 nm laser excitation from a Spectra Physics 2020 5 W argon laser. Analyzed gas phases include CO_2, CO, CH_4, N_2, H_2S, H_2, and NH_3. Results are reported in Appendix 4.10. The analysis revealed that the gas phase in all the inclusion types contained only CO_2 and other gas species were not detected.

4.6 Estimation of Pressure and Trapping Conditions

4.6.1 Estimation of Density and Pressure of Type Ia and Ib – CO_2 rich inclusions

Densities of type I fluid inclusions were calculated using the equation of Brown and Lamb (1989) using FlinCor 1.4 software (Brown, 1989). Primary type Ia fluid inclusions homogenize between -17.1 and -0.5°C (Section 4.4.1, Figure 4.1B, Table 4.4 and Appendix 4.1) which correspond to CO_2 densities between 0.931 and 1.021 g/cm^3. Pseudosecondary Ib fluid inclusions homogenize between -1.1 and 30.5°C (Section 4.4.1, Figure 4.1B, Table 4.4 and Appendix 4.2) at temperatures generally higher than

type Ia fluid inclusions, which results in densities lower than type I a inclusions between 0.569 and 0.935 g/cm^3.

Pressure for type Ia and type Ib fluid inclusions was estimated using the method described by Roedder and Bodnar (1980) based on the comparison of the homogenization temperature (Th) with independent geothermometers. Isochores for type Ia and Ib were calculated using the software FlinCor 1.4 (Brown, 1989) and the equation of Brown and Lamb (1989). Several independent geothermometers were used to estimate the pressure of entrapment of type I fluid inclusions. Three potential geothermometers were considered to estimate the maximum trapping pressure of type I fluid inclusions:

i. The temperature defined by mineralogy and texture of the granite clasts that hosts primary and pseudosecondary CO_2 fluid inclusions. The mineral assemblage of the granite clasts consists of quartz and albite and the textures observed indicate that the crystallizing melt was volatile-saturated (Chapter 3). The solidus temperature for the system Ab–Qtz–H_2O in water-saturated conditions at 3kbar (the estimated pressure for the contact aureole around the northwestern contact of the Saxby granite; Rubenach et al., 2007) is ~ 740°C (Wen and Nekvasil, 1994). However, evidence from primary fluid inclusions indicates that the volatile phase comprises other components in addition to water. The effect of CO_2 and other possible volatile phases is discussed further in below.

ii. The estimated temperature for the aureole around the northwestern contact of the Saxby granite (Rubenach et al., 2007), which outcrops

approximately 2 km from the SRBP (Figure 3.1), that was inferred around 670°C at 3kbar from the observed mineral assemblage that consists of K-feldspar - sillimanite - andalusite.

iii. The estimated temperature of equilibrium of albite and quartz in the aplitic and pegmatitic components of albite-actinolite-apatite–rich rocks determined by oxygen isotope studies (Mark and Foster, 2000). These rocks form the carapace at the top of a small dome-like intrusion of the Roxmere pluton, located at the northern end of the Mount Angelay igneous complex in the Cloncurry district, and are mineralogically and texturally very similar to the pegmatite clasts described in this study and hosting the CO_2-rich fluid inclusions. The albite and quartz equilibrium in the rocks described by Mark and Foster (2000) defines temperatures between 510 and 540°C.

The calculated isochores for type Ia and Ib inclusions are plotted in Figures 4.10, 4.11 and 4.12, where they are compared to the different geothermometers applied. Isochores of early type Ia inclusions define a narrower and higher range of pressures compared to isochores of later pseudosecondary type Ib fluid inclusions. The maximum pressure for type Ia fluid inclusions is ~ 6.2 kbar at 740°C (Figure 4.10), ~ 5.7 kbar at 670°C (Figure 4.11) and ~ 4.7 kbar at 540°C (Figure 4.12). The maximum pressure for type Ib fluid inclusions is ~ 4.5 kbar at 670°C (Figure 4.10), ~ 4.9 kbar at 740°C (Figure 4.11) and ~ 3.7 kbar at 540°C (Figure 4.12).

The estimated pressures vary considerably using the different geothermometers. The highest pressures are associated with the geothermometer derived by the solidus

temperature of the system Ab-Qtz-H_2O in water-saturated conditions at 3 kbar. However, primary and pseudosecondary CO_2-rich fluid inclusions, and likely primary mixed aqueous-carbonic and brine-carbonic fluid inclusions (section 4.3.2), indicate the presence of a carbonic phase and other solutes in addition to H_2O. The addition of one component, for example CO_2, to a water-bearing magma has the effect decreasing the solubility of H_2O in the magma and vice versa (Blank and Brooker, 1994; Lowenstern, 2000; Lowenstern, 2001). The addition of CO_2 to a granitic water-bearing magma results in a reduction of H_2O activity in the melt and, as a consequence, in an increase of the liquidus and solidus temperature of the magma (Swanson, 1979; Keppler, 1989; Ebadi and Johannes, 1991; Holtz et al., 1992; Scaillet et al., 1995; Nabelek and Ternes, 1997). Therefore, the solidus temperature for a system containing Ab-Qtz-H_2O-CO_2 was likely higher than 740 °C calculated for the Ab-Qtz-H_2O system. On the other hand, the crystallizing magma also potentially contained elements such as Li, B, F, P, as suggested by the presence of accessory apatite in some samples and by results of crush leach analysis (Chapter 5), that can significantly lower the liquidus and solidus temperature of the melt (London, 1992; London, 2005). Thus, there are several volatile components that may have affected the solidus temperature of the melt and the estimated 740°C temperature value.

The second geothermometer is derived from an estimate of the T-P conditions at the contact aureole of the Saxby Granite in its northwestern section, approximately 2km from the SRBP (Rubenach et al., 2007). Whilst the pressure is not expected to have significantly changed over the 2 km distance, the temperature most likely decreased away from the contact aureole, implying temperatures almost certainly lower than 670°C in the proximity of the breccia pipe and therefore pressures lower than 5.7 kbar.

The estimated equilibrium temperature (540°C) determined for the albite-quartz assemblage in albite-actinolite-apatite–rich rocks by oxygen isotope calculations (Mark and Foster, 2000) is considered the best estimate of the maximum temperature for the formation of type I fluid inclusions because of the similarities (mineralogical, textural and occurrence) of these rocks with the rocks described in this study.

The estimate for the minimum temperature (360°C) of entrapment of type I inclusions is obtained from homogenization of type III inclusions. The latter are in fact secondary and therefore postdate the formation of primary and pseudosecondary inclusions. The maximum observed temperature of homogenization for type III inclusions is 360°C. The minimum pressure for type Ia and type Ib fluid inclusions at 360°C is ~ 2.6 kbar (Figure 4.10, 4.11 and 4.12) and ~ 0.9 kbar (Figure 4.10, 4.11 and 4.12) respectively.

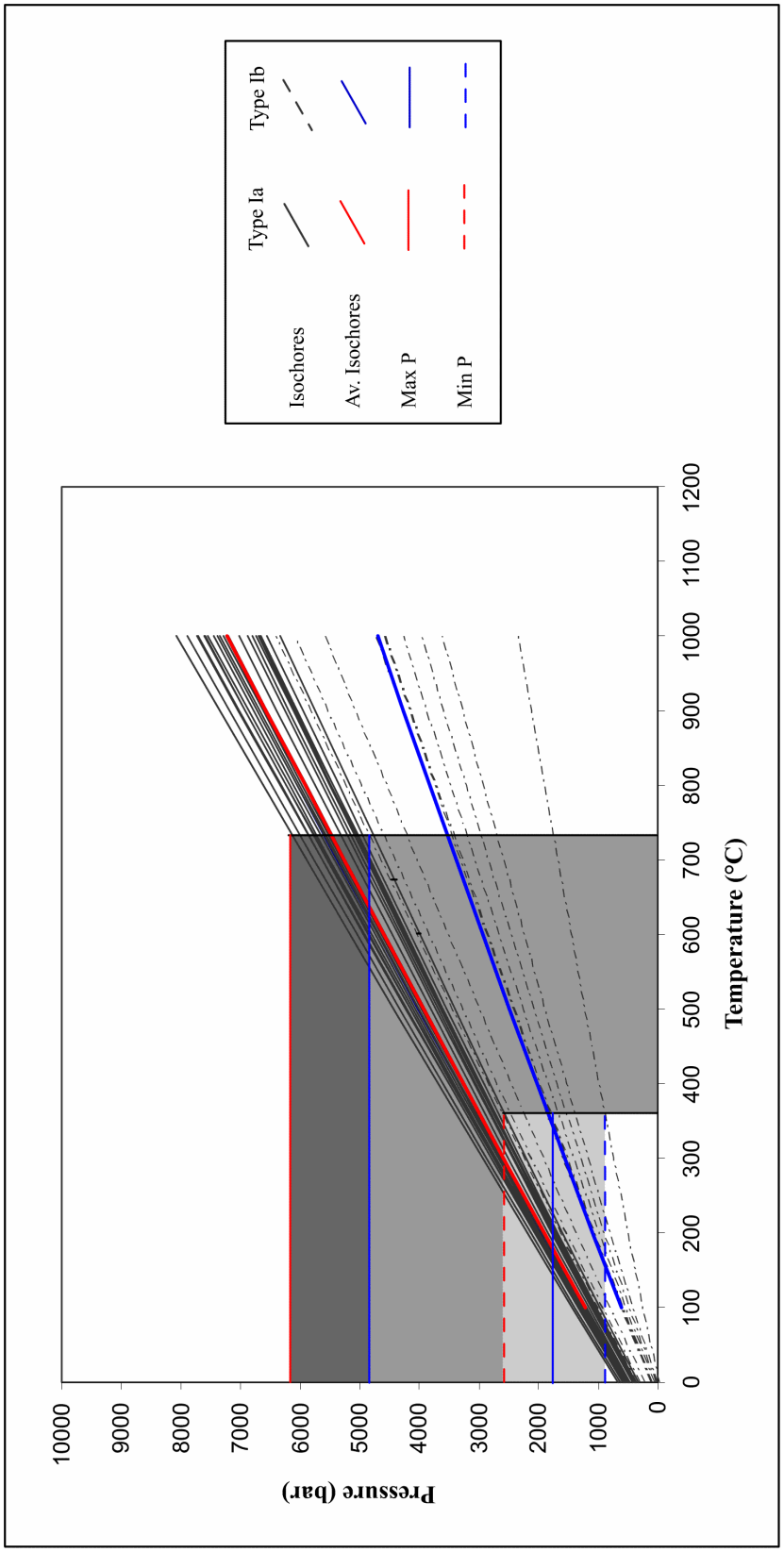

Figure 4.10 Pressure-temperatures diagram for type Ia and Ib fluid inclusions. Isochores were calculated based on the homogenization temperatures of the inclusions using the program Flincor (Brown, 1989). Solid and dashed lines represent isochores of type Ia and Ib respectively. Independent geothermometers used are the temperature of the calculated equilibrium of the quartz-albite-H_2O system in water saturated conditions (~ 740°C) and the maximum temperature determined for secondary type III fluid inclusions (~ 360°C). Estimated pressures for type Ia range from a maximum of around 6.2 kbar at 740°C to a minimum of approximately 2.6 kbar at 360°C. Pressures for type Ib fluid inclusions range from a maximum of ~4.9 kbar at 740°C to a minimum of ~0.9 kbar at 360°C.

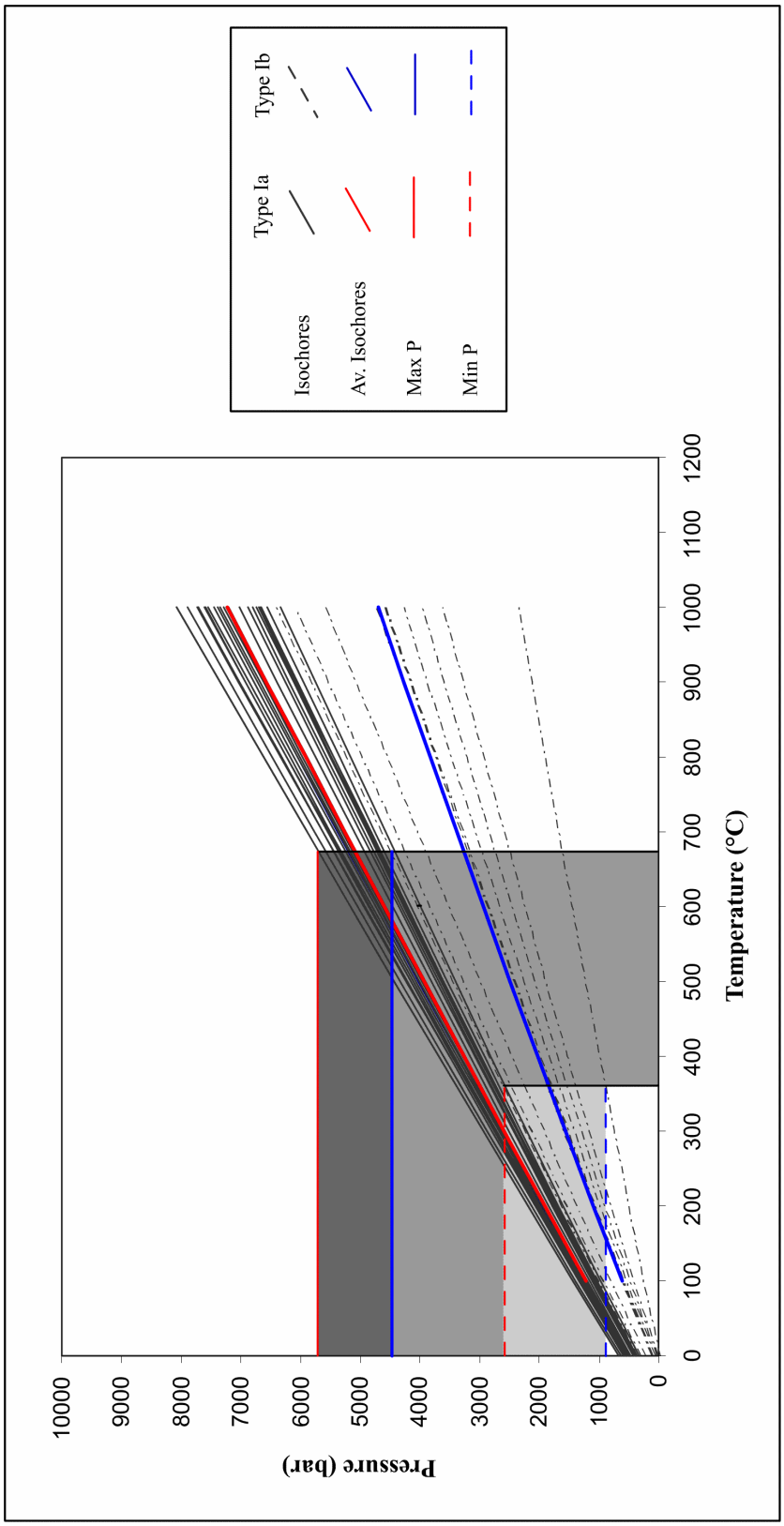

Figure 4.11 Pressure-temperatures diagram for type Ia and Ib fluid inclusions. Isochores were calculated based on the homogenization temperatures of the inclusions using the program Flincor (Brown, 1989). Solid and dashed lines represent isochores of type Ia and Ib respectively. Independent geothermometers used are the temperature of the contact aureole of the Saxby granite (~ 670°C) and the maximum temperature determined for secondary type III fluid inclusions (~ 360°C). Estimated pressures for type Ia range from a maximum of ~5.7 kbar at 670°C to a minimum of ~2.6 kbar at 360°C. Estimated pressures for type Ib fluid inclusions range from a maximum of ~4.5 kbar at 670°C to a minimum of ~0.9 kbar at 360°C.

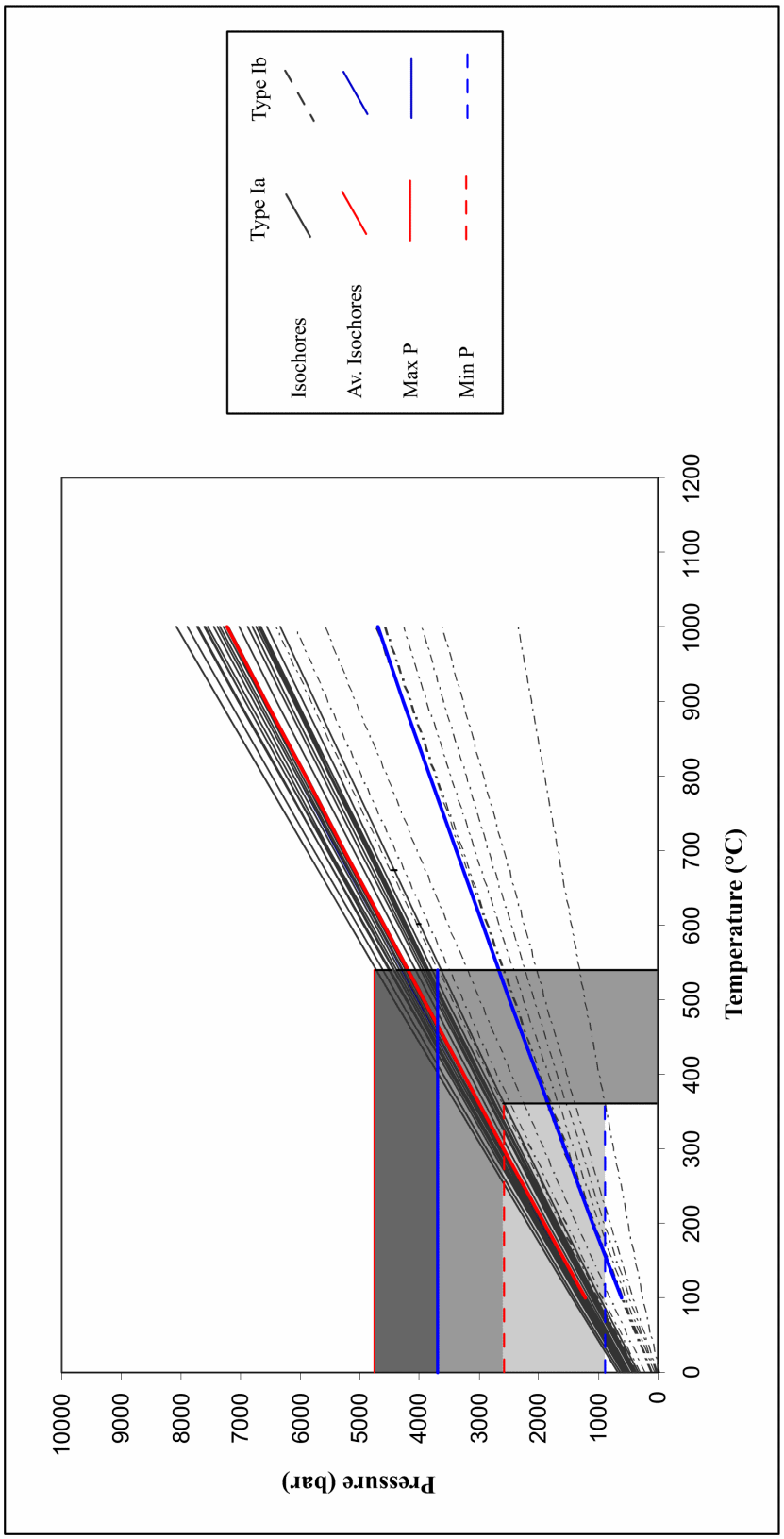

Figure 4.12 Pressure-temperatures diagram for type Ia and Ib fluid inclusions. Isochores were calculated based on the homogenization temperatures of the inclusions using the program Flincor (Brown, 1989). Solid and dashed lines represent isochores of type Ia and Ib respectively. Independent geothermometers used are the temperature of the calculated equilibrium of the quartz-albite assemblage (~ 540°C) in the aplitic and pegmatitic components of albite-actinolite-apatite –rich rocks determined by oxygen isotope studies (Mark and Foster, 2001) and the maximum temperature determined for secondary type III fluid inclusions (~ 360°C). Estimated pressures for type Ia range from a maximum of around 4.7 kbar at 540°C to a minimum of approximately 2.6 kbar at 360°C. Pressures for type Ib fluid inclusions range from a maximum of ~3.7 kbar at 540°C to a minimum of ~0.9 kbar at 360°C.

The estimated average pressure for type Ia inclusions trapped in primary growth zones in the quartz-albite layers in the granite clast at 540°C is 4.2 kbar. However, this exceeds the independent pressure estimate obtained for the contact aureole of the Saxby granite (3 kbar; Rubenach et al., 2007) by approximately 1.2 kb. This difference may represent overpressuring produced by release of volatiles during the crystallization of magma and that ultimately may have been responsible for the brecciation event (Chapter 7). The pressures calculated from pseudosecondary type Ib inclusions indicate lower values compared to primary inclusions and a wider range of pressures. The average pressure at 540°C for type Ib fluid inclusions is 2.7 kbar, similar to the independent pressure estimate obtained for the contact aureole of the Saxby granite, and 1.5 kbar lower than the value recorded by type Ia fluid inclusions at the same temperature. This indicates that large pressure fluctuations are most likely responsible for the formation of the transitional magmatic-hydrothermal textures observed in the granite clasts and they result from the cyclic accumulation and release of volatiles at the top of the granite.

4.6.2 Type III – Liquid rich inclusions

Pressure for type III fluid inclusions was estimated using the method described by Roedder and Bodnar (1980) for fluid inclusions containing daughter phases. Type IIIa fluid inclusions display homogenization behaviour characterized by vapour-bubble disappearance (Th_{L-V}) at temperatures below the dissolution of halite ($Ts > Th_{L-V}$). The temperature of halite dissolution (Ts) provides a minimum value for the trapping

temperature of the inclusions, whereas the pressure at Ts along the liquid-vapor-solid curve represents a minimum trapping pressure (Figure 4.13; Roedder and Bodnar, 1980). The method requires the knowledge of the slope and position of the isochore, the P-T position of the liquidus curve and its intersection with the appropriate isochore (Figure 4.13; Bodnar, 1994). Isochores were calculated based on Th_{L-V} using the software FlinCor 1.4 (Brown, 1989). An attempt to calculate the liquidus curve and its position was carried out using the method provided by Bodnar (1994). However, the isochore and the liquidus curve for single inclusions intersected at a temperature different from the measured Ts. Although the difference was in the order of few degrees, the effect on the estimated pressure was dramatic, approximately two orders of magnitude higher, due to the steep slope of the liquidus curve. The method proposed by Bodnar (1994) for the calculation of the liquidus curve was intended for a simple NaCl system while type III inclusions displayed more complex composition (see section 4.4.4) and this is likely the reason for the intersection of the isochores and liquidus curves at temperatures different from Ts. The minimum trapping pressure for type IIIa inclusions was therefore estimated as the pressure at Ts along the calculated isochores (Figure 4.14). The estimated minimum trapping pressures range between 600 and approximately 2700 bar, with average values around 1600 bar. Type III fluid inclusions are associated with the albite alteration event that affects rocks within and adjacent to the SRBP and therefore the estimated pressures represent also minimum pressures for the albitization event.

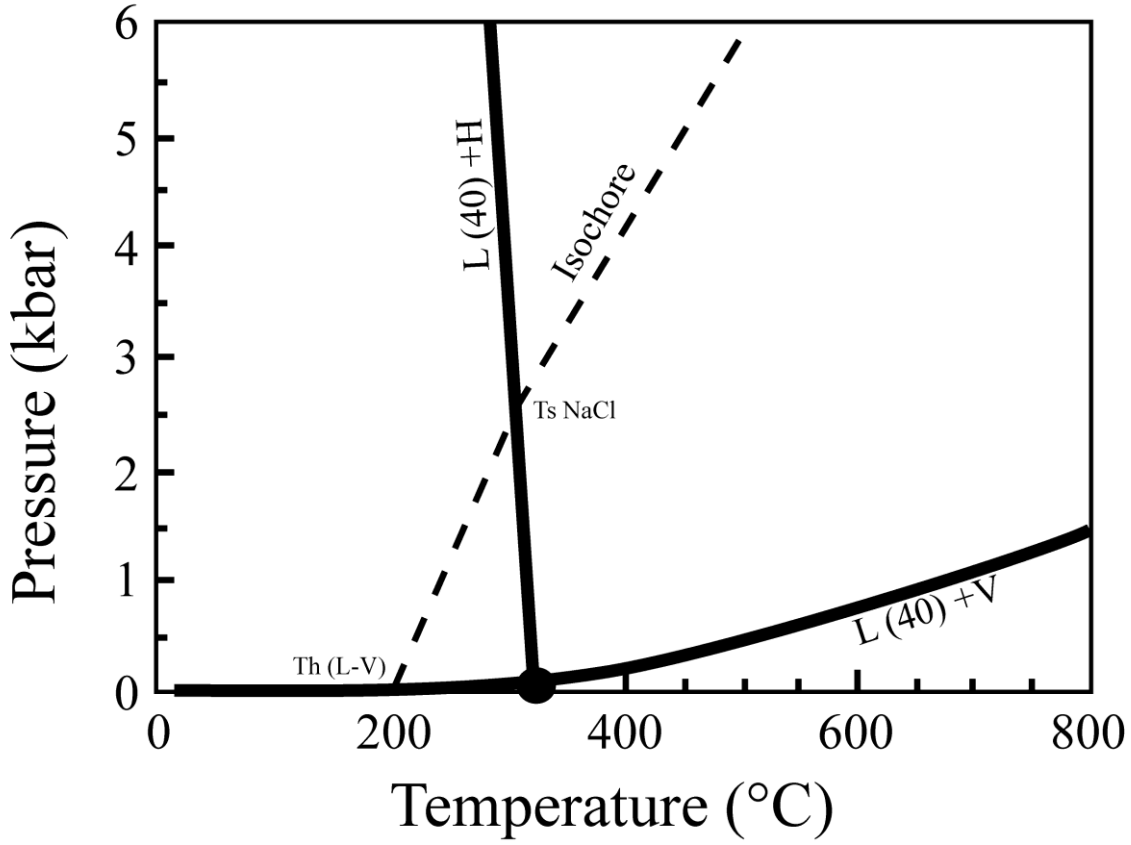

Figure 4. 13 Diagram illustrating the relationship between the P-T formation conditions and the mode of homogenization of H_20-NaCI fluid inclusions with a salinity of 40 wt%. The inclusion follows the solid-liquid-vapor curve until vapor phase homogenization. The inclusion then follows a path through the liquid + halite field (dashed line) until halite dissolution at higher temperature when the path intersects the liquidus. Pressure and temperature at Ts represent minimum trapping temperature and pressure. Modified after Bodnar (1994).

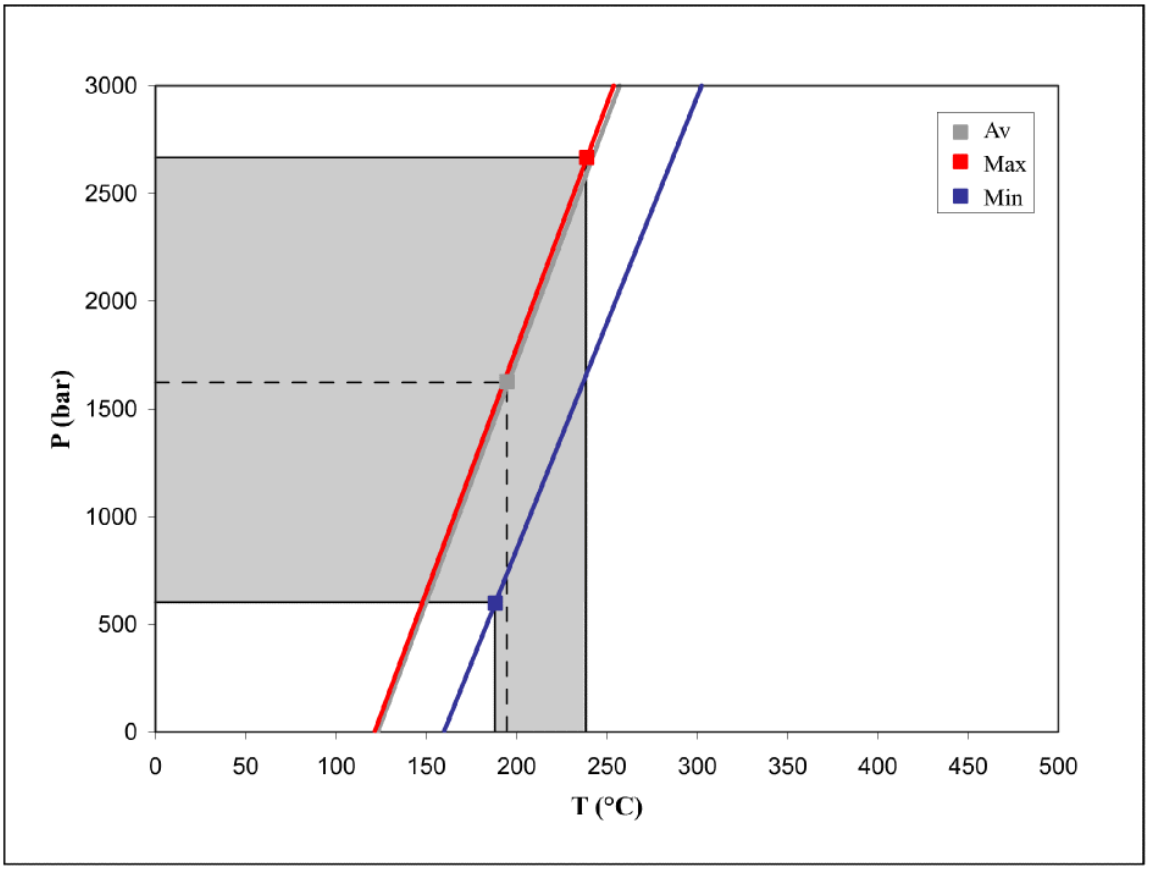

Figure 4.14 Pressure-temperatures diagram for type IIIa fluid inclusions. Isochores were calculated based on the vapor homogenization temperatures using the software Flincor (Brown, 1989). The minimum trapping pressure for the single inclusions was estimated as the pressure value at Ts along the calculated isochores. Symbols in the graph represent the minimum (blue), average (grey) and maximum (red) pressure plotted on the corresponding isochore obtained from the inclusions. The shown isochores do not represent the minimum, maximum and average isochores, but the isochores along which lie the minimum, maximum and average pressures calculated for type III fluid inclusions. Calculated pressures vary from around 600 to approximately 2600 bar.

4.7 Summary

Five types of fluid inclusions have been identified based on their origin and composition, summarized in Table 4.2, 4.3 and 4.4. Type I and type II all contain CO_2. Temperatures of melting of the CO_2 phase suggest a composition close to pure CO_2, confirmed by laser Raman analysis. Type Ia and Ib are respectively primary and pseudosecondary monophase CO_2 inclusions and were observed only in granite clast samples. Type Ia fluid inclusions in general homogenized at lower temperatures than type Ib, implying higher densities for the primary inclusions. Type IIa and IIb are mixed carbonic-brine inclusions, the latter containing a halite crystal at room temperature. The origin of these inclusions is uncertain, although due to their association with type Ia, a primary origin is inferred. The dominant type of inclusions are secondary sodic (-calcic) three phase (type IIIa) and two phase liquid-rich (type IIIb) fluid inclusions that display high to moderate temperature and high salinity. These inclusions were found in trails associated with albite alteration (Chapter 3 and section 4.2) and, therefore, they are interpreted to represent the fluid that caused the albitization. Type IV fluid inclusions are secondary two phase liquid-rich (type IVb) and three phase (type IVa) and are generally similar to type III, but display lower eutectic temperatures, suggesting a difference in composition. They are high to moderate temperature (from 203.6 to 253.7°C) and high salinity (average 33.4 NaCl equiv.) fluid inclusions. Type V fluid inclusions are secondary liquid-rich moderate temperature (144 to 245°C) and salinity (8.8 and 12.84 wt% NaCl equiv.) fluid inclusions.

Pressure estimated from type Ia inclusions exceed the maximum estimate for the contact aureole for the Saxby granite and the excess likely represents the overpressuring generated at the top the granite by exsolution of volatile phases during the

crystallization, as also supported by magmatic-hydrothermal transitional textures observed in granite clasts (Chapter 3). The overpressuring may ultimately be responsible for the brecciation event. Later pseudosecondary type Ib fluid inclusions indicate in general lower and wider interval of pressures than type Ia. This can be interpreted as a general drop of pressure that is likely responsible for the formation of the magmatic-hydrothermal textures observed in the granite clasts, which result from the cyclic accumulation and release of volatiles at the top of the granite. These hypotheses are further discussed in chapter 7. Pressures obtained from secondary sodic (-calcic) type IIIa fluid inclusions associated with albite alteration range from 0.6 to approximately 2.6 kbar. These represent minimum pressure estimate for the albitization event.

Chapter 5

Chapter 5 – Fluid Chemistry and Conditions of the Suicide Ridge Breccia Pipe (II): Microanalytical, Bulk and Microprobe Analysis

5.1 Introduction

In Chapter 4 results are presented from conventional fluid inclusions studies including paragenesis and classification of fluid inclusions and microthermometric analysis. This chapter focuses on the investigation of the chemistry of the fluids associated the Suicide Ridge Breccia Pipe (SRBP) with the aid of several analytical techniques that include laser Raman, LA ICP MS, bulk crush-leach and microprobe analysis.

5.2 LA ICP MS analysis of fluid inclusions

5.2.1 Methodology

LA ICP MS analysis was undertaken to determine the chemistry of type III and IV fluid inclusions and was carried out at the School of Earth and Environment at the University of Leeds. The methodology is described thoroughly in Gunther et al. (1998) and Heinrich et al. (2003); details on the instrumentation and analytical procedures for the analyses presented in this study can be found in Allan et al. (2005). The

instrumentation employed includes a GeoLas Q Plus excimer laser (ArF, 193nm, Microlas, Göttingen, Germany) to open the inclusion and volatilize its content, and an Agilent 7500c ICPMS to analyze the ablated material (Allan et al., 2005). Two separate suites of analyses were carried out, comprising Na, K, Ca, Mn, Fe and Sr and Na, K, Cu, Zn, Ba and Pb. For the analysis of the first set of data the ICP reaction cell was pressurized with H_2 to eliminate the interference of $^{40}Ar^+$ and $^{40}Ar^{16}O^+$ (Ar is the carrier gas) on $^{40}Ca^+$ and $^{56}Fe^+$ respectively (Allan et al., 2005). However, this setting has the disadvantage of reducing the sensitivity for element masses with no interferences and therefore minor elements were analyzed in a separate suite without gas in the reaction cell (Allan et al., 2005). The concentrations of Na and K were determined in both sets of analysis, because Na was used as the internal standard (see below) and K was used as a control on the quality of the analysis. Concentrations of K determined in the two series of analysis are similar ranging from ~ 1000 ppm to around 60000 ppm for both suites and displaying average values for all the inclusions of approximately of 20000 and 19000 ppm for the first and second suites of analysis respectively. In the data presented K values obtained in the first series of analysis were used for their immediate correlation with other major elements (i.e. Ca, Fe). Ablation spots and spectra for the first and the second suite of elements are shown in Figures 5.1 and 5.2. Detection limits vary as a complex function of the mass of the element, the size and shape of the inclusion and the number of elements measured from a single inclusion, and must be determined for each element in each inclusion (Heinrich et al., 2003). The limits of detection normally decrease with decreasing size of the inclusion (Heinrich et al., 2003) and in this study the small inclusions (≤ 20μm) often resulted in concentrations below limits of detection for many elements, in particular Mn but also Cu, Zn and Pb. In such instances the detection limit can be used as a maximum estimate of concentration.

Limits of detection for the analyzed elements were calculated on the basis of 3 times the standard deviation of the signal containing zero analyte. Some elements display a relatively large standard deviation. This does not appear to be related to analytical problems or to fluid inclusion leakage or necking down, but rather appear to reflect variable compositions of the inclusions even within single samples. Signals with spikes, isolated signal usually higher than the actual signal, were removed as they lead to an overestimate of element concentrations; these were mainly related to Mg and less frequently to Fe, Cu, Zn and Ba. Results for Mg were dismissed and are not presented here since all the signals were considered to be spikes.

The element ratios obtained from LA ICP MS analysis were converted to absolute element concentrations using value of Na as an internal standard (Section 5.2.2). The Na value employed for the conversion was calculated using a charge-balance method based on the charge–balance of all the major cations measured to the chlorine concentration estimated from microthermometry using the following equations:

(1) $$mCl = mNa + \sum_i ni \cdot mXi$$

(2) $$mNa = mCl \cdot \left(1 + \sum_i \frac{ni \cdot mXi}{mNa}\right)^{-1}$$

where *m* is the molality, n*i* is the charge of each cations and mX_i/ mNa are molar ratios that are obtained from laser ablation analysis (Allan et al., 2005).

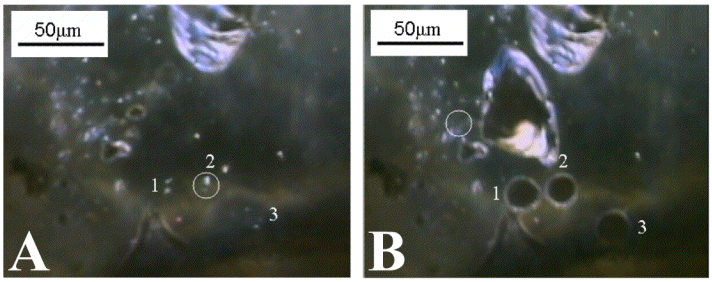

Figure 5.1 Picture of type III fluid inclusions before (A) and after (B) ablation. Sample MT11

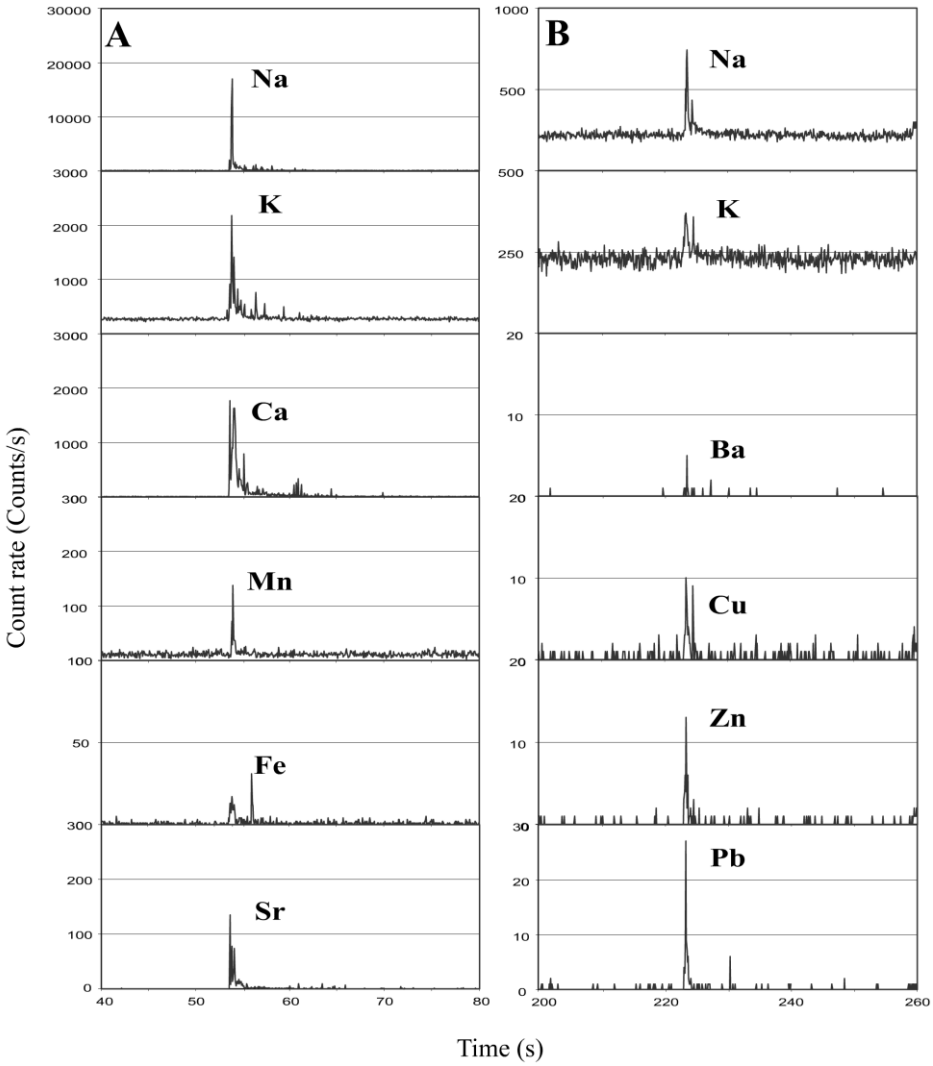

Figure 5.2 LA ICP MS signals obtained from ablation of type III fluid inclusions for the first (A) and the second (B) suite of analyzed elements. Fluid inclusions in samples MT12 and MT19.

5.2.2 Sample and fluid inclusion selection

LA ICP MS analysis was undertaken to determine the composition of fluid inclusions associated with the SRBP. Fluid inclusions analyzed are mostly type III due to their abundance in all samples studied and occurrence as homogeneous populations of inclusions. In particular, these inclusions were linked to the albitic alteration that affects rocks in and around the breccia pipe (Chapters 3 and 4). Type II fluid inclusions were not analyzed due to their small size (mostly ≤ 10μm) and occurrence in association with other types of inclusions, dominantly type I but also type III and IV fluid inclusions, resulting in difficulties in obtaining accurate and confident analysis of type II only inclusions. An attempt was also made to analyze type IV fluid inclusions. However, their analysis was difficult because of their small size (mostly below 20μm), their scarcity and their occurrence in association with other inclusions, dominantly type III. Type IV fluid inclusions were observed and analyzed only in two areas, one in granite clast sample MT11, and the other in the ironstone sample MT12, which are labelled as MT11_Z2 and MT12_Z1 respectively.

The Na value for the conversion from element ratios obtained from LA ICP MS analysis was calculated using the charge-balance method described in Section 5.2.1. The chlorinity was derived from the average salinity of type III fluid inclusions estimated from microthermometry (Chapter 4). LA ICP MS analysis revealed that Na, K and Ca are the most abundant cations in the fluid; therefore the following charge balance approximation was used (Allan, 2006):

$$m\mathrm{Cl} \approx m\mathrm{Na} + m\mathrm{K} + 2m\mathrm{Ca}$$

The calculated Na value was ~ 85000 ppm. This value was used for the conversion from element ratios obtained from LA ICP MS analysis to absolute element concentrations for both type III and IV fluid inclusions. The reason for using the same Na value for the conversion is due primarily to the uncertainties associated with the analyses of type IV fluid inclusions, particularly their occurrence in mixed population where type III are the dominant inclusions types. Using the same Na value to convert element ratios for both inclusion types does not significantly influence the calculated absolute concentrations. In fact, the Na value calculated for type IV fluid inclusions (~ 88000 ppm) do not differ significantly from the previous calculated value.

5.2.3 Results

Results of laser ablation analysis on 67 fluid inclusions for the first suite of elements and on 57 for the second suite of elements are reported in Table 5.1 and Appendix 5.1. Average, minimum and maximum concentrations for each sample of the analyzed elements are also reported in Table 5.1 and plotted in Figure 5.3. In Table 5.2 and Figure 5.4 are summarized average, minimum and maximum concentrations for type III and IV fluid inclusions. Figure 5.5 compares average values between each sample and between the different types of samples (granite clasts vs ironstones); the latter are also reported in Table 5.3. Figure 5.6 compares fluid inclusion element ratios. Element ratios are widely used to characterize fluid inclusions and represent an easy way to compare the fluid inclusion chemistry. The ratios selected here include most of the commonly ratios used to characterize fluid inclusions (e.g. K/Ca, Mn/Fe) together with element ratios of specific interest for IOCG systems (e.g. Ba/Cu, Zn/Pb: Williams

et al., 2001). Table 5.1 reports two different averages; one calculated using all the data including values below detection limit (in these cases the detection limit for the given element in the given inclusion was used for the calculation as a maximum estimate of concentration; Section 5.2.1), and the other calculated using only data above detection limits. In the following discussion the average is calculated on the basis of all values including those below detection limit unless otherwise stated.

In addition to Na, type III fluid inclusions are dominated by Ca and K with concentrations from about 9000 ppm to 49000 ppm and from around 7000 ppm to 41000 ppm for Ca and K respectively (Figure 5.4; Tables 5.1 and 5.2). Average concentrations generally range from around 16000 to approximately 25000 ppm for both elements in most samples (Figures 5.3 and 5.5; Tables 5.1 and 5.2). The average K/Ca ratio is close to one for most of the samples, with the exception of sample MT11 that shows a slight enrichment in Ca compared to K (Figures 5.3, 5.5 and 5.6A; Table 5.1).

Iron concentrations for type III fluid inclusions range from around 100 ppm to 8000 ppm (average ~ 2000 ppm) (Figure 5.4; Tables 5.1 and 5.2). However, fluid inclusions analyzed in different samples display different Fe contents and can be broadly subdivided into two groups. The first group includes inclusions from granite clast samples MT11, MT20 and ironstone sample MT19. These have Fe values for single inclusions spanning from a few hundreds to thousands of ppm and average Fe concentrations between approximately 1000 and 2000 ppm (Figures 5.3A, C, E and 5.5; Table 5.1). The second group includes fluid inclusions from granite sample MT13A and ironstone MT12 that display Fe values for single inclusions consistently in the order of thousands of ppm and average concentrations around 4500 ppm (Figures 5.3B, D and 5.5; Table 5.1).

Table 5.1 Fluid composition obtained from LA ICP MS analysis. Composition in ppm.

Sample/Analysis	Na	K	Ca	Mn	Fe	Sr	Analysis	Cu	Zn	Ba	Pb	K/Ca	Mn/Fe	Ca/Sr	Cu/Zn	Zn/Pb	Ba/Cu
Type III fluid inclusions																	
Sample MT11 (Granite clast)																	
25: MT11-3A.	85000	35408	29335	*3688*	1013	694	27: MT11_SF.	287	1263	spike	60	1.21	*3.64*	42.25	0.23	20.98	
27: MT11-3B.	85000	11654	16582	*1053*	401	281	53: MT11_SL.	95	430	2165	159	0.70	*2.63*	59.11	0.22	2.71	22.86
28: MT11-3B.	85000	18968	33505	*4759*	1641	553	55: MT11_SL.	467	1511	spike	*139*	0.57	*2.90*	60.63	0.31	*10.89*	
35: MT11-3E.	85000	10872	25611	8349	2526	818	59: MT11_4A.	162	150	*41*	*22*	0.42	3.30	31.30	1.08	*6.72*	*0.25*
42: MT11-3SA	85000	9120	22124	*1550*	spike	435	60: MT11_4A.	611	1125	*196*	*106*	0.41		50.88	0.54	*10.59*	*0.32*
43: MT11-3SA	85000	14119	22514	*533*	2786	494	61: MT11_4A.	325	2036	2453	*77*	0.63	*0.19*	45.53	0.16	*26.32*	7.54
45: MT11-3SB	85000	7473	11633	*142*	182	128	23: MT11_3I.	*112*	475	581	58	0.64	*0.78*	90.94	*0.23*	8.16	*5.21*
46: MT11-3SB	85000	7107	8982	*721*	*220*	231	39: MT11_SI.	*88*	238	1273	19	0.79	*3.28*	38.85	*0.37*	12.27	*14.50*
48: MT11-3SC	85000	15379	33571	*1861*	622	636	46: MT11_SJ.	*246*	530	2203	49	0.46	*2.99*	52.76	*0.46*	10.78	*8.96*
52: MT11-3SC	85000	30691	41323	*872*	3733	825	64: MT11_4B.	*180*	102	929	*53*	0.74	*0.23*	50.11	*1.77*	*1.90*	*5.17*
							66: MT11_4C.	*536*	903	2968	*175*				*0.59*	*5.17*	*5.54*
							67: MT11_4C.	*543*	1245	1068	*177*				*0.44*	*7.04*	*1.97*
							68: MT11_4C.	*230*	592	783	*75*				*0.39*	*7.90*	*3.41*
							71: MT11_4E.	133	*157*	291	*13*				*0.85*	*12.17*	*2.18*
							26: MT11_SE.	*261*	*505*	1104	213				*0.52*	*2.37*	4.24
							47: MT11_SK.	*194*	*524*	980	51				*0.37*	*10.21*	*5.04*
Min		7107	8982	142	182	128		88	102	41	13	0.41	0.19	31.30	0.16	1.90	0.25
Max		35408	41323	8349	3733	825		611	2036	2968	213	1.21	3.64	90.94	1.77	26.32	22.86
Average		16079	24518	2353	1458	509		279	737	1217	90	0.66	2.22	52.24	0.53	9.76	6.23
Average *		16079	24518	8349	1613	509		297	815	1400	87	0.66	3.30	52.24	0.42	10.98	11.55
Stdev		9715	10272	2564	1289	242		171	557	899	63	0.23	1.40	16.28	0.41	6.46	6.05
Type III fluid inclusions																	
Sample MT13A (Granite clast)																	
61: MT13A-6F	85000	23338	20062	*36085*	spike	81	100: MT13A_6	*301*	1040	488	*71*	1.16		247.33	*0.29*	*14.56*	*1.62*
64: MT13A-6g	85000	23354	34298	*9029*	spike	331	102: MT13A_6	697	590	686	*79*	0.68		103.66	1.18	*7.50*	0.98
65: MT13A-6g	85000	11573	16944	*7171*	spike	195	103: MT13A_6	*414*	887	625	118	0.68		86.72	*0.47*	7.54	*1.51*
69: MT13A-6i	85000	23140	19255	*7382*	3307	226	105: MT13A_6	993	700	1341	450	1.20	*2.23*	85.16	1.42	1.55	1.35
72: MT13A-6i	85000	34827	11505	*18073*	7875	131	107: MT13A_6	1048	823	3467	178	3.03	*2.29*	87.71	1.27	4.63	3.31
75: MT13A-6l	85000	11955	19533	*12901*	*4020*	123	109: MT13A_6	105	127	334	85	0.61	*3.21*	158.87	0.83	1.48	3.19
76: MT13A-6l	85000	18642	9724	*4123*	spike	119	110: MT13A_6	*193*	357	spike	*52*	1.92		81.58	*0.54*	*6.79*	
79: MT13A-6m	85000	9147	22639	*10028*	spike	244	112: MT13A_6	*200*	324	spike	*54*	0.40		92.70	*0.62*	*5.95*	
82: MT13A-6n	85000	13333	17999	*12744*	*3550*	162						0.74	*3.59*	110.80			
Min		9147	9724	4123	3307	81		105	127	334	52	0.40	2.23	81.58	0.29	1.48	0.98
Max		34827	34298	36085	7875	331		1048	1040	3467	450	3.03	3.59	247.33	1.42	14.56	3.31
Average		18812	19107	13060	4688	179		494	606	1157	136	1.16	2.83	117.17	0.83	6.25	1.99
Average *		18812	19107		3785	179		711	606	1157	208	1.16		117.17	1.17	3.80	2.21
Stdev		8210	7036	9537	2145	78		372	315	1183	133	0.83	0.67	54.30	0.42	*4.14*	1.00

Average *: average calculated based only on values above detection limit

Numbers printed in italics refer to values below detection, substituted by the actual detection limit for the specific element in the specific inclusion

Table 5.1 Continued

Sample/Analysis	Na	K	Ca	Mn	Fe	Sr	Analysis	Cu	Zn	Ba	Pb	K/Ca	Mn/Fe	Ca/Sr	Cu/Zn	Zn/Pb	Ba/Cu
Type III fluid inclusions																	
Sample MT20 (Granite clast)																	
7: MT20-4d.	85000	7596	10962	*8526*	3807	90	3: MT20-6o.	*225*	spike	426	95	0.69	*2.24*	121.79			*1.89*
15: MT20-4c.	85000	9330	13450	*11287*	*3228*	102	4: MT20-6o.	*179*	spike	171	32	0.69	*3.50*	132.15			*0.95*
36: MT20-6c.	85000	7399	13798	*3656*	1490	152	5: MT20-6o.	*33*	151	447	27	0.54	*2.45*	90.99	*0.22*	5.57	*13.42*
37: MT20-6c.	85000	16194	11748	*3899*	*1246*	192	41: MT20-5g.	*144*	462	1997	58	1.38	*3.13*	61.05	*0.31*	7.90	*13.83*
43: MT20-6e.	85000	25660	26260	*12622*	*4641*	195	42: MT20-5g.	*69*	214	spike	28	0.98	*2.72*	134.41	*0.33*	7.57	
70: MT20-5i.	85000	18098	15061	*590*	697	530	8: MT20-6p.	457	spike	517	*72*	1.20	*0.85*	28.40			1.13
72: MT20-5i.	85000	20718	13206	*389*	*204*	115	10: MT20-6r.	374	spike	85	*120*	1.57	*1.90*	114.77			0.23
74: MT20-5i.	85000	15846	10801	*205*	*108*	95	12: MT20-6r.	123	275	275	*48*	1.47	*1.90*	113.63	0.45	*5.70*	2.23
75: MT20-5l.	85000	*21292*	17895	*651*	660	300	43: MT20-5g.	440	spike	376	123	*1.19*	*0.99*	59.68			0.86
76: MT20-5l.	85000	20989	21551	*486*	440	190						0.97	*1.11*	113.13			
77: MT20-5l.	85000	13952	10897	*228*	237	120						1.28	*0.96*	90.97			
78: MT20-5l.	85000	23461	21081	*320*	813	286						1.11	*0.39*	73.59			
79: MT20-5m.	85000	*15128*	17410	413	858	478						*0.87*	0.48	36.41			
82: MT20-5m.	85000	10776	14881	*180*	476	180						0.72	*0.38*	82.69			
84: MT20-5m.	85000	13775	15825	*267*	753	298						0.87	*0.35*	53.04			
94: MT20-5p.	85000	27565	25531	*696*	509	242						1.08	*1.37*	105.40			
95: MT20-5p.	85000	22045	12921	*407*	823	188						1.71	*0.49*	68.73			
Min		7399	10801	180	108	90		33	151	85	27	0.54	0.35	28.40	0.22	5.57	0.23
Max		27565	26260	12622	4641	530		457	462	1997	123	1.71	3.50	134.41	0.45	7.90	13.83
Average		17048	16075	2637	1235	221		227	275	537	67	1.08	1.48	87.11	0.33	6.69	4.32
Av (values above d.l)		16894	16075	413	964	221		349	275	537	62	1.08	0.48	87.11	0.45	7.01	7.52
Stdev		6157	4909	4124	1338	127		159	134	608	38	0.33	1.03	32.72	0.09	1.23	5.78
Type III fluid inclusions																	
Sample MT12 (Ironstone)																	
10: MT12-4G.	85000	10311	14235	*528*	2625	268	1: MT12_3G.	130	*297*	360	*29*	0.72	*0.20*	53.18	*0.44*	*10.27*	2.77
11: MT12-4G.	85000	23382	17947	*1257*	spike	573	3: MT12_3I.	553	*937*	268	*80*	1.30		31.34	*0.59*	*11.71*	0.48
12: MT12-3A.	85000	13439	33790	545	spike	538	5: MT12_3J.	160	339	704	*38*	0.40		62.83	0.47	*9.01*	4.39
15: MT12-3B.	85000	19602	21771	*3431*	spike	563	6: MT12_3J.	*108*	*247*	735	34	0.90		38.64	*0.44*	7.19	*6.80*
16: MT12-3C.	85000	22961	24205	*2712*	5090	489						0.95	*0.53*	49.48			
17: MT12-3C.	85000	28243	21048	*4360*	5616	408						1.34	*0.78*	51.60			
18: MT12-3D.	85000	23807	25538	*1451*	2972	732						0.93	*0.49*	34.88			
22: MT12-3F.	85000	28628	16403	*3814*	5646	433						1.75	*0.68*	37.92			
Min		10311	14235	528	2625	268		108	247	268	29	0.40	0.20	31.34	0.44	7.19	0.48
Max		28628	33790	4360	5646	732		553	937	735	80	1.75	0.78	62.83	0.59	11.71	6.80
Average		21297	21867	2262	4390	500		238	455	517	45	1.04	0.53	44.98	0.48	9.54	3.61
Average *		21297	21867	545	4390	500		281	339	517	34	1.04		44.98	0.47	7.19	2.55
Stdev		6555	6156	1512	1474	137		211	324	238	23	0.42	0.22	10.88	0.07	1.92	2.66

Table 5.1 Continued

Sample/Analysis	Na	K	Ca	Mn	Fe	Sr	Analysis	Cu	Zn	Ba	Pb	K/Ca	Mn/Fe	Ca/Sr	Cu/Zn	Zn/Pb	Ba/Cu
Type III fluid inclusions																	
Sample MT19 (Ironstone)																	
2: MT19-1h.	85000	*15152*	11239	*866*	907	92	47: MT19-1a.	288	903	259	302	*1.35*	*0.95*	121.92	0.32	2.99	0.90
4: MT19-1h.	85000	*24597*	14358	*1405*	1199	101	48: MT19-1a.	590	*593*	133	103	*1.71*	*1.17*	142.65	*0.99*	*5.75*	0.23
5: MT19-1h.	85000	21705	23325	*547*	4498	121	61: MT19-1f.	*68*	258	80	*14*	0.93	*0.12*	192.12	*0.26*	*18.18*	*1.18*
13: MT19-1l.	85000	32376	23670	*475*	487	160	54: MT19-2a	*374*	1992	410	541	1.37	*0.98*	147.77	*0.19*	3.68	*1.10*
14: MT19-1m.	85000	17460	22616	*610*	1718	216	55: MT19-2a	*200*	1519	441	251	0.77	*0.35*	104.75	*0.13*	6.05	*2.20*
15: MT19-1m.	85000	*17083*	33909	*888*	1268	231	56: MT19-2c	*175*	716	202	43	*0.50*	*0.70*	146.74	*0.24*	16.51	*1.15*
17: MT19-1m.	85000	25449	23521	629	6611	180	66: MT19-2e	*80*	1740	1031	417	1.08	0.10	130.95	*0.05*	4.17	*12.95*
20: MT19-1n.	85000	*41373*	20368	*1985*	1579	118	57: MT19-2d	110	442	159	75	*2.03*	*1.26*	172.11	0.25	5.89	1.44
26: MT19-1o.	85000	19215	29503	*520*	3007	166	59: MT19-2d	20	551	265	79	0.65	*0.17*	177.73	0.04	7.02	13.28
27: MT19-1o.	85000	19910	49044	*575*	935	249	71: MT19-2f	105	994	62	160	0.41	*0.61*	196.85	0.11	6.22	0.59
30: MT19-2g.	85000	19846	16603	*458*	*198*	156	72: MT19-2f	111	1783	241	502	1.20	*2.31*	106.22	0.06	3.55	2.16
31: MT19-2g.	85000	24875	10321	*462*	232	90						2.41	*1.99*	114.86			
33: MT19-2h.	85000	*32767*	37665	*1814*	*684*	133						*0.87*	*2.65*	282.87			
34: MT19-2h.	85000	*24763*	12697	*1371*	*517*	114						*1.95*	*2.65*	111.06			
Min		15152	10321	458	198	90		20	258	62	14	0.41	0.10	104.75	0.04	2.99	0.23
Max		41373	49044	1985	6611	249		590	1992	1031	541	2.41	2.65	282.87	0.99	18.18	13.28
Average		24041	23488	900	1703	152		193	1045	298	226	1.23	1.14	153.47	0.24	7.27	3.38
Average *		22604	23488	629	2040	152		204	1090	298	247	1.10	0.10	153.47	0.15	6.23	3.10
Stdev		7252	11024	526	1832	52		167	609	271	190	0.61	0.92	48.56	0.27	5.16	4.85
Type IV fluid inclusions																	
Sample MT11_Z2 (Granite clast)																	
98: MT11-2i.	85000	12859	24729	*10548*	spike	282	77: MT11_2A.	*409*	1212	6739	*102*	0.52		87.54	*0.34*	*11.84*	*16.48*
99: MT11-2i.	85000	*10141*	16087	*11524*	6044	186	83: MT11_2C.	1391	*1028*	147	136	*0.63*	*1.91*	86.42	*1.35*	*7.55*	0.11
106: MT11-2n	85000	27669	spike	spike	6709	324	85: MT11_2C.	*143*	484	389	*36*				*0.30*	*13.38*	*2.72*
Min		10141	16087	10548	6044	186		143	484	147	36	0.52	1.91	86.42	0.30	7.55	0.11
Max		27669	24729	11524	6709	324		1391	1212	6739	136	0.63	1.91	87.54	1.35	13.38	16.48
Average		16890	20408	11036	6376	264		648	908	2425	92	0.58	1.91	86.98	0.66	10.92	6.43
Average *		20264	20408		6376	264		1391	848	2425	136	0.52	1.91	87.54			0.11
Stdev		9434	6111	690	470	71		657	378	3738	51	0.08		0.79	0.60	3.02	8.80
Type IV fluid inclusions																	
Sample MT12_Z1 (Ironstone)																	
56: MT12-1c.	85000	60983	30185	*1170*	943	115	89: MT12_1A.	1029	1758	783	76	2.02	*1.24*	263.11	0.59	23.21	0.76
59: MT12-1e.	85000	17947	24988	*805*	1372	156	90: MT12_1A.	137	1333	106	261	0.72	*0.59*	159.71	0.10	5.11	0.77
63: MT12-1f.	85000	12421	50043	419	954	186	91: MT12_1B.	105	1388	250	75	0.25	0.44	269.75	0.08	18.43	2.39
64: MT12-1f.	85000	*34177*	26535	*1802*	351	149	92: MT12_1B.	3115	9496	267	205	*1.29*	*5.14*	177.74	0.33	46.33	0.09
65: MT12-1f.	85000	*29497*	50090	*1555*	1638	193	93: MT12_1B.	*187*	2609	189	*33*	*0.59*	*0.95*	260.18	*0.07*	*79.34*	1.01
68: MT12-1g.	85000	*11428*	21192	*560*	510	237	94: MT12_1B.	*321*	1137	*289*	71	*0.54*	*1.10*	89.43	*0.28*	16.06	*0.90*
Min		11428	21192	419	351	115		105	1137	106	33	0.25	0.44	89.43	0.07	5.11	0.09
Max		60983	50090	1802	1638	237		3115	9496	783	261	2.02	5.14	269.75	0.59	79.34	2.39
Average		27742	33839	1052	961	173		816	2953	314	120	0.90	1.58	203.32	0.24	31.41	0.99
Average *		30451	33839	419	961	173		1096	2953	319	138	1.00	0.44	203.32	0.27	21.83	1.00
Stdev		18688	12897	553	491	42		1178	3247	239	91	0.65	1.77	73.14	0.20	27.14	0.76

Data for Mn are below limits of detection in the majority of cases and only 4 values above detection limits were obtained. These inclusions are found in granite clast sample MT20 and ironstone samples MT12, MT19 and indicate Mn concentration approximately between 400 ppm and 700 ppm and display Mn/Fe ratios between 0.10 and 0.48 (Figure 5.6B and Table 5.1); one remaining value for an inclusion in granite clast MT11 indicates a Mn content of 8349 ppm with a Mn/Fe ratio of 3.30 (Figure 5.6B and Table 5.1). The fact that most of data for Mn are below detection limit suggests that actual Mn/Fe ratios are expected to be generally lower than values reported here.

Trace elements analyzed include Sr, Ba, Zn, Pb and Cu. Strontium ranges from ~ 100 ppm to a few hundreds of ppm with an average between approximately 150 and 220 ppm for type III fluid inclusions in most samples (Figures 5.3 and 5.5; Table 5.1); type III inclusions in two samples, MT11 and MT12, have slightly wider Sr ranges, from around 100 to 800 ppm and from about 300 to 700 ppm for MT11 and MT12 respectively, and averages, around 500 ppm for both samples (Figures 5.3 and 5.5; Table 5.1). Type III fluid inclusions in most samples display variable Ba concentrations spanning over two orders of magnitude from few tens of ppm to a few thousand ppm (Figure 5.3 and Table 5.1). Type III fluid inclusions in granite clast samples have the highest Ba concentrations that range from around 50 to 3500 ppm and with average values higher than 1,000 ppm for sample MT11 (~ 1200 ppm) and MT13A (~ 1150 ppm) and only sample MT20 displaying a lower value (~ 500 ppm) (Figures 5.3A, B, C and 5.5; Table 5.1). Type III fluid inclusions in ironstones samples have in general a lower and narrower range of values (mostly below 1000 ppm) and lower average values than those in granite clast samples; average values for Ba in these samples are around 500 ppm for MT12 and about 300 ppm for MT19 (Figures 5.3D, E, and 5.5; Table 5.1).

Values obtained for Cu are below limits of detection in 50% of cases; therefore Cu concentrations are expected to be generally lower than reported here. The concentration of Cu in the fluid is below 1000 ppm for most of the inclusions with average values varying between around 200 ppm and 300 ppm for fluid inclusions in samples MT11, MT12, M12 and MT19 and higher for fluid inclusions in sample MT13A (~ 500 ppm) (Figures 5.3 and 5.5; Table 5.1). Ba/Cu ratios vary over a wide range, from ~ 0.1 up to around 23 for most samples with averages spanning from around 2 to about 6 (Figure 5.6C and Table 5.1). Zinc concentrations range from few hundreds to few thousands of ppm for fluid inclusions in most samples, with average values between about 600 to around 1000 ppm (Figures 5.3 and 5.5; Table 5.1). Type III fluid inclusions in sample MT20 and MT12 display lower Zn content with values consistently below 1000 ppm and average around 300 and 450 ppm respectively (Figures 5.3C, D, and 5.5; Table 5.1). Cu/Zn ratios are normally below 1 for most of the inclusions, but variable for inclusions in samples M11 and MT13A between approximately 0.1 and 1.8, whereas the remaining samples display particularly low Cu/Zn ratios consistently below 1 but dominantly below 0.5 (Table 5.1). Around 35% of Pb values obtained from the analysis are below detection limits. However, the range of values and average concentrations do not appreciably vary considering or excluding values below detection limits. Lead concentrations are typically between tens to a few hundreds of ppm, with average values ranging from around 50 to about 250 ppm (Figures 5.3, 5.4 and 5.5; Tables 5.1 and 5.2). Zn/Pb ratios span over a wide range of values from around 1.5 up to almost 2.

Table 5.2 Average, maximum and minimum composition of type III (samples MT11, MT13A, MT20, MT12 and MT19) and IV (samples MT11_Z2 and MT12_Z1) fluid inclusions determined using LA ICP MS analysis. Values in ppm.

Fluid inclusions type		K	Ca	Mn	Fe	Sr	Ba	Cu	Zn	Pb
Type III	**Min**	7107	8982	142	108	81	41	20	102	13
	Max	41373	49044	36085	7875	825	3467	1048	2036	541
	Average	19429	20590	3734	2013	286	782	282	722	121
	Average *	18694	20590	2484	2106	286	814	349	772	147
	Stdev	7855	8612	5968	1933	201	814	231	529	126
Type IV	**Min**	10141	16087	419	351	115	106	105	484	33
	Max	60983	50090	11524	6709	324	6739	3115	9496	261
	Average	24125	30481	3548	2315	203	1018	760	2272	111
	Average *	26376	30481	419	2315	203	1109	1155	2427	137
	Stdev	16431	12759	4653	2547	67	2155	991	2770	77

Average *: average calculated based only on values above detection limit

Type IV fluid inclusions have in general higher Ca (average ~ 30000 ppm) concentrations, ranging from 16000 to 50000 ppm, compared with type III fluid inclusions (Figure 5.4 and Table 5.2). Approximately 44% of K values are below detection limits suggesting than K values are generally lower than reported here. Type IV fluid inclusions contain K (average ~ 24000) concentrations ranging from around 10000 to 60000 ppm (Figure 5.4 and Table 5.2). Type IV fluid inclusions in both samples are in general more enriched in Ca compared to K (Figures 5.3 and 5.5; Table 5.1).

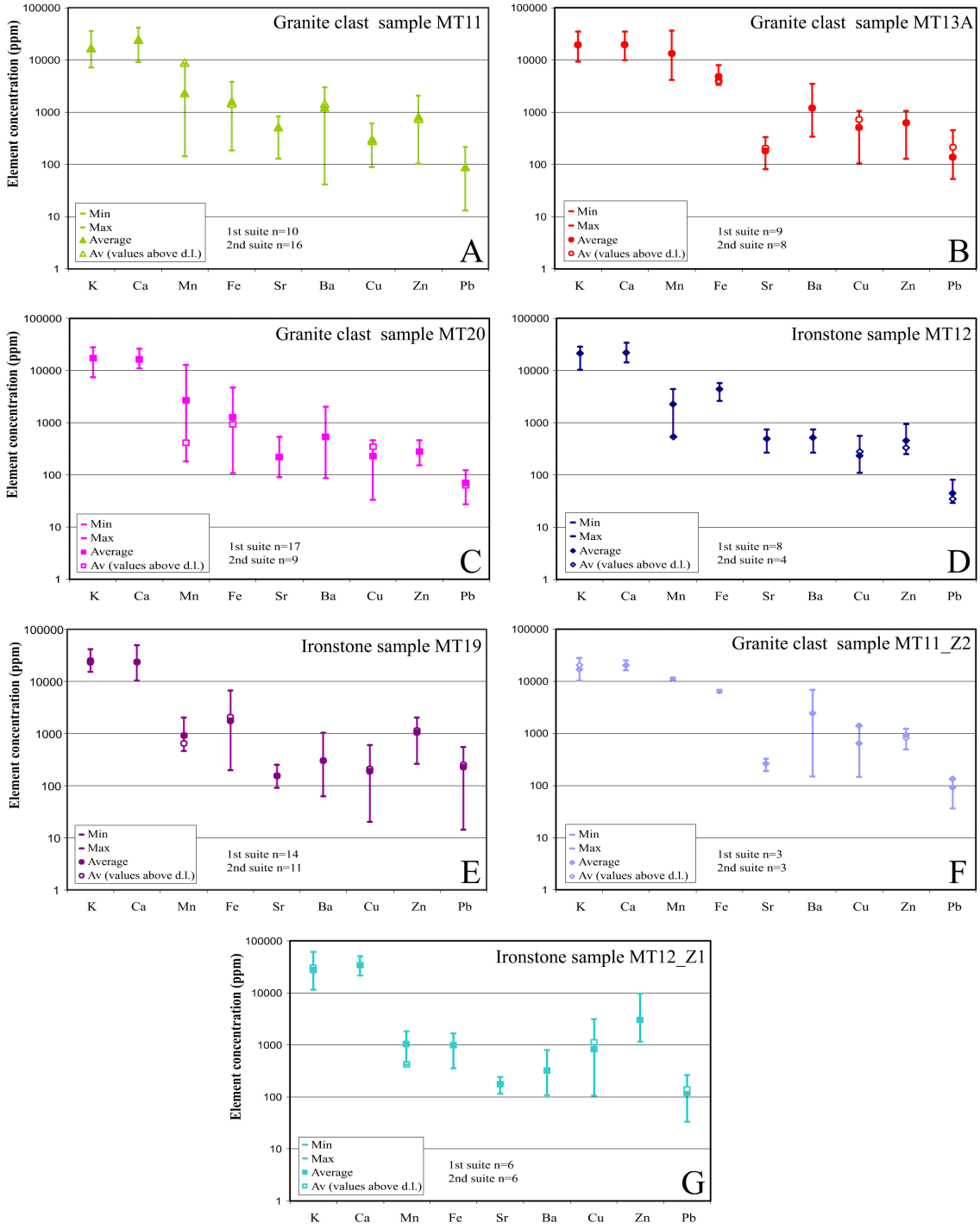

Figure 5.3 Diagram displaying minimum, maximum and average concentrations of major and trace elements of fluid inclusions for each sample determined from LA ICP MS analysis. Bars represent the range of concentrations of each element in the fluid. MT11_Z2 and MT12_Z1 refer to wafers of samples MT11 and MT12 respectively where type IV inclusions were observed. Concentrations of K, Ca, Mn, Fe and Sr were measured in the first routine of analysis, whereas Ba, Cu, Zn and Pb were determined in the second routine of analysis.

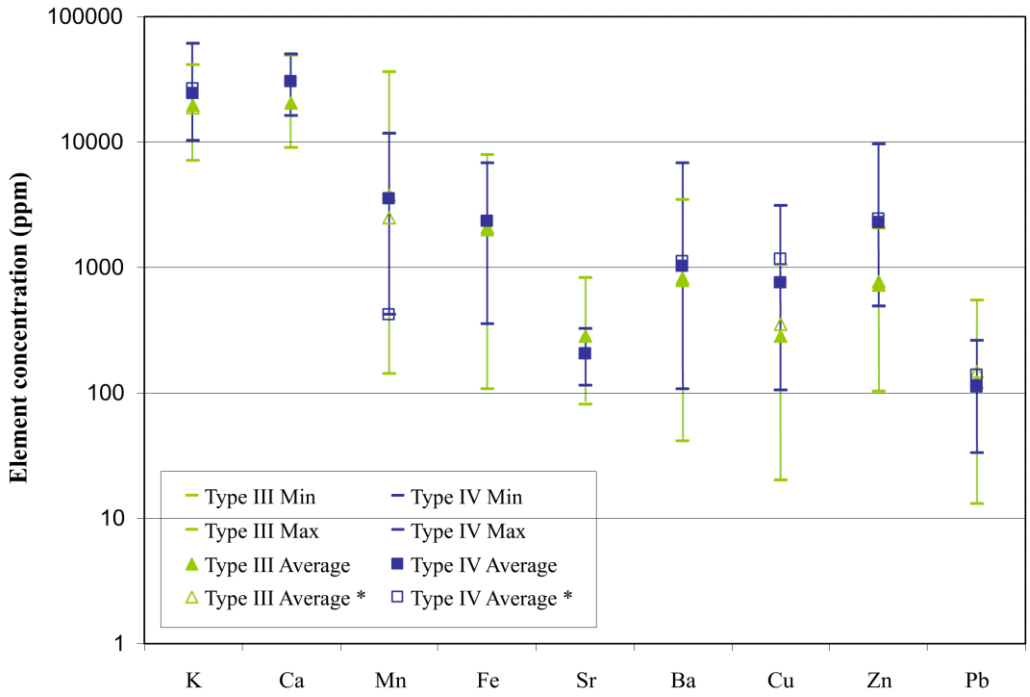

Figure 5.4 Diagram displaying minimum, maximum and average concentrations of major and trace elements of type III and IV fluid inclusions determined from LA ICP MS analysis. Bars represent the range of concentrations of each element in the fluid. Average *: average calculated based only of values above detection limit

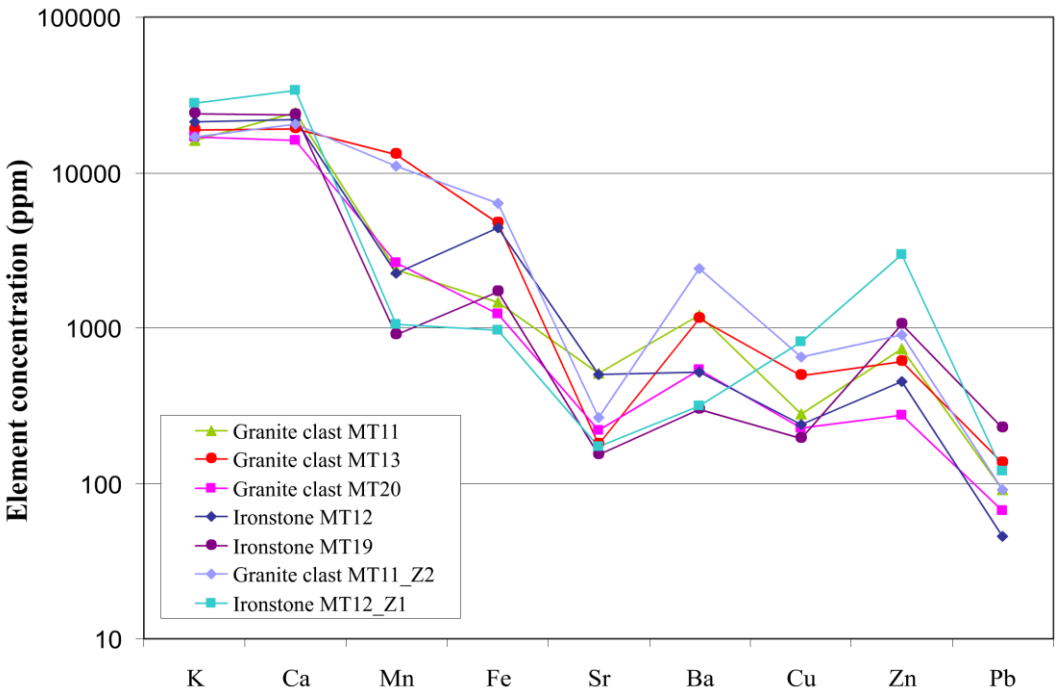

Figure 5.5 Average fluid inclusion composition (calculated using all values including those below detection limits) for each sample determined using LA-ICP-MS.

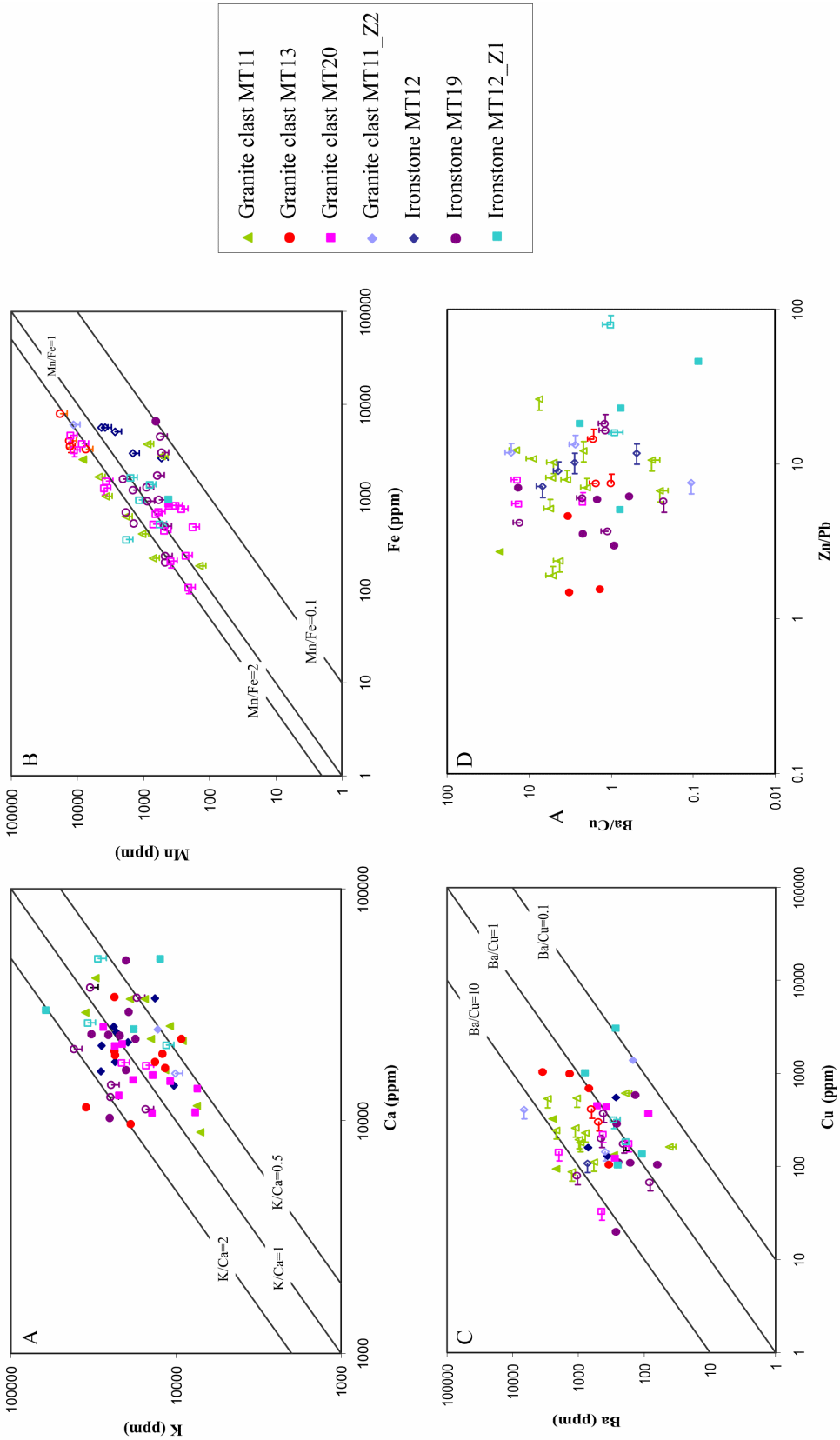

Figure 5.6 Plots of the concentrations of major and trace elements in fluid inclusions from the SRBP. Open symbols refer to values below detection limit and bars indicate that the corresponding element is below detection limit.

Type IV fluid inclusions have Fe concentrations similar to type III fluids inclusions. However, the Fe content in type IV fluid inclusions differs greatly between the inclusions analyzed in the two samples. The only two Fe values obtained from type IV inclusions in sample MT11_Z2 indicate Fe concentration of 6044 and 6709 ppm (Table 5.1), whereas type IV inclusions in sample MT12_Z1 display much lower Fe concentrations ranging from approximately 300 ppm to 1600 ppm for an average Fe content ~ 950 ppm (Figures 5.3G and 5.5; Table 5.1). Only one Mn value was above the detection limit in sample MT12_Z1. The Mn concentration in this inclusion is 419 ppm and the Mn/Fe ratio is 0.44 (Table 5.1).

Strontium ranges from ~ 100 ppm to few hundreds of ppm with an average of 264 ppm and 173 ppm for type IV fluid inclusions in sample MT11_Z2 and MT12_Z1 respectively (Figures 5.3F,G, and 5.5; Tables 5.1), similar to most type III inclusions. Type IV fluid inclusions display Ba concentrations mostly below 1000 ppm, ranging between approximately 100 ppm to 800 ppm for the majority of the inclusions (average ~ 800 ppm; Figures 5.3F, G, and 5.4; Tables 5.1 and 5.2) similar to Ba concentration obtained for type III fluid inclusions in ironstone samples and granite clast sample MT20 (Figures 5.3 and 5.5; Table 5.1). Approximately 45% of the Cu values are below detection limits. The concentration of Cu in the fluid is variable, below 500 ppm for most of the inclusions and with a few values in the order of thousand ppm (Table 5.1). Average values are around ~ 650 ppm and ~ 800 ppm for inclusions in sample MT11_Z2 and MT12_Z1 respectively (Figures 5.3 and 5.5; Table 5.1). Type IV inclusions display a narrower and lower range of Ba/Cu values compared to type III fluid inclusions, mostly comprised between ~ 0.1 and ~ 2.4 and average ~ 0.9 (Figure 5.5C and Table 5.1). Zinc concentrations are higher in type IV fluid inclusions compared to type III, particularly in sample MT12_Z1, and range from ~ 500 to ~ 9500

ppm with an average value ~ 2000 ppm (Figure 5.4 and Table 5.2). Type IV fluid inclusions display Cu/Zn ratios mostly between 0.1 and 0.6 similar to the majority of type III fluid inclusions (Table 5.1). Around 44% of Pb values are below detection limit. Lead concentrations vary in a range (from ~ 30 to ~ 250 ppm; average ~ 100 ppm) similar to type III fluid inclusions (Figure 5.4 and Table 5.2).

In summary, type IV fluid inclusions differ from type III fluid inclusions in that they exhibit or higher average concentrations of Zn, in particular, and of Ba and Ca. Data for Zn are reliable being consistently above 1100 ppm for all the inclusions analyzed in sample MT12_Z1 (Table 5.1). The differences between type III and type IV inclusions are particularly marked when considering type IV fluid inclusions in sample MT12_Z1; some differences in composition (e.g., Ba) between type IV fluid inclusions measured in the two samples may result from the accidental analysis of type III fluid inclusions that occurred in a mixed population with type IV or, alternatively, may be the result natural compositional variations. However, the results for both types of inclusions show in general a good agreement between the different samples; minor differences do not appear to be related to specific samples and can be explained as natural variations of composition.

The results also show a good agreement between type III fluid inclusions occurring in granite clast and ironstone samples. The only significant difference is the lower average concentration of Ba in ironstone samples (~ 350 ppm) compared to granite clasts (~ 1000 ppm) (Figure 5.7 and Table 5.3). However, the Ba concentrations vary significantly even within inclusions of the same sample and generally range over one order of magnitude for most samples.

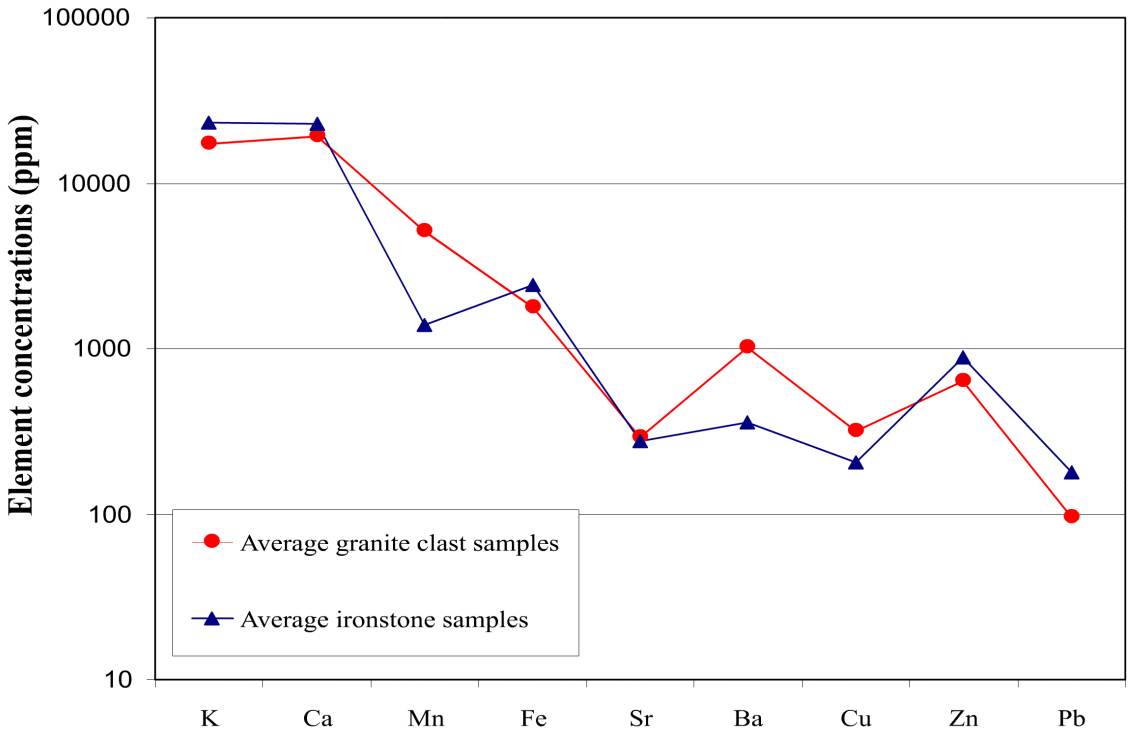

Figure 5.7 Average fluid inclusion composition (calculated using all values including those below detection limits) for granite clast and ironstone samples determined using LA-ICP-MS.

Table 5.3 Average, maximum and minimum composition of type III fluid inclusions in granite clast and ironstone samples determined using LA ICP MS analysis. Values in ppm.

Type III		K	Ca	Mn	Fe	Sr	Cu	Zn	Ba	Pb
Granite clast samples										
	Min	7107	8982	142	108	81	33	102	41	13
	Max	35408	41323	36085	7875	825	1048	2036	3467	450
	Average	17220	19178	5163	1762	291	317	633	1010	95
	Average *	16887	19178	4381	1620	291	421	662	1078	104
	Stdev	7619	7892	7186	1815	208	247	475	915	82
Ironstone samples										
	Min	10311	10321	458	198	90	20	247	62	14
	Max	41373	49044	4360	6611	732	590	1992	1031	541
	Average	23043	22899	1396	2410	279	205	888	357	178
	Average *	22604	22899	587	2040	279	230	1034	357	210
	Stdev	6979	9408	1176	2094	193	173	600	273	181

Average *: average calculated based only on values above detection limit

5.3 Crush Leach Analysis

5.3.1 Methodology

Crush leach analysis of fluid inclusions was carried out at the University of Leeds using the bulk crush-leach method described by Bottrell and Yardley (1988), Banks and Yardley (1992) and Banks et al. (2000). The technique is destructive and provides measurements of concentrations of major and trace elements for the fluid inclusions analyzed. The crush-leach method is particularly useful for determination of anion concentrations and of electrolyte composition of small and/or deep inclusions difficult to analyze by single fluid inclusions techniques. Only anions concentrations were measured from fluids in this study and analyzed elements include Cl, Br, F and SO_4. Samples in this study (e.g., granite clasts MT22) that contain very small fluid inclusions (<5μm) on which microthermometry and LA ICP MS analysis could not be performed were analyzed by crush-leach in addition to samples MT11, MT12, MT13A, MT19 and MT20. Sample MT22v, a quartz vein cutting the granite clast sample MT22, was also analyzed (Table 4.1).

The method required quartz to be crushed to 1-2 mm grain size and cleaned using aqua regia. Contaminating mineral grains were removed and all samples were then further cleaned by boiling several times in double distilled water and/or nitric acid. The samples were allowed to dry and then crushed to a fine powder in an agate pestle and mortar. The powder was then leached with double distilled water. Concentrations of anions were determined by ion chromatography. Replicate analyses show that the precision is ~ 10% RSD for the analysis of these samples (Banks and Yardley, 1992). Contamination is one of the major problems that affects the quality of the analysis and therefore the preparation of the sample represents the most important and delicate step

of the analysis (Bottrell and Yardley, 1988; Banks and Yardley, 1992). Solid contamination occurred for granite clast samples in particular sample MT13A, MT20 and MT22. These samples consist of albite and quartz intergrowths with crystal dimensions in the millimeter scale (Chapter 3) and therefore very difficult to separate, and solid albite contamination is therefore likely. Contamination problems were limited for granite clast sample MT11 in which quartz can reach size up to the centimeter scale and for ironstone samples (Chapter 3). Other problems may arise from adsorption of ions on to surfaces created during the process of crushing can that particularly affect the measured concentrations of cations.

5.3.2 Results

The results of the crush leach analyses are presented in Table 5.4. The data show that Cl is the dominant anion but that the fluid also contains SO_4 and F and lesser Br. To investigate the relationship between the anions a series of bivariate element plots were constructed (Figures 5.8A-D). In Figures 5.8A-C, F, SO_4 and Br respectively are plotted against Cl. The plots clearly show that the samples form two distinct groups with the granite breccia samples displaying higher concentrations of F and SO_4 and lower concentration of Br and Cl than the ironstone and the quartz vein samples. In Figure 5.8D, F is plotted against SO_4 showing that the granite clasts are more enriched in F than SO_4 (F/SO_4 ratios > 1) with the exception of sample MT13A, whereas the ironstones and the quartz vein sample contain slightly higher concentrations of SO_4 compared to F.

Table 5.4 Summary of results obtained from Crush Leach analysis. Values in ppb.

Samples		Cl	Br	F	SO4	Br/Cl x10^3 (mol)
Granite clast						
	MT-11	1658	3.4	125	56	0.91
	MT-13A	2114	3.2	89	125	0.67
	MT-20	2535	2.5	79	67	0.44
	MT-22	1289	1.6	158	89	0.55
Ironstones						
	MT-12	3812	18.6	36	49	2.17
	MT-19	4259	29.2	39	52	3.04
Quartz vein						
	MT-22v	5638	34.8	45	53	2.74

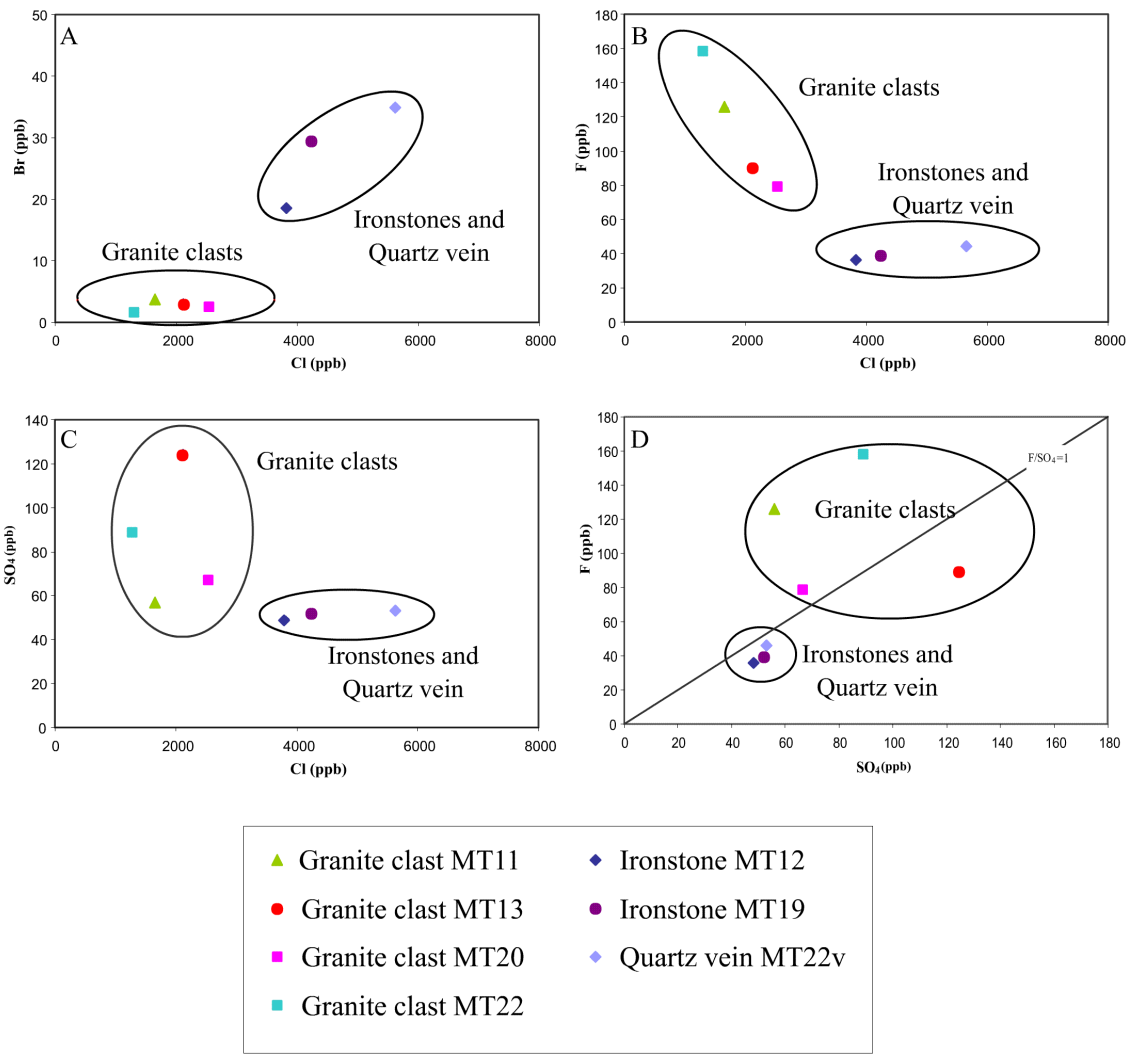

Figure 5.8 Bivariate plots displaying the relationships and relative abundances of anions measured with crush leach analysis

Halogens can be used to determine the origin of salinity of fluids based on their conservative behavior. Such elements are normally not accepted within the lattice of common minerals and as a consequence their concentrations are generally not modified by fluid-wallrock reactions (Yardley et al., 2000). Among the halogens Cl and Br are the most widely used to investigate the origin of fluids (Bohlke and Irwin, 1992b; Fontes and Matray, 1993; Banks et al., 2000; Yardley et al., 2000). Fontes and Matray (1993) reviewed the conservative behavior of Cl and Br and found that the Br/ Cl ratios can only be modified by: (1) dissolution or precipitation of solid chlorides (i.e. interaction with evaporites) and (2) mixing of fluids.

The molar Br/Cl ratios are lower for the granite samples than those of the ironstones and quartz vein (Table 5.4 and Figure 5.9). Molar Br/Cl values for the granite samples range from 0.44 $x10^3$ to 0.91 $x10^3$, lower than that of seawater (1.52 $x10^3$; Fontes and Matray, 1993). These Br/Cl ratios are lower than values obtained from mantle samples (Johnson et al., 2000) and for porphyry copper deposits (Kendrick et al., 2001), but lie in the same range of values determined for volcanic fumaroles (Bohlke and Irwin, 1992b). The reported values are also compatible with water that acquired its salinity through dissolution of halite (Bohlke and Irwin, 1992a) and meta-evaporite horizons are recognized in Cover Sequence 2 of the Mt Isa Inlier. The observed Br/Cl ratios may also be produced by melting of metamorphic scapolite that is abundant in the district and derived by metamorphism of evaporites as recently proposed by Kendrick et al. (2006). The ironstones and the quartz vein samples display Br/Cl values that range from 2.17 $x10^3$ to 3.04 $x10^3$. The values are compatible with those of a fluid produced by evaporation of seawater (bittern brines) (Hanor, 1994; Kendrick et al., 2002a; Kendrick et al., 2002b).

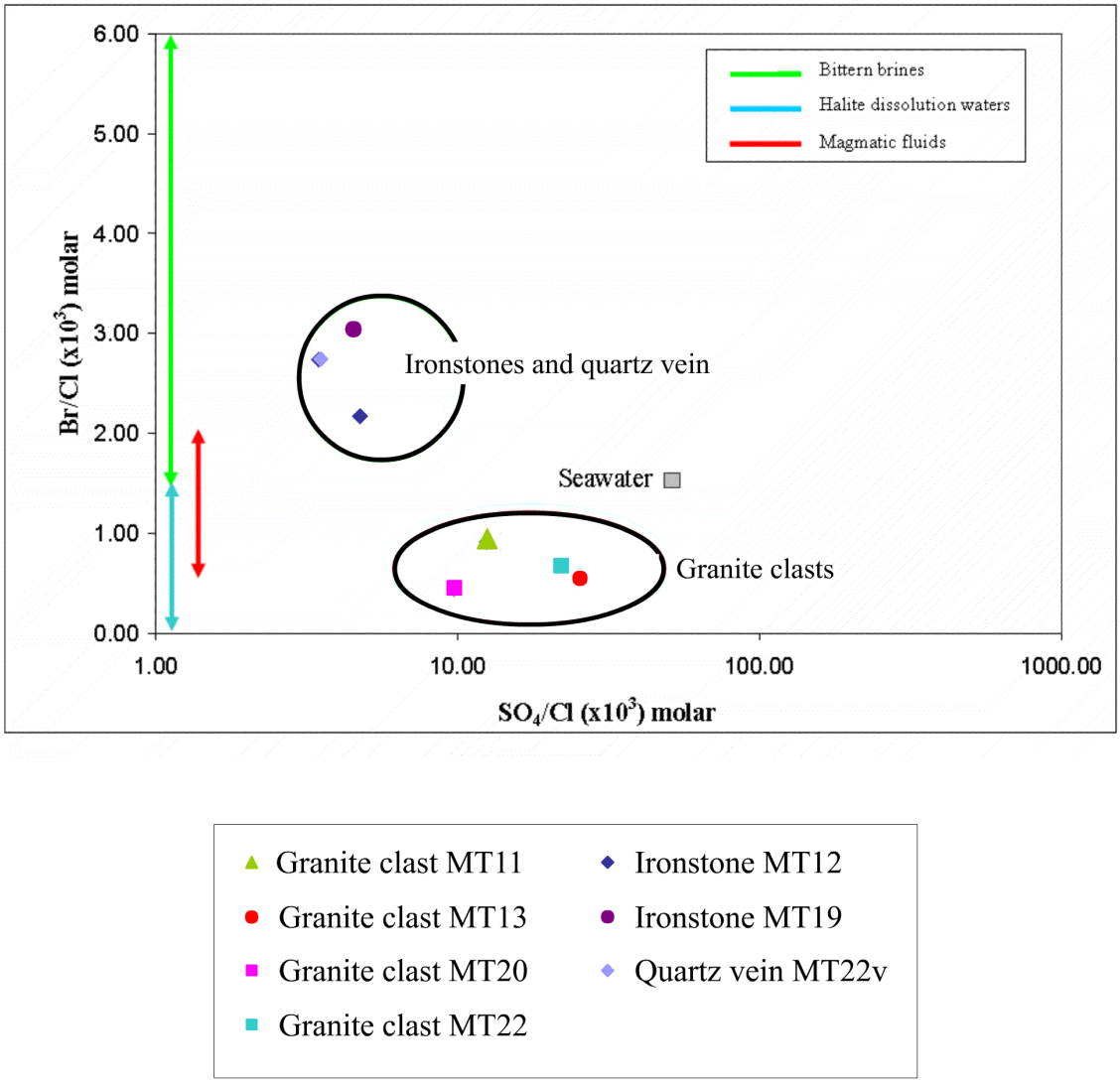

Figure 5.9 Br/Cl ($x10^3$) mol ratios versus SO_4/Cl mol ratios obtained from crush leach data. As a reference Br/Cl and SO_4/Cl ($x10^3$) mol ratios of seawater (data from Fontes and Matray, 1993) and interval of Br/Cl ($x10^3$) mol ratios characteristic of fluid from different geological environment are also showed.

Results from crush-leach analysis clearly indicate the presence of two types of fluids with different concentrations of anions (Table 5.4 and Figures 5.8A-D) and distinct that possibly occurred during the preparation of the samples is a possible explanation of the different halogen signature and anion concentrations of fluid inclusions in granite clast and ironstone samples. Contamination problems were related

in particular to solid albite contamination in granite clasts samples (Section 5.3.1). Alternatively, the observed differences may be related to different populations of inclusions, to their distribution and to their relative abundance within the different samples (Table 4.3). The main difference between granite clast samples and ironstones is that the former contain type I carbonic, type II mixed brine-carbonic fluid inclusions in addition to abundant type III sodic (-calcic) fluid inclusions (Table 4.3). In granite clast samples MT20 and MT11 type IIa fluid inclusions are common to abundant (Table 4.3) and likely contributed to the fluid halogen signature. In granite clast samples MT13A and MT22 these types of inclusions were not observed; however these samples contain common inclusions that were not classified and analyzed with microthermometry and laser ablation techniques because of their small size (< 5μm) and that could possibly be type II fluid inclusions.

Type III fluid inclusions are abundant both in granite clast and ironstone samples. The different composition of type III fluid inclusions between granite clast and in ironstone samples may explain the different halogen signature and anion concentrations of the two types of samples. However, this is inconsistent with LA ICP MS results that did not reveal significant differences between type III fluid inclusions analyzed in granite clast and in ironstone samples (Section 5.2.3). Granite clast samples also contain common to abundant type I and type IIa inclusions, whereas the ironstone samples are dominated almost exclusively by type III inclusions (Table 4.3) and were therefore likely the dominant contributor to the halogen signature of the ironstone samples. Type IV fluid inclusions are not abundant and they dominantly occur in the ironstone sample MT12 and the granite clast MT11 (Table 4.3), samples that display a different halogen signature and therefore these inclusions are unlikely responsible for the observed different halogens signature of the fluids in the two groups of samples.

Type V inclusions are common, but not abundant, and were observed dominantly in sample MT12 whereas they are common to rare in ironstone sample MT19, that displays similar halogen signature and anion composition of fluids in sample MT12 (Table 4.3). The analysis of the relative abundances of the different fluid inclusion populations in the different samples suggests that type IIa fluid inclusions are likely responsible for the halogen signature of fluids in granite clasts, whereas type III fluid inclusions are responsible for the halogen compositions of fluids in ironstone and quartz vein samples.

5.4 Apatite chemistry

5.4.1 Introduction and Methodology

The apatite group minerals are the most abundant among the phosphates and they commonly occur as accessory minerals in igneous as well as in sedimentary and metamorphic rocks. Their formula can be expressed as

$Ca_{10}\ (PO_4)_6\ (OH, F, Cl)_2$

The structure of apatite allows a large number of substitutions in all three sites by a wide range of elements (Pan and Fleet, 2002). Due to this property, apatite is very sensitive to the environment in which it formed and its analysis offers valuable information relative to the fluid chemistry at the time of formation. Accessory and secondary apatites in granite breccia clasts and ironstones from the SRBP were analyzed to further define the chemistry of fluids associated with pipe.

Microprobe analyses were carried out with a JEOL JXA-8200 Superprobe at the Advanced Analytical Centre (AAC), James Cook University, Townsville, and include quantitative analysis using a wavelength-dispersive collector (WDS). Carbon-coated polished thin sections were analysed at 15 kv and 20 nA using a 2 to 5 μm diameter electron beam. The analyses were undertaken on apatites from both ironstones and granite breccia clasts, in order to identify possible differences between apatites in the two host rocks with potential implication for volatile behavior. Analyzed phases include primary accessory apatites in granite clast samples MT20 and MT22, secondary apatite related to actinolite-apatite-titanite alteration in granite clasts sample MT13A, and accessory apatite in ironstone sample MT19 (Chapter 3; Table 5.5).

5.4.2 Results

Results of microprobe analysis and calculated chemical formulas are reported in Appendix 5.2 and summarized in Table 5.5. The chemical formulas were calculated from the microprobe analysis on the basis of ten atoms in the cation position. No attempt was made to calculate the concentration of OH, since the sum of Cl and F always exceed the fluoropatite stoichiometry.

All the apatites analyzed are fluoroapatites with average concentration of fluorine ranging between 3.71 and 3.95 wt%, thus slightly lower or exceeding the stoichiometric value (3.77 wt%). Chlorine is also abundant displaying average concentrations in the range of 0.50 and 0.75 wt%.

The CaO and PO_4^{3-} concentrations do not vary significantly and range from ~53.42 to ~55.83 wt% and from around 40.61 to about 41.73 wt% respectively.

However, the apatites display distinct minor element compositions. The tetrahedral site substitutions of PO_4^{3-} by other anionic groups, namely SiO_2, SO_3 and As_2O_5, are very low for primary and secondary apatites in granite clasts samples, with measured concentrations often below limit of detection (As is below detection limit for apatites in all samples). The average concentration of these anion groups overall varies from 0.01 to 0.02 wt%, although some values below detection suggest possibly lower concentrations. Apatites in ironstone sample MT19 on the other hand have a significantly higher content of all three anionic groups with average concentrations for SiO_2, SO_3 and As_2O_5 being 0.12 wt% for SiO_2 and SO_3 and 0.2 wt% for As_2O_5, with a total average concentration of almost 0.5 wt%. Apatites in sample MT19 also have higher average concentrations of Ce (0.47 wt%), Na (0.17 wt%) and Sr (0.09 wt%) compared to primary and secondary apatites in granite clast samples (Ce from 0.07 to 0.18 wt%; Na from 0.04 to 0.09 wt%; Sr from 0.02 and 0.04 wt%). The average concentrations of Fe and Mn also vary considerably and generally define two different sets of values. Average Fe concentrations are lower (between 0.06 and 0.07 wt%) for primary apatites in granite clast sample MT20 and secondary apatites in granite clast sample MT13A and higher (between 0.20 and 0.28 wt%) for primary apatites in granite clast sample MT22 and accessory apatites in ironstone sample MT19. Average Mn concentrations have similar distributions but with lower values for secondary apatites in granite clast sample MT13A and for accessory apatites in ironstone sample MT19 (0.03 and 0.09 wt% respectively) and higher values for primary apatites in granite clast samples MT20 and MT22 (0.21 and 0.55 wt%).

From the calculated formula it appears there is a clear deficiency in the tetrahedral site for all the apatites and particularly for primary apatites in samples MT20 and sample MT19. Since this deficiency does not seem to be linked to analytical

uncertainty, it can be inferred that the missing element\s is\are not measurable. Possible substitutions for P in the tetrahedral position include SiO_4^{4-}, SO_4^{2-}, As^{5+}, which were all measured and V^{5+} and CO_3^{2-}which were not measured. The latter hypothesis seems the more likely considering that several studies have reported an excess of fluorine in CO_2-bearing apatites compared to the stoichiometry (Binder and Troll, 1989; McClellan and Van Kauwenbergh, 1991; Veiderma et al., 2005). The deficiency in the tetrahedral site and the excess of fluorine can be explained involving a coupled substitution expressed as:

$$PO_4^{3-} \rightarrow CO_3^{2-} F^-$$

in which one carbon replaces one phosphorus in the phosphate radical and the charge balance is maintained by the substitution of O^{2-} by F^- (Binder and Troll, 1989; McClellan and Van Kauwenbergh, 1991). The general formula can be then expressed as:

$$Ca_{10} [(PO_4)_{6-x} (CO_3 .F)_x] (F, OH, Cl)_2$$

(Binder and Troll, 1989).

In summary, apatites in granite clasts have similar major and trace composition suggesting that they have a common origin, although they occur in different paragenetic stages. Apatites in samples MT20 and MT22 are of primary igneous origin, whereas those in sample MT13A are secondary and related to actinolite-apatite-titanite alteration. In general, these apatites are different from those in ironstone sample MT19

which have different minor element compositions. All apatites are characterized by a deficiency in the tetrahedral site that possibly indicates the presence of CO_2.

Table 5.5 Summary of microprobe analysis of apatites from granite clasts and ironstones found within the breccia pipe.

Rock type	**Granite breccia clasts**						**Ironstones**	
Samples	**MT20**		**MT13A**		**MT22**		**MT19**	
Analyses (n)	14	Stdev	15	Stdev	11	Stdev	7	Stdev
P_2O_5	41.73	0.26	40.75	0.21	40.71	0.16	40.61	0.30
SO_3	0.02	0.02	*0.01*	0.01	0.01	0.01	0.12	0.06
SiO_2	0.01	0.02	0.01	0.01	*0.00*	0.00	0.12	0.04
As_2O_5	*0.01*	0.01	*0.01*	0.01	*0.00*	0.00	0.17	0.22
CaO	55.83	0.49	53.88	0.11	53.42	0.15	54.45	0.25
Ce_2O_3	0.14	0.05	0.18	0.08	0.07	0.05	0.47	0.15
FeO	0.07	0.04	0.06	0.04	0.28	0.07	0.20	0.04
Na_2O	0.05	0.01	0.09	0.02	0.04	0.01	0.17	0.04
MnO	0.21	0.08	0.03	0.02	0.55	0.08	0.09	0.03
SrO	0.04	0.02	0.02	0.02	0.02	0.02	0.09	0.05
F	3.94	0.55	3.71	0.34	3.77	0.38	3.95	0.70
Cl	0.67	0.09	0.50	0.07	0.54	0.05	0.75	0.17
Total	100.98	0.63	97.56	0.22	97.70	0.28	99.36	0.48
P	5.866		5.944		5.937		5.813	
S	0.002		0.001		0.001		0.016	
Si	0.002		0.002		0.000		0.020	
As	0.001		0.000		0.000		0.015	
Ca	9.931		9.946		9.860		9.863	
Ce	0.008		0.012		0.004		0.029	
Fe	0.010		0.008		0.040		0.028	
Na	0.017		0.029		0.014		0.057	
Mn	0.030		0.004		0.081		0.013	
Sr	0.003		0.002		0.002		0.009	
F	2.067		2.125		2.125		2.109	
Cl	0.189		0.035		0.035		0.214	

5.5 Summary

LA ICP MS analysis of type III fluid inclusions revealed that the fluid contains similar average concentrations of K (~19500ppm) and Ca (~20500ppm), but single inclusions have variable K/Ca ratios. The inclusions also contain Ba (average ~ 800 ppm), and Sr (average ~ 300 ppm). Among the metals Fe is the most abundant (average ~2000 ppm), followed by Zn (average ~ 800 ppm) and Pb (~ 100 ppm). Most of Mn concentrations are below detection limits. Approximately half of Cu values are below detection limits and therefore concentrations are expected to be generally lower than reported here (average ~ 300 ppm). Type IV fluid inclusions generally have similar average concentrations of Fe (~ 2500 ppm), Sr (~ 200 ppm) and Pb (~ 100 ppm) compared to type III fluid inclusions but contain more Ca (~ 30500 ppm), Zn (~ 2000 ppm) and Ba (~ 1000 ppm) than type III fluid inclusions. Only one Mn value (419 ppm) was above detection limits for these inclusions.

Results of crush leach analysis clearly defined two distinct fluids based on anion concentrations and molar Br/Cl ratios. Fluid inclusions in the granite clasts display higher concentrations of F and SO_4 and lower content of Br and Cl; fluid inclusions in the ironstones and the late quartz vein display lower values of F and SO_4 and higher content of Br and Cl. The Br/Cl ratios obtained for fluid inclusions in the granite clast samples are compatible with a magmatic origin or with an origin via dissolution of evaporites (or mixing of the two) or by melting of metamorphic scapolite. The ironstones and the quartz vein sample display Br/Cl ratios consistent with an origin via evaporation of seawater(Hanor, 1994; Kendrick et al., 2002a; Kendrick et al., 2002b).

Apatite analysis revealed that apatites in granite clasts have similar major and trace composition, but different from those in ironstone sample MT19. The

compositional differences of apatites of ironstone sample MT19 compared to those in granite clasts may suggest a different origin, related to a distinct hydrothermal or possibly metamorphic event. All apatites are characterized by a deficiency in the tetrahedral site that is likely related to the presence of CO_2.

Chapter 6

Chapter 6 – A comparison of hydrothermal fluids related to the Eloise Cu-Au deposit and to the Suicide Ridge Breccia Pipe

6.1. Introduction

A number of fluid inclusions studies (Adshead, 1996; Rotherham, 1997; Baker, 1998; Williams et al., 2001; Mark et al., 2004; Mustard et al., 2004; Williams, personal communication) have been conducted in recent years on fluids related to iron oxide copper gold (IOCG) deposits in the Cloncurry district in Australia with the aim of determining the chemistry and fluid processes associated with these systems and ultimately the mechanism that led to their formation. One of the aims of this chapter is to expand the knowledge of the chemistry of fluids associated with IOCG deposit in the Cloncurry district by complementing the existing data with new results from LA ICP MS analysis of fluid inclusions from the Eloise Cu-Au deposit. The other main aim of this chapter is to understand the key differences that led to the formation of mineralized and barren systems in the Cloncurry area, and for this purpose the fluid inclusions associated with the Eloise deposit are compared to fluid inclusions related to the SRBP (Chapters 4 and 5).

6.2. The Eloise Cu-Au Deposit

6.2.1. Background Geology

The Eloise Cu-Au deposit (3.1 Mt @ 5.5 % Cu, 1.4 g/t Au and 16 g/t Ag; Baker, 1998) is located approximately 60 km southeast of Cloncurry and is one of the several IOCG deposits hosted in the Proterozoic rocks of the Cloncurry district in the Eastern fold belt (Figure 6.1). The deposit characteristics have been thoroughly described by Baker and Laing (1998), Baker (1998) and Baker et al. (2001) and are briefly summarized in this and the following section that focuses on fluid inclusions studies. The host rocks at Eloise include dominantly meta-arkose, quartz-biotite schists and amphibolite all ascribed to the Soldiers Cap Group (Figure 6.2; Baker and Laing, 1998). Metamorphic mineral assemblages in amphibolite and in metasedimentary rocks indicate that the rocks reached amphibolite facies metamorphic conditions with temperatures between 550°C and 600°C at pressures lower than 3.5 kbars during D_2 regional deformation (Baker and Laing, 1998). Mineralization and alteration are localized within and around the Levuka shear zone, a large shear zone that manifests as a major north-trending regional magnetic feature, the Levuka trend (Baker and Laing, 1998). The Levuka shear zone can be subdivided in a number of minor shear zones, the Southern shear zone, the Scrubby Creek shear zone and the Eloise shear zone, that lie parallel to the main S_2 foliation in the area, and display a north-south strike with a steep to subvertical east or west dip (Baker and Laing, 1998). Other structures at Eloise include the Median and the Middle fault that locally contain mineralization and are believed to have been active during and after the mineralization event (Baker and Laing, 1998). Alteration and mineralization are inferred to have formed synchronously with D_3 ductile-brittle deformation (Baker and Laing, 1998). The mineralized system develops

along a distance of approximately 2km and is zoned with magnetite-pyrite-rich mineralization in the south (Magnetite-Pyrite Zone), chalcopyrite-pyrrhotite-rich mineralization in the central lode zone (Chalcopyrite-Pyrrhotite Zone) and pyrrhotite-rich mineralization occurring in the north (Pyrrhotite Zone) (Figure 6.2; Baker, 1998). The two main lodes, the Elrose and Levuka lodes, form a limited portion of the mineralized system and occur in the central Chalcopyrite-Pyrrhotite Zone (Baker, 1998). Baker (1998) recognized and described seven metasomatic events that include three main stages (stages I, II and III), rare pre-D_2 veining, localized post-mineralized veining (stage IV), and two veining events occurring syn- to late- ore (stages V and VI). The main alteration stages are illustrated in Figure 6.3. Stage I albitization predates the mineralization event and comprises mainly albite with minor quartz, apatite, titanite and rutile. Stage I alteration is overprinted by Stage II hornblende-biotite-quartz alteration, which is developed in veins, wall-rock alteration and shear zones. Stage III is the main ore stage and commonly replaced and veined earlier maficsilicate alteration. Ore stage minerals include pyrrhotite, chalcopyrite, pyrite and magnetite, while main gangue phases consist of quartz, calcite, actinolite/hornblende and chlorite. $^{40}Ar/^{39}Ar$ dating on hornblende and micas from pre- to post- mineralization stages indicates an age for the mineralizing event between ca 1514 and 1530 Ma (Baker et al. 2001).

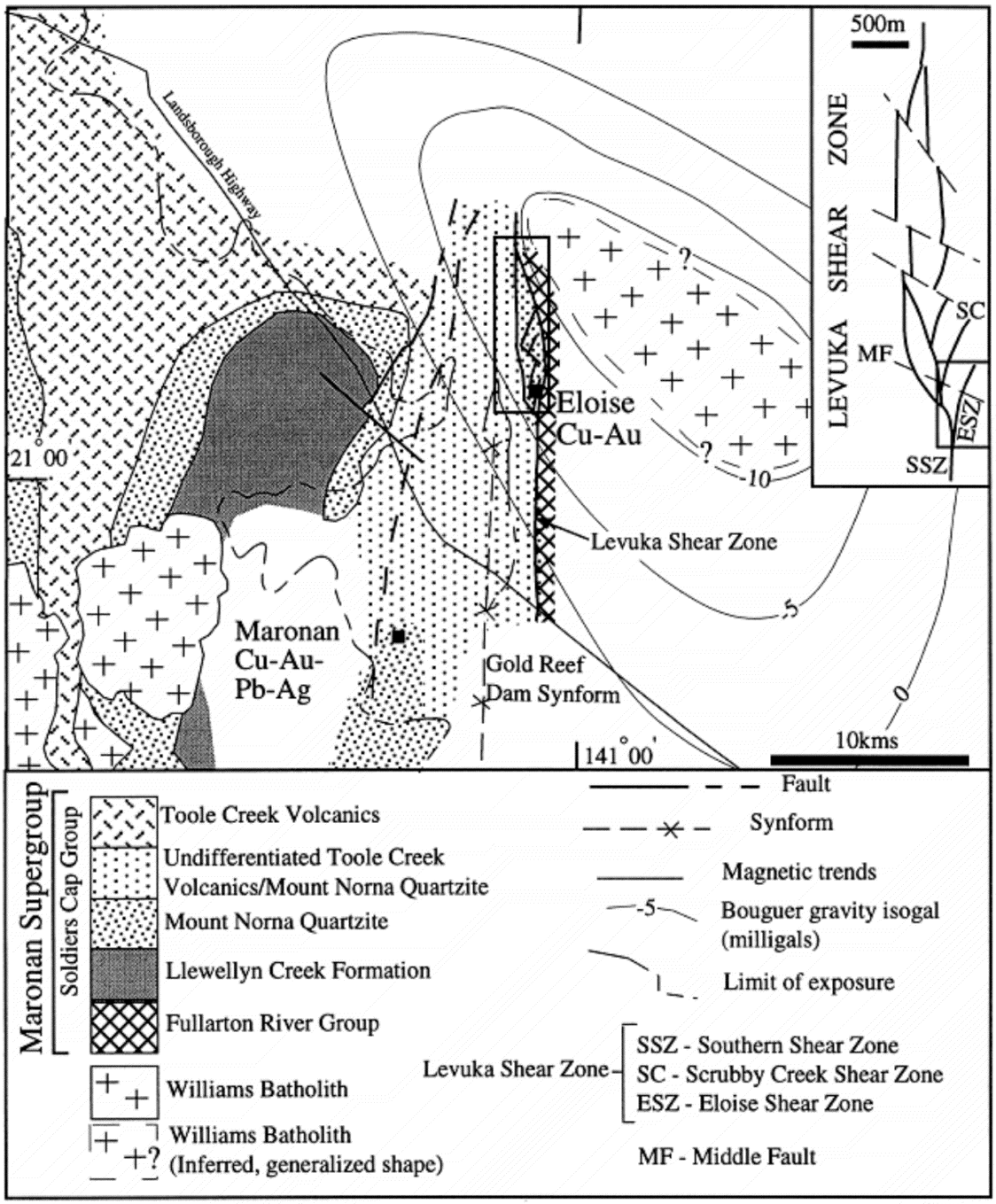

Figure 6.1 Regional geological setting of the Eloise deposit. Modified from Baker and Laing. (1998).

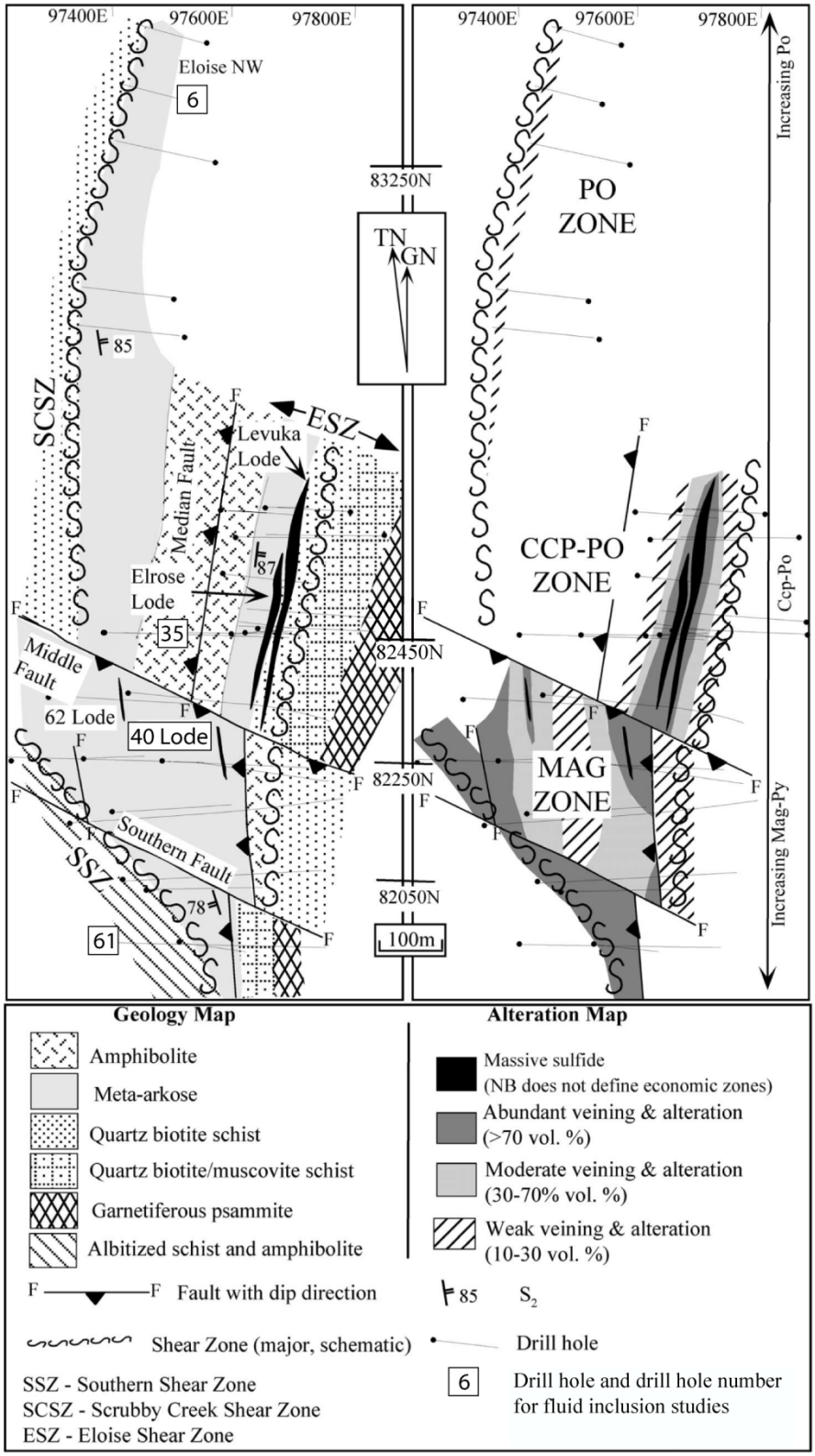

Figure 6.2 Geology and alteration map of the Eloise deposit. Mineral abbreviations after Kretz (1983). Modified after Baker (1998).

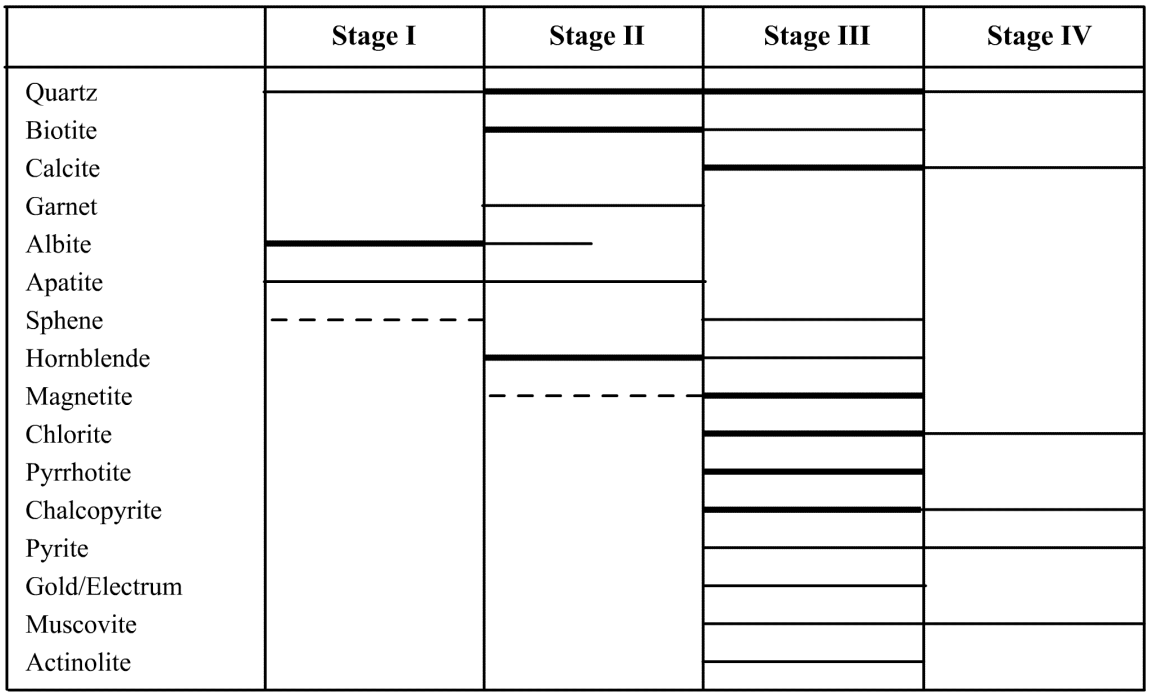

Figure 6.3 Paragenesis of alteration and veins at the Eloise deposit. Modified after Baker (1998).

6.2.2. Summary of fluid inclusions studies

Fluid inclusions associated with the Eloise deposit have been described in detail by Baker (1998). He recognized four main compositional types of fluid inclusions: multisolid, halite-bearing, liquid-rich and carbonic fluid inclusions that he further classified into eight fluid inclusion types based on criteria of primary, pseudosecondary and secondary origin (Roedder, 1984) and on the paragenetic stage in which the inclusions occurred (Table 6.1). Type 1, 2 and 4 are multiphase fluid inclusions observed in samples from pre- (type 1), syn- (type 1 and 2) and post-mineralization stage (type 4). These inclusions are usually observed in three-dimensional groups or as isolated inclusions commonly occupying the central areas of the quartz host (Baker,

1998). They contain several different types of daughter phases that include halite and sylvite, common in all three inclusions types, a Fe-Mn-Cl-Si phase observed in type 1 fluid inclusions and, finally, a Fe-chloride phase common in type 1 and 2 fluid inclusions (Baker, 1998). Homogenization temperatures range from 277 to 540°C, from 101 to 330°C and from 137 to 258°C for type 1, 2 and 4 respectively (Table 6.1). The inclusions display very high salinities spanning from 32 to 60 wt% NaCl equiv., 30 to 40 wt% NaCl equiv. and 29 to 35 wt% NaCl equiv. for type 1, 2 and 4 respectively (Table 6.1; Baker, 1998). Type 3 fluid inclusions are rare CO_2-rich fluid inclusions observed exclusively in mineralized samples (Baker, 1998). These are two or three phase H_2O-CO_2 inclusions and generally occur in isolation or in clusters of few inclusions. No data from microthermometry were available for type 3 fluid inclusions.

Type 5 and 6 fluid inclusions are liquid-rich fluid inclusions and they normally contain a halite crystal. Type 5 are pseudosecondary syn-mineralization fluid inclusions, whereas type 6 occur as secondary inclusions that formed syn- to post- mineralization (Baker, 1998). Homogenization temperatures range from 127 to 199°C and from 121 to 315°C for type 5 and 6 respectively (Table 6.1; Baker, 1998). Both inclusion types display high salinities from 30 to 32 wt% NaCl equiv. and 28 to 39 wt% NaCl equiv. for type 5 and 6 respectively (Table 6.1; Baker, 1998). Type 7 are liquid-rich fluid inclusions observed in deformed quartz samples and postdate the mineralization stage (Baker, 1998). They display homogenization temperatures from 101 to 145°C and low to moderate salinities from 4 to 17 wt% NaCl equiv. (Table 6.1; Baker, 1998). Type 8 are either empty or liquid-rich inclusions and do not display any heating or freezing behaviour (Baker, 1998).

Table 6.1 Summary of fluid inclusion characteristics from the Eloise deposit. Modified after Baker (1998).

Paragenetic Stage	Type	Origin	Phases	Daughter Salts	Size (m)	Fluid Inclusion	Th (°C)	Salinity (wt% NaCl eq)
Stage I-III	**Type 1 Multiphase**		L+V+nS (n= 1-5)	Halite ± Fe-Mn-Cl-Si ± Fe-chloride ± sylvite ± unknown	<5-20		277 to 540	32 to 60
Stage III	**Type 2 Multiphase or liquid-rich**	Primary to secondary	L+V+nS (n= 1-3)	Halite ± Fe-Mn-Cl-Si ± Fe-chloride ± sylvite ± unknown	<5-20		101 to 330	30 to 40
	Type 3 Liquid- rich CO2-rich		CO_2 (L-V) +H_2O (L)	None	<5-10			
Stage IV	**Type 4 Multiphase or liquid-rich**		L+V+nS (n= 0-3)	± Halite ± sylvite ± Fe-chloride	5-40		137 to 258	29 to 35
Stage III	**Type 5 Liquid-rich**	Pseudo-secondary	L+V±S	± Halite	5-20		127 to 199	30 to 32
Syn- to post stage III	**Type 6 Liquid-rich**		L+V±S	± Halite	<5-10		121 to 315	18 to 39
Deformed quartz post-mineralization	**Type 7 Liquid-rich**	Secondary	L+V	None	<5-10		101 to 145	4 to 17
Post stage III	**Type 8 Liquid-only?**		L+V	None	<5-15			

6.2.3. Fluid evolution and genetic model for the Eloise Cu-Au deposit

Baker (1998) interpreted the fluid inclusions observed at Eloise as the result of evolving fluid history, with type I multiphase high-temperature, high salinity fluid inclusions representing the earliest fluid. Baker (1998) suggested that this fluid possibly had a magmatic origin based on its ultrasaline nature. Fluid inclusions related to the mineralization stage display generally lower salinities and a wider range of homogenization temperatures compared with pre-mineralization fluid inclusions and may be the result of fluid mixing between an early, hot high salinity fluid with a cooler,

lower salinity fluid (Baker, 1998). This hypothesis is also supported by the presence of different inclusions types occurring within the same clusters in the mineralization stage (Baker, 1998). Fluid inclusions that postdate mineralization usually have lower salinity and lower homogenization temperatures than inclusions that formed pre- to syn-mineralization (Baker, 1998).

High temperature, high salinity fluid inclusions recognized at Eloise are interpreted as the fluid responsible for mineralization. Their highly saline nature, in fact, suggests that that they would have been able to carry significant amount of metals (Baker, 1998). Ductile-brittle shear zones and faults are believed to have played a major role in channelling the metasomatic fluids, with the ultrasaline fluid interpreted to have moved from south to north based on mineral zonation (Baker, 1998). Decreasing temperature and salinity, likely due to fluid mixing and sulfidation of Fe-silicate, are believed to have played a major role in ore deposition (Baker, 1998; Baker et al., 2001).

6.3. LA ICP MS analysis of fluid inclusions from the Cu-Au Eloise Deposit

6.3.1. Methodology and sample and fluid inclusion selection

LA ICP MS analysis was undertaken to determine the composition of multiphase and halite-bearing inclusions from the Eloise deposit. The characteristics of the samples selected from fluid inclusion studies are summarized in Table 6.2. The chemistry of fluid inclusions from the Eloise deposit was determined with LA ICP MS analysis undertaken at the School of Earth and Environment at the University of Leeds.

Table 6. 2 Summary of samples selected for fluid inclusion LA ICP MS analysis.

Sample	Sample/Drillhole/Depth (m)	Alteration zone	Paragenetic stage	Mineralogy
48164	END61/588.3	Levuka Lode	Stage II/III	Hbl-qtz-ccp vein, albite alteration in meta-arkose
EWD6	EWD6/285	Eloise NW	Stage II/III	Hbl-qtz-po-calc in albitizied meta-arkose
48170	END61/635.3	Levuka Lode	Stage II/III	Cal-qtz-ccp-po vein
48076	END40a/314.4	40 Lode	Stage II/III	Cal-py vein in meta-arkose
48178	END35C/311.1	Elrose Lode	Stage II/III	Po-ccp-qtz-hbl-vein

The instrumentation and analytical procedures for the analyses are same used for the analysis of liquid-rich and halite-bearing type III and IV fluid inclusions associated with the barren SRBP (Chapter 5; Allan et al., 2005). Concentrations of Na, K, Ca, Mn, Fe, Cu, Zn, Pb, Li, Mg, Rb, Sr, Cs, Ba, Co, Ni, As, Ag, Au, Cl and Br were measured in five distinct analytical routines. The first comprised Na, K, Ca, Mn, Fe, Cu, Zn, and Pb, the second included Na, K, Co, Ni, Cu, Zn, As and Pb, the third Na, Cu, As, Ag and Au, the fourth included Na, Cl and Br and the final one consisted of Na, Li, K, Ba Mg, Rb, Sr and Cs. In the analysis of the first routine H_2 was introduced into the ICP reaction cell in order to eliminate the interference between $^{40}Ar^+$ and $^{40}Ar^{16}O^+$ (Ar is the carrier gas) and $^{40}Ca^+$ and $^{56}Fe^+$ respectively (Chapter 5; Allan et al., 2005). This setting was not employed for the analysis of the remaining suites in which Ca and Fe were not analyzed. The Na concentrations were determined in all sets of analysis because Na was used as the internal standard (see below), while K contents were determined in all but one series as a control on the quality of the analysis. Potassium values obtained in the

first series of analysis were used in tables and plots (unless otherwise stated) for its immediate correlation with other major elements (i.e. Ca). Ablation spots and spectra for the suites of elements are shown in Figures 6.4 and 6.5. Limits of the detection for the analyzed elements were calculated on the basis of 3 times the standard deviation of the signal containing zero analyte (Chapter 5; Allan et al., 2005). Unfortunately all values for Li, Co, Ni, As, Ag and Br and almost all of Cl values were below the limits of detection and are not considered in the discussion. Results for the second suite are mostly below detection limits, particularly Zn and Cu in one sample analyzed and Zn, Cu and Pb for the other sample analyzed (only two samples were analyzed for this suite). Values for Cu were below detection limits in the majority of cases in all the series in which they were measured. For the final results and discussion values for Zn, Cu and Pb are those measured in the first series of analysis. The choice of using Zn, Cu and Pb from the first series is due to better quality of Zn and Pb measured in this suite (i.e. Zn values measured in the first suite are more consistently above detection limit compared to those obtained in the second set of analyses) and the combined elemental suite enables comparison between major and base metal elements. Values below the detection limit were replaced with the calculated detection limit for the specific element in the given inclusions and used as a maximum concentration estimate. Some elements display a relatively large standard deviation. This does not appear to be related to analytical problems or to fluid inclusion leakage or necking down, but rather appear to reflect variable compositions of the inclusions even Signals with spikes were removed as they lead to an overestimate of element concentrations; these were mainly related to Mg and less frequently to Ca and occasionally to K, Fe, Cu and Pb. Results for Mg were dismissed and are not presented here since all the signals were considered to be spikes.

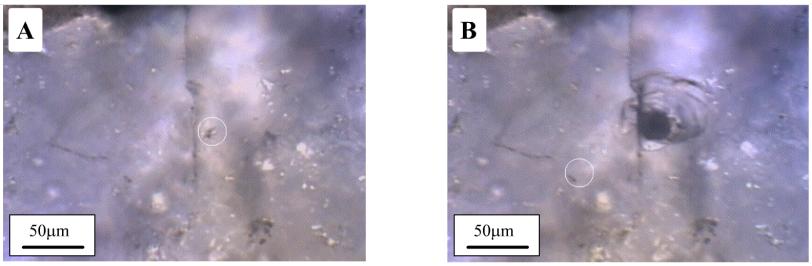

Figure 6.4 Picture of halite-bearing fluid inclusion before (A) and after (B) ablation. Sample EWD6.

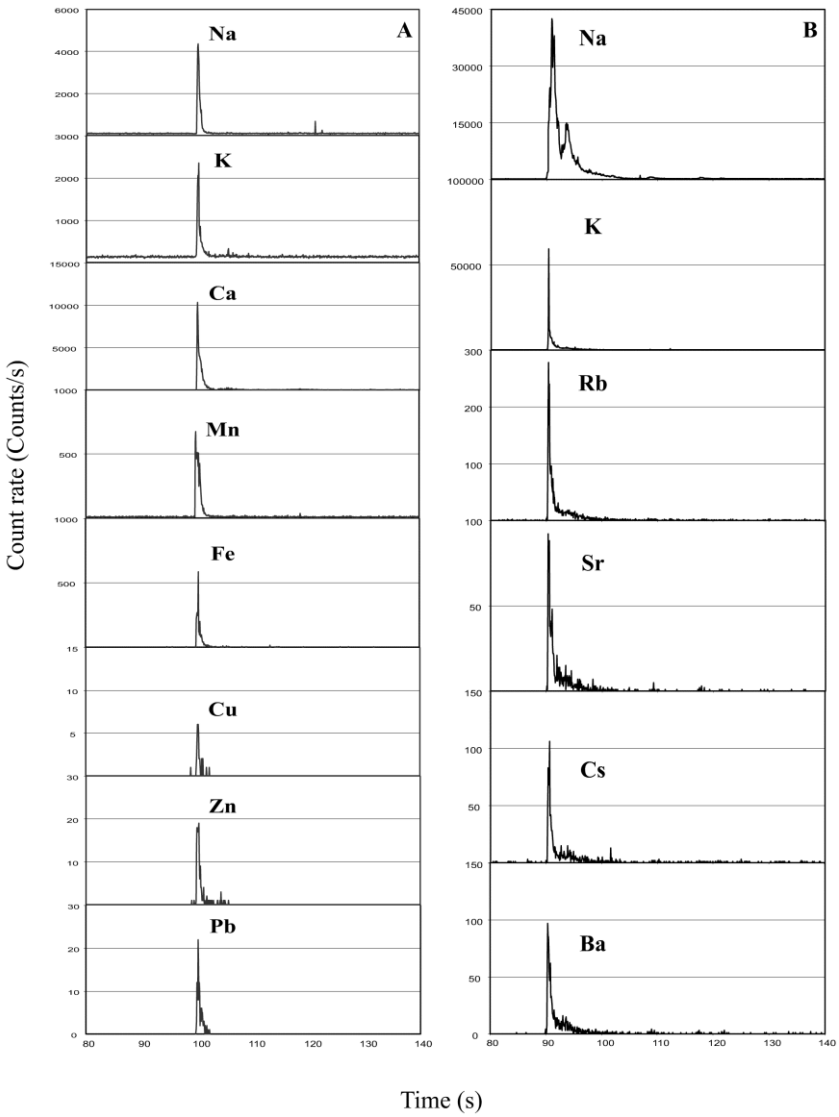

Figure 6.5 LA ICP MS signals obtained from Eloise fluid inclusions for the first (A) and the fifth (B) suite of analyzed elements. Fluid inclusions in samples 48178 (A) and 48170 (B).

The element ratios obtained from LA ICP MS analysis were converted to absolute element concentrations using value of Na as internal standard calculated using the charge-balance method described in section 5.2.1. The chlorinity was derived from the average salinity estimated from microthermometry. LA ICP MS analysis revealed that Na, K, Ca, Fe and Mn are the most abundant cations in multisolid fluid inclusions; therefore the following charge balance approximation was used (Allan, 2006):

$$m\mathrm{Cl} \approx m\mathrm{Na} + m\mathrm{K} + 2(m\mathrm{Ca} + m\mathrm{Fe} + m\mathrm{Mn})$$

LA ICP MS analysis also revealed that Na, K and Ca are the most abundant cations in halite-bearing fluid inclusions and the following charge balance approximation was used (Allan, 2006):

$$m\mathrm{Cl} \approx m\mathrm{Na} + m\mathrm{K} + 2m\mathrm{Ca}$$

The calculated Na values are around 90000 ppm and 63000 ppm for multisolid and halite-bearing fluid inclusions respectively.

6.3.2. Results and Discussion

Results of laser ablation analysis on 38 fluid inclusions (19 multisolid and 19 halite-bearing) for the first suite of elements and on 41 (17 multisolid and 24 halite-bearing) for the fifth suite of elements are reported in Table 6.3 and Appendix 6.1. Table 6.3 reports two different averages, one calculated using all the data including values below detection limit (in these cases the detection limit for the given element in the given inclusion was used for the calculation), the other calculated using only data above detection limits. In the following discussion averages quoted are calculated using all the data unless otherwise stated.

Both inclusion types are dominated by Na, K and Ca. Multisolid fluid inclusions have K concentrations ranging from around 3000 to 108000 ppm (average ~ 28000 ppm) and Ca concentrations between around 3000 and 87000 ppm (average ~ 37000 ppm) (Figures 6.6 and 6.7; Table 6.3). Halite-bearing fluid inclusions display K concentrations spanning between about 3000 and 66000 ppm (average ~ 27000 ppm) and Ca concentrations from approximately 9000 and 99000 ppm (average ~ 51000 ppm) (Figures 6.6 and 6.7; Table 6.3). Halite-bearing fluid inclusions in general have higher Ca concentrations and lower K/Ca ratios compared with multiphase fluid inclusions (Figures 6.7 and 6.8A; Table 6.3). K/Ca ratios for halite-bearing fluid inclusions are consistently <1 and range from 0.07 and 0.88 (Figure 6.8A and Table 6.3). Multisolid fluid inclusions display a wide range of K/Ca ratios that vary over one order of magnitude between 0.29 and 3 (Figure 6.8A and Table 6.3). Multisolid fluid inclusions are clearly distinct from halite-bearing inclusions based on the Mn and Fe concentrations. Multiphase fluid inclusions contain Fe in concentrations mostly between 10000 and 50000 ppm (average ~ 27000 ppm), and lower Mn concentrations mostly

between 1000 and 30000 ppm (average ~ 11000 ppm) (Figures 6.6 and 6.7; Table 6.3). Halite-bearing fluid inclusions have both Mn and Fe concentrations mostly between 1000 and 10000 ppm and similar averages for the two elements around 5300 ppm (Figures 6.6 and 6.7; Table 6.3). Mn/Fe ratios are around 1 for the majority of halite-bearing fluid inclusions, whereas most multiphase fluid inclusions have Mn/Fe ratios below 1 mostly between 0.05 and 0.9 (Figure 6.8B and Table 6.3).

Barium concentrations range from 50 to 9000 ppm (average ~ 3600 ppm) for multisolid fluid inclusions (Figures 6.6, 6.7 and 6.8C; Table 6.3), whereas Ba values for halite-bearing fluid inclusions are below detection limits in the 36% of cases. Considering all values, Ba concentrations range from around 20 to 1500 ppm (average ~ 400 ppm) for halite-bearing fluid inclusions (Figure 6.6 and Table 6.3). These values do not significantly vary excluding values below detection limit. Concentrations of Sr are similar for the two inclusions types and vary from around 10 to 1400 (average ~ 580 ppm) and from around 20 to 1600 ppm (average ~ 450 ppm) for multisolid and halite-bearing fluid inclusions respectively (Figures 6.6 and 6.7; Table 6.3).

Multisolid fluid inclusions display Rb concentrations between around 20 and 900 ppm (average ~ 400 ppm) (Figures 6.6 and 6.7; Table 6.3). Approximately 55% of Rb values are below detection limits for halite-bearing fluid inclusions. Rubidium concentrations vary between around 10 and 900 ppm (average ~ 300 ppm), similar to multisolid fluid inclusions (Figures 6.6 and 6.7; Table 6.3).

Table 6.3 Chemistry of fluid inclusions from the Eloise deposit determined with LA ICP MS analysis. Values in ppm.

Sample/ Analysis	Na	K	Ca	Mn	Fe	Cu	Zn	Pb	Analysis	K	Rb	Sr	Cs	Ba	K/Ca	Mn/Fe	Fe/Cu	Zn/Pb	Cu/Zn
Multisolid fluid inclusions																			
Sample 48164																			
B8	90000	20567	spike	6364	1533	*687*	2109	2506	A8	24586	209	488	73	5819		4.15	*2.23*	0.84	*0.33*
B12	90000	27928	57933	32671		*1792*	1922	1062	A2	28242	*921*	1223	*425*	9265	0.48			1.81	*0.93*
B13	90000	*10548*	15958	16362	33236	*671*	694	*487*	A9	37613	368	825	125	6220	*0.66*	0.49	*49.54*	*1.43*	*0.97*
B17	90000	29274	spike	11679	35404	2270	2881	spike	A10	*11883*	*427*	340	*149*	2363		0.33	15.60		0.79
B18	90000	12897	43750	12057	13427	spike	1318	425	A12	*4728*	212	809	195	3085	0.29	0.90		3.10	
B19	90000	3138	9495	1685	968	*151*	185	54	A13	*576*	*17*	173	16	1058	0.33	1.74	*6.39*	3.43	*0.82*
B20	90000	24661	63293	27327	spike	spike	2393	810	A14	23451	488	983	91	5509	0.39			2.96	
B22	90000	*13734*	18643	14014	42568	*984*	1375	313	A16	63176	857	1382	*231*	6622	*0.74*	0.33	*43.25*	4.39	*0.72*
									A17	69854	443	1237	*189*	9136					
									A19	34230	300	1035	*143*	9016					
Min		3138	9495	1685	968	151	185	54		576	17	173	16	1058	0.29	0.33	2.23	0.84	0.33
Max		29274	63293	32671	42568	2270	2881	2506		69854	921	1382	425	9265	0.74	4.15	49.54	4.39	0.97
Average		17843	34845	15270	21189	1093	1610	808		29834	424	850	164	5809	0.48	1.32	23.40	2.56	0.76
Average *		19744	34845	15270	21189	2270	1610	862		40165	411	850	100	5809	0.37	1.32	15.60	2.75	0.79
Stdev		9235	23167	10268	18220	789	893	818		22785	282	405	112	2908	0.18	1.48	21.66	1.25	0.23
Sample 48170																			
E1	90000	8500	10010	2529	53891	*57*	91	*105*	D10	37894	388	247	279	1544	0.85	0.05	*944.10*	*0.87*	*0.63*
E2	90000	54977	25393	7614	36420	*642*	1366	*893*	A18	16682	247	33	34	258	2.17	0.21	*56.74*	*1.53*	*0.47*
E3	90000	13645	19250	4460	44338	*302*	452	*601*	A17	12221	165	36	27	273	0.71	0.10	*146.92*	*0.75*	*0.67*
E4	90000	36828	56999	*4059*	9616	2542	1181	*2673*	D12	1908	30	7	10	53	0.65	*0.42*	3.78	*0.44*	2.15
E5	90000	*4169*	3326	*870*	6894	*266*	487	194	D13	4170	33	13	12	99	*1.25*	*0.13*	*25.92*	2.51	*0.55*
E8	90000	33911	53159	*8923*	45006	*2386*	2090	1603	D14	*21623*	*915*	217	*323*	*855*	0.64	*0.20*	*18.87*	1.30	*1.14*
E9	90000	48973	28444	5551	15437	*3345*	4624	1087	D16	16503	287	879	*97*	*684*	1.72	0.36	*4.61*	4.25	*0.72*
E11	90000	107739	86875	22728	34089	5612	5207	3872							1.24	0.67	6.07	1.34	1.08
E13	90000	spike	62025	19456	36558	*4015*	8155	4225								0.53	*9.10*	1.93	*0.49*
E14	90000	40851	13631	2716	11964	*765*	2717	*1254*							3.00	0.23	*15.65*	*2.17*	*0.28*
E15	90000	19918	66617	12312	39967	*1358*	1468	*1714*							0.30	0.31	*29.43*	*0.86*	*0.92*
Min		4169	3326	870	6894	57	91	105		1908	30	7	10	53	0.30	0.05	3.78	0.44	0.28
Max		107739	86875	22728	53891	5612	8155	4225		37894	915	879	323	1544	3.00	0.67	944.10	4.25	2.15
Average		36951	38703	8293	30380	1935	2531	1656		15857	295	204	112	538	1.25	0.29	114.66	1.63	0.83
Average *		32200	38703	7945	30380	2944	2531	1602		14896	192	204	72	445	1.25	0.31	4.93	2.27	1.62
Stdev		30226	27480	7138	16392	1810	2493	1388		12002	303	314	133	534	0.83	0.19	278.18	1.08	0.51
Total multisolid fluid inclusions																			
Min		3138	3326	870	968	57	91	54		576	17	7	10	53	0.29	0.05	2.23	0.44	0.28
Max		107739	86875	32671	53891	5612	8155	4225		69854	921	1382	425	9265	3.00	4.15	944.10	4.39	2.15
Average		28459	37341	11230	27136	1638	2143	1327		24079	371	584	142	3639	0.96	0.66	86.14	1.99	0.80
Average *		32254	37341	12470	27136	3474	2143	1468		28502	310	584	86	4021	0.96	0.74	8.49	2.53	1.34
Stdev		24784	25363	9046	17093	1554	1995	1245		19908	289	486	120	3466	0.76	0.99	231.56	1.20	0.43

Average *: average calculated based only on values above detection limit

Numbers printed in italics refer to values below detection, substituted by the actual detection limit for the specific element in the specific inclusion

Table 6.3 Continued

Sample/ Analysis	Na	K	Ca	Mn	Fe	Cu	Zn	Pb	Analysis	K	Rb	Sr	Cs	Ba	K/Ca	Mn/Fe	Fe/Cu	Zn/Pb	Cu/Zn
Halite-bearing fluid inclusions																			
Sample 48178																			
C1	63000	11441	57271	7714	9134	372	719	1102	A1	26087	830	1257	219	638	0.20	0.84	24.57	0.65	0.52
C2	63000	13530	54951	7808	7528	*403*	1522	1138	A4	5472	*86*	110	*38*	223	0.25	1.04	*18.68*	1.34	*0.26*
C3	63000	14126	53349	2444	3460	*536*	809	739	A3	1250	32	52	*13*	43	0.26	0.71	*6.45*	1.09	*0.66*
C4	63000	49805	spike	11935	10086	1634	3301	4688	A6	26573	890	1285	296	1493		1.18	6.17	0.70	0.49
C5	63000	44407	spike	10717	5442	*636*	2431	3635	A7	11070	425	784	145	671		1.97	*8.55*	0.67	*0.26*
C7	63000	20089	98801	4118	6926	1501	1154	*1716*	B1	1311	35	49	11	34	0.20	0.59	4.61	*0.67*	1.30
C9	63000	21314	spike	5289	6109	*2003*	1413	1837	B2	10178	419	657	112	833		0.87	*3.05*	0.77	*1.42*
C11	63000	52143	spike	4570	2830	*646*	2018	6514	B3	11143	461	1067	*146*	658		1.62	*4.38*	0.31	*0.32*
C13	63000	65926	spike	9437	8083	*1219*	1639	2643	B4	16413	570	991	202	1336		1.17	*6.63*	0.62	*0.74*
C14	63000	29293	spike	6961	10362	*1967*	1186	2098								0.67	*5.27*	0.57	*1.66*
Min		11441	53349	2444	2830	372	719	739		1285	32	49	11	34	0.20	0.59	3.05	0.31	0.26
Max		65926	98801	11935	10362	2003	3301	6514		14070	890	1285	296	1493	0.26	1.97	24.57	1.34	1.66
av		32208	66093	7099	6996	1092	1619	2611		7361	417	695	132	659	0.23	1.07	8.84	0.74	0.76
av*		32208	66093	7099	6996	1169	1619	2710		10585	458	695	164	659	0.23	1.07	11.79	0.75	0.77
Stdev		19362	21865	3038	2582	648	787	1832		4389	321	509	99	518	0.03	0.44	7.04	0.29	0.51
Sample 48076																			
C1	63000	40479	spike	8766	8023	*2932*	1876	*1554*	D1	*6103*	*239*	237	*113*	118		1.09	*2.74*	*1.21*	*1.56*
C2	63000	31195	72486	*3287*	3699	*1341*	894	*994*	D2	*7783*	*374*	196	*149*	*280*	0.43	*0.89*	*2.76*	*0.90*	*1.50*
C5	63000	25193	39554	*3150*	6204	*1299*	875	*1032*	D4	*1285*	*103*	95	*51*	35	0.64	*0.51*	*4.78*	*0.85*	*1.48*
C23	63000	*52470*	59873	*6566*	3668	*2606*	150	99	D6	11898	*234*	313	*117*	92	*0.88*	*1.79*	*1.41*	1.52	*17.34*
									D7	14070	*381*	235	*183*	333					
									D9	11937	170	327	37	741					
									D10	*3271*	*106*	356	*76*	*186*					
									D11	4437	*150*	105	*75*	*282*					
									D13	*5466*	*644*	170	*334*	*1020*					
Min		25193	39554	3150	3668	1299	150	99		1285	103	95	37	35	0.43	0.51	1.41	0.85	1.48
Max		52470	72486	8766	8023	2932	1876	1554		14070	644	356	334	1020	0.88	1.79	4.78	1.52	17.34
av		37334	57304	5442	5399	2044	949	920		7361	267	226	126	343	0.65	1.07	2.92	1.12	5.47
av*		32289	57304	8766	5399	–	949	99		10585	170	226	37	264	0.53	1.09		1.52	
Stdev		11890	16616	2721	2115	847	709	604		4389	175	94	91	327	0.22	0.54	1.39	0.31	7.91

Table 6.3 Continued

Sample/ Analysis	Na	K	Ca	Mn	Fe	Cu	Zn	Pb	Analysis	K	Rb	Sr	Cs	Ba	K/Ca	Mn/Fe	Fe/Cu	Zn/Pb	Cu/Zn
Halite-bearing fluid inclusions																			
Sample EWD6																			
A1	63000	3470	49496	999	633	*216*	136	*246*	B9	*643*	*21*	17	*7*	*29*	0.07	1.58	*2.94*	*0.55*	*1.58*
A2	63000	*7116*	20354	*983*	336	*359*	*444*	154	B10	*12395*	*506*	328	*150*	*427*	*0.35*	*2.92*	*0.94*	*2.88*	*0.81*
A3	63000	*26556*	73209	*3405*	1489	*1381*	*1707*	370	B12	15491	498	1623	206	626	*0.36*	*2.29*	*1.08*	*4.61*	*0.81*
A16	63000	*6905*	26455	*1090*	871	*499*	715	511	B13	*1825*	*37*	22	*20*	*75*	*0.26*	*1.25*	*1.74*	1.40	*0.70*
A17	63000	*4982*	9164	869	5147	*395*	774	221	B14	*2654*	*55*	106	*29*	*85*	*0.54*	0.17	*13.05*	3.51	*0.51*
									B16	319	*8*	26	*3*	*18*					
									B17	15912	331	1015	*81*	223					
Min		3470	9164	869	336	216	136	154		319	8	17	3	18	0.07	0.17	0.94	0.55	0.51
Max		26556	73209	3405	5147	1381	1707	511		15912	506	1623	206	626	0.54	2.92	13.05	4.61	1.58
av		9806	35735	1469	1695	570	755	300		7034	208	448	71	212	0.32	1.64	3.95	2.59	0.88
av*		3470	35735	934	1695	–	542	314		10574	414	448	206	425	0.07	0.87		2.45	
Stdev		9482	25605	1085	1976	465	589	141		7203	229	630	79	232	0.17	1.05	5.15	1.63	0.41
Total halite-bearing fluid inclusions																			
Min		3470	9164	869	336	216	136	99		319	8	17	3	18	0.07	0.17	0.94	0.31	0.26
Max		65926	98801	11935	10362	2932	3301	6514		26573	890	1623	334	1493	0.88	2.92	24.57	4.61	17.34
av		27392	51247	5269	5265	1155	1251	1647		8999	304	457	113	420	0.37	1.22	6.31	1.31	1.79
av*		30172	51247	6279	5265	1169	1271	1839		11473	424	457	154	506	0.29	1.04	14.59	1.10	0.77
Stdev		18755	24870	3462	3187	807	796	1697		7400	256	479	91	418	0.22	0.68	6.22	1.14	3.80

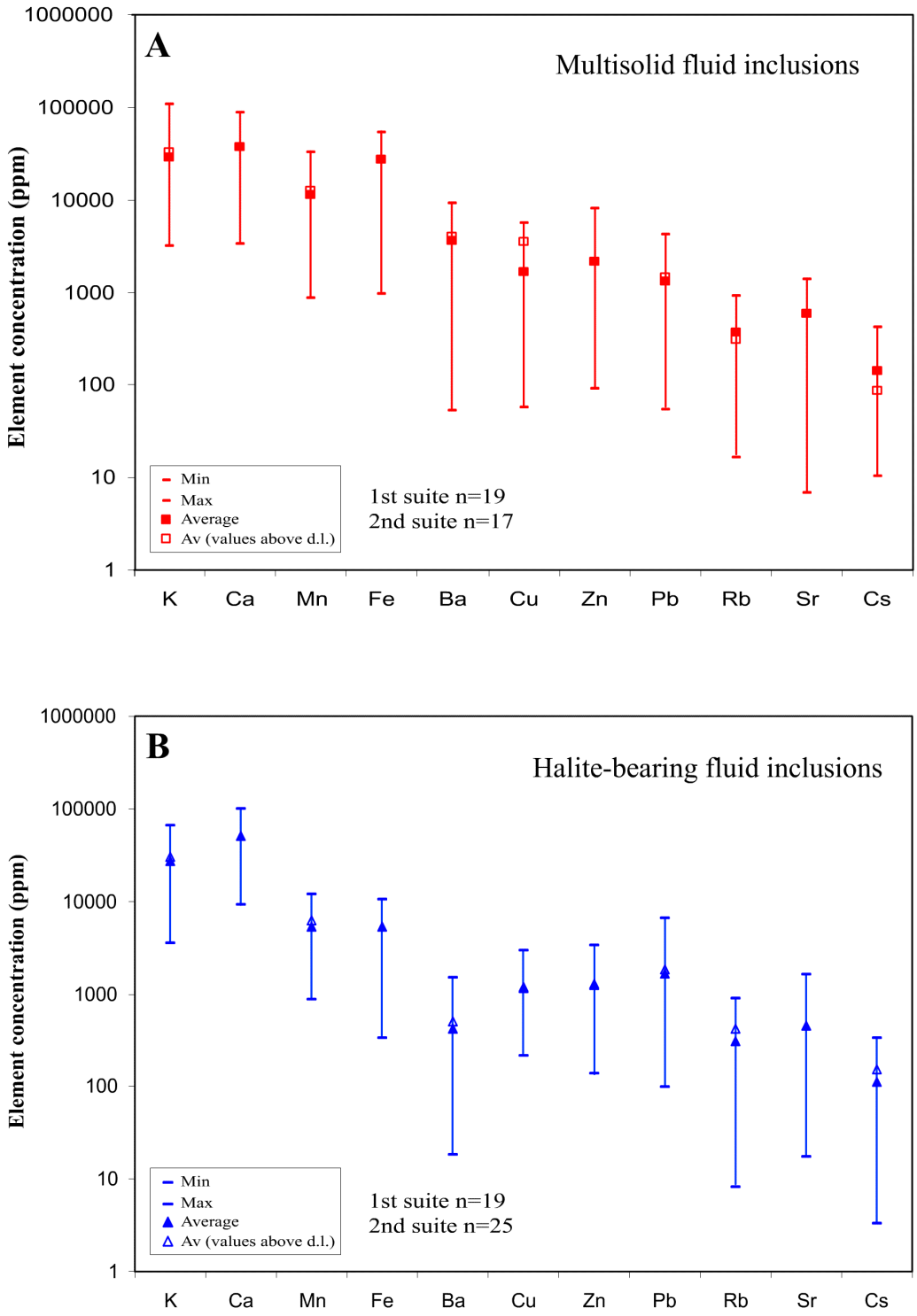

Figure 6.6 Diagram displaying minimum, maximum and average concentrations of major and trace elements for multisolid (A) and halite-bearing (B) fluid inclusions determined from LA ICP MS analysis. Bars represent the range of concentrations of each element in the fluid. Concentrations of K, Ca, Mn, Fe, Cu, Zn and Pb were measured in the first routine of analysis, whereas Ba, Sr, Rb and Cs were determined in the second routine of analysis.

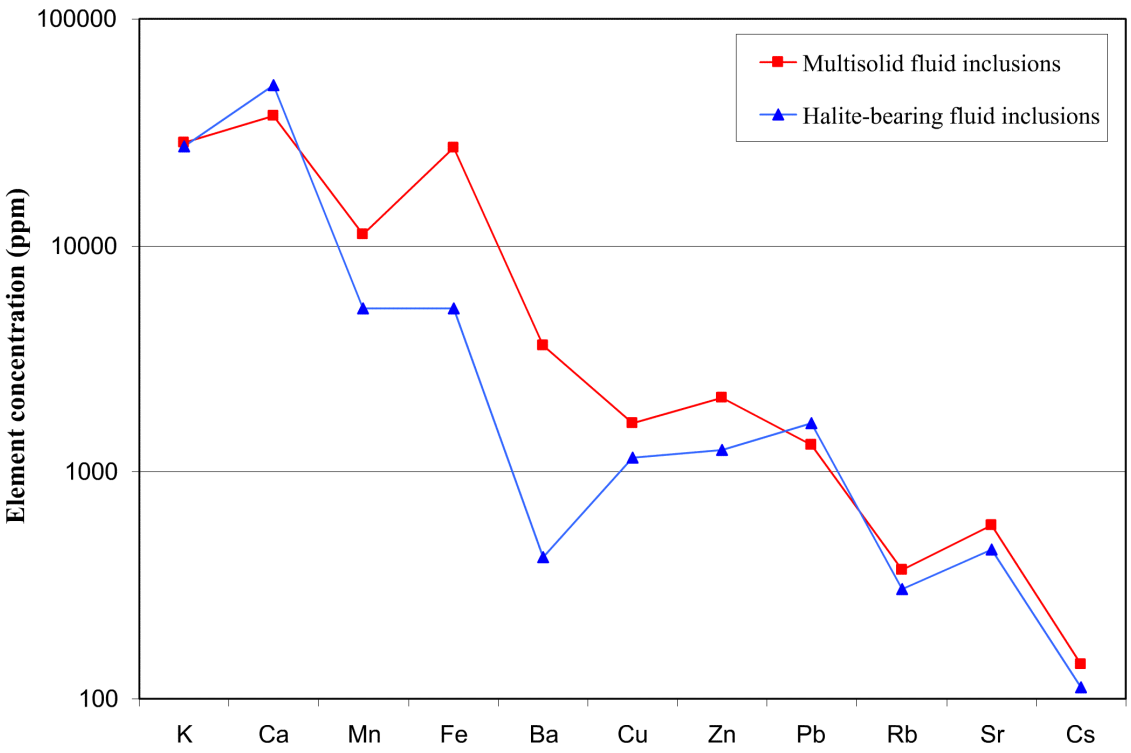

Figure 6.7 Average composition (calculated using all values including those below detection limits) of multisolid and halite-bearing fluid inclusions from the Eloise deposit determined using LA-ICP-MS analysis.

Approximately 40% and 70% of Cs values are below detection limits for multisolid and halite-bearing fluid inclusions respectively. Multisolid fluid inclusions display Cs concentrations mostly between 10 and 400 ppm (average ~ 150 ppm) (Figures 6.6 and 6.7; Table 6.3). Halite-bearing fluid inclusions display similar Cs concentrations compared to multisolid fluid inclusions spanning mostly from 10 to 300 ppm and with slightly lower average concentration around 100 ppm (Figures 6.6 and 6.7; Table 6.3). The range of concentrations and average values do not vary significantly excluding concentrations below detection limits.

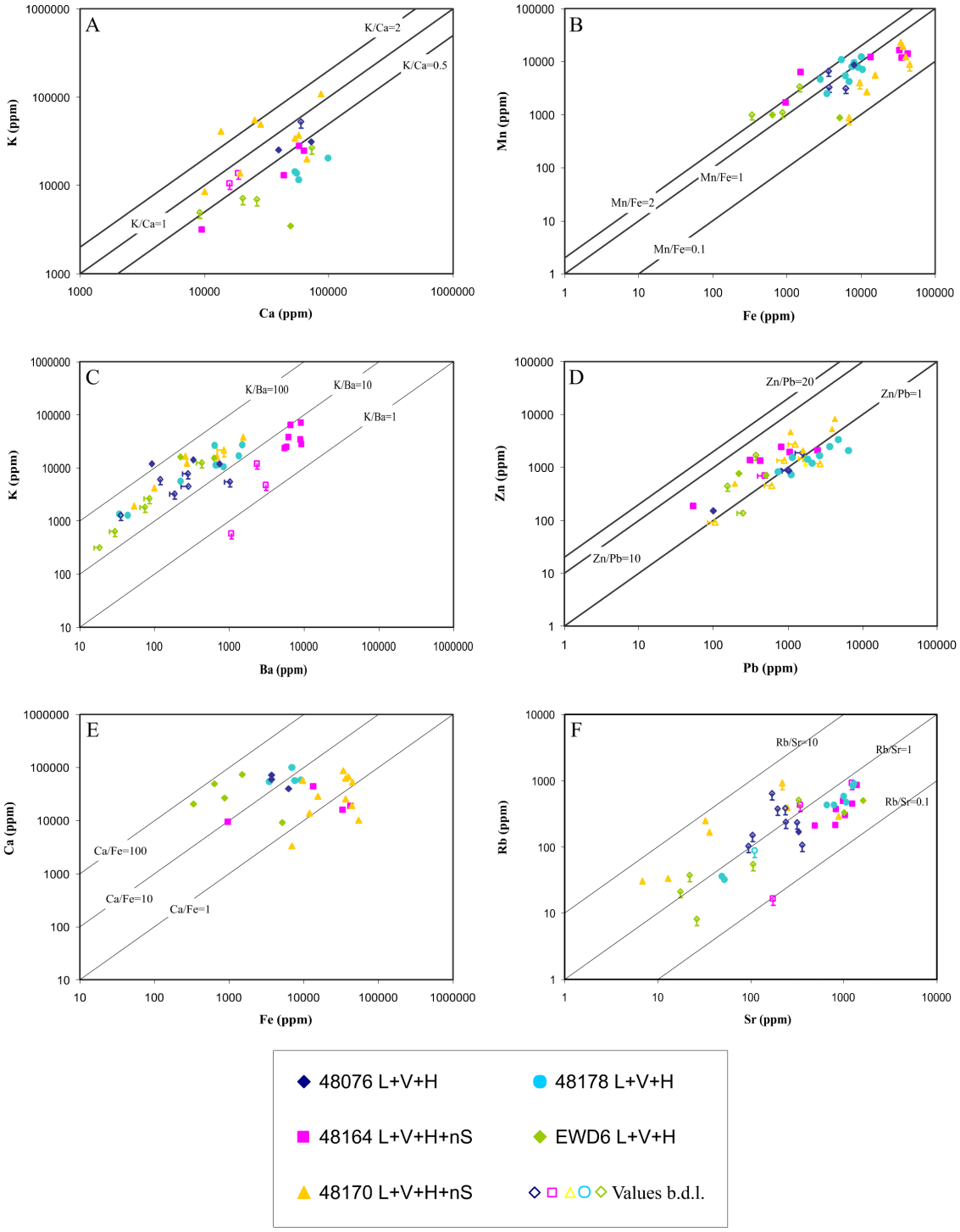

Figure 6.8 Plots of the concentrations of major and trace elements in fluid inclusions from the Eloise deposit. Open symbols refer to values below detection limit and bars indicate that the corresponding element is below detection limit.

Zn has the highest concentrations among the base metals with values ranging between about 100 and 8000 ppm (average ~ 2100 ppm) for multiphase fluid inclusions, and from around 100 to 3000 ppm (average ~ 1300 ppm) for halite-bearing fluid inclusions (Figures 6.6 and 6.7; Table 6.3). Copper concentrations are mostly below detection limits, around 75% and approximately 90% for multisolid and halite-bearing fluid inclusions respectively. When only considering values above detection limits, multiphase fluid inclusions display higher Cu concentrations (two values ~ 2500 ppm and one ~ 5500 ppm) compared with halite-bearing fluid inclusions (two values ~ 1500 ppm and one ~ 400 ppm) (Table 6.3). Cu/Zn values above detection limits are generally higher for multisolid (from ~ 0.8 to ~ 2.1) compared with halite-bearing fluid inclusions (from ~ 0.5 to ~ 1.3) (Table 6.3). Multisolid and halite-bearing fluid inclusions have 35% and 25% of Pb concentrations below detection limits respectively. Lead concentrations range from around 50 to 4000 ppm and from 100 to 6500 ppm for multisolid and halite-bearing fluid respectively (Figure 6.6 and Table 6.3). Average Pb concentrations are ~1400 ppm for multisolid fluid inclusions and slightly higher around 1600 ppm for halite-bearing fluid inclusions (Figure 6.7 and Table 6.3). Excluding values below detection limits, the range of concentrations for both inclusions types do not change, whereas Pb averages are slightly higher, ~ 1600 ppm and 1800 ppm for multisolid and halite-bearing fluid inclusions respectively (Table 6.3 and Figure 6.6). Zn/Pb ratios display similar range for both inclusion types spanning from 0.4 to 4.4 and from 0.5 to 4.6 for multisolid and halite-bearing fluid inclusions respectively (Figure 6.8D and Table 6.3). However, among the fluid inclusions with Zn/Pb ≤1, the majority has Pb values below detection limit implying higher Zn/Pb ratios, with the exception of the halite-bearing fluid inclusions in sample 48178, which consistently display Pb in the order of thousand of ppm (Figure 6.8D and Table 6.3).

The results indicate that multisolid fluid inclusions have higher absolute concentrations of all analyzed elements compared with halite-bearing fluid inclusions, with the exception of Ca and Pb (Figure 6.7). The most significant differences between the two types of inclusions are related to the enrichment in Fe, Mn and Ba in multisolid fluid inclusions compared to halite-bearing fluid inclusions (Figures 6.6 and 6.7). Multisolid fluid inclusions also have generally lower Pb and Ca concentrations compared with halite-bearing fluid inclusions (Figures 6.6 and 6.7). As a consequence multisolid fluid inclusions display generally higher K/Ca and Zn/Pb ratios and lower Mn/Fe and Ca/Fe ratios compared with halite-bearingfluid inclusions (Figures 6.8A-E). Concentrations of Sr, Rb and Cs vary within similar ranges for the two types of inclusions (Figures 6.6, 6.7 and 6.8F).

6.4. Comparison of fluids from Eloise deposit with fluids associated to the Suicide Ridge barren breccia pipe

In this section fluid inclusions from the Eloise deposit are compared with fluid inclusions related to the barren SRBP. The purpose of the comparison is to identify possible differences in the chemistry of the inclusions that may explain the formation of barren versus mineralized hydrothermal systems. The main fluid inclusion types associated with the two systems are compared in Table 6.4 together with a summary of the main results from microthermometry.

The main difference between Eloise and the SRBP is the absence in the latter of multisolid, high-temperature, high-salinity fluid inclusions (Table 6.4). Both systems are characterized by abundant secondary liquid-rich dominantly halite-bearing (L+V±H)

fluid inclusions. Eutectic temperatures for halite-bearing fluid inclusions span over a wide range in both systems from -55 to -34°C and from -69.7 to -29.1°C for Eloise and SRBP respectively. However, the majority of these inclusions both at Eloise and in the SRBP display temperatures of first melting around and below -50°C indicating fluids of dominantly sodic (-calcic) composition. The inclusions display similar homogenization temperatures, although slightly lower, from 121 to 315°C for Eloise fluid inclusions and from 109.2 to 360°C for the SRBP. Salinities for these inclusions are also comparable although the SRBP fluid inclusions display a wider range (22.4 to 45.4 wt% NaCl + $CaCl_2$ equiv.) compared to Eloise fluid inclusions (32 to 40.4 wt% NaCl + $CaCl_2$ equiv.). Liquid-rich secondary fluid inclusions are common in both systems. At Eloise liquid-rich fluid inclusions generally have higher eutectic temperatures, consistently lower homogenization temperatures and a wider range of salinities compared with liquid-rich fluid inclusions from the SRBP (Table 6.4). Both systems contain carbonic inclusions but these are less common at Eloise and more abundant at the SRBP. The SRBP also locally contains high salinity mixed brine-carbonic (Chapter 4) fluid inclusions that were not observed at Eloise.

LA ICP MS analysis was carried out on multisolid and halite-bearing fluid inclusions from the Eloise deposit (Section 6.3; Figures 6.6-6.8, Table 6.3 and Appendix 6.1) and on type III sodic (-calcic) fluid inclusions from the SRBP (Section 5.3; Figures 5.3-5.6, Tables 5.1-5.2 and Appendix 5.2) and results are summarized in Table 6.5. Average values for the three types of inclusions analyzed are plotted in Figure 6.9.

Table 6.4 Comparison of the main fluid inclusion features from the Eloise deposit and the SRBP. The main difference between the two systems is the absence of high temperature, ultrasaline brines at the SRBP compared with the Eloise deposit.

		Multiphase	Liquid-rich - halite-bearing	Liquid-rich	Carbonic
Eloise fluid inclusions		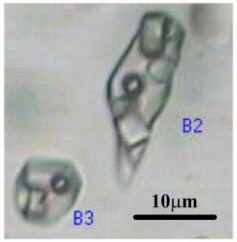	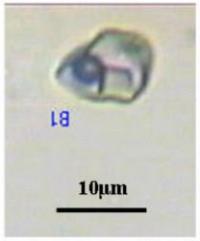	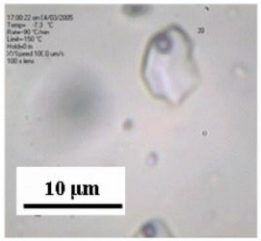	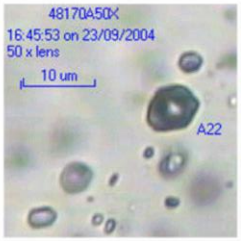
	Abundance	Abundant	Abundant/Common	Common	Rare
	Phases	L+V+nS (n= 0-5)	L+V±H	L+V	CO_2(L-V) +H_2O
	Th	101 to 540 °C	121 to 315 °C	101 to 145 °C	
	Salinity	34 to 68 (wt% NaCl + CaCl2 eq)	32 to 40 (wt% NaCl + CaCl2 eq)	4 to 17 (wt% NaCleq)	
Suicide Ridge Beccia Pipe fluid inclusions		**Liquid-rich - halite-bearing**	**Liquid-rich**	**Carbonic**	
		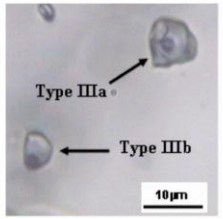	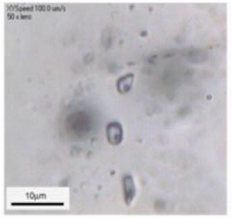	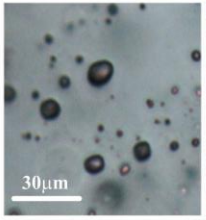	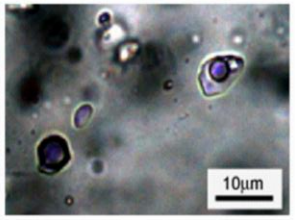
	Abundance	Abundant	Common	Abundant/Common	Common/Rare
	Phases	L+V±H	L+V	CO_2 (L)	CO_2 (L) ± H_2O ± H
	Th	109 to 360 °C	144 to 245 °C	–17.5 to -30.5 °C	T Dec 249 to 462 °C
	Salinity	22 to 45 (wt% NaCl + CaCl2 eq)	9 to 13 (wt% NaCl)		22 to 39 (wt% NaCl eq.)

The results show significant differences in terms of absolute element concentrations between barren and mineralized systems. Fluids inclusions related to the SRBP have in general considerably lower concentrations of all elements compared with fluid inclusions from Eloise, with the exception of Ba whose average concentration is higher than that in halite-bearing fluid inclusions from Eloise (Figure 6.9). Fluid inclusions associated with the SRBP and multisolid fluid inclusions from Eloise display a similar range of K/Ca ratios, while halite-bearing fluid inclusions from Eloise display generally lower K/Ca ratios, mostly below 0.5 (Tables 6.3, 6.5 and Figure 6.10A). Fluid inclusions from the SRBP have a very wide range of Mn/Fe ratios with quite a few values ≥ 2, opposed to fluid inclusions from Eloise that generally display narrower range of Mn/Fe values mostly around 1 for halite-bearing and lower between 0.05 and 0.67 for multisolid fluid inclusions (Figure 6.10B). However, a comparison of Mn/Fe between barren and deposit fluid inclusions is difficult since the majority of fluid inclusions from the SRBP have Mn below detection limit implying generally lower Mn/Fe ratios. The inclusions form three distinct groups in a Fe versus Ca plot, with multisolid inclusions having higher Fe and lower Ca/Fe ratios compared to the halite-bearing and the SRBP fluid inclusions that display a similar range of Fe content and Ca/Fe ratios (Figure 6.10C). Fluid inclusions from the SRBP have generally lower Ca concentrations compared to fluid inclusions from Eloise (Figures 6.9, 6.10C; Table 6.5). Ba shows important differences in concentrations between the different inclusions. Fluid inclusions from the SRBP have higher Ba concentrations than halite-bearing but lower than multisolid fluid inclusions. Values of Ba for single inclusions can be compared with K, which was measured in almost all sets of analysis. Fluid inclusions from the SRBP and halite-bearing inclusions from Eloise display a similar range of K/Ba ratios, mostly between 10 and 100, although the latter display a narrower range of

K/Ba values compared with the former (Figure 6.10D). Multisolid fluid inclusions have lower K/Ba ratios, dominantly between 1 and 10, compared with the other inclusions due to their relative enrichment in Ba. Fluid inclusions from the SRBP appear more enriched in Zn than Cu and Pb compared with fluid inclusions from the Eloise deposit, displaying mostly higher Zn/Cu and Zn/Pb ratios than the latter (Figures 6.9, 6.10E and F).

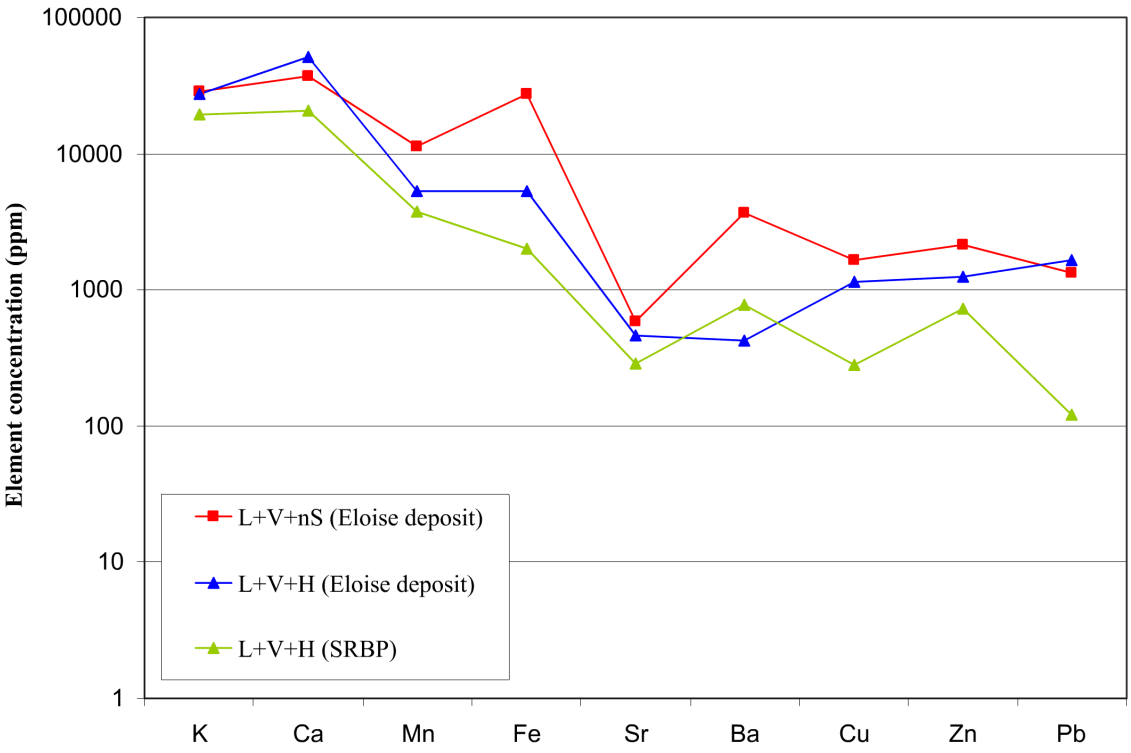

Figure 6.9 Comparison between average fluid inclusions composition of fluid inclusions from the Eloise deposit and from the SRBP determined from LA-ICP-MS analysis.

Table 6.5 Average, minimum and maximum composition of fluid inclusions from the Eloise deposit and from the SRBP. Values in ppm.

	K	Ca	Mn	Fe	Sr	Ba	Cu	Zn	Pb	K/Ca	Mn/Fe	Zn/Pb	Cu/Zn
L+V+nS (Eloise deposit)													
Min	3138	3326	870	968	7	53	57	91	54	0.29	0.05	0.44	0.28
Max	107739	86875	32671	53891	1382	9265	5612	8155	4225	3.00	4.15	4.39	2.15
Average	28459	37341	11230	27136	584	3639	1638	2143	1327	0.96	0.66	1.99	0.80
Average*	32254	37341	12470	27136	584	4021	2941	2143	1468	0.96	0.74	2.53	1.34
Stdev	24784	25363	9046	17093	486	3466	1554	1995	1245	0.76	0.99	1.20	0.43
L+V+H (Eloise deposit)													
Min	3470	9164	869	336	17	18	216	136	99	0.07	0.17	0.31	0.06
Max	65926	98801	11935	10362	1623	1493	2932	3301	6514	0.88	2.92	4.61	3.82
Average	27392	51247	5269	5265	457	420	1155	1251	1647	0.37	1.22	1.31	1.48
Average*	30172	51247	6279	5265	457	506	1169	1271	1839	0.29	1.04	1.10	1.57
Stdev	18755	24870	3462	3187	479	418	807	796	1697	0.22	0.68	1.14	1.08
L+V+H Suicide Ridge breccia pipe													
Min	7107	8982	142	108	81	41	20	102	13	0.40	0.10	1.48	0.57
Max	41373	49044	36085	7875	825	3467	1048	2036	541	3.03	3.64	26.32	27.68
Average	19429	20590	3734	2013	286	782	282	722	121	1.05	1.53	8.17	4.21
Average*	18694	20590	2484	2106	286	814	349	772	147	1.01	1.29	7.01	5.26
Stdev	7855	8612	5968	1933	201	814	231	529	126	0.53	1.15	5.17	5.37

Average *: average calculated based only on values above detection limit

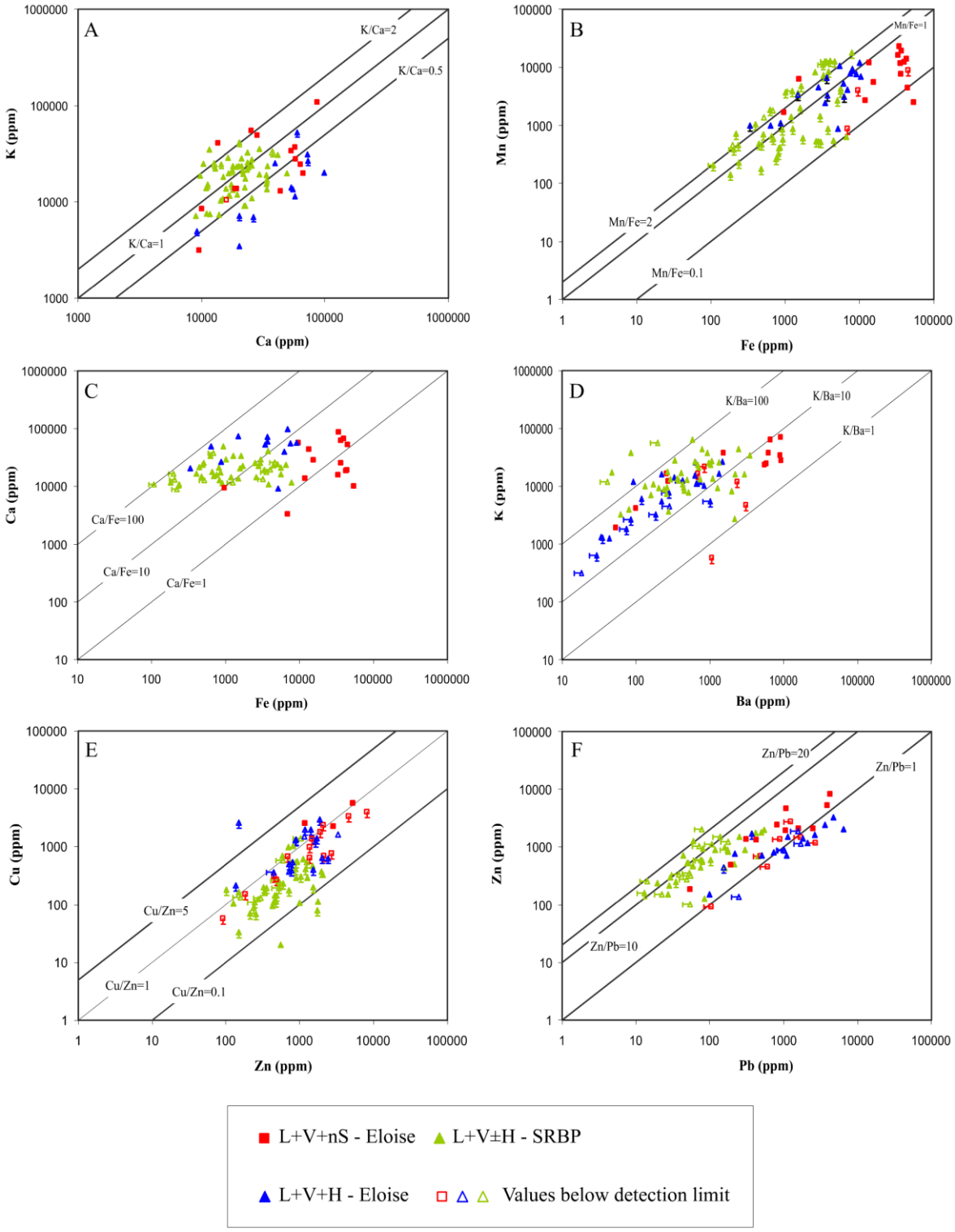

Figure 6.10 Plots of the concentrations of major and trace elements in fluid inclusions from the Eloise deposit and from the SRBP. Open symbols refer to values below detection limit and bars indicate that the corresponding element is below detection limit.

6.5. Summary

Results from LA ICP MS analysis of fluid inclusions from the Eloise Cu-Au deposit have shown that both multisolid and halite-bearing fluid inclusions contain high concentrations of Na, K, Ca, Fe and Mn. Among the base metals Zn is the most abundant, followed by Cu and Pb. Multisolid fluid inclusions generally have higher absolute element concentrations compared to halite-bearing fluid inclusions for all elements with exception of Ca and Pb. The most significant differences between the two types of inclusions are related to the general enrichment in Fe, Mn and Ba and to the lower Pb concentrations of multisolid fluid inclusions compared with halite-bearing fluid inclusions. These differences result in generally higher K/Ca ratios and lower Mn/Fe and Ca/Fe values of multisolid compared with halite-bearing fluid inclusions. Multisolid fluid inclusions are in general more enriched in Zn and Cu and depleted in Pb compared with halite-bearing fluid inclusions. The high Pb concentration of halite-bearing fluid inclusions results in lower Zn/Pb ratios for these inclusions compared to multisolid fluid inclusions, whereas the Cu/Zn ratios are similar for both inclusion types.

The main difference between fluids associated with the mineralized Eloise system and with the SRBP is the absence in the latter of high temperature, high salinity multisolid fluid inclusions. Halite-bearing fluid inclusions from the two systems display similar ranges in salinity and homogenization temperatures. LA ICP MS analysis show that fluid inclusions from the SRBP have lower absolute element concentrations compared to Eloise fluid inclusions, with the exception of Ba which has lower concentrations in halite-bearing fluid inclusions from Eloise. Fluid inclusions from the SRBP display a range K/Ca ratios similar to multisolid fluid inclusions from Eloise,

generally higher than halite-bearing fluid inclusions from Eloise, and a general enrichment in Zn compared to Cu and Pb, displaying mostly higher Zn/Cu and Zn/Pb ratios than fluid inclusions from Eloise.

Chapter 7

Chapter 7 - Part I Discussion

7.1. Introduction

This chapter concludes the first part of thesis that deals with the geology, fluid characteristics and genesis of the Suicide Ridge Breccia Pipe (SRBP). The chapter is organised in three main sections: 1) in the first section the genesis and evolution of the SRBP is discussed on the basis of breccia characteristics associated with the SRBP; 2) in the second section the characteristics of fluids associated with the Eloise Cu-Au deposit are discussed together with possible implications for the genesis of the deposit; and 3) in the final section fluids from the SRBP are compared with other regional fluids and with fluids from IOCG deposits and granites in the Cloncurry district.

7.2. Genesis of the Suicide Ridge Breccia Pipe

The breccia in this study is characterized by fragments of variable size, degree of rounding, although mostly rounded, and composition that includes dominant calc-silicate clasts of the Corella formation that underlie rocks of the Soldiers Cap Group that host the pipe; rocks of the Soldiers Cap Group are rarely observed as clasts in the breccia (Chapter 3). Together all these features, and in particular the abundance of calc-silicate clasts of the underlying Corella formation, are indicative of a dominant upward transport of the fragments (McCallum, 1985; Taylor and Pollard, 1993; Oliver et al., 2006), which is commonly explained as the result of sudden explosive release of

expanding high pressure fluids (e. g. Taylor and Pollard, 1993). High fluid pressure gradients may be generated during the emplacement and crystallization of hydrous magma in subvolcanic environments by exsolution of an aqueous fluid phase as a consequence of second boiling process (H_2O-saturated melt → crystal + H_2O vapor) and subsequent decompression (Burnham, 1985). Alternatively, fluid overpressuring can be produced by the interaction of magma and an external source of water, in which the magma may directly interact with fluid or solely act as a heat source (Sillitoe, 1985). The hypothesis of a direct involvement of the magma in the brecciation event at the SRBP is supported by the occurrence of small volumes of intrusive rocks as breccia clasts (cf Sillitoe, 1985). Furthermore, the granite locally displays fragmentation and brecciated and lobate margins, as also documented by Marshall (2003) and Oliver et al. (2006), suggesting that the magma was introduced into the pipe when it was not completely solidified and that its formation was broadly synchronous with the brecciation event.

The granite breccia fragments display mineralogical compositions and textures typical of pegmatites. These rocks are characterized by a very simple mineralogy that consists almost exclusively of albite and quartz, indicative of a highly differentiated system. The granites display a variety of textures including layered bodies, graphic granite, granophyric quartz-albite intergrowth and granitic textures. Similar textures were described elsewhere in the district in intrusive complexes (Tolman, 1998; Perring et al., 2000), in breccias (Marshall, 2003) and in intrusion carapaces (Mark and Foster, 2000). Alternating nearly monomineralic albite- and quartz-rich layers have been interpreted as the result of episodic release of aqueous fluid, that causes isothermal oscillation in the compositional location of the albite-quartz cotectic, due to overpressure (Jahns and Tuttle, 1963a; London, 1992; London, 2005). Experimental

work on crystal growth (Lofgren and Donaldson, 1975; Fenn, 1977; Swanson and Fenn, 1986; London, 1992) showed that the shape of quartz and feldspar crystals is strongly dependent on the degree of undercooling (ΔT), and cooling rate ($\Delta T/\Delta t$). Euhedral crystals normally develop with a low degree of undercooling and low cooling rate, while a larger degree of undercooling and a high cooling rate are required to produce more complex shapes such as dendritic, curved, branching or skeletal crystals. Undercooled conditions may normally be linked to the rapid cooling following the emplacement of a magmatic body (Drever and Johnston, 1957; Lofgren and Donaldson, 1975). Alternatively, such conditions may be induced by increasing the liquidus temperature of a water-bearing magma above its actual temperature either by a change in the water content or by a change in the confining pressure (Jahns and Tuttle, 1963b; Jahns and Burnham, 1969; Lofgren and Donaldson, 1975). In SRBP granite clasts, the pressure variations are suggested by the variable density of primary and pseudosecondary CO_2 fluid inclusions occurring within the magmatic-hydrothermal textures. Recorded pressure values are variable for both inclusions types indicating pressure fluctuations, and suggest a general pressure drop moving from primary to pseudosecondary fluid inclusions. Volatile solubility in melts is largely dependent on pressure and in particular a pressure decrease may have caused the magma to become volatile-saturated and as a consequence to release a fluid phase. The latter would have had the effect to increase the liquidus temperature of the water-bearing magma above its actual temperature, again generating undercooled conditions. However, the presence of abundant primary CO_2 inclusions indicates that the magma contained CO_2 in addition to water. The abundance of CO_2 fluid inclusions observed in granite clast samples contrasts with the low CO_2 solubility in silicate melts (Holloway, 1976). CO_2 solubility in magmas depends primarily on their composition, being generally higher for mafic

magmas compared to felsic magmas (Lowenstern, 2001). The solubility of CO_2 in felsic magmas is diversely affected by variations in pressure and temperature, increasing linearly with pressure and decreasing as the temperature increases (Fogel and Rutherford, 1990; Blank and Brooker, 1994; Lowenstern, 2000; Lowenstern, 2001). However, in general temperature variations have a much smaller impact on CO_2 solubility compared to pressure and melt composition (Blank and Brooker, 1994; Lowenstern, 2000; Lowenstern, 2001). The solubility of CO_2 is also strongly dependent on the composition of the volatile phase. In general the addition of other components such as H_2O to a CO_2-rich melt causes a decrease of CO_2 solubility (Lowenstern, 2000; Lowenstern, 2001). CO_2-only fluid inclusions at the SRBP are sometimes associated with CO_2-rich brine fluid inclusions of unclear origin that may represent later fluids exsolved from the melt (see below) and indicate that an aqueous phase was present in addition to CO_2. Furthermore, mixed CO_2- brine inclusions are interpreted as the major contributor to the halogen and anionic composition of fluids in the granite clasts that crush leach analysis revealed being enriched in F and SO_4 (Chapter 5). The presence of these volatile phases may therefore have contributed to lower the CO_2 solubility in the melt at the SRBP. Pressure is a critical factor controlling not only the solubility of the fluid phase but also the composition and evolution of fluid exsolved from a magma (Thompson et al., 1999; Baker and Lang, 2001). Baker and Lang (2001) observed that the composition of fluid in intrusion-related gold deposits varied as a function of the depth of emplacement of the magma with deeper systems containing dominantly low salinity CO_2-rich aqueous inclusions and shallower systems being dominated by immiscible brine and CO_2-rich vapors. They inferred that the depth of emplacement of the magma controlled the composition of the exsolved fluid due to the lower solubility of CO_2 compared with H_2O in felsic magmas. CO_2 is in fact approximately ten times

less soluble than H_2O (Webster and Holloway, 1988; Fogel and Rutherford, 1990; Blank et al., 1993) supporting the idea that when a magma reaches volatile saturation, the first fluid exsolved must be CO_2 (Nabelek and Ternes, 1997). This is consistent with the formation of early primary CO_2 fluid inclusions observed at the SRBP. However, the release of CO_2 leaves the magma enriched in H_2O with the effect of lowering the liquidus temperature of the melt (Nabelek and Ternes, 1997). Therefore, undercooling due to an increase of the liquidus temperature of the magma above its actual temperature is not supported at least in this phase of the magma evolution. Magmas eventually become saturated in H_2O and later exsolved fluid will progressively become more saline and H_2O-rich (Nabelek and Ternes, 1997; Baker and Lang, 2001). Mixed CO_2-rich aqueous and brine inclusions are sometimes associated with CO_2-only fluid inclusions at the SRBP and may represent later fluids exsolved from the melt. At this stage the release of water from the magma would have caused undercooling conditions followed by cyclic release of water due to undercooling conditions. Therefore, the observed textures in this study are likely the result of combined variations in pressure and in volatile content of the melt. Equigranular textures likely formed by equilibrium crystallization of fluid under-saturated melts and layered textures, graphic granite and granophyric quartz-albite intergrowth formed from a fluid-saturated melt due to pressure variations combined with exsolution of a fluid phase.

This model is in agreement with the model proposed by Burnham (1985), however, Burnham's model was developed for shallow systems in subvolcanic environments, while iron oxide copper gold deposits and associated breccia systems formed deeper in crust, about 10 km for some Cloncurry deposits (Williams et al., 2005). The SRBP is estimated to have formed at depth exceeding 10 km based on metamorphic phase relationships within the contact aureole of the Saxby granite

(Pattison et al., 2002; Oliver et al., 2006; Rubenach et al., 2007) and fluid inclusion data presented here. In shallow systems brecciation occurs in response to overpressuring generated by the release of an aqueous phase from the crystallizing magma (Burnham, 1985). In deeper systems such as the SRBP the volatile phase exsolved from the magma dominantly consists of CO_2 at least in the initial phases of magma crystallization (e.g. Baker and Lang, 2001; Nabelek and Ternes, 1997). Evidence provided in this study strongly indicates that high fluid pressure and consequent brecciation in this context was generated by volume expansion of CO_2 released from the crystallizing magma. A similar model was also invoked by Oliver et al. (2006) for the formation of breccia pipes in the Cloncurry district and is analogous to models proposed for kimberlite pipe formation (Wilson and Head, 2004). Collectively all these observations support an origin of the breccia pipe due to fluid overpressuring generated by release of fluids during the cooling and crystallization of a magmatic body (Figure 7.1).

The estimated pressures for primary CO_2 fluid inclusions vary from 3.6 to 4.7 kbar at 540°C, the estimated temperature of trapping for primary inclusions (Chapter 4, Figure 4.11). The estimated pressure for pseudosecondary CO_2 fluid inclusions vary from 1.3 to 3.7 kbar at 540°C (Chapter 4, Figure 4.11). Pressures indicated by primary CO_2 inclusions (~ 4.2 kbar) mostly exceed the lithostatic independent pressure obtained for the contact aureole of the Saxby Granite (~ 3kbar; Rubenach et al., 2007), whereas the average pressure for pseudosecondary CO_2 fluid inclusions at 540°C is 2.7 kbar, similar to the lithostatic pressure value obtained in the contact aureole (Chapter 4, Figure 4.11). The pressure cycling recorded in the granite clasts was responsible for the formation of the observed magmatic-hydrothermal textures and at some point the fluid overpressuring likely initiated the brecciation (Figure 7.1).

Oliver et al. (2006) suggested that CO_2 in the Cloncurry district may have been

sourced from mantle-derived magmas (cf Touret, 1992; Touret and Huizenga, 1999). Evidence of mantle activity during the emplacement of the Williams-Naraku Batholiths is provided by the occurrence of mafic magmas and its simultaneous emplacement with felsic intrusions in igneous complexes throughout the Cloncurry district (Blake, 1987; Mitchell, 1993; Pollard et al., 1998; Mark, 2001). Furthermore, processes such as mixing and mingling between mafic and felsic magmas have been indicated as frequent mechanisms for generating eruptions in felsic magmas (Sparks and Walker, 1977; Folch and Marti, 1998). Alternatively, CO_2 may have been sourced by partial melting and assimilation of carbonate-bearing crustal rocks (Lowenstern, 2001). In a recent study, Kendrick et al. (Kendrick et al., 2007a) determined halogen and noble gas signature of fluid inclusions related to regional albitization (Figure 7.2; Section 7.4.1). CO_2 fluid inclusions display noble gas data consistent with a dominant metamorphic origin for CO_2 and were likely sourced from devolatilization of calcite-rich calc-silicate rocks (Kendrick et al., 2007a).

The origin of mixed brine-CO_2 fluid inclusions is uncertain. Problems in the interpretation of these inclusions arise from difficulties obtaining good microthermometric data due to their complex composition, tendency to decrepitate before complete homogenization and for halite-bearing CO_2-brine fluid inclusions their rarity. Possible origins for these inclusions include unmixing of an original H_2O-CO_2-NaCl fluid (Beardsmore, 1992; Adshead, 1995; Perring et al., 2000; Pollard, 2001; Fu et al., 2003; Mustard et al., 2004), fluid mixing (e.g. Fu et al., 2003) of CO_2 with aqueous brine fluids and trapping of a heterogeneous fluid. As above stated, mixed CO_2-rich aqueous and brine inclusions are sometimes associated with CO_2-only fluid inclusions at the SRBP and may represent later fluids exsolved from the melt. This has important implications for the genesis of the SRBP as the evolution of the exsolving fluids from

CO_2-rich to aqueous-rich and possibly the unmixing of CO_2 from the aqueous phase may have provided additional overpressure driving the brecciation. Pollard (2001) inferred that unmixing of H_2O-CO_2-NaCl±$CaCl_2$-KCl magmatic fluids was the process dominantly responsible for the formation of sodic (-calcic) alteration in the Cloncurry district. The high Na concentrations needed for the albitization are provided by CO_2-rich fluids that contain higher Na/(Na + K) ratios compared to Cl-bearing fluids (Iiyama, 1965; Pollard, 2001). Therefore, when unmixing occurs due to temperature and/or pressure decrease (Bowers and Helgeson, 1983) the aqueous fluid has a Na/(Na + K) ratio higher than the equilibrium value of an unmixed Cl-bearing fluid (Pollard, 2001). Consequently, to re-establish equilibrium conditions the aqueous fluid needs to precipitate Na producing albite alteration (Pollard, 2001). In Pollard's model the volume expansion generated by the release and unmixing of magmatic fluid is inferred as a likely mechanism to cause brecciation, whereas later aqueous fluids generated from the unmixing of the early magmatic fluids are interpreted to be responsible for the albite alteration (Pollard, 2001).

At the SRBP there is evidence of exsolution of magmatic CO_2 fluids and of a later evolution of these fluids to more H_2O-rich compositions and the overpressuring generated by their release is interpreted as the cause of brecciation. However, these fluids are unrelated to the later sodic (-calcic) fluid inclusions responsible for albitization at the SRBP (Figure 7.1). Petrographic and cathodoluminescence analysis clearly linked abundant sodic (-calcic) fluid inclusions to the later influx of fluids that produced widespread pervasive albitic alteration at the SRBP system following the brecciation event (Chapters 3 and 4). Unmixing of a H_2O-CO_2-NaCl fluid would have produced the contemporaneous trapping of two distinct types of inclusions characterized by similar homogenization temperature but contrasting density (e.g. lower

density vapor-rich inclusions and higher density liquid-rich inclusions) and homogenization behavior with one type homogenizing into the liquid and the other into the vapor (Ramboz et al., 1982; Hagemann and Brown, 1996). At the SRBP unmixing of a H_2O-CO_2-NaCl fluid is not supported by the fluid inclusions paragenesis, as sodic (-calcic) inclusions are secondary and clearly postdate the entrapment of primary of CO_2 and CO_2-aqueous fluid inclusions. Moreover, mixed CO_2-aqueous and sodic (-calcic) fluid inclusions are interpreted as responsible for the halogen signature obtained for fluids in granite clast samples and ironstone and quartz vein samples respectively, the former compatible with either a magmatic or with halite dissolution origin (or mixing of the two), in contrast with the dominant bittern origin for the fluid that produced extensive albitization. An origin via fluid unmixing for the fluid that produced regional albitization in the district was also excluded by Kendrick et al. (2007a) based on the distinct noble gas signature displayed by CO_2 (maximum $^{40}Ar/^{36}Ar$ value of 6000-7000) and aqueous fluid inclusions (maximum $^{40}Ar/^{36}Ar$ value of 2700) (Figure 7.2; Section 7.4.1). Kendrick et al. (2007a) proposed that mixed inclusions formed mostly by fluid mixing. However, another possibility is that type I and type IIb fluid inclusions represent the immiscible end-member fluids resulting from unmixing of an original H_2O-CO_2-NaCl, with type IIa a mixture of these two fluids. Unfortunately, homogenization temperatures for type II fluid inclusions and densities for type IIb fluid inclusions were not obtained and the lack of these data preclude the verification of this hypothesis.

A final possibility is that the type II fluid inclusions represent a heterogeneously trapped two-phase fluid. The comparison of type IIa fluid inclusion properties with experimental data by Schmidt and Bodnar (2000) for the system H_2O-NaCl-CO_2 suggest that immiscibility for this fluid in this study occurred at temperatures and pressures

below 500°C and 2500 bar and possibly even at higher conditions (Chapter 4). In fact, type IIa fluid inclusions contain in general more CO_2 than fluid inclusions presented by Schmidt and Bodnar (2000) and the addition of CO_2 to H2O-NaCl fluid causes a shift of the critical point and the solvus towards higher temperatures and pressures. These temperatures and pressures cannot be accurately determined due to the lack of experimental data for fluids of such composition. Therefore, it not possible to estimate if at the inferred lithostatic pressure (~3 kbar, the estimated lithostatic pressure by Rubenach et al., 2007) and temperature (~ 540°C) the fluid was homogeneous or had already unmixed.

The limited data at the SRBP do not allow a conclusive interpretation about the origin of mixed CO_2-aqueous and, in particular, about their potential role in the brecciation process. However, these inclusions are commonly associated with CO_2-only fluid inclusions, which may indicate a primary origin and are interpreted as later evolved fluid exsolved from the magma.

Albitization at the SRBP was more likely produced by a hot externally-derived fluid that acquired Na and Cl from the interaction of evaporitic sequences and that was heated by a magmatic source that provided the necessary heat to promote its circulation. This model is in agreement with the model proposed by Barton and Johnson (1996; 2000) and Kendrick et al (2007a) for the formation of albitization associated with IOCG mineralization.

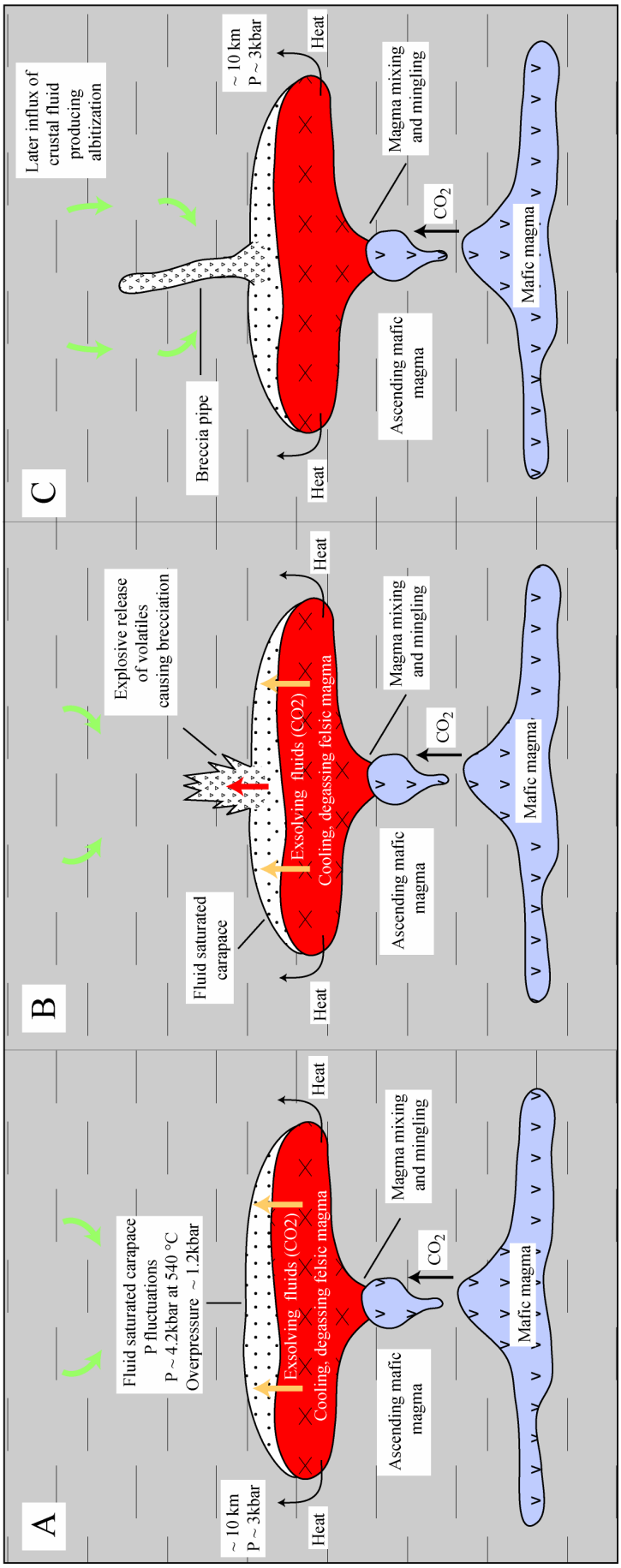

Figure 7.1 Proposed model for the formation of the SRBP. (A) The release and progressive accumulation of volatile phases of dominant CO_2 composition toward the top of the carapace during the crystallization of the felsic melt caused overpressuring. The estimated average pressure for primary CO_2 inclusions is 4.2 kbar and exceeds the estimated lithostatic pressure (3 kbar; Rubenach et al., 2007) by approximately 1.2 kbar. CO_2 was sourced from mafic magma likely through processes of magma mixing and mingling. (B) Overpressuring produced by the volatile release from the magma eventually overcame the rock tensile strength causing brecciation. (C) After the brecciation event the system was characterized by a later influx of fluid that produced widespread albitization of breccia and country rocks. Halogens data are consistent with the dominant bittern-derived origin for the fluid responsible for albitization at the SRBP.

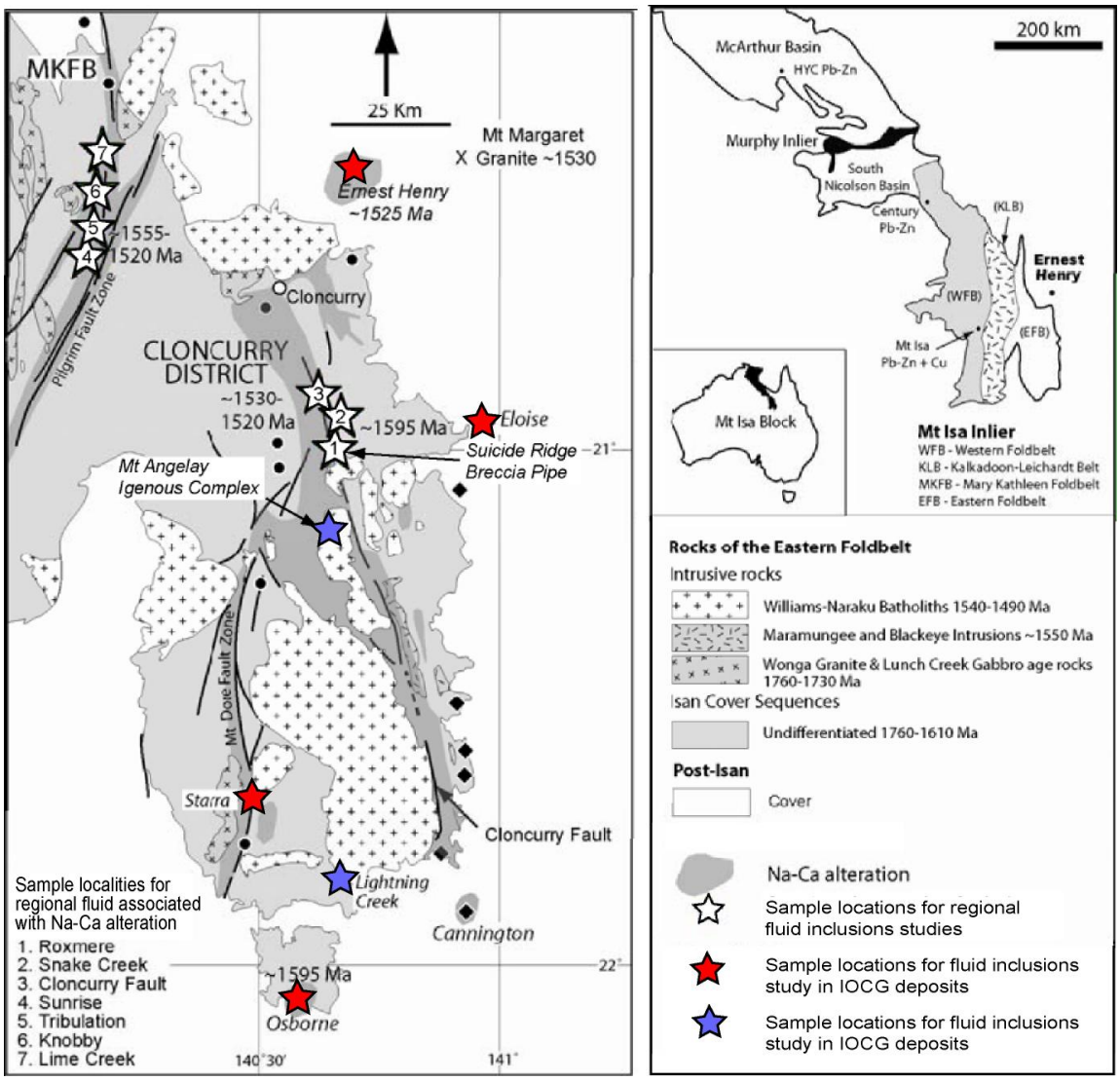

Figure 7.2 Simplified map of the Eastern Fold Belt showing sample locations for previous fluid inclusions studies. See text for references. Modified after Kendrick et al. (2007a).

7.3. Fluid geochemistry insights into the evolution and formation of the Eloise Cu-Au deposit

The chemistry of multisolid and liquid-rich halite-bearing fluid inclusions from the Eloise deposit was determined by LA ICP MS analysis (Chapter 6). Results indicate that multisolid fluid inclusions have higher absolute concentrations of all elements compared to halite-bearing fluid inclusions, with the exception of Ca and Pb. The most significant differences between the two types of inclusions are related to the enrichment of Fe, Mn and Ba in multisolid fluid inclusions compared with halite-bearing fluid inclusions. These differences are most likely due to the higher salinities and temperatures of multisolid fluid inclusions promoting metal transport (Hemley et al., 1992; Yardley et al., 2003; Yardley, 2005). This observation suggests that multisolid fluid inclusions were the "carrier" fluid and support the generally accepted idea that these represent the ore-forming fluids in IOCG systems (Beardsmore, 1992; Adshead, 1996; Adshead et al., 1998; Baker, 1998; Rotherham et al., 1998; Mark and Foster, 2000; Williams and Skirrow, 2000; Baker et al., 2001; Williams et al., 2001; Williams et al., 2005; Mark et al., 2006a; Mark et al., 2006b; Williams, personal communication). Multisolid and halite-bearing fluid inclusions may represent different stages in the evolution of the hydrothermal system at Eloise or two distinctly different fluids (Baker, 1998) (Figure 7.3).

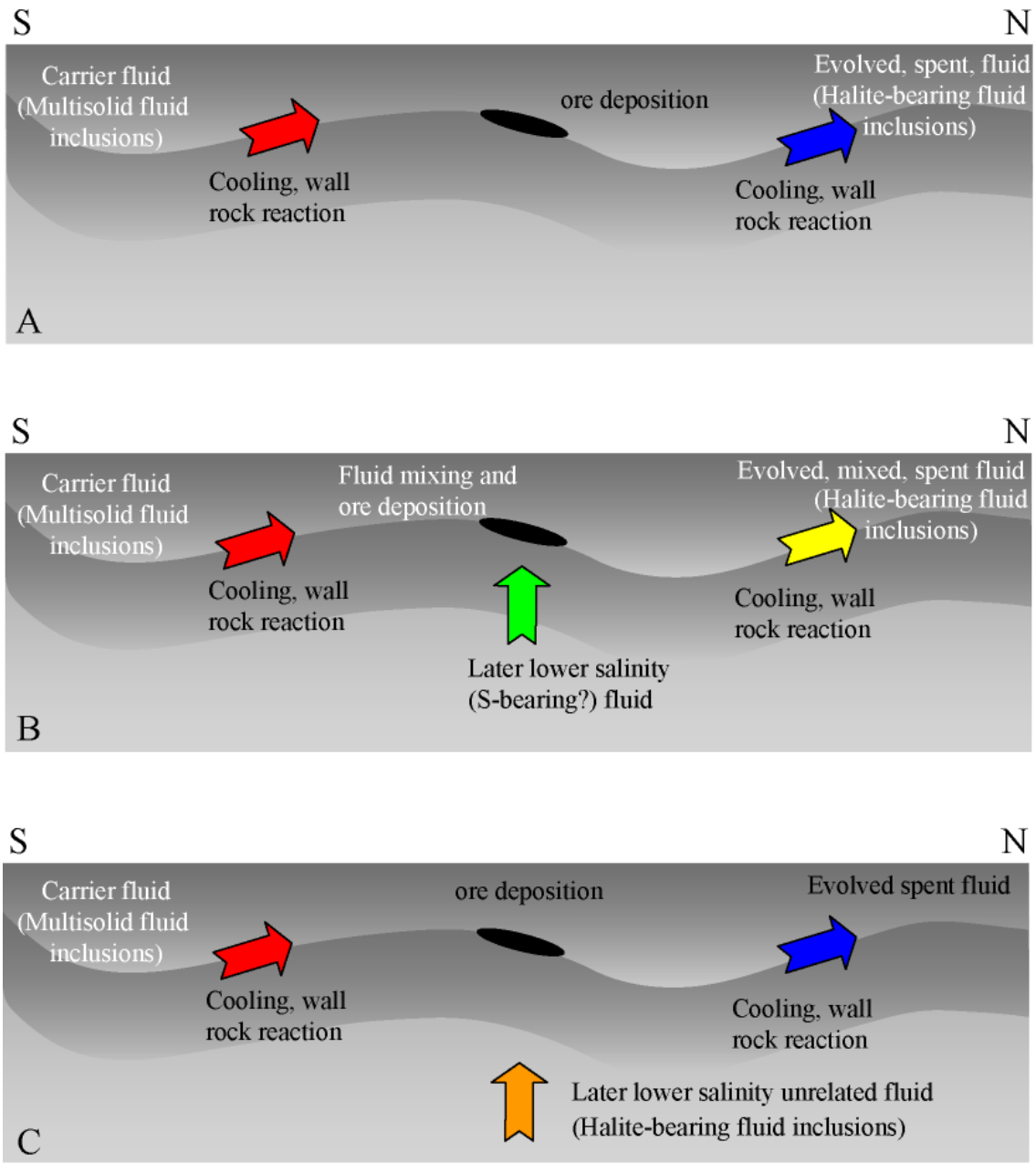

Figure 7.3 Schematic diagrams illustrating the possible relationships between multisolid and halite-bearing fluid inclusions and implication for ore deposition at Eloise Cu-Au deposit. (A) In this first scenario halite-bearing fluid inclusions form from the evolution of hot saline fluids that precipitate ore and gangue phases while migrating from south to north in response to cooling and wall rock reaction, likely in collaboration with other processes (e.g. sulfidation). In this context multisolid fluid inclusions represent the "carrier" fluid and halite-bearing fluid inclusions a lower-temperature, lower salinity "spending" or "spent" fluid. (B) In the hypothesis of fluid mixing multisolid fluid inclusions represent the "carrier" fluid and the halite-bearing fluid inclusions represent the result of mixing between the hot, ultrasaline fluid and a later fluid. This hypothesis is supported by the compositional differences displayed by multisolid and halite-bearing fluid inclusions and by the same inclusion type (Figure 7.5), differences that are compatible with a mixing trend (Figure 7.6). Fluid mixing would also explain the significant lower salinity of halite-bearing compared to multisolid fluid inclusions that cannot be attributed to

precipitation of Cl-bearing phase at Eloise. Fluid mixing likely promoted ore deposition and, in this context, cooling would have been important as an ore deposition mechanisms causing decrease in metal solubility as well as a fO_2 and fS_2. The hypothesis of fluid mixing is also supported by the S-poor nature of multisolid fluid inclusions, although the nature of the S-bearing fluid is uncertain. (C) In this scenario multisolid and halite-bearing fluid inclusions represent two distinct unrelated fluids. In this case ore deposition may result from the evolution of the carrier fluid similar to the first scenario, but halite-bearing fluid inclusions do not represent the evolved, spent fluid but another unrelated fluid. (See text for discussion).

In the first hypothesis (Figure 7.3A) halite-bearing fluid inclusions formed from multisolid fluids in response to cooling that would have caused, likely in conjunction with other processes (e.g. wall rock reaction and sulfidation; see below), the precipitation of ore and gangue phases. In this perspective halite-bearing fluid inclusions would represent a lower-temperature, lower salinity “spent” or “spending” fluid (Figure 7.3A). The hot, ultrasaline evolving fluids were likely migrating from south to north as proposed by Baker (1998) to explain the zonation of alteration and mineralization observed at Eloise. In the case of an evolving model, the compositional differences between the two types of inclusions should be reflected in corresponding variation in the host rock geochemistry. For example, the general depletion of Fe in halite-bearing inclusions is compatible with the precipitation of both ore and gangue phases that are enriched in Fe (Baker, 1998). However, Eloise is characterized by a rather complex evolution history that consisted of several alteration stages, in each of which different elements were diversely added or stripped away from the host rocks, and variably distributed within the deposit within compositional complex host rock (Baker, 1998). Therefore, it is difficult to directly relate specific fluid types to specific alteration, and comparison between fluid and host rock chemistry needs a careful consideration of several variables.

Isocon analysis comparing gains and losses of major and minor elements during the main alteration stages are shown in Figure 7.4 (from Baker, 1996). The geochemistry of host rock and alteration assemblages shows a Ca loss from the host rocks during albitization, followed by Ca enrichment during the formation of mafic silicates (e.g. hornblende) in meta-arkose rocks, and Ca loss in amphibolite due to the formation of biotite at the expense of Ca-bearing metamorphic minerals (amphibole and plagioclase), and finally Ca enrichment during the mineralization stage due to the formation of abundant calcite (Baker, 1996, 1998). The precipitation of calcite during the ore stage (Baker, 1998) likely resulted in depletion of Ca in the mineralizing fluid, although Ca may have been sourced directly from the altered rocks with calcite produced by reaction of CO_2 and hornblende.

Albitization results in a general depletion of Ba from the host rock followed by a substantial Ba enrichment during K-Fe alteration due to biotite precipitation and seriticization of albite (Baker, 1996). The ore stage is characterized by a general loss of Ba in the host rocks (Baker, 1996). Therefore the lower Ba content of the halite-bearing fluid inclusions compared to multisolid fluid inclusions may in part be due to Ba-enrichment during precipitation of biotite bearing K-Fe alteration (Baker, 1996). Albitization produced a general depletion in Mn from the host rock, similar to Ca and Ba. During K-Fe alteration there is a general Mn enrichment due to mafic silicate precipitation in altered meta-arkose rocks and Mn depletion during biotitization of amphibolite (Baker, 1996). There is no appreciable variation in the Mn content of the host rock during the ore stage (Baker, 1996). The lower Mn concentrations of halite-bearing fluid inclusions compared to multisolid fluid inclusions are possibly related to the formation of pre-ore mafic silicates, although microprobe analysis revealed a general Mn-poor nature of the hornblende (Baker, 1998).

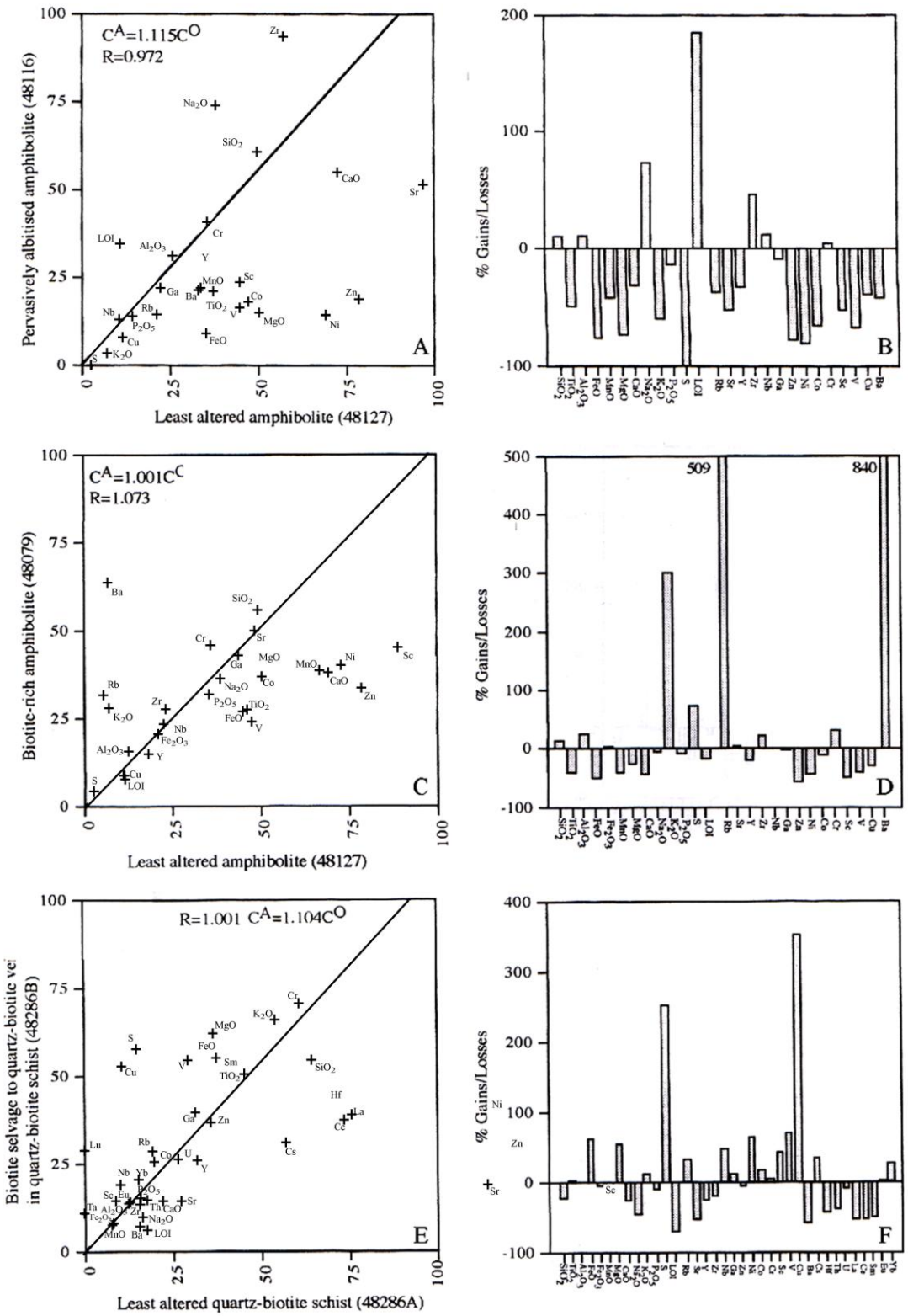

Figure 7.4 Isocon diagrams illustrating rock geochemistry variations related to the major alteration stages. (A) and (B) Isocon diagram comparing least altered amphibolite with albitized amphibolite. (C) and (D) Isocon diagram comparing least altered amphibolite with biotite-rich amphibolite. (E) and (F) Isocon diagram comparing the biotite-rich selvage of a quartz biotite vein to the quartz biotite schist host rock from eastern side of the Levuka Lode (after Baker, 1996).

Trace element geochemistry indicates that the ore contains more Cu than Zn and Pb, although locally post-ore veins contain minor sphalerite and low Cu (Baker, 1998), that should be reflected by a general increase in Zn/Cu and Pb/Cu ratios as Cu precipitated from the mineralizing fluid. However, a correlation between the relative enrichment and depletion between the rocks and the fluids is complicated and can be misleading due to the Cu data being mostly below detection limits for the majority of fluid inclusions (Chapter 6). The main mineralization stage also contains higher Zn concentrations compared to Pb (Baker, 1998) and this is consistent with the dominantly lower Zn/Pb ratios displayed by halite-bearing fluid inclusions compared to multisolid fluid inclusions. The low concentrations of Zn and Pb in the ore phases may suggest that their contents in the liquid phase, although higher or comparable to Cu content, were not high enough to reach saturation, which is consistent with the lower solubility of Cu at higher temperature compared with these two elements (Hemley et al., 1992; Baker, 1998). These observations indicate that significant amount Zn and Pb passed through the Eloise system but the conditions were not favourable to their deposition.

The hypothesis of fluid evolution can therefore explain the general lower absolute element concentrations displayed by halite-bearing fluid inclusions compared to multisolid fluid inclusions, and variations in chemistry between the two types can in part be attributed to mineral precipitation. However, this hypothesis does not account for the substantial drop in salinity between early ultrasaline brines and the later high salinity halite-bearing fluid inclusions. The salinity decrease is a key aspect for ore-deposition since Cl, with temperature, exerts a major control on the metal content that can be transported by hydrothermal fluids (Yardley, 2005). The Cl concentrations in the fluid can be reduced by precipitation of Cl-bearing minerals. Biotite and hornblende are commonly observed at Eloise in the K-Fe alteration stage (Baker, 1998), but their Cl

content is typically low (less than 0.5 wt %) and other Cl-bearing minerals do not occur (Baker, 1998; Baker et al., 2001). Baker et al. (2001) suggested that the decrease may be related to a different pulse of magmatic fluid characterized by different composition or alternatively to a distinct fluid derived by different magmatic source. Chlorine concentrations in the fluid may also decrease in response to dilution. Therefore, fluid mixing with a less saline fluid is a possible explanation for the significant salinity drop between multisolid and halite-bearing fluid inclusions as also inferred by Baker (1998) and Baker et al. (2001).

In the second hypothesis of mixing (Figure 7.3B), the two inclusion types may represent two unrelated distinct fluids that have mixed to some extent, with multisolid fluid inclusions representing the carrier fluid and the halite-bearing fluid inclusions representing a product of mixing between the hot, ultrasaline fluid and a later fluid. Fluid mixing likely occurred along the evolution path of the ore-forming fluid from south to north (Baker, 1998). In this context the composition of fluid inclusions across the deposit should reflect different degrees of mixing. For example fluid inclusions from the south should broadly represent the carrier fluid, whereas fluid inclusions in the north should represent a mixed, spent fluid (Figure 7.3B). Samples for fluid inclusion analysis were collected in different areas of the deposit (Figure 6.2). The two samples containing multisolid fluid inclusions are the most southerly located and occurred in the southerly extensions of the Levuka Lode. Samples containing halite-bearing fluid inclusions are from the 40 Lode (sample 48076), the Elrose Lode (sample 48178) and from Eloise NW (sample EWD6). Fluid inclusions in sample EWD6 are the most northerly located and therefore likely represent the most evolved fluid.

To test the hypothesis of fluid mixing the compositions of the two inferred fluid end-members are compared, multisolid fluid inclusions as the carrier fluid and halite-

bearing fluid inclusions in sample EWD6 as the mixed, spent fluid (Figures 7.5 and 7.6). Fluid inclusions in the remaining samples should display elements abundances and ratios between the two fluid end-members. Fluid inclusions in sample EWD6 have the lowest absolute concentrations of all elements, with the exception of Sr, of all fluid inclusions in all samples consistent with a "mixed, spent" fluid that lost part of the carried elements (Figures 7.5 and 7.6A). In a K/Ca versus Mn/Fe plot multisolid fluid inclusion lie at the top left corner, displaying the highest K/Ca and lowest Mn/Fe ratios, whereas fluid inclusions in sample EWD6 sit on the bottom, right corner, characterized by the lowest K/Ca and highest Mn/Fe ratios. The remaining halite-bearing fluid inclusions display K/Ca and Mn/Fe ratios mostly between the two end-members consistent with an origin via fluid mixing. In Figure 7.6B Ca and Fe also show the two fluid end-members sitting at opposite sides of the diagram with multisolid fluid inclusions having the highest Fe and fluid inclusions in sample EWD6 with the lowest Fe, and the remaining halite-bearing fluid inclusions in the middle. There is a variation of over three orders of magnitude in Fe concentrations between the two fluid inclusion end-members, whereas Ca concentrations, although generally lower for multisolid fluid inclusions compared to halite-bearing fluid inclusions, mostly vary within the same range for all the inclusions. The trend toward Fe depleted fluids with increasing Mn/Fe is compatible with the Fe-rich nature of ore and gangue at Eloise. Ba is generally higher in multisolid fluid inclusions compared to halite-bearing fluid inclusions. In Figure 7.6C multisolid fluid inclusions display the highest Ba and K concentrations and lowest K/Ba ratios and halite-bearing fluid inclusions in sample EWD6 have the lowest K and Ba content. The plot indicates a general trend towards lower K and Ba concentrations that is consistent with the hypothesis of fluid mixing an ultrasaline Ba enriched fluid and a later lower salinity fluid. The high Ba concentrations of the carrier fluid represent a key

argument supporting the hypothesis of fluid mixing because high Ba contents in the fluid are interpreted as an indication of a S-poor fluid due to the low solubility of Ba in S-bearing fluids (Williams, 2001; Williams, personal communication). Williams et al. (personal communication) analyzed and compared the chemistry of fluid inclusions from Ernest Henry, Osborne and Lightning Creek and suggested that the generally low Zn concentration in the ore compared to its high concentration in the fluid, may also reflect a S-poor fluid. This is also observed at Eloise where the ore-forming fluid contains abundant Zn (average ~ 2000 ppm) yet the mineralization is not significantly enriched (Baker, 1998). These observations suggest that the ore fluid was potentially S-poor and therefore must have reacted with a S-bearing fluid or rock in order for ore deposition to have occurred. The pre-ore stage alteration and host rocks at Eloise are characterized by an oxidized mineral assemblage. Baker (1998) described textural evidence indicating progressive sulfidation of pre-ore silicates during the main mineralization stage and suggested that this process may have played a significant role in ore deposition and the observed ore zonation. Baker et al. (2001) proposed that sulfidation occurred via reaction of a S-bearing solution with Fe oxide-rich rocks during cooling. However, a S-bearing fluid is in contrast to the above observation that suggests the ultrasaline fluid inclusions represent a S-poor fluid. Most likely S was transported by a second fluid and ore deposition was the result of the mixing between the metal rich ore fluid and a S-bearing fluid. In this context, cooling would have been important as an ore deposition mechanism causing a decrease in metal solubility as well as a fO_2 and fS_2 variation (Hemley et al., 1992). However, the nature of the S-bearing fluid is uncertain due the inability to measure S in fluid inclusions using the techniques utilized in this study. Possible sources of sulphur include the later halite-bearing fluid inclusions and the CO_2-rich fluid inclusions as suggested by Oliver et al (2004).

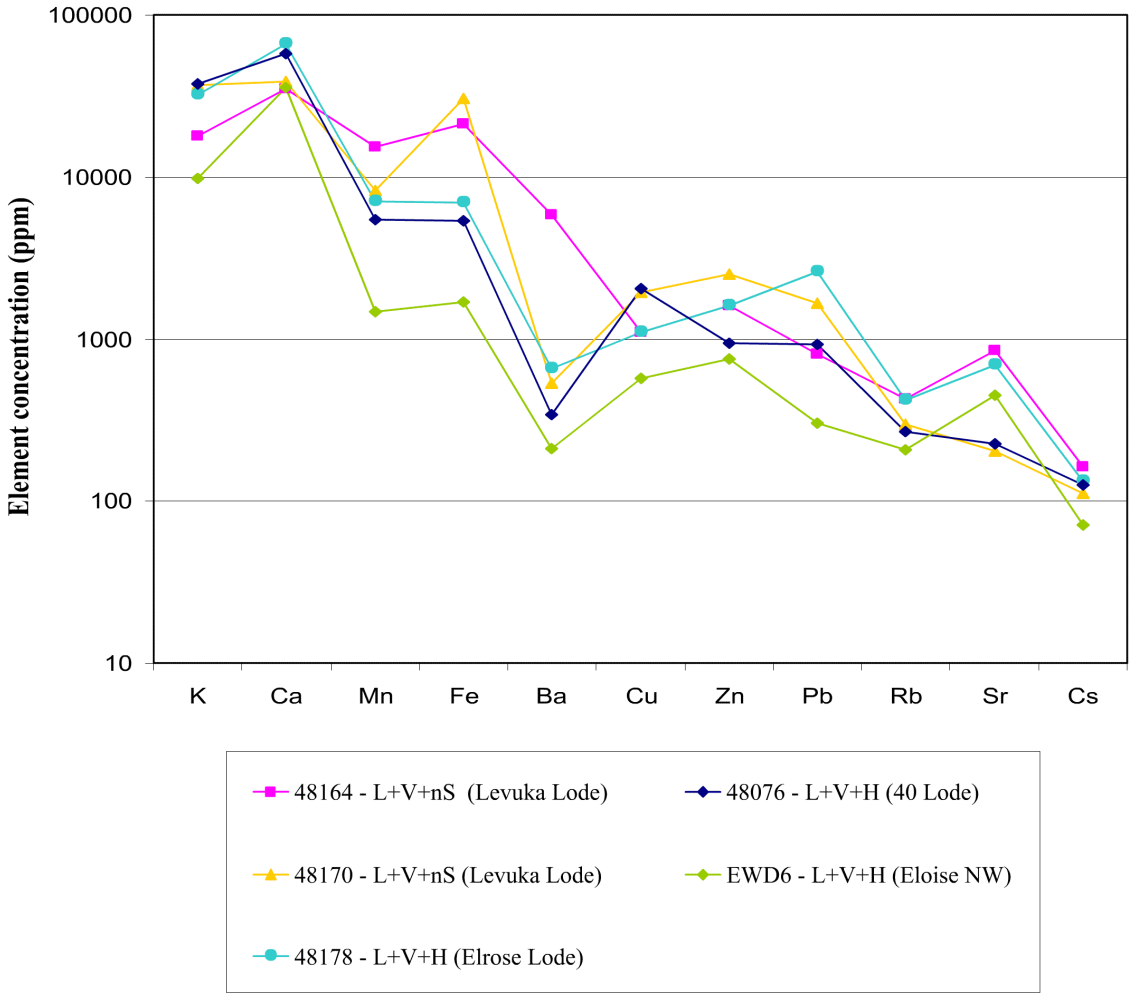

Figure 7.5 Average fluid inclusion composition for each sample determined from LA ICP Ms analysis.

A final hypothesis is that the two fluid inclusion types represent two completely distinct unrelated fluids (Figure 7.3C). In this case ore deposition may have resulted from the evolution of the carrier fluid similar to the first scenario or more likely by mixing with a S-bearing fluid, perhaps represented by CO_2 fluid inclusions, due to the S-poor nature of multisolid fluid inclusion, but halite-bearing fluid inclusions do not represent the evolved, spent fluid but another unrelated fluid. However, the possibility that the two types of inclusions represent two distinct fluids is in contrast with the general mixing trend displayed by fluid inclusions data (Figure 7.6) and the fluid inclusion paragenesis at Eloise that indicates a substantial temporal overlap between multisolid and halite-bearing fluid inclusions (Baker, 1998).

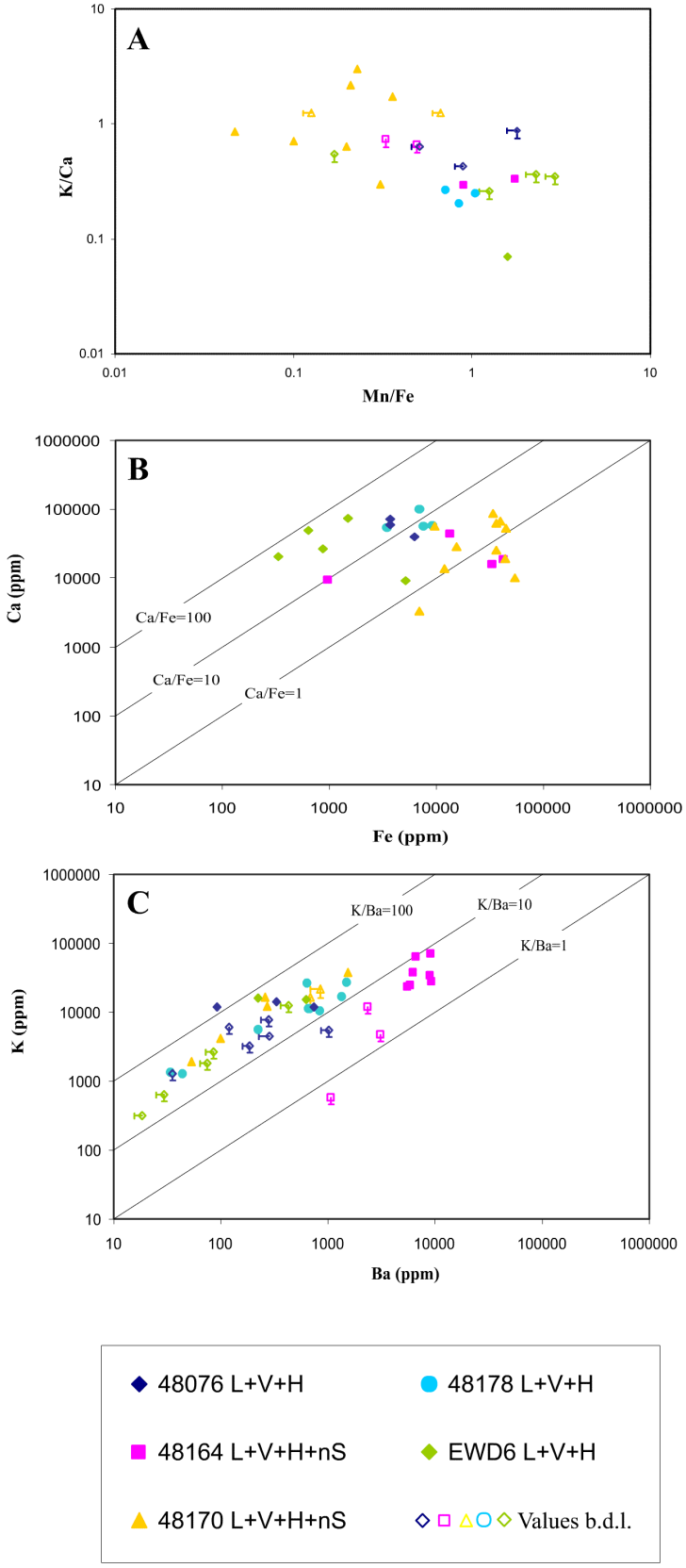

Figure 7.6 Selected plots comparing the chemistry of multisolid and halite-bearing fluid inclusions. Open symbols refer to values below detection limits and bars indicate that the corresponding element below detection limit. Concentrations in ppm.

The favoured model for ore formation at Eloise is therefore a fluid mixing model combined with fluid-rock interaction, sulphidation and temperature decrease. Fluid mixing is also consistent with the general variability of absolute and relative element concentrations observed even between inclusions of the same type. For example the variable K/Ca and Mn/Fe ratios between different types of inclusions and between inclusions of the same type occurring in different samples may reflect different degrees of mixing (Figure 7.5). A possibility of fluid mixing at Eloise was inferred by Baker (1998) and has been recently proposed for other IOCG deposits in the Cloncurry district (Mark et al., 2000; Williams et al., 2001; Mark et al., 2006b; Kendrick et al., 2007b; Williams, personal communication).

Baker (1998) and Baker et al. (2001) inferred a magmatic origin for the early fluids at Eloise based on their ultrasaline nature and on stable isotope data. Baker et al. (2001) inferred a magmatic origin also for the later fluids based on stable isotope data and proposed that these fluids may represent either a different pulse of magmatic fluid compared to that responsible for the early fluids or a distinct magmatic hydrothermal fluid. Kendrick et al. (2006) invoked the involvement of an external fluid with a possible halite dissolution component in the mineralization event at Eloise based on halogen and noble gas data for primary multisolid and daughter phase-bearing fluid inclusions. Br/Cl ($0.3x10^{-3}$ - 10^{-3}) and I/Cl (10^{-6} - $5x10^{-6}$) ratios for these inclusions are lower than values considered representative of juvenile magmatic fluids (Johnson et al., 2000; Kendrick et al., 2001), although Br/Cl ratios fall mostly in the range of values determined for volcanic fumaroles (Bohlke and Irwin, 1992b), and are higher than values representative of halite dissolution water (Bohlke and Irwin, 1992a; Kendrick et al., 2006). Kendrick et al. (2006) inferred that such values may be the result of incomplete halite dissolution, or dissolution of evaporite minerals other than halite or

finally of fluid mixing between halite dissolution water and a magmatic fluid. Alternatively, the fluid may have acquired its salinity from melting of metamorphic scapolites abundant throughout the district (Kendrick et al., 2006).

7.4. Regional vs IOCG fluids – Implication for formation of IOCG

7.4.1. Comparison of fluids from the Suicide Ridge Breccia Pipe with other regional fluids

Previous research on regional fluids in the Cloncurry includes studies by De Jong and Williams (1995) and Fu et al (2003; 2004a; 2004b) (Figure 7.2). De Jong and Williams (1995) described the distribution and evolution of the metasomatism in large and extensively altered breccia systems adjacent to the Cloncurry Fault in the Fullarton River and Maramungee Creek area in the Cloncurry district. The breccia systems are dominated by sodic (-calcic) alteration that produced albite-actinolite-titanite±quartz±magnetite±diopside assemblages in calcsilicate rocks, metabasites, metapelites and in felsic igneous rocks (de Jong and Williams, 1995). Albitization is followed by more localized potassic alteration and silicification (de Jong and Williams, 1995). Research included the study of fluid inclusions associated with the different alteration stages.

Fu et al. (2003; 2004a; 2004b) studied fluid inclusions related to albitization occurring in veins and host rocks from several locations that include Knobby, Tribulation, Lime Creek and Sunrise in the Mary Kathleen Fold Belt and from Mt Avarice, Roxmere-Marimo, Snake Creek and Gilded Rose in the Cloncurry district.

Samples for fluid inclusion studies were collected from quartz-calcite-pyroxene±amphibole veins associated with albitization in the metamorphosed calc-silicate and dolerite wall rocks and from breccias in the Mary Kathleen Group (Corella type) and Soldier's Cap Group (Gilded Rose type) that contained quartz clasts (Fu et al., 2004a; Fu et al., 2004b).

The geological settings of these studies are similar to the SRBP. Both the studies of De Jong and Williams (1995) and Fu et al. (2003; 2004a; 2004b) focused on fluid inclusions dominantly related to albitization. Analyzed samples mostly come from strongly brecciated rocks spatially and temporally associated with the emplacement of the Williams-Naraku batholith and the development of the broadly coeval Na (-Ca) metasomatism (Mark, 1998; Pollard et al., 1998; Mark and Foster, 2000; Pollard, 2001).

Fluid inclusions described in these studies share many similarities with inclusions associated with the SRBP. A common feature of regional fluid is the scarcity and, in some cases (as is case for the barren breccia pipe in this study), the absence of multisolid high temperature, high salinity fluid inclusions. This may be the main reason for the absence of mineralization in these systems (Baker et al., 2006). Fu et al. (2003; 2004a; 2004b) described rare multisolid fluid inclusions containing up to 6 solid phases including halite, sylvite, carbonate, magnetite and/or hematite. PIXE analysis revealed that these inclusions are dominated by Na, K, Ca, Fe and Mn with generally high average K/Ca ratios (~ 8) (Fu et al., 2004a; Fu et al., 2004b; Baker, 2006). These inclusions also contain Zn (average ~ 2000 ppm), Cu (average ~ 200 ppm), Pb (average ~ 1000 ppm) and significant Ba (average ~ 7000 ppm) (Fu et al., 2004a; Fu et al., 2004b; Baker, 2006). Fu et al. (2003; 2004a; 2004b) also reported common pure CO_2 fluid inclusions similar to those associated with the SRBP, although in some cases small amounts of N_2 and/or CH_4 were detected. These inclusions have a wide range of

homogenization temperatures, from –37.0 to +30.2°C, which is also common to CO_2 fluid inclusions reported in this study.

Three phase halite-bearing and two phase liquid-rich fluid inclusions are the most abundant type of inclusions in all regional systems (Baker et al., 2006). In all the previous studies first melting temperatures for these inclusions were commonly < -50°C indicating a Ca-rich fluid. De Jong and Williams (1995) documented homogenization temperatures generally between 100 and 300°C and salinities ranging from 12 to 41 wt% NaCl equiv. for sodic (-calcic) fluid inclusions. Fu et al. (2004a and b) reported homogenization temperatures mostly between 100 and 200°C for similar liquid-rich sodic (-calcic) fluid inclusions. Overall, fluid inclusions in these previous studies display similar eutectic temperatures, homogenization temperatures and salinities of type III sodic (-calcic) fluid inclusions reported in this study.

PIXE analysis results (Fu et al., 2004a and b; Baker, 2006) on halite-bearing sodic (-calcic) fluid inclusions indicate that these inclusions are dominated by Na, K and Ca, display highly variable K/Ca ratios and contain significant concentrations of Fe (average ~ 20000 ppm). These inclusions display consistently higher absolute element concentrations compared to the sodic (-calcic) fluid inclusions in this study (Fu et al., 2004a and b; Baker, 2006). Major differences are related to Fe, Ba and Sr that display an enrichment of about one order of magnitude in fluid inclusions studied by Fu et al. (2003, 2004a and b) compared to fluid inclusions associated with the SRBP. Average Cu concentrations for inclusions in all the studies are similar. The observed difference between the composition of sodic (-calcic) fluid inclusions in the different studies may represent actual compositional dissimilarities reflecting local processes (e.g. host rock, fluid mixing) or may indicate two distinct fluids (see below). Alternatively, the compositional differences between the two fluid inclusions types may be the result of

the different quantification processes employed by PIXE and LA ICP MS techniques, as also observed and discussed in Chapter 8. A fourth type of inclusion was documented by Fu et al. (2003; 2004a and b). These are secondary two phase liquid-rich fluid inclusions found in annealed microfractures. These inclusions are characterized by compositions close to pure NaCl (eutectic temperature ~ -21°C) and homogenization temperatures between 80 and 200°C (Fu et al., 2004a). Similar secondary late inclusions with comparable homogenization temperatures were also observed at the SRBP although these display higher eutectic temperatures (~ -30°C).

PIXE analysis by Fu et al. (2004a and b) suggested that multisolid and sodic (-calcic) halite-bearing fluid inclusions might have a different source, however, these two inclusion types display a similar wide range of Br/Cl values that span from 0.35 to 5.22 (Fu et al., 2004a; Fu et al., 2004b; Baker, 2006). These values possibly indicate multiple fluid sources for these fluids or mixing between fluids originated from different sources. Later liquid-rich fluid inclusions have Br/Cl ratios mostly above the seawater value in the bittern brine field (Fu et al., 2004a; Fu et al., 2004b; Baker, 2006). Kendrick et al. (2007a) determined halogen and noble gas signatures of fluid inclusions related to albitization from the same localities of previous regional studies by de Jong and Williams (1995) and Fu et al. (2003; 2004a and 2004b) (Figure 7.2). The analyzed inclusions include aqueous (sodic (-calcic) and later lower salinity fluid inclusions), liquid CO_2 and mixed aqueous-carbonic. Aqueous fluid inclusions from the Cloncurry district display $^{40}Ar/^{36}Ar$ values lower than 2700 for most of the samples and variable molar Br/Cl values ($0.3\text{-}1.9\times10^{-3}$) and I/Cl values ($0.2\text{-}10\times10^{-6}$) that are interpreted to represent upper crustal sedimentary fluids that have acquired their salinity by dissolving variable quantities of halite or scapolite (Kendrick et al., 2007a). Most fluid inclusions in samples from the Mary Kathleen Fold Belt have higher Br/Cl ($0.4\text{-}4\times10^{-3}$) and I/Cl

($3.7\text{-}35\times10^{-6}$) values and lower maximum $^{40}Ar/^{36}Ar$ values compared with fluid inclusions in samples from the Cloncurry district, consistent with a bittern-derived origin (Kendrick et al., 2007a). Kendrick et al. (2007a) suggested a similar bittern but distinct origin for fluid inclusions in the two areas before the acquisition of a halite dissolution component for fluids in the Cloncurry district. Fluid inclusions from the Snake Creek Anticline display the highest $^{40}Ar/^{36}Ar$ values (~25,000) and are interpreted to have a magmatic origin (Kendrick et al., 2007a). In general, fluids associated with albitization in the Cloncurry district have a dominant origin related to halite dissolution waters but also include a magmatic-derived component similar to fluids associated with IOCG deposits in the Cloncurry district, suggesting a possible genetic link between regional albitization and IOCG mineralization in the Cloncurry district (Fisher et al., 2005; Kendrick et al., 2006; 2007a; 2007b). Noble gas data for CO_2 fluid inclusions are consistent with a dominant metamorphic origin for CO_2 (Kendrick et al., 2007a).

The Br/Cl ratios ($2.2\text{-}3.0\text{x}10^{-3}$) obtained for sodic (-calcic) fluid inclusions associated with SRBP (Chapter 5) are higher than Br/Cl ratios obtained for regional aqueous inclusions in the Cloncurry district and similar to Br/Cl values of regional fluid inclusions from the Mary Kathleen Fold Belt (Kendrick et al., 2007a). These values are consistent with an original bittern although distinct origin as inferred by Kendrick et al. (2007a) for regional fluid inclusions in the two districts. This possibly suggests that albitization was the product of multiple hydrothermal alteration events characterized by fluids with similar origin but distinct evolution history.

7.4.2. Comparison of fluids associated with IOCG deposits, granites and barren regional systems

The main difference between fluids associated with the Eloise Cu-Au deposit and with the SRBP pipe is the absence in the latter of ultrasaline high-temperature multisolid fluid inclusions. Such fluids are common in other IOCG deposits in the Cloncurry district (Adshead, 1996; Adshead et al., 1998; Baker, 1998; Rotherham et al., 1998; Mark et al., 2000) and fluid inclusion analysis revealed that they carried significant amount of metals (Williams et al., 2001; Baker, 2006; Williams, personal communication) supporting the generally accepted idea that these represent the ore-forming fluids in IOCG systems (Adshead, 1996; Adshead et al., 1998; Baker, 1998; Baker et al., 2001; Williams et al., 2001; Williams et al., 2005; Mark et al., 2006b; Williams, personal communication). Their absence at the SRBP is almost certainly the reason for the absence of mineralization.

Halite-bearing fluid inclusions at Eloise and similar fluid inclusions associated with the SRBP display similar homogenization temperatures and salinities but have generally distinct chemistry. Fluid inclusions from Eloise have generally higher absolute element concentrations, with the exception of Ba, and lower Zn/Pb and K/Ca ratios. The two types of inclusions also display distinct Br/Cl values, with sodic (-calcic) fluid inclusions from the SRBP displaying Br/Cl molar ratios ranging from 2.2×10^{-3} to 3.0×10^{-3} consistent with a bittern origin (Chapter 5). In contrast lower Br/Cl values (0.3×10^{-3} to 10^{-3}) obtained from halite-bearing fluid inclusions at Eloise indicate a magmatic-derived component, consistent with stable isotope data presented by Baker et al. (2001), or with an origin via dissolution of evaporites or via mixing of a magmatic fluid with halite dissolution water (Section 7.3) (Kendrick et al., 2006).

Fluid inclusion data from other IOCG deposits, granite-related systems and regional environments in the Cloncurry district largely support the considerations about the difference between mineralized and barren systems based on data from the SRBP and the Eloise Cu-Au deposit presented in this study. The absence or scarcity of multisolid fluid inclusions, commonly observed in IOCG deposits and granites, is a common feature of regional environments and most likely the reason for the lack of mineralization in these systems.

Fluid inclusions from Eloise share many common features with fluids associated with other IOCG deposits and granites in the Cloncurry district (Figure 7.2). Multisolid fluid inclusions in all the system are characterized by high temperature (mostly between 200 and 550°C) and salinity (30 to 60 wt% NaCl equiv.) and are typically enriched in K (average concentrations are 21000 ppm at Ernest Henry, 26000 ppm at Starra and 36000 at Osborne), Ca (average concentrations are 12000 ppm, 16000 ppm, 45000 ppm for Osborne, Ernest Henry and Starra respectively), Fe (average concentrations are 18000 ppm at Ernest Henry, 45000 ppm at Starra, 66000 at Osborne) and Mn (average concentrations are 6000 at Osborne, 11000 ppm at Starra and 33000 ppm at Ernest Henry) (Adshead, 1995; Rotherham et al., 1998; Williams et al., 2001; Baker, 2006). K/Ca ratios are mostly >1 but variable (Williams et al., 2001; Baker, 2006). Starra is an exception since high temperature, high salinity fluid inclusions display lower K/Ca values (~ 0.7) (Williams et al., 2001; Williams et al., 2004; Baker, 2006). Mn/Fe values vary greatly among the different deposits in the Cloncurry district, being low for fluids from Osborne and Starra (average values between 0.1 and 0.4) and much higher (average ~ 5.8) for multisolid fluid inclusions from Ernest Henry (Baker, 2006). Eloise multisolid fluid inclusions have a higher average Mn/Fe ratio (0.7) compared to fluid inclusions at Osborne (average Mn/Fe value ~ 0.1) and Starra (average Mn/Fe value ~

0.4). Multisolid fluid inclusions from the different deposits also generally contain significant although variable Ba concentrations. Barium concentrations are particularly high for multisolid fluid inclusions at Starra (~ 20000 ppm), and one order of magnitude less approximately 2000 ppm for inclusions at Osborne (Baker, 2006). Multisolid fluid inclusions from Eloise have Ba concentration around 3500 ppm similar to Osborne fluid inclusions. Fluid inclusions at Osborne and Ernest Henry contain Cu concentrations around 150 ppm, one order of magnitude less than fluid inclusions at Starra (average Cu ~ 1000 ppm). Fluid inclusions from Eloise have Cu values mostly below detection limit.

Fluid inclusions in granite-related systems in the Cloncurry district were documented by Perring et al. (2000) and Mark et al. (2004) (Figure 7.2). Perring et al. (2000) studied fluid inclusions from the Lightning Creek prospect hosted in dominant quartz monzodiorite and monzogranite rocks. These host rocks are cut by a set of mineralogically and texturally complex sills varying from equigranular quartz-plagioclase-rich rocks to albite-magnetite-quartz rocks that display a range of magmatic-hydrothermal transition textures (Perring et al., 2000). Fluid inclusions analyzed occurred in samples from high temperature quartz-magnetite ±pyrite ± albite veins and from spherulitic albite-quartz-magnetite sills (Perring et al., 2000). The Mt Angelay Igneous complex (MAIC) is located in the central area of the Cloncurry district and dominantly consists of K-rich, magnetite-bearing mafic and felsic intrusive rocks that were emplaced during the Williams-Naraku magmatic event into rocks of the Soldiers Cap Group and calc-silicate rocks of the Mary Kathleen Group (Mark et al., 1999; Mark, 2001; Mark et al., 2004). The intrusions have compositions varying from monzodiorite to biotite syenogranite and are cut by late alkali pegmatites and Na-rich albitites that display balloon-textures (Mark et al., 2004). The main phase of the MAIC hosts a km-scale magmatic-hydrothermal breccia-vein system characterized by

gradation from composite breccias, filled with synchronously formed magmatic intrusions and hydrothermal mineral precipitates in the topographic lows, to systems of fracture-related hydrothermal veins in the topographic highs (Mark et al., 2004). Samples for fluid inclusion analysis were from quartz in biotite syenogranite and alkali pegmatite that respectively predate and are synchronous with the formation of the kilometre-scale magmatic hydrothermal breccia-vein system in the MAIC (Mark et al., 2004).

At Lightning Creek and MAIC abundant high temperature, high salinity multisolid fluid inclusions were documented (Perring et al., 2000; Mark et al., 2004). Multisolid fluid inclusions from Lightning Creek homogenize at temperatures in excess of 420 °C and display salinities ranging from 35 to 50 wt% NaCl equiv. (Perring et al., 2000). Multisolid fluid inclusions from MAIC have salinities exceeding 50 wt% NaCl equiv. and homogenization temperatures are mostly higher than 400 °C (Mark et al., 2004). Multisolid fluid inclusions from granite systems have similar composition to multisolid fluid inclusions in the IOCG deposits displaying high concentrations of K, Ca and Fe and K/Ca ratios consistently >1, although fluid inclusions from Mount Angelay Igneous Complex (MAIC) display variable K/Ca ratios (~ 0.1 to ~5.0) (Perring et al., 2000; Mark et al., 2004; Baker, 2006). Copper concentrations in fluid inclusions from MAIC vary between from around 50 to 3000 with average ~ 400 ppm, higher than Cu concentrations of fluid inclusions from Osborne and Ernest Henry but lower than inclusions from Starra (Mark et al., 2004; Baker, 2006). Fluid inclusions from Lightning Creek are characterized by very high concentrations of Fe (90000 to 130000 ppm) and Cu (10000 to 19000 ppm) (Perring et al., 2000). Rare multisolid fluid inclusions from regional studies are similar to fluid inclusions associated with IOCG deposits and

granites with generally high concentrations of major elements an metals (Section 7.4.1; Fu et al., 2004a; Fu et al. 2004b; Baker, 2006).

Halite-bearing fluid inclusions from IOCG, granite-related systems and from barren breccia systems generally display lower absolute element concentrations due to their lower temperature and salinity (cf Yardley, 2005) but in general have lower K/Ca ratios. Hypotheses for the relationship between halite-bearing and multisolid fluid inclusions are similar to those formulated for the Eloise Cu-Au deposit (Section 7.3). Halite-bearing fluid inclusions may represent a lower temperature, lower salinity evolution of multisolid fluid inclusions in response to cooling and wall rock reaction that would have caused ore deposition. Alternatively, halite-bearing fluid inclusions may represent a late distinct fluid that has mixed to a certain extent with the ultrasaline carrier fluid or, finally, a completely unrelated fluid. An origin via fluid mixing was preferred for halite-bearing fluid inclusions at Eloise based on fluid inclusion salinity and chemistry, deposit geochemistry and noble gas and halogen data (Section 7.3).

There is evidence of fluid mixing in other IOCG deposits in the district, and this likely explains the origin of multisolid and halite-bearing fluid inclusions. Most of the fluid inclusions from Osborne display halogen and noble gas values similar to fluid from Eloise (Section 7.3), whereas one sample displays Br/Cl and I/Cl ratios compatible with a magmatic origin (Kendrick et al., 2006). These data suggest the involvement of different fluids with different origins for the formation of the mineralization at Osborne.

Multisolid fluid inclusions from Ernest Henry can be divided into two populations based on halogen and noble gas signature (Kendrick et al., 2007b). The first population has halogen and noble gas data compatible with a magmatic-derived fluid, whereas the second population of multisolid inclusions is characterized by halogen and noble gas data interpreted as halite-dissolution water (Kendrick et al., 2007b). Kendrick

et al. (2007b) interpreted the observed variability in Ernest Henry noble gas and halogen data for multisolid fluid inclusions as a result of mixing between two high-salinity fluids characterized by distinct origins and proposed a model for the formation of Cu-Au mineralization at Ernest Henry that include mixing between a magmatic fluids derived from regionally abundant granites, related to the Williams-Naraku magmatic event, and a high salinity halite dissolution upper crustal brine.

An origin of the mineralization due to fluid mixing was also proposed for Starra by Williams et al. (2001) based on the significant Ba enrichment (~ 20000 ppm) of multisolid fluid inclusions that was interpreted to suggest a S-poor nature of the mineralizing fluid and implying that S was transported by a different fluid.

Overall the data available suggest multiple fluid sources for the fluid associated with IOCG deposits. It is highly unlikely that mineralization was produced by the evolution of a single fluid and more likely different fluids with different origins contributed to mineralization with fluid mixing playing a major role in the ore deposition.

Part II: Testing ore-forming processes for the origin of the Zn-Pb Bismark deposit: constraints from geochemical modelling and LA ICP MS Analysis of Fluid Inclusions

Chapter 8

Chapter 8 - Geochemical modelling of a Zn-Pb skarn: constraints from LA-ICP-MS Analysis of Fluid Inclusions

Abstract

The Bismark deposit (northern Chihuahua, Mexico) is one of several base metal-rich high-temperature, carbonate-replacement deposits hosted in northern Mexico. Previous fluid inclusion studies based on microthermometry and PIXE have shown that the Zn-rich, Pb-poor Bismark deposit formed from a moderate salinity magmatic fluid (Baker and Lang, 2003; Baker et al., 2004). The exact precipitation mechanisms are unclear and may involve cooling, salinity decrease and wall rock reaction. Furthermore, PIXE data of fluid inclusions suggested that Pb and Zn concentrations were comparable which is inconsistent with the Zn-rich nature of the ore. In this study LA ICP MS analysis was carried out on the same fluid inclusion populations to compare with the PIXE data and the new results are used to model possible ore deposition mechanisms. The new laser ablation data reveal overall lower concentrations of Pb in the ore fluid (average value ~336ppm) than previously indicated by PIXE analysis (average value ~713ppm). Chemical modeling using the new laser ablation data tested the following ore deposition processes: 1) cooling; 2) fluid-rock reaction at constant temperature; 3) cooling and simultaneous fluid-rock interaction. Modeling results show that the gangue and ore minerals observed at Bismark are best reproduced by fluid-rock interaction and simultaneous cooling. Results from the simulations strongly indicate that ore deposition was mainly driven by a pH increase due to the neutralization of the acidic ore fluid (pH

= 3.9) as the result of the reaction with the limestone. Modelling results also suggest that the deposit likely formed under cooling conditions, but do not support the hypothesis of a temperature decrease as the principal ore-forming process.

Keywords: fluid inclusions; LA ICP MS analysis; geochemical modelling; Zn/Pb ratios.

8.1. Introduction

Ore deposition in hydrothermal systems is the result of a complex interplay between several geochemical processes. Geochemical modelling can be used to explore the chemical effects of a wide range of processes and can aid the determination of the most likely mechanism responsible for ore formation. Any geochemical modelling exercise must be approached from an initial conceptual model which is based on well constrained field observations, data collection and a number of geological and geochemical assumptions. The validity of the model is strictly dependent on the quality and quantity of the data and on the consistency of assumptions on which the model is based. In chemical models of geological systems one of the key areas of uncertainty is the chemical composition of the fluids that interacted with the rocks. Fluid inclusions are a sample of the fluids trapped during fluid-rock reactions, but techniques to determine their detailed chemical composition, such as Proton Induced X-ray Emission (PIXE, Ryan et al., 1991; Heinrich et al., 1992; Ryan et al., 1993; Ryan et al., 2001) and Laser Ablation Inductively Coupled Plasma Mass Spectrometry (LA ICP MS; (Gunther et al., 1998; Ulrich et al., 1999; Heinrich et al., 2003), have only recently been developed. Prior to these developments, geochemical modelling studies of fluid-rock

interaction in geological systems have relied upon the assumption that the model fluid composition is controlled by equilibrium with a model rock prior to entering the system (Sverjensky, 1987; Changsheng Lu et al., 1992; Komninou and Sverjensky, 1995; Komninou and Sverjensky, 1996). The latest progress of microanalytical techniques now allows in situ determination of the composition of fluid inclusions. The data from fluid inclusion analysis can now be employed to help constrain the chemical system for input into geochemical models (e.g. Heinrich et al., 2004). In this study results of numerical simulations of ore-forming processes are presented for the Bismark Zn deposit using new LA ICP MS analysis of fluid inclusions to constrain the composition of the model ore-forming fluid. The Bismark deposit is a Zn-rich skarn deposit located in the northern Chihuahua district, Mexico, and the paragenesis of the alteration and the fluid evolution history of this deposit have been described in detail by the previous studies of Baker and Lang (2003) and Baker et al. (2004). The well constrained geology together with the fluid inclusion data make this an ideal case study for geochemical modelling of an ore-forming system. Although these aspects are well constrained it is not clear which key processes led to ore precipitation. Furthermore, PIXE analysis of fluid inclusions indicate a comparable Pb and Zn concentration, in the ore fluid but the ore reserves contain 8% Zn and only 0.5% Pb. In this study new results from LA ICP MS analysis of ore stage fluid inclusions are presented and compared with the existing PIXE data (Baker et al., 2004). The fluid chemical data are then used as input into geochemical simulations of the potential ore forming processes.

8.2. Background Geology & Summary of Previous Studies

The Bismark deposit is a Zn-rich skarn located in the northern Chihuahua district, Mexico (Figure 8.1). The deposit contains Zn (8%), Pb (0.5%), Cu (0.2%) and Ag (50g/t) (Haptonstall, 1994; Baker and Lang, 2003). Rocks in the Bismark area comprise a sequence of massive to thickly-bedded Cretaceous limestones interbedded with thin layers of quartzite and shales, and intruded by a suite of Tertiary igneous rocks (~ 42 Ma K–Ar age on biotite, unpublished internal data of Minera Bismark S.A.) that include the Bismark stock and several dikes and sills (Figure 8.1). Emplacement of the Bismark stock was controlled by the WNW-oriented Bismark and the Diana faults that border the stock on the south and on the north respectively (Baker and Lang, 2003). The intrusion comprises a biotite-rich quartz monzonite porphyry and a minor finer-grained equivalent phase with lesser biotite (Baker and Lang, 2003).

The main ore bodies occur at the contact between the Bismark stock and the carbonate host rock along the Bismark fault. Mineralization is predominantly found as replacement of garnet-pyroxene exoskarn and limestone, in both the foot wall and the hanging wall of the Bismark fault while intrusion-hosted mineralization is rare. The paragenesis of the alteration and mineralization at the Bismark deposit is summarized in Figure 8.2. Alteration of the intrusion consists of three stages that comprise early pervasive potassic (K feldspar, biotite) alteration, later fracture-controlled kaolinite alteration and a final stage of sericite-sulphide alteration. Alteration of the limestone has been subdivided into two main stages: a mostly barren prograde exoskarn that consists primarily of green-garnet of andradite-grossular composition and with quartz, calcite, fluorite, K-feldspar, pyroxene, vesuvianite and trace apatite; the final stages of the prograde skarn include the precipitation of pyrite, pyrrhotite, chalcopyrite and

sphalerite. The later ore stage is composed predominantly of sphalerite, galena, pyrrhotite, pyrite, and chalcopyrite, with gangue calcite, lesser quartz, fluorite and chlorite.

Baker and Lang (2003) have recognized several populations of fluid inclusions at the Bismark deposit characterized by different temperatures and compositions (Table 8.1). The earliest fluid inclusion types comprise high-temperature (400 to 600°C) halite-bearing brine (32 to 62 wt% NaCl equivalent) coexisting with vapour inclusions (>80% vol. vapour) found within early fluorite and predating the main ore stage. A later population of inclusions display critical to near critical behaviour and have salinity estimates ranging between 8.4 and 10.9 wt% NaCl equivalent and homogenization temperatures between 351 to 438°C. These inclusions were found in quartz veins associated with the mineralization and are interpreted to be samples of the ore-forming fluid (Baker et al., 2004). Finally a population of syn- to post-ore liquid-rich fluid inclusions have salinity values that range between 5.1 to 11.8 wt% NaCl equivalent and homogenization temperatures between 104 to 336°C. PIXE analysis on selected fluid inclusions from each population revealed that both early and ore stage fluids are charged with metals and showed that at higher temperature Zn and Pb were preferentially concentrated in the brine whereas Cu partitioned in the coexisting vapour phase (Baker et al., 2004). PIXE analysis of ore stage fluid inclusions also highlighted an apparent difference between the contents of Zn and Pb in the fluid and the ore grade of the deposit. The analyses measured comparable concentrations of Zn and Pb, though the deposit is very Zn-rich (8%) relative to Pb (0.5%). The Pb, however, was commonly below the limit of detection for PIXE and the data presented by Baker et al. (2004) are regarded as the maximum concentrations of Pb in the fluid because the detection limits were used as a maximum estimate. New LA ICP MS analysis carried out in this study

allow for lower detection limits compared to PIXE, thus constraining the uncertainty related to the Pb data (Table 8.2).

Baker and Lang (2003) and Baker et al. (2004) inferred a common magmatic origin for both early and later fluids and interpreted their diversities as the result of the evolution of a magmatic fluid that underwent high temperature phase separation of immiscible brine and vapour, followed by the formation of later lower temperature, lower salinity ore forming fluid that formed in response to changes in temperature and pressure conditions. Similar models have been proposed for the formation of porphyry copper deposits (Shinohara and Hedenquist, 1997) and more recently also for skarns (Meinert et al., 2003). However, the process responsible for ore deposition is still unclear. Baker and Lang (2003) and Baker et al. (2004) proposed the following possible ore deposition mechanisms: temperature decrease, salinity decrease, pressure decrease and reaction of the ore-forming fluid with the host rock. The purpose of this paper is therefore to test ore deposition processes using geochemical modelling and new ore stage fluid inclusion data to constrain the initial composition of the fluid used in the simulations. Initial pressures and temperatures of 200 bars and 350°C were used in the modelling based on results from microthermometric analysis of the ore stage fluid inclusions (Baker and Lang, 2003).

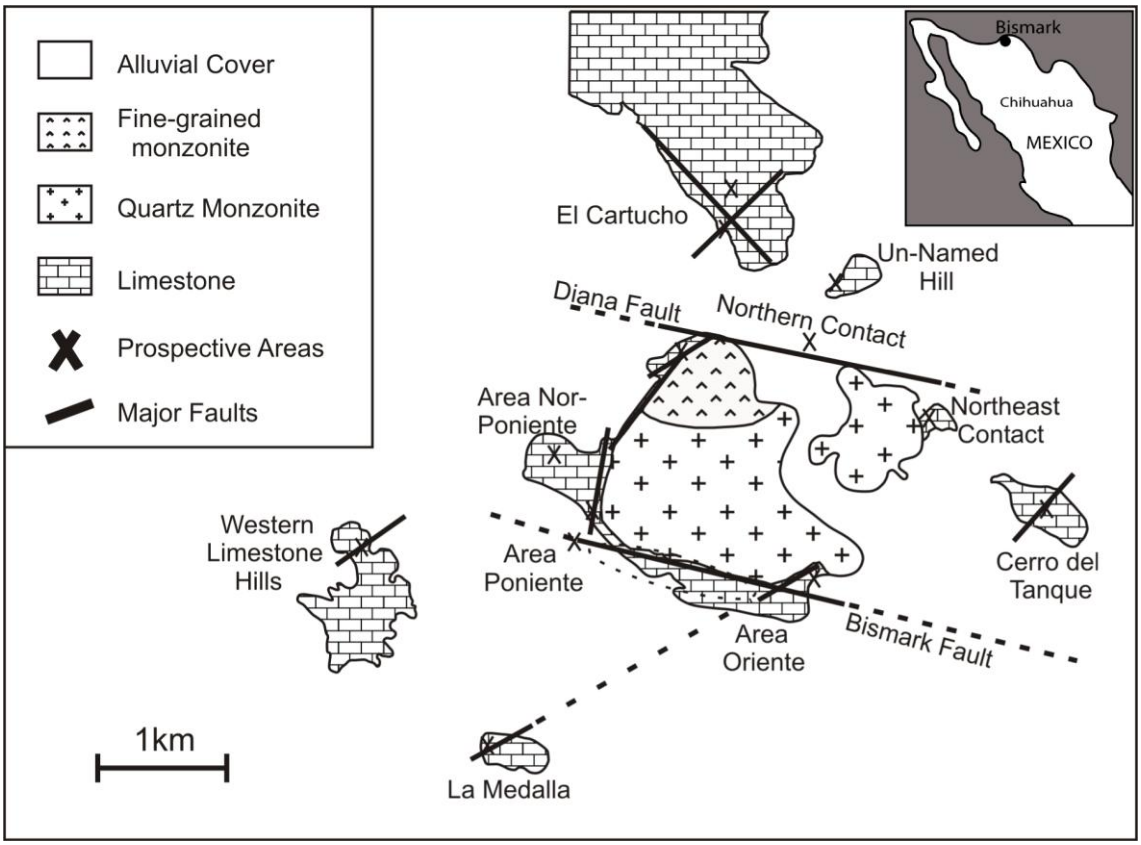

Figure 8.1 Location map and geology of the Bismark deposits, Chihuahua. Modified from Baker & Lang (2003)

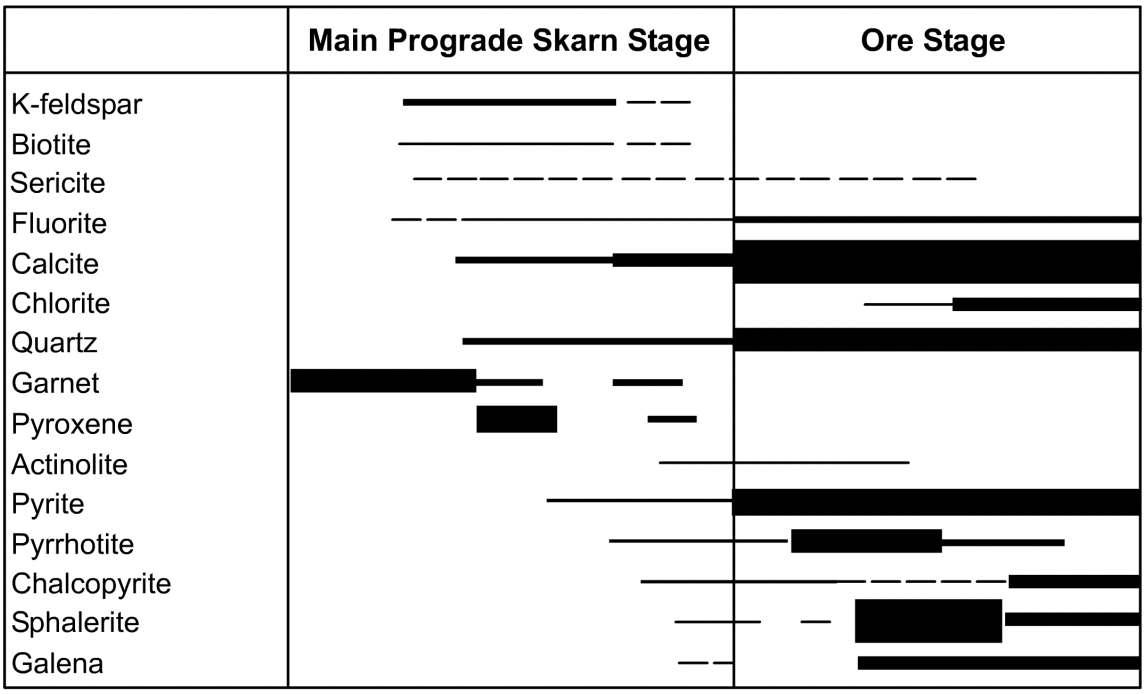

Figure 8.2 Diagram showing the paragenesis of alteration within the limestone at the Bismark deposit. Modified from Baker & Lang (2003)

Table 8.1 Summary of fluid inclusions characteristics of the Bismark deposit. Modified from Baker et Lang (2003)

Type	Phases	V (vol%)	Host	Salinity	Th (°C)
Pre-ore brine	L-V-Hal±Syl±n	<10	Fl, Qtz	32-62	400-600
Pre-ore vapour	V-L	>80	Fl, Qtz, Cal		
Syn-ore critical	L-V±op.	40-60	Qtz	8.4-10.9	351-438
Syn-ore liquid-rich	L-V±op.	10-40	Fl, Qtz, Cal	5.1-11.8	104-336

Table 8.2 PIXE analysis of ore stage low-salinity fluid inclusions from the Bismark deposit. Numbers printed in italic refer to values that are below the detection limits. Conc. = concentration; LOD = limit of detection.

		K	Ca	Fe	Mn	Zn	Cu	Pb	Cl	Zn/Pb	Zn/Cu	Pb/Cu	K/Ca	Fe/Mn	Zn/Fe	Fe/Pb
	Conc. (ppm)	5277	2995	400	395	198	94	*402*	12289	0.5	2.1	4.3	1.8	1	0.5	1
3	LOD (ppm)	163	119	51	60	56	60	459	466							
	Error (ppm)	101	68	36	33	27	26	154	364							
	Conc. (ppm)	22776	2813	559	200	395	349	*954*	56698	0.4	1.1	2.7	8.1	2.8	0.7	0.6
5	LOD (ppm)	192	160	95	109	110	118	954	348							
	Error (ppm)	244	89	51	76	50	58	309	422							
	Conc. (ppm)	31408	4206	588	247	479	474	*935*	94672	0.5	1	2	7.5	2.4	0.8	0.6
7	LOD (ppm)	235	185	97	112	109	115	935	531							
	Error (ppm)	355	125	51	70	53	50	303	515							
	Conc. (ppm)	7405	2348	270	*103*	286	200	*862*	20795	0.3	1.4	4.3	3.2	2.6	1.1	0.3
8	LOD (ppm)	183	153	90	103	104	110	862	316							
	Error (ppm)	147	107	51	75	47	54	283	292							
	Conc. (ppm)	16513	7151	1554	263	1605	336	*1547*	56296	1	4.8	4.6	2.3	5.9	1	1
9	LOD (ppm)	1142	674	184	209	185	205	1547	6962							
	Error (ppm)	605	359	142	115	119	99	496	4667							
	Conc. (ppm)	2070	865	147	138	*46*	104	*465*	4831	0.1	0.4	4.5	2.4	1.1	0.3	0.3
12	LOD (ppm)	270	171	51	62	55	59	465	1267							
	Error (ppm)	137	87	29	36	25	26	150	606							
	Conc. (ppm)	2540	3196	432	164	369	56	*402*	7568	0.9	6.6	7.2	0.8	2.6	0.9	1.1
14	LOD (ppm)	202	135	48	57	52	55	402	770							
	Error (ppm)	117	86	32	31	27	23	133	510							
	Conc. (ppm)	5926	2685	518	102	441	122	332	16026	1.3	3.6	2.7	2.2	5.1	0.9	1.6
15	LOD (ppm)	172	123	41	48	44	47	307	663							
	Error (ppm)	109	92	25	26	27	20	118	401							
	Conc. (ppm)	4069	961	96	115	76	73	*522*	10353	0.1	1	7.2	4.2	0.8	0.8	0.2
16	LOD (ppm)	315	198	57	69	63	64	522	1494							
	Error (ppm)	171	127	31	40	27	30	168	770							
Average		10887	3024	507	192	433	201	713	31059	0.6	2.5	4.4	3.6	2.6	0.8	0.7

8.3. LA ICP MS analysis of fluid inclusions

The chemistry of ore-stage fluid inclusions from the Bismark deposit was determined by LA ICP MS analysis undertaken at the facilities of Research School of Earth Sciences of the Australian National University. The instrumentation employed combines a 193nm excimer laser (Lambda Physik, Germany) to open the inclusion and volatilize its content, and an Agilent 7500s ICP MS which analyzes the ablated material (Gunther et al., 1998; Heinrich et al., 2003). The technique provides multi-element analysis and quantitative measurement of element ratios. The value of Na determined from microthermometry (3.7 wt%, average composition of ore stage fluid inclusions at Bismark; Baker and Lang, 2003) was used as internal standard to convert the element ratios to absolute concentrations (Gunther et al., 1998; Heinrich et al., 2003). Analytical precision using Na as an internal standard is typically within 20% (Gunther et al., 1998; Heinrich et al., 2003). Detection limits are highly variable and must be determined for each element in each inclusion because they are a function of the mass of the element, the size and shape of the inclusion and the number of elements measured from a single inclusion (Heinrich et al., 2003). Standard detection limits for fluid inclusions of 25μm are in the μg range (Heinrich et al., 2003). Uncertainties are primarily linked to imperfect sampling of inclusions, particularly of inclusions containing daughter crystals (Heinrich et al., 2003).

A total of 11 low salinity ore stage fluid inclusions were analysed, all from the same sample of syn-ore quartz vein (Table 8.3). Here results are presented only for the elements that we used in our modelling simulations: K, Ca, F, Mg, Mn, Zn, Cu, Pb, and Ag (Table 8.3, Figure 8.3). The data reveal high concentrations of K and Ca ranging from about 23000 to approximately 100000 ppm and from around 7000 to about 56000

ppm respectively. Magnesium content in the fluid varies from approximately 400 ppm to around 6000 ppm. The fluid carries a considerable concentration of metals: Fe and Zn are particularly enriched in the fluid, displaying average concentrations higher than 1000 ppm while Cu, Pb and Ag concentrations are generally lower than 1000 ppm. Manganese concentrations range from 120 to 535 ppm.

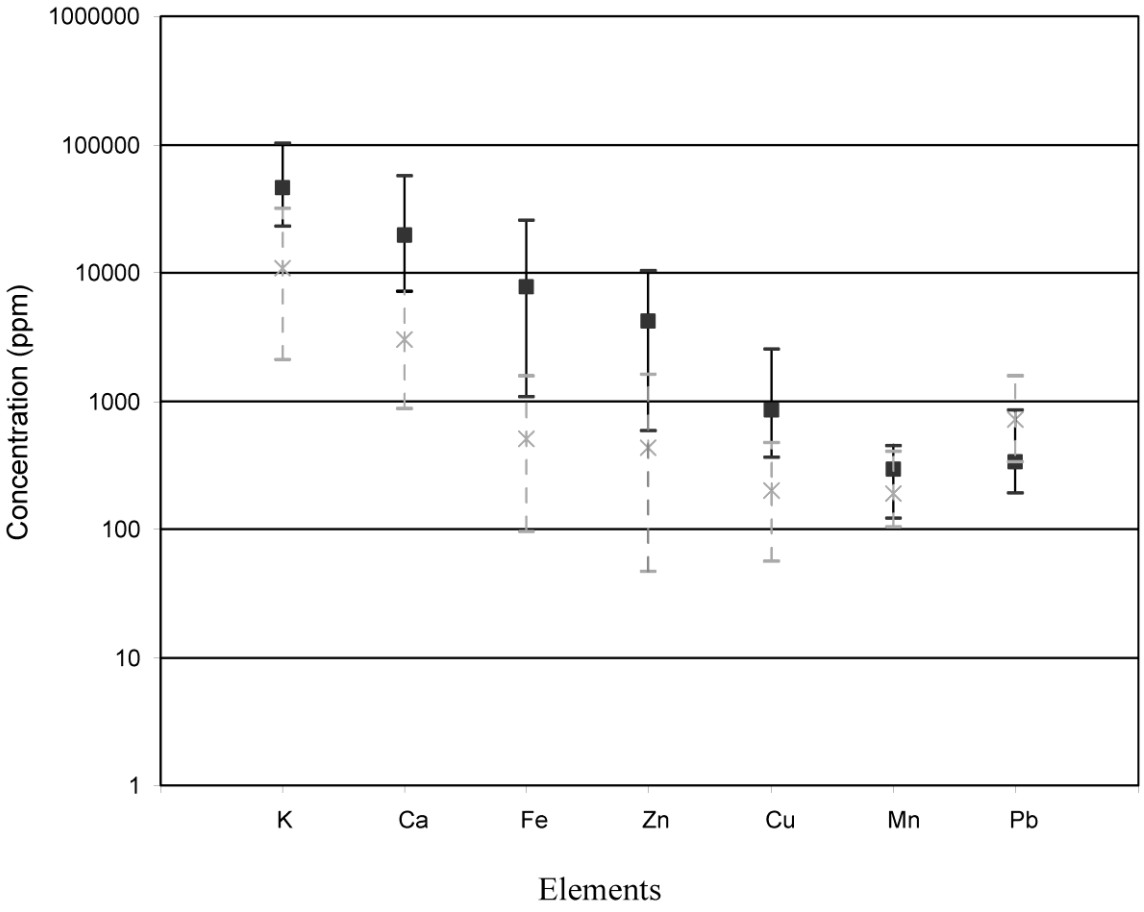

Figure 8.3 Element concentrations determined by LA ICP MS (represented in black) and PIXE (represented in grey). Bars represent the range of concentrations of each element in the fluid; squares and crosses indicate the average concentrations of each element determined by LA ICP MS and PIXE respectively.

Table 8.3 LA ICP MS analysis of ore stage low-salinity fluid inclusions from the Bismark deposit. Values in ppm. Numbers printed in italic refer to values that are below the detection limits.

	5	*7*	*6*	*8*	*52*	*53*	*57*	*60 A*	*60 B*	*61*	*62*	*Average*
K	36340	41983	37191	54951	32180	22998	50467	38009	35170	101083	44961	45030
Ca	7884	7575	22109	12372	11649	21581	56106	*7011*	18548	29286	20926	19550
Mg	1444	467	439	2670	965	849	5946	2253	756	1624	1970	1762
Fe	1184	1070	5124	2767	25482	3269	15824	7871	10188	6808	4483	7643
Zn	1454	583	3168	2638	3303	2501	10368	6630	8211	4112	3078	4186
Cu	703	413	743	734	705	564	2502	356	712	716	1100	841
Mn	249	323	419	120	254	353	303	338	151	267	441	293
Pb	206	188	285	368	282	221	839	377	300	375	249	336
Ag	3.47	3.15	8.98	2.11	*3.25*	*1.41*	26.93	3.27	1.42	*6.68*	*6.49*	6
Zn/Pb	7.1	3.1	11.1	7.2	11.7	11.3	12.4	17.6	27.4	11.0	12.4	12.0
Zn/Cu	2.1	1.4	4.3	3.6	4.7	4.4	4.1	18.6	11.5	5.7	2.8	5.8
Pb/Cu	0.3	0.5	0.4	0.5	0.4	0.4	0.3	1.1	0.4	0.5	0.2	0.5
K/Ca	4.6	5.5	1.7	4.4	2.8	1.1	0.9	5.4	1.9	3.5	2.1	3.4
Fe/Mn	4.8	3.3	12.2	23.1	100.4	9.3	52.1	23.3	67.6	25.5	10.2	33.8
Zn/Fe	1.2	0.5	0.6	1.0	0.1	0.8	0.7	0.8	0.8	0.6	0.7	1.0
Fe/Pb	5.8	5.7	18.0	7.5	90.3	14.8	18.9	20.9	33.9	18.1	18.0	140.6

8.4. Comparison of LA ICP MS and PIXE data

In this section results obtained from PIXE analysis by (Baker et al., 2004) are compared with laser ablation analysis of ore stage fluid inclusions measured in this study. The discussion is restricted to elements measured with both techniques. The range of calculated absolute values and average values for each element from each dataset are plotted in Figure 8.3. The comparison of the two datasets shows that absolute element concentrations measured by the PIXE method are consistently lower than those obtained from laser ablation for all the elements except Pb and Mn. The systematic error between the two datasets (excluding Pb and Mn) likely reflects the different quantification processes employed by the two techniques (Ryan et al., 1991; Heinrich et al., 1992; Ryan et al., 1993; Ryan et al., 2001; Heinrich et al., 2003). Quantification of PIXE analysis requires modelling of the fluid inclusion geometry and estimation of depth and thickness all of which may result in significant errors (up to 30 %; Heinrich et al., 1992). Geometry related errors result from the deviation of the actual inclusion shape to that of a modelled ellipse (Ryan et al., 1991; Heinrich et al., 1992). Depth in particular affects the determination of concentrations of light elements due to absorption of low-energy X-rays (K lines for $Z < 21$ and L lines for $Z < 50$) producing, for example, errors of more than 50 percent in Cl concentrations for depth uncertainty of ±1.5μm (Heinrich et al., 1992). However, high-energy X-rays (K lines $Z > 25$ and L lines $Z > 60$) are less sensitive to depth. Uncertainties in the thickness of the inclusions create errors in the estimation of their volume that may produce an approximate proportional error in the element concentrations (Ryan et al., 1991). Heterogeneities in the inclusion, such as the presence of vapour and/or daughter phases represent additional sources of error in the element concentrations due to variations in X-ray

absorption and variations in beam intensity for different vapour bubble and/or crystal position (Ryan et al., 1991; Heinrich et al., 1992).

By comparison LA ICP MS does not suffer depth-related or inclusion size and geometry problems as much as PIXE (Heinrich et al., 2003; Allan et al., 2005). Detection limits do depend on the inclusion size but the detection limits are typically significantly lower than PIXE (ppm to ppb compared with tens of ppm respectively; Ryan et al., 1991; Heinrich et al., 1992; Ryan et al., 1993; Ryan et al., 2001; Heinrich et al., 2003; Allan et al., 2005). Imperfect ablation of inclusions, especially of those containing daughter phases, can be an additional problem, and care also needs to be taken when selecting an internal standard (Heinrich et al., 2003). In this case, Na was chosen and a value of 37400ppm was applied to convert element ratios obtained from the analysis to absolute element concentrations. This corresponds to ~ 9.6 wt % NaCl equivalent which is the average salinity of the inclusions determined from microthermometry (Baker and Lang, 2003). The total salinity range for the inclusions varies from 8.4 to 10.9 wt % NaCl equivalent (~33000 to 43000 ppm Na). The maximum and minimum Na values were used to recalculate the absolute element concentrations, and resulted in maximum absolute concentration increasing by an average of ~15 % and minimum absolute concentrations reduced by an average of ~12%. Further explanation for the different concentrations measured by the two techniques may be found in the natural variability that characterizes fluid inclusions even within the same populations (observed by an order of magnitude variation in almost the entire suite of element concentrations measured), however, this is unlikely to result in systematic differences between the two techniques in this case where the same inclusion populations, and indeed some of the same inclusions, have been analyzed.

In order to remove the affects of the quantification procedures, and assess how well the two data sets compare, element ratios were calculated (Tables 8.2 and 8.3) and plotted on X-Y scatter plots (Figure 8.4). The results show excellent correlation between the two datasets for interelement ratios that include K, Ca, Fe, Zn and to a lesser extent Cu, however, comparison of ratios that use Mn and Pb are poor. Lead PIXE data are mostly below detection limits (shown in italics in Table 8.2 and considered a maximum concentration estimate), whereas Mn PIXE data are mostly near detection limits when considering the analytical error (Table 8.2). It therefore seems that the laser ablation data, with much lower detection limits than PIXE, provides a better estimate of the fluid composition. Interestingly the ore grade ratios for Zn, Pb and Cu also have a better correlation with the laser ablation data than PIXE (Figure 8.4D).

An important purpose of comparing the data was to select a reliable single analysis to apply to the modelling of ore-forming processes for the Bismark deposit. The LA data were selected for the modelling experiment because of the low detection limits for Pb and Mn and the fact that all other elements appear to be proportionally similar between the two analytical methods. In particular, inclusion 53 was chosen to constrain the initial fluid composition because of the good overlapping displayed between the two sets of data (Figure 8.4).

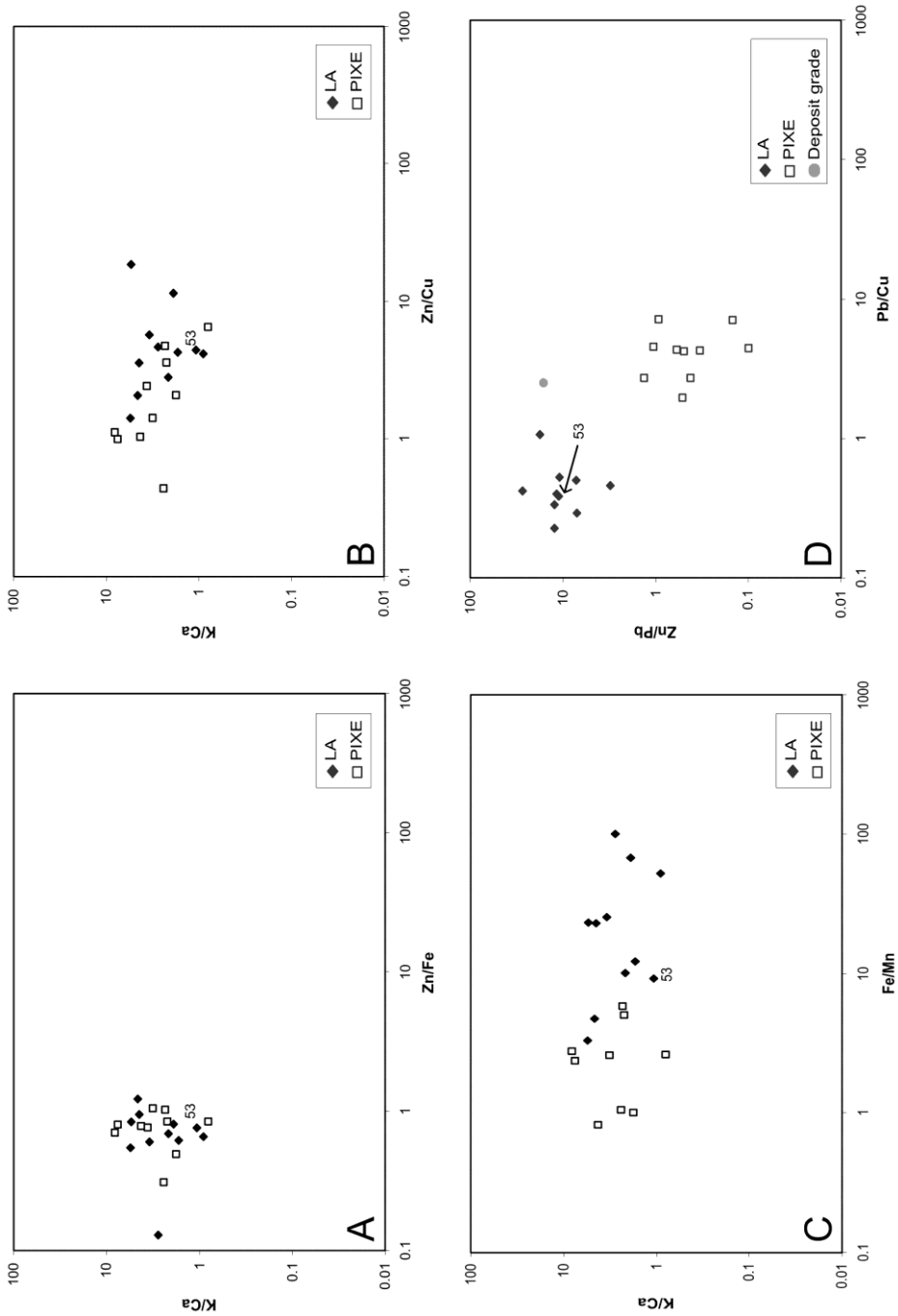

Figure 8.4 Scatter plot illustrating the interelement ratio variation between PIXE and LA ICP MS. K, Ca, Fe and Zn correlate well between the two techniques (A), whereas ratio plots including Pb and Mn have a poor correlation (B, C and D). D also illustrates that the metal ratios from LA ICP MS are more consistent with the deposit ore grade ratio. Fluid inclusion 53 was chosen to constrain the initial fluid composition used in the modelling simulations.

8.5. Geochemical modelling

8.5.1. Overview of the method

Thermodynamic calculations were carried out using the program React included in The Geochemists Workbench (GWB) software package (Bethke, 1996; Bethke, 2002). React can model equilibrium states and chemical reactions of systems involving an aqueous phase, minerals and gases. React was used to determine the initial composition of the fluid for the simulations and to run simulations of ore-forming processes. The thermodynamic dataset used was specifically created for this study case to fit the T-P conditions (350°C, 200 bars) at which the deposit is thought to have formed. These are higher than the T-P working conditions of GWB default datafiles (temperatures up to 300°C and pressures along the curve of water). The source of thermodynamic data was the Geoscience Australia's version of the UNITHERM database (Bastrakov, 2003), a utility database included in HCh software package (Shvarov and Bastrakov, 1999), consistent with the freeGs database (Bastrakov et al., 2004). Within the UNITHERM database, the selected thermodynamic data for the majority of aluminosilicates and for carbonates were compiled by Berman (1988). The rest of the mineral data as well as data for aqueous species were taken from a modified SUPCRT database (Pokrovskii et al., 1998). The file containing the thermodynamic data was then adapted to the GWB environment using utilities developed by Cleverley and Bastrakov (2005). Activity coefficients for aqueous species are calculated based on method described by Helgeson (1969).

8.5.2. Fluid composition

The ore fluid composition used in the simulations was reconstructed utilizing the laser ablation data of the low salinity inclusions at Bismark and from phase equilibria relationships. It was assumed that the fluid was in equilibrium with the late main skarn mineral assemblage consisting of quartz, pyrite, fluorite, pyrrhotite, chalcopyrite, muscovite and minor sphalerite (Figure 8.2). The pre-ore assemblage also includes calcite, which, however, does not occur throughout the deposit. The fluid was not set in equibrilium with calcite in the assumption that the fluid had not reacted enough with the rock to be in equilibrium with calcite. Here the steps followed to define the fluid composition are summarized (Table 8.4):

1. Element concentrations of Ca, K, Fe, Zn, Pb, Mg, Mn, and Ag were taken from the laser ablation data of fluid inclusion 53. The concentration of Fe was set to a slightly higher value (4500 ppm) than the one of the inclusion (3269 ppm) to allow for the coexistence of pyrrhotite and pyrite which occur together in the deposit mineral assemblage.
2. Pyrite, quartz, fluorite, chalcopyrite and K-feldspar were used to constrain the amount of total sulphur, $SiO_{2(aq)}$, F, Cu and Al respectively. Copper was constrained by setting chalcopyrite in the initial system in order to increase the amount of total sulphur and allow the simultaneous equilibrium of pyrite, chalcopyrite and pyrrhotite.
3. Temperature (350°C), pressure (200 bar), Na (37000 ppm) and Cl (58000 ppm) contents were defined by microthermometric studies (Baker and Lang, 2003).

4. CO_2 was set equal to 0.01 molality unit, based on previous studies on a similar skarn system (Changsheng Lu et al., 1992), because no data on CO_2 content were available from Bismark.
5. Oxygen fugacity was calculated based on the assumption of the coexistence of pyrrhotite and pyrite at the conditions of the model.
6. The pH value was set at 4 that provides equilibrium with muscovite.

The equilibrium fluid was saturated with quartz, pyrite, sphalerite, pyrite, pyrrhotite, chalcopyrite, and muscovite. The concentration of major elements largely reflects the element concentrations set initially to constrain the system; Zn concentration in the final fluid (2000 ppm) is slightly less than in the fluid inclusion (2501 ppm). Copper concentration in the final fluid (36 ppm) is one order of magnitude less than in the fluid inclusion (564 ppm). However, this latter value was obtained by setting chalcopyrite for Cu in the initial system and not the inclusion content. Attempts at setting copper concentrations in the initial system invariably lead to low copper concentrations in the final fluid, suggesting that Cu has probably low solubility in such fluid conditions. The final oxidation state ($\log fO_2$ = -31.019) and pH (3.9) of the fluid does not vary significantly from the input data ($\log fO_2$ = -31.3 and pH = 4). Data relative to the distribution of aqueous species for Zn, Pb, Cu and Fe show that these elements are transported mainly as chloride complexes.

Table 8.4 Input data used to constrain the initial fluid composition of the fluid used for simulation of ore-forming processes.

Elements		
Analyzed		
K+	from LA analysis	22998
Ca++	“	21581
Mg++	“	849
Mn++	“	353
Fe++	“	4500
Zn++	“	2501
Pb++	“	221
Ag+	“	3.3
Cl-	from microthermometry	58000
Na+	“	37400
Calculated at 350°C and 200 bar (ppm)		
H_2S(aq)	Equilibrium with pyrrhotite	2952
SiO_2(aq)	Equilibrium with quartz	618
Al+++	Equilibrium with kfeldspar	18.7
Cu+	Equilibrium with chalcopyrite	34.8
F-	Equilibrium with fluorite	111
pH		3.9
logfO_2		-31.019
CO_2(aq)		440

8.5.3. Process modeling

The first model tested is an example of a polythermal path model that in our case consists of a temperature decrease from 350°C to 100°C at a constant rate through a series of steps; at the end of each step the program calculates the new equilibrium state

of the system. The second model tested the reaction of the ore fluid with the host rock. It is an example of a titration model in which a fixed amount of rock is progressively added to the initial system. This type of model is useful to identify the series of reactions taking place when a rock reacts with fluid of a given composition, as well as recognize the type of alteration produced by the reactions. For our simulation of fluid-rock interaction we used 100 g of rock reacting with 1.3 kg of fluid. The composition of the rock has been reconstructed in order to be representative of the real composition of the host rock at Bismark and consists of 90 % calcite, 5 % quartz, 3 % kaolinite and 2 % clinochlore. The final process tested represents a combination of the previous two, i.e. fluid-rock interaction and simultaneous cooling.

8.6. Results

8.6.1. Temperature decrease

The predicted mineral assemblage from the cooling simulation includes three main stages (Figure 8.5A): at higher temperature the system comprises quartz, pyrite, minor muscovite and fluorite (T = 350-320°C), followed by a pyrite-quartz stage (T = 320-150°C) and finally at lower temperature the mineral assemblages include sphalerite, pyrite and quartz with minor chalcopyrite (already present for T < 240°C) and a little acanthite (T 140-125°C). Changes in the fluid composition comprise a decrease in the concentrations of $SiO_{2\ (aq)}$, $H_2S_{\ (aq)}$, Cu, Zn and Fe due to the precipitation of quartz, chalcopyrite, sphalerite, pyrite and acanthite (not shown in Figure 8.5A due to the very low amount precipitated; Figure 8.5B). The oxygen fugacity of the system and the pH rapidly decrease from log -31 to log -61 and from 3.9 to 1.1 respectively due to the lack of any mineral to buffer the system (Figure 8.5C).

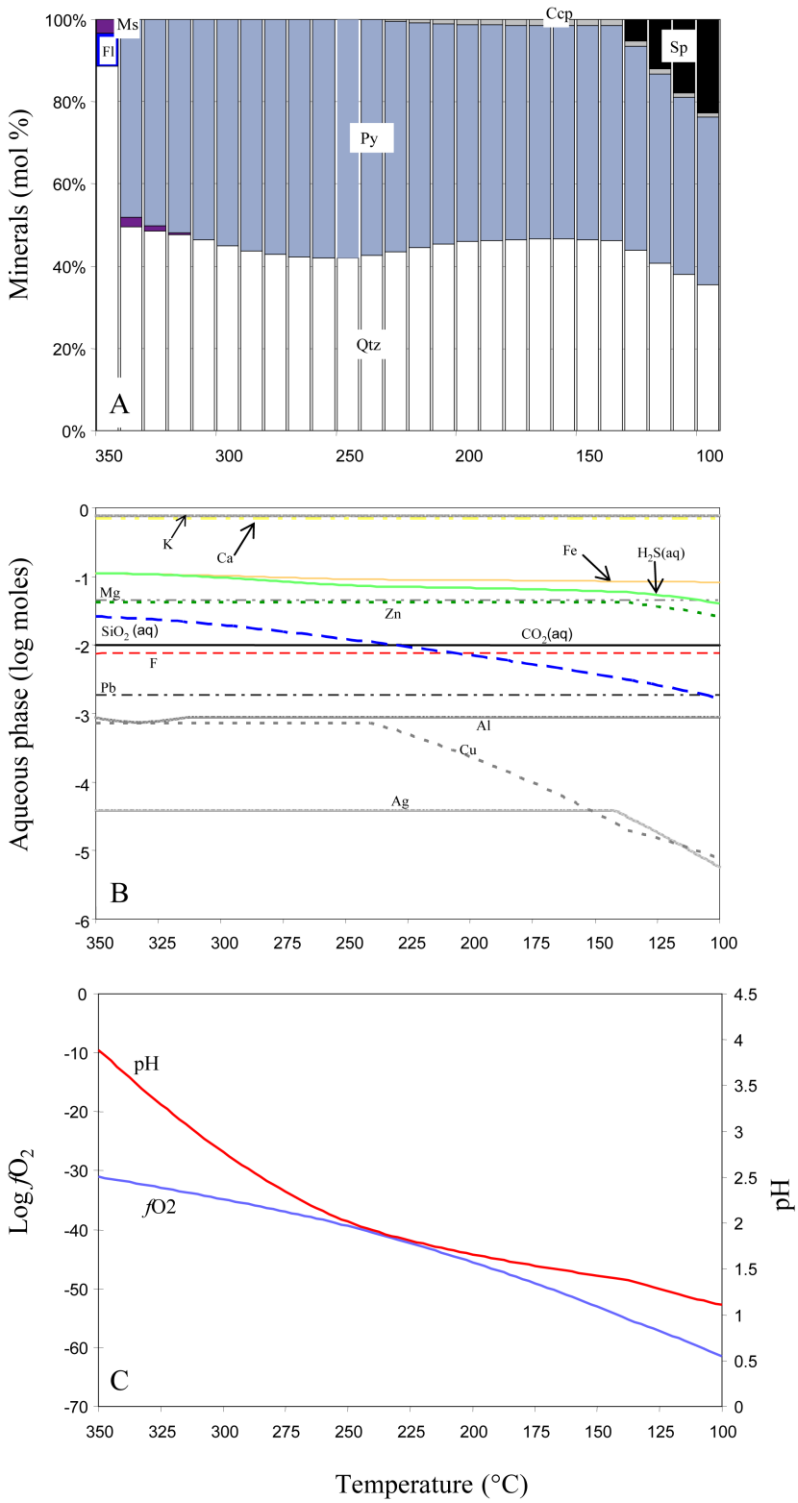

Figure 8.5 Mineral assemblages, composition of the aqueous phase and gases resulting from cooling the ore fluid from 350°C to 100°C. (A) Alteration and ore mineral assemblages (the acanthite concentration was very low and cannot be visualized); (B) Total element concentrations; (C) pH and oxygen fugacity. Mineral abbreviation after Kretz (1983): chalcopyrite (ccp), fluorite (fl), muscovite (ms), quartz (qtz), pyrite (py), sphalerite (sp).

8.6.2. Host rock reaction

The fluid-rock interaction at constant temperature and pressure (T = 350°C, P = 200 bar) initially precipitates pyrrhotite, sphalerite, quartz, muscovite and fluorite (Figures 8.6A and 6B). As new rock is added to the fluid, quartz and muscovite are rapidly consumed and the initial stage minerals are replaced by the simultaneous precipitation of a sequence of skarn minerals and sulfides (Figures 8.6A and 6B). Skarn minerals predicted include Mg-chlorite, talc, tremolite, diopside, epidote, and calcite. Development of skarn alteration is synchronous with the precipitation of ore minerals: pyrrhotite and sphalerite precipitate initially and further progression of the reaction yields a rapid increase in their amounts together with the precipitation of magnetite, galena and chalcopyrite (chalcopyrite is among the minerals that precipitate initially but is then redissolved in the fluid when less than 10 grams of rock has reacted and then it precipitates again along with the other ore minerals; Figure 8.6B). The sulfide precipitation is driven by an increase in the pH due to the reaction between the acidic fluid (pH = 3.9) and the carbonate rock (Figure 8.6D). The neutralization reaction consumes hydrogen forcing the pH to rise and consequently reducing the stability of Cl-complexes, leading to sulfide precipitation. The pH stops rising when calcite equilibrates with the fluid. Thus, one can consider the reaction completed when calcite precipitates for 23 grams of rock reacted. The subsequent reaction produces a few changes that mainly consist of variations in the abundances of minerals. However, epidote is also precipitated and continuing reactions convert tremolite to diopside and diopside back to tremolite (Figure 8.6B). The mineral assemblage when calcite first appears consists of pyrrhotite (45 %), sphalerite (29.6 %), magnetite (13 %), tremolite (3.3 %), clinochlore (2.9 %), calcite (2.8 %), fluorite (2.7 %), galena (0.4 %) and

chalcopyrite (0.3 %). Changes in the fluid composition reflect the evolution of the mineral assemblages during the reaction (Figure 8.6C). The concentrations of Fe, Mg, Al, Zn, F, $H_2S_{(aq)}$, and $SiO_{2(aq)}$ significantly decrease (more than one order of magnitude) in the interval 0-23 grams of rock reacted due to the precipitation of ore and alteration minerals. The fluid is depleted by lesser amounts in Cu and Pb with concentrations decreasing less than one order of magnitude due to the precipitation of chalcopyrite and galena respectively (Figure 8.6C). In this interval the concentration of $CO_{2(aq)}$ rapidly increases from 0.01 to 0.2 moles as shown in Figure 8.6C as a result of calcite consumption to neutralize the fluid. After calcite equilibrates with the fluid there are no major further changes in the fluid composition, except an increase of aluminum, due to the dissolution of talc and the decrease of chlorite content, and a drop in the magnesium concentration caused by the precipitation of diopside (Figures 8.6B and 8.6C).

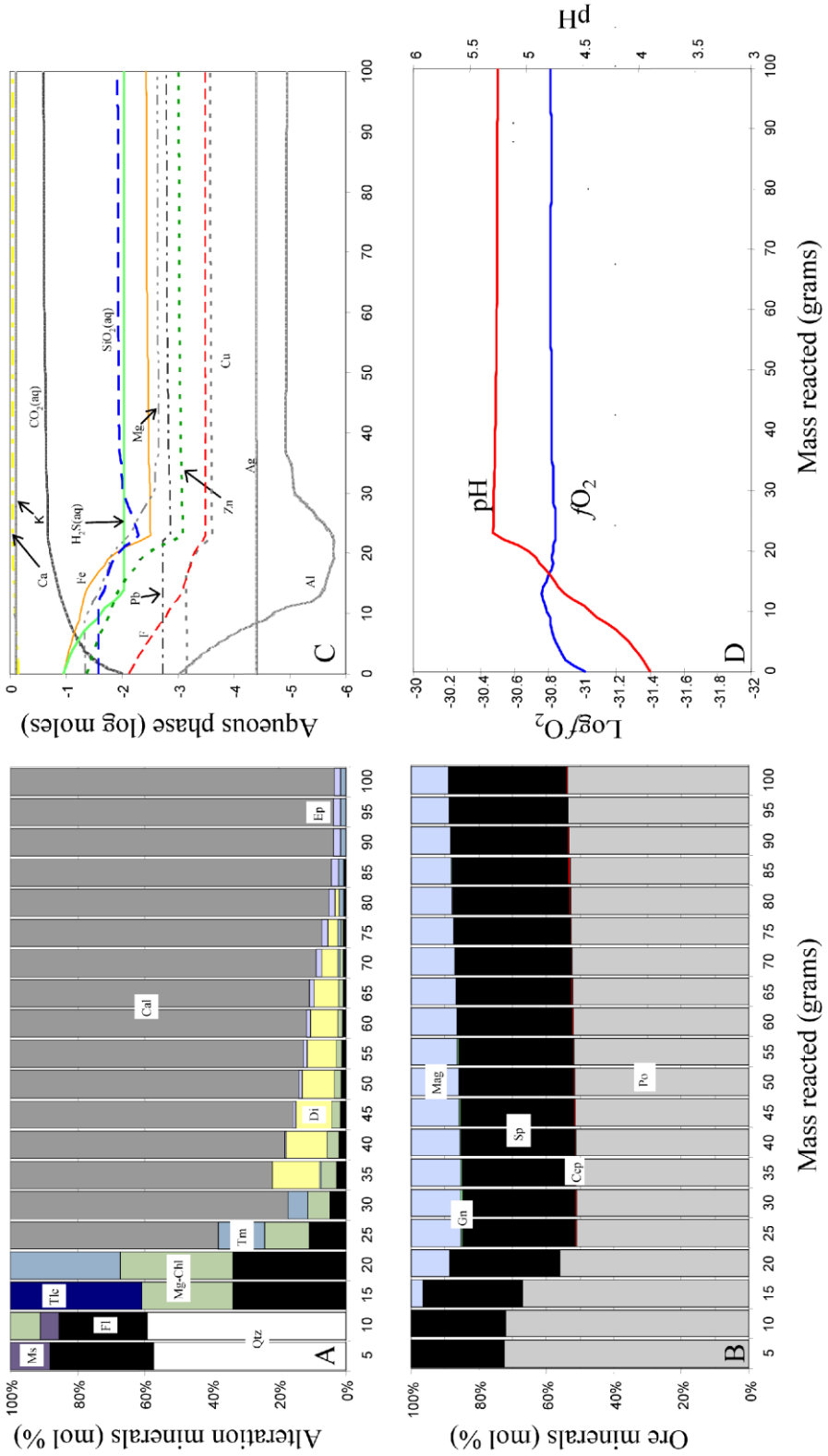

Figure 8.6 Results of reaction of the ore fluid (1.3kg) with host rock (100g) at constant temperature (350°C) in terms of (A) alteration minerals, (B) ore minerals (C) composition of the aqueous phase, (D) pH and oxygen fugacity. Mineral abbreviation after Kretz (1983): calcite (cal), chalcopyrite (ccp), diopside (di), epidote (ep), fluorite (fl),galena (gn), magnesium-chlorite (mg-chl), magnetite (mag), muscovite (ms), quartz (qtz), pyrrhotite (po), sphalerite (sp), talc (tlc), tremolite (tr).

8.6.3. Host rock reaction and cooling

The results of a fluid-host rock reaction with cooling are shown in Figures 8.7A-D. For high fluid/rock ratio the resulting mineral assemblage consists mainly of pyrrhotite and sphalerite with pyrite, quartz and lesser muscovite and fluorite (Figures 8.7A and 8.7B). As in the case of a fluid reacting with the host rock, the initial mineral assemblage is replaced at lower fluid/rock ratio and lower temperature by a series of skarn minerals and sulfides. Skarn minerals include talc, chlorite, and calcite (Figure 8.7A). Sulfide minerals at this stage comprise abundant pyrrhotite, sphalerite, magnetite and lesser galena and chalcopyrite (Figure 8.7B). Pyrite present in the initial stage is replaced by pyrrhotite (Figure 8.7B). The precipitation of sulfide is again controlled by the increase in pH due to the neutralization of the acidic fluid (Figure 8.7D). The pH stops increasing when calcite precipitates at 22 grams of rock reacted. The mineral assemblage now consists of pyrrhotite (48.9 %), sphalerite (28.9 %), magnetite (11.6 %), clinochlore (2.7 %), fluorite (2.6 %), tremolite (1.8 %), talc (1.3 %), calcite (1.1 %) and chalcopyrite (0.5 %). The fluid at this stage is depleted by more than one order of magnitude in Fe, Al, Zn, Cu, Fl and $H_2S_{(aq)}$ and to a lesser extent in Pb, Mg and $SiO_{2(aq)}$ (Figure 8.7C). By further adding rock mass to the fluid and lowering the temperature the reaction precipitates carbonates (siderite and dolomite), K-feldspar, quartz and graphite that leaves the fluid depleted in $CO_{2\ (aq)}$, $SiO_{2(aq)}$, Fe and K (Figures 8.7A and 8.7C). Ore minerals in this late stage include abundant pyrite and sphalerite and lesser galena, chalcopyrite and acanthite. Pyrrhotite is no longer stable at lower temperature and is replaced by pyrite.

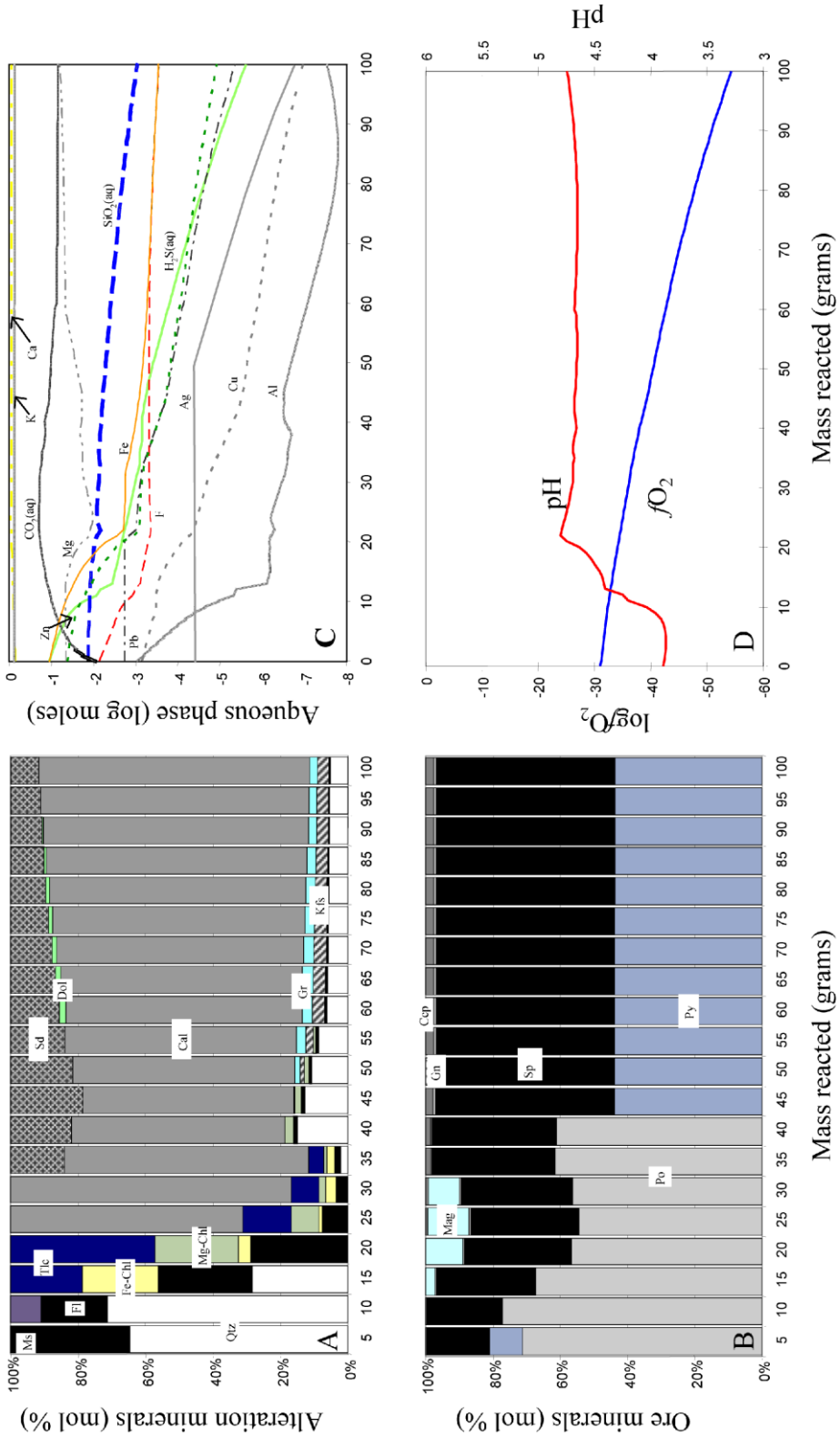

Figure 8.7 Results of ore fluid- host rock interaction (1.3kg-100g) and cooling of the system from 350°C to 100°C. A) alteration minerals, (B) ore minerals (C) composition of the aqueous phase, (D) pH and oxygen fugacity. Mineral abbreviation after Kretz (1983): calcite (cal), chalcopyrite (ccp), dolomite (dol), ferroan-chlorite (fe-chl), fluorite (fl),galena (gn), graphite (gr), kfeldspars (kfs), magnesium-chlorite (mg-chl), magnetite (mag), muscovite (ms), quartz (qtz), pyrite (py), pyrrhotite (po), sphalerite (sp), siderite (sd), talc (tlc).

8.7. Discussion of modelling results and comparison with the Bismark ore stage minerals assemblage

The simulation of ore formation through just cooling process correctly predicts part of the assemblage observed at the Bismark deposit (Figure 8.5A), however, the model does not produce pyrrhotite, galena and skarn minerals. The latter is expected, since there is no carbonate rock available. All these observations suggest that cooling alone was not responsible for skarn alteration and sulfide deposition, but was likely a contributing factor in the formation of the Bismark deposit.

The simulation of fluid-rock reaction reproduces with good approximation both ore and gangue minerals present at the Bismark deposit (Figures 8.6A and 8.6B). The alteration minerals produced show a reasonably good correspondence with the skarn assemblage at Bismark, the only difference is the presence of tremolite instead of actinolite, but this is probably due to the inability of GWB to model solid solutions (Bethke, 1996; Bethke, 2002). On the other hand the model predicts minerals not present at Bismark, such as epidote and talc. A complete skarn sequence comprises early anhydrous skarn followed by the precipitation of hydrous calc-silicates and sulfide. The model only predicts the formation of a hydrous skarn with anhydrous skarn represented by a small amount of pyroxene. The explanation is most likely the relatively low temperature (350°C) used in the calculation, because prograde skarn assemblages usually form at temperatures ranging from 650 to 400°C (Einaudi, 1981). In terms of ore minerals, the fluid-rock simulation correctly predicts pyrrhotite, sphalerite, galena and chalcopyrite, but magnetite is not observed at the Bismark deposit. Relative abundances are also consistent to those observed at Bismark with sphalerite more abundant than galena, however, the model fails to produce pyrite and silver. Sulfides

precipitate during the first phases of the reaction in the interval 0-23 grams of rock reacted with the fluid. In this interval the pH increased from 3.9 to 5.3, while the other parameters that may cause ore precipitation are constant (e.g. temperature, pressure and oxidation state; Figure 8.6D). When calcite equilibrates with the fluid the pH stops increasing resulting in the cessation of sulfide precipitation. The abundance of sulfide does not significantly vary as the reaction continues. These observations suggest that the primary control on ore deposition was the pH increase due to the reaction between the fluid and the dominantly carbonate host rock. This is confirmed in the result of the last process tested.

Simulation of fluid-rock reaction and simultaneous cooling presents a good prediction of ore and gangue minerals and offers the best matches between modelling results and the natural system (Figures 8.7A and 8.7B). All the ore phases observed at the Bismark deposit are predicted by the model and their relative abundances are consistent with those of the deposit. Alteration minerals can be subdivided into two different stages; 1) at high temperature and high fluid/rock ratio the alteration assemblage is very similar to those produced for the simple reaction with the host rock (chlorite, talc, fluorite, tremolite and calcite); 2) at lower temperature and lower fluid/rock ratio these minerals are replaced (excluding calcite) by retrograde alteration phases siderite, dolomite, quartz, K-feldspar and graphite. Talc and graphite are not observed at Bismark, whereas K-feldspar is present during the early stages of skarn development. Finally, calcite, siderite and dolomite carbonates are present in the final phase of the ore stage. As in the previous process sulfide precipitated during the first phases of the reaction in the interval 0-22 grams of rock reacted with the fluid. At this stage the temperature is still high (342°C), while pH values increase from 3.9 to 4.9, providing further evidence that the primary control on ore deposition was the reaction

with the carbonate host rock (Figure 8.7D). Further progressing of the reaction leads to the precipitation of pyrite which replaced pyrrhotite (Figure 8.7B). The pyrite-pyrrhotite transition is primarily controlled by temperature variations. The equilibrium between pyrite and pyrrhotite at constant temperature and pressure depends on the fO_2, with pyrite and pyrrhotite stable at higher and lower fO_2 values respectively. As the temperature decrease, as it is the case here, the pyrite-pyrrhotite equilibrium shifts towards lower fO_2 values. The fO_2 decreases as the reaction progresses but not enough to stabilize pyrrhotite (Figure 8.7D). This observation indicates that the temperature decrease was a key factor in controlling the precipitation of pyrrhotite first and its later transition to pyrite.

8.8. Conclusions

Geochemical modeling simulations allow to draw some important conclusions on the genesis of the Bismark deposit and some considerations on the behavior of zinc and lead in skarn deposits in general.

1. The modelling results indicate that ore deposition was the result of fluid neutralization caused by the reaction with the limestone host rock. This hypothesis is supported by the precipitation of sulfide in correspondence of the sudden increase of the pH in the first steps of the fluid-rock reaction. A temperature variation is likely to have contributed to ore deposition, particularly to the precipitation of pyrite, though simple fluid cooling was not the main mechanism that led to the formation of the Bismark deposit.

2. The trials, together with the analysis of the laser ablation data of ore stage fluid inclusions, also demonstrate that the amount of Zn and Pb precipitating from the ore fluid are dependent on the initial concentrations of Zn and Pb of the fluid.
3. Results from the modelling, in particular the close reproduction of ore stage minerals of the Bismark deposit, support the application of fluid inclusion data to constrain geochemical modelling simulations as a valuable method to investigate geochemical processes.

Microanalytical results show excellent correlation between laser ablation and PIXE data for most interelement ratios, although laser ablation provides a better estimate of the fluid composition due to its higher sensitivity compared to PIXE.

Chapter 9

Chapter 9 - Conclusions

9.1. Genesis of the Suicide Ridge Breccia Pipe and implication for the formation of sodic (-calcic) alteration in the Cloncurry district

Evidence from field relationships, breccia characteristics, mineralogy and textures of granite clasts within the pipe and fluid inclusion studies support an origin of the SRBP in response to fluid overpressuring generated by the release and expansion of fluids from a crystallizing magma beneath and adjacent to the pipe. Whilst this model is in broad in agreement with models proposed by Burnham (1985), the depth of formation contrasts greatly, being up to 4-5 km for subvolcanic environments (Burnham, 1985) and in excess of 10 km for the SRBP (Pattison et al., 2002; Oliver et al., 2006; Rubenach et al., 2007). At this depth high fluid pressures were most likely generated by the release of CO_2 from the magma as indicated by the abundant CO_2-only fluid inclusions observed in primary magmatic textures in granite breccia clasts. CO_2 fluid inclusions are generally abundant in deep magmatic-related deposits due to the lower solubility of CO_2 compared to H_2O (Webster and Holloway, 1988; Fogel and Rutherford, 1990; Thompson et al, 1999; Baker and Lang, 2001; Blank et al., 1993), supporting the idea that when a magma reaches volatile saturation the first fluid exsolved must be CO_2 (Nabelek and Ternes, 1997). CO_2-only fluid inclusions record large pressure variations and in particular significant overpressuring conditions (> 1 kbar) that are interpreted as the driving force that caused brecciation and provide evidence that large amounts of potentially catastrophic energy can be released from felsic magma at significant depth. The CO_2 was most likely sourced from mafic magmas

emplaced during the Williams-Naraku igneous event, in particular through processes of felsic-mafic magma mixing and mingling commonly observed throughout the Cloncurry District. Alternatively, CO_2 may have been sourced from devolatilization of calcite-rich calc-silicate rocks (Kendrick et al., 2007a). High fluid pressures produced by magmatic bodies in response to cooling and crystallization were invoked to explain the formation of other breccia pipe occurrences in the Cloncurry district (Oliver et al., 2006).

The evolution of the SRBP system following the initiation of brecciation is characterized by a later influx of fluids that produced widespread pervasive albitic alteration. Abundant sodic (-calcic) fluid inclusions were clearly linked to albite alteration by petrographic and cathodoluminescence analysis and are interpreted to represent the fluid that produced albitic alteration commonly widespread within breccias and host rock. The origin of fluids responsible for Na-(Ca) alteration temporally associated with the emplacement of the Williams Batholith in the Cloncurry district is controversial and proposed models include a dominant magmatic source (Mark, 1998; Mark and Foster, 2000; Perring et al., 2000; Pollard, 2001) and a dominant crustal evaporitic and/or halite dissolution origin for the these fluids (Barton and Johnson, 1996; Barton and Johnson 2000; Kendrick et al., 2007a). Results from this study indicate halogen signatures compatible with a dominant bittern-derived source of salinity for the fluid that produced extensive albitization similar to other regional fluids (Kendrick et al., 2007a). The mixed CO_2-aqueous inclusions are likely responsible for the halogen signature of fluids in granite breccia samples, consistent with either a magmatic or halite dissolution origin of the fluid. Albitization at the SRBP was likely produced by a hot externally-derived fluid that acquired Na and Cl from the interaction of evaporitic sequences and that was heated by a magmatic source that provided the

necessary heat to promote its circulation. This is consistent with the model proposed by Barton and Johnson (1996; 2000) and Kendrick et al. (2007a) for the formation of albitization in terrains that contain IOCG mineralization.

9.2. Fluid geochemistry insights into the evolution and formation of the Eloise Cu-Au deposit

Results from LA ICP MS analysis of multisolid and halite-bearing fluid inclusions from Eloise together with host rocks, alteration and mineralization geochemistry (Baker, 1998) and fluid sources (Kendrick et al., 2006) are not consistent with hypothesis of the evolution of a single magmatic-derived fluid for the genesis of Eloise. Instead the data indicate the presence of at least two fluids with possibly different origins. Several lines of evidence suggest that fluid mixing occurred at Eloise. These include the significant drop in salinity between early ultrasaline brines and later high salinity halite-bearing fluid inclusions that cannot be attributed to precipitation of Cl-bearing minerals but most likely resulted of fluid mixing between the ultrasaline and a later less saline fluid. Fluid mixing is also consistent with the variation of fluid inclusion chemistry across the deposit and the general variability of absolute and relative element concentrations observed even between inclusions of the same type. Together these data support an origin for the halite-bearing fluid inclusions by mixing between a hot, ultrasaline fluid and a later lower salinity fluid. Another indication of fluid mixing is represented by the S-poor nature of the multisolid fluid inclusions,

suggested by the generally high Ba concentrations, that, together with the oxidized nature of the host rock at Eloise, support the hypothesis that S was introduced in the system by a second fluid (cf Williams et al, 2001). However, the nature of the S-bearing fluid is uncertain and possible sources of S include later halite-bearing fluid inclusions and CO_2-rich fluid inclusions (cf Oliver et al., 2004). Overall, these observations support an origin for Cu-Au mineralization at Eloise in response to fluid mixing between hot, ultrasaline Cu-bearing, S-poor fluid, evolving as the result of cooling and wall rock reaction as it migrated in northerly direction, and mixed with a S-bearing cooler fluid. Halogen and noble gas values for multisolid and halite-bearing fluid inclusions are compatible with halite dissolution origin, or of fluid mixing between halite dissolution water and a magmatic fluid (Kendrick et al., 2006).

9.3. Regional vs IOCG fluids – Implication for formation of IOCG

Barren regional fluids were compared with fluids associated with IOCG deposits in the Eastern Fold Belt to reveal the key ingredient for the formation of mineralization. Fluid inclusions associated with the barren breccia pipe are similar to fluid inclusions in barren regional albite alteration (Fu et al., 2003; de Jong and Williams, 1995). However, the key difference between the barren breccia pipe and IOCG deposits is the absence in the former of multisolid high salinity, high temperature fluid inclusions, suggesting that these were critical for the formation of IOCG deposits. Chemical analysis reported in this and other studies indicate that these fluids carry significant amount of metals (e.g

Cu ~ 1000 ppm at Starra; Williams et al., 2001) supporting the generally accepted hypothesis that they represent the ore-forming fluid.

9.4. Testing ore-forming processes for the origin of the Zn-Pb Bismark deposit: constraints from geochemical modelling and LA ICP MS analysis of fluid inclusions

The geochemical modeling simulations of possible depositional processes for the formation the Bismark Zn deposit indicate that ore deposition was the result primarily of fluid neutralization caused by the reaction with the limestone host rock. This hypothesis is supported by the precipitation of sulfide in correspondence with the sudden increase of the pH in the first steps of the fluid-rock reaction. Cooling likely contributed to ore deposition, particularly in the precipitation of pyrite, though simple fluid cooling alone was not the main mechanism that led to ore formation. Results from modelling simulations and laser ablation analysis of ore stage fluid inclusions also demonstrate that the amount of Zn and Pb precipitating from the ore fluid are dependent on the initial concentrations of Zn and Pb of the fluid.

The modeling results, and particularly the close reproduction of ore stage minerals of the Bismark deposit, validate the application of fluid inclusion analytical data to constrain geochemical modelling simulations as an effective and relatively inexpensive method to quickly test specific hypotheses about ore genesis and in general to investigate geochemical processes. However, the modelling process relies on

appropriate thermodynamic data and these are currently unavailable for the fluid chemistry and conditions found in hydrothermal systems in the Cloncurry district.

9.5. Future work

The analysis of mixed CO_2-aqueous fluid inclusions was challenging and unfortunately the data collected did not allow a full appraisal of their composition. Further investigation is needed for mixed CO_2-aqueous fluid inclusions to clarify their origin (i.e. homogeneous vs heterogeneous entrapment) and the role played in the process of pressure build-up. The brecciation model presented here could be further refined by a detailed study of fluids associated with breccia related granites in the Cloncurry district. The source of CO_2 also needs further investigation, and this could be addressed by isotopic analysis of fluid inclusions from the SRBP or similar occurrences in the Cloncurry district. Detailed fluid inclusion studies should also be carried out in rocks that potentially sourced CO_2 (i.e. mafic and calcite-rich calc-silicate rocks).

Recent fluid inclusions research in IOCG deposits has predominantly focused on brine inclusions, while little attention has been paid to CO_2 fluid inclusions. Further investigation of these inclusions is needed to clarify their role in the mineralization process, particularly for their potential role in transporting volatiles (i.e. S). Further work is also needed to constrain the source of fluids associated with IOCG. Geochemical modelling simulations of potential ore forming processes would be useful to constrain genetic models for IOGC. However, application of thermodynamic simulations to model complex, highly saline fluids is still limited by the scarce

knowledge of the thermodynamic properties of such fluids. An improvement of the current thermodynamic data is needed in order to enable an accurate prediction of the variations of aqueous properties (e.g. activities) in response to external modifications (e.g. variation in pressure-temperature conditions, reaction with a fluid or rock).

References

Adshead, N.D., 1995. Geology, alteration and geochemistry of the Osborne Cu-Au Deposit, Cloncurry District, N.W. Queensland, Australia. Unpublished PhD Thesis, James Cook University, Townsville, 382 pp.

Adshead, N.D., 1996. The role of hypersaline hydrothermal fluids in the formation of the Osborne Cu-Au deposit, Cloncurry District, NW Queensland. In T. Baker, J.F. Rtherham, J. M. Richmond, G.Mark, P. J. Williams (Editors), MIC '96; New developments in metallogenic research; the McArthur-Mount Isa-Cloncurry minerals province, James Cook University EGRU Contribution, 55: 1-4.

Adshead, N.D., Voulgaris, P. and Muscio, V.N., 1998. Osborne copper-gold deposit. In Geology of Australian and Papua New Guinean mineral deposits, Australasian Institute of Mining Monograph Series, 22:793-799.

Adshead-Bell, N.S., 1998. Evolution of the Starra and Selwyn high-strain zones, Eastern fold belt, Mount Isa Inlier; implications for Au-Cu mineralization. Economic Geology, 93(8): 1450-1462.

Allan, M.M., 2006. Hydrothermal processes in the Mount Leyshon intrusive complex, Australia. Microanalytical insights. Unpublished PhD Thesis, The University of Leeds, Leeds, 321 pp.

Allan, M.M. Yardley, B. W. D., Forbes, L. J., Shmulovich, K. I., Banks, D. A. and Shepherd, T. J., 2005. Validation of LA-ICP-MS fluid inclusion analysis with synthetic fluid inclusions. American Mineralogist, 90(11-12): 1767-1775.

Baker, T., 1996. The geology and genesis of the Eloise Cu-Au deposit, Cloncurry District, N.W. Queensland, Australia. PhD Thesis (Unpublished). School of Earth Sciences, James Cook University, Townsville, 287 p.

Baker, T., 1998. Alteration, mineralization, and fluid evolution at the Eloise Cu-Au deposit, Cloncurry District, Northwest Queensland, Australia. Economic Geology, 93: 1213-1236.

Baker, T., 2006. Micrometallogeny of hydrothermal fluids. Project F3 Final Report, predictive mineral discovery Cooperative Research Centre, 44 p.

Baker, T. and Laing, W.P., 1998. The Eloise Cu-Au deposit, East Mt Isa Block: structural environment and structural controls on ore. Australian Journal of Earth Sciences, 45(3): 429-444.

Baker, T. and Lang, J.R., 2001. Fluid inclusion characteristics of intrusion-related gold mineralization, Tombstone tungsten magmatic belt, Yukon Territory, Canada Mineralium Deposita 36(6): 563-582.

Baker, T. and Lang, J.R., 2003. Reconciling fluid inclusion types, fluid processes, and fluid sources in skarns: an example from the Bismark Deposit, Mexico. Mineralium Deposita, 38: 474-495.

Baker, T., Bertelli, M., Fisher, L., Fu, B., Hodgson, W., Kendrick, M., Mark, G., Mustard, R., Ryan, C., Williams, P.J., 2006. Salt and copper in iron oxide-copper-gold systems, Cloncurry district, Australia. Geochimica et Cosmochimica Acta, 70(18, Supplement 1): A30.

Baker, T., Perkins, C., Blake, K.L. and Williams, P.J., 2001. Radiogenic and Stable Isotope Constraints on the Genesis of the Eloise Cu-Au Deposit, Cloncurry District, Northwest Queensland. Economic Geology, 96(4): 723-742.

Baker, T., van Achterberg, E., Ryan, C.G. and Lang, J.R., 2004. Composition and evolution of ore fluids in a magmatic-hydrothermal skarn deposit. Geology (Boulder), 32(2): 117-120.

Bakker, R.J., 1997. Clathrates: Computer programs to calculate fluid inclusion V-X properties using clathrate melting temperatures. Computers & Geosciences, 23(1): 1-18.

Bakker, R.J., 2003. Package FLUIDS; 1, Computer programs for analysis of fluid inclusion data and for modelling bulk fluid properties. Chemical Geology, 194(1-3): 3-23.

Bakker, R.J. and Brown, P.E., 2003. Computer modeling in fluid inclusion research. In: I. Samson, A. Anderson, D. Marshall (Editors), Fluid Inclusions: Analysis and Interpretation, Mineralogical Association of Canada, Short Course Volume 32, pp. 75-212.

Banks, D.A. and Yardley, B.W.D., 1992. Crush-leach analysis of fluid inclusions in small natural and synthetic samples. Geochimica et Cosmochimica Acta, 56(1): 245-248.

Banks, D.A., Giuliani, G., Yardley, B.W.D. and Cheilletz, A., 2000. Emerald mineralisation in Colombia; fluid chemistry and the role of brine mixing Mineralium Deposita 35(8): 699-713.

Barker, D.S., 1970. Compositions of granophyre, myrmekite, and graphic granite. GSA Bulletin, 81(11): 3339-3350.

Barton, M.D. and Johnson, D.A., 1996. Evaporitic-source model for igneous-related Fe oxide-(REE-Cu-Au-U) mineralization. Geology, 24(3): 259-262.

Barton, M.D. and Johnson, D.A., 2000. Alternative brine sources for Fe-oxide(-Cu-Au) systems; implications for hydrothermal alteration and metals. In: Porter, T.M., (Editor), Hydrothermal iron oxide copper-gold and related deposits; a global perspective, Australian Mineral Foundation, Glenside, South Aust., Vol. 1, pp. 43-60.

Bastrakov, E., 2003. Geoscience Australia version of UNITHERM database for the HCh package for geochemical modelling. Unpublished computer file.

Bastrakov, E., Shvarov, Y., Girvan, S., Cleverley, J. and L, W., 2004. FreeGs: web-enabled thermodynamic database for modelling of geochemical processes. In McPhie J., McGoldrick P. (Eds), Dynamic Earth: Past, Present and Future. Abstracts - Geological Society of Australia (2004), 73 52

Beardsmore, T.J., 1992. Petrogenesis of Mount Dore-style breccia-hosted copper ± gold mineralization in the Kuridala-Selwyn region of northwestern Queensland. PhD Thesis (Unpublished). School of Earth Sciences, James Cook University, Townsville 292 p.

Bell, T.H., 1983. Thrusting and duplex formation at Mount Isa, Queensland, Australia. Nature, 304(5926): 493-497.

Berman, R.G., 1988. Internally-consistent thermodynamic data for minerals in the system Na2O–K2O–CaO–MgO–FeO–Fe2O3–Al2O3–SiO2–TiO2–H2O–CO2. Journal of Petrology, 29(2): 445-522.

Bethke, C., 1996. Geochemical reaction modeling; concepts and applications. Oxford University Press, New York, 397 pp.

Bethke, C.M., 2002. The Geochemist's Workbench, Release 4.0. University of Illinois, USA.

Betts, P. Giles, D., Mark, G., Lister, G., Goleby, B. and Aillères, L., 2006. Synthesis of the proterozoic evolution of the Mt Isa Inlier. Australian Journal of Earth Sciences, 53(1): 187-211.

Binder, G. and Troll, G., 1989. Coupled anion substitution in natural carbon-bearing apatites Contributions to Mineralogy and Petrology 101(4): 394-401.

Blake, D.H., 1987. Geology of the Mount Isa inlier and environs, Queensland and Northern Territory. BMR Geol. Geophys. Bull., 225, 83 pp.

Blake, D.H. and Stewart, A.J., 1992. Stratigraphic framework, Mount Isa Inlier. In: Blake, D.H. and Stewart, A.J., (Editors), Detailed studies of the Mount Isa Inlier. AGSO Bulletin, 243: 1-12.

Blank, J.G. and Brooker, R.A., 1994. Experimental studies of carbon dioxide in silicate melts; solubility, speciation, and stable carbon isotope behavior. Reviews in Mineralogy and Geochemistry, 30(1): 157-186.

Blank, J.G., Stolper, E.M. and Carroll, M.R., 1993. Solubilities of carbon dioxide and water in rhyolitic melt at 850° C and 750 bars Earth and Planetary Science Letters 119(1-2): 27-36.

Bodnar, R.J., 1993. Revised equation and table for determining the freezing point depression of H2O-NaCl solutions. Geochimica et Cosmochimica Acta, 57(3): 683-684.

Bodnar, R.J., 1994. Synthetic fluid inclusions; XII, The system H_2O-NaCl; experimental determination of the halite liquidus and isochores for a 40 wt% NaCl solution. Geochimica et Cosmochimica Acta, 58(3): 1053-1063.

Bodon, S.B., 1998. Paragenetic relationships and their implications for ore genesis at the Cannington Ag-Pb-Zn deposit, Mount Isa Inlier, Queensland, Australia. Economic Geology, 93(8): 1463-1488.

Bohlke, J.K. and Irwin, J.J., 1992a. Brine history indicated by argon, krypton, chlorine, bromine, and iodine analyses of fluid inclusions from the mississippi valley type lead-fluorite-barite deposits at Hansonburg, New Mexico Earth and Planetary Science Letters 110(1-4): 51-66.

Bohlke, J.K. and Irwin, J.J., 1992b. Laser microprobe analyses of Cl, Br, I, and K in fluid inclusions; implications for sources of salinity in some ancient hydrothermal fluids. In Current research on fluid inclusions; PACROFI III; papers presented at the Third biennial pan-American conference on Fluid inclusions. Geochimica et Cosmochimica Acta, 56(1): 203-225.

Boiron, M.-C. and Dubessy, J., 1994. Determination of fluid inclusions compositions: Microanalytical techniques. In: B. De Vivo, M. L. Frezzotti (Editors), Fluid inclusions in minerals: Methods and application, Short Course Volume, Virginia Polytechnic Institute and State University, pp. 45-71.

Bottrell, S.H. and Yardley, B.W.D., 1988. The composition of a primary granite-derived ore fluid from S.W. England, determined by fluid inclusion analysis. Geochimica et Cosmochimica Acta, 52(2): 585-588.

Bowers, T.S. and Helgeson, H.C., 1983. Calculation of the thermodynamic and geochemical consequences of nonideal mixing in the system H_2O-CO_2-NaCl on phase relations in geologic systems; equation of state for H_2O-CO_2-NaCl fluids at high pressures and temperatures Geochimica et Cosmochimica Acta 47(7): 1247-1275.

Brown, P.E., 1989. FLINCOR; a microcomputer program for the reduction and investigation of fluid-inclusion data. American Mineralogist, 74(11-12): 1390-1393.

Brown, P.E. and Lamb, W.M., 1989. P-V-T properties of fluids in the system $H_2O \pm CO_2 \pm NaCl$; new graphical presentations and implications for fluid inclusion studies. Geochimica et Cosmochimica Acta, 53(6): 1209-1221.

Buhn, B. and Rankin, A.H., 1999. Composition of natural, volatile-rich Na-Ca-REE-Sr carbonatitic fluids trapped in fluid inclusions. Geochimica et Cosmochimica Acta, 63(22): 3781-3797.

Burke, E.A.J., 2001. Raman microspectrometry of fluid inclusions. Lithos, 55(1-4): 139-158.

Burnham, C.W., 1985. Energy release in subvolcanic environments; implications for breccia formation. Economic Geology, 80(6): 1515-1522.

Burruss, R.C., 1981. Analysis of phase equilibria in C-O-H-S fluid inclusions. In: L.S. Hollister and M.L. Crawford (Editors), Fluid inclusions, applications to petrology. Mineralogical Association of Canada, Short Course Handbook 6, pp. 39-74.

Burruss, R.C., 2003. Raman Spectroscopy of Fluid Inclusions, In: Samson, I., Anderson A., and Marshall D. (Editors), Fluid Inclusions: Analysis and Interpretation, Mineralogical Association of Canada, Short Course Volume 32, pp. 279-289.

Cauzid, J. Philippot, P., Somogyi, A., Ménez, B., Simionovici, A. and Bleuet, 2006. Standardless quantification of single fluid inclusions using synchrotron radiation induced X-ray fluorescence. Chemical Geology, 227(3-4): 165-183.

Cauzid, J., Philippot, P., Somogyi, A., Simionovici, A. and Bleuet, P., 2004. Quantification of Single Fluid Inclusions by Combining Synchrotron Radiation-Induced-X-ray Fluorescence and Transmission. Anal. Chem., 76(14): 3988-3994.

Changsheng Lu, Reed, M.H. and Misra, K.C., 1992. Zinc-lead skarn mineralization at Tin Creek, Alaska: Fluid inclusions and skarn-forming reactions*1. Geochimica et Cosmochimica Acta, 56(1): 109-119.

Chapman, L.H. and Williams, P.J., 1998. Evolution of pyroxene-pyroxenoid-garnet alteration at the Cannington Ag-Pb-Zn deposit, Cloncurry District, Queensland, Australia. Economic Geology, 93(8): 1390-1405.

Cleverley, J.S. and Bastrakov, E.N., 2005. K2GWB: Utility for generating thermodynamic data files for The Geochemist's Workbench(R) at 0-1000 [deg]C and 1-5000 bar from UT2K and the UNITHERM database. Computers & Geosciences, 31(6): 756-767.

Davis, B.K., Davis, B. K., Pollard, P. J., Lally, J. H., McNaughton, N. J., Blake, K. and Williams, P. J., 2001. Deformation history of the Naraku Batholith, Mt Isa Inlier, Australia; implications for pluton ages and geometries from structural study of the Dipvale Granodiorite and Levian Granite. Australian Journal of Earth Sciences, 48(1): 113-129.

de Jong, G. and Williams, P.J., 1995. Giant metasomatic system formed during exhumation of mid-crustal Proterozoic rocks in the vicinity of the Cloncurry Fault, Northwest Queensland. Australian Journal of Earth Sciences, 42(3): 281-290.

Derrick, G.M., 1977. Metasomatic hystory and origin of uranium mineralization at Mary Kathleen, northwest Queensland. BMR Journal of Australian Geology and Geophysics, 2: 123-130.

Derrick, G.M., 1980. Marraba, Queensland, 1:100 000 Geological Map Commentary. Bureau of Mineral Resources, Canberra.

Diamond, L.w., 2003. Introduction to gas-bearing, aqueous fluid inclusions. In: I. Samson, A. Anderson, D. Marshall (Editors), Fluid Inclusions: Analysis and Interpretation, Mineralogical Association of Canada, Short Course Volume 32, pp. 101-158.

Dixon, G. and Davidson, G.J., 1996. Stable isotope evidence for thermochemical sulfate reduction in the Dugald River (Australia) strata-bound shale-hosted zinc-lead deposit Chemical Geology 129(3-4): 227-246.

Drever, H.I. and Johnston, R., 1957. Crystal growth of forsteritic olivine in magmas and melts. Transactions of the Royal Society of Edinburgh, 63,: 289-315.

Duan, Z., Moller, N. and Weare, J.H., 1992a. An equation of state for the CH4-CO2-H2O system: I. Pure systems from 0 to 1000°C and 0 to 8000 bar. Geochimica et Cosmochimica Acta, 56(7): 2605-2617.

Duan, Z., Moller, N. and Weare, J.H., 1992b. An equation of state for the CH4-CO2-H2O system: II. Mixtures from 50 to 1000°C and 0 to 1000 bar. Geochimica et Cosmochimica Acta, 56(7): 2619-2631.

Dubessy, J., Poty, B. and Ramboz, C., 1989. Advances in C-O-H-N-S fluid geochemistry based on micro-Raman spectrometric analysis of fluid inclusions European Journal of Mineralogy 1(4): 517-534.

Ebadi, A. and Johannes, W., 1991. Beginning of melting and composition of first melts in the system Qz-Ab-Or-H_2O-CO_2. Contributions to Mineralogy and Petrology, 106(3): 286-295.

Einaudi, M.T., Meinert, L.D., and Newberry, R.J., 1981. Skarn deposits. In Skinner, B.J. (Ed.), Economic Geology seventy-fifth anniversary volume. Boulder, Colorado, Society of Economic Geologists, p. 317–391.

Fenn, P.M., 1977. The nucleation and growth of alkali feldspars from hydrous melts The Canadian Mineralogist 15, Part 2: 135-161.

Fisher, L.A., Kendrick, M.A. and Mustard, R., 2005. Noble gas and halogen evidence for the source of mineralizing fluids in the Osborne IOCG deposit, Mt Isa Inlier, Australia. In: Hancock, H. et al. (Editors), Structure Tectonics and Ore Mineralisation Processes (STOMP), James Cook University, Townsville, Australia, p 49.

Fogel, R.A. and Rutherford, M.J., 1990. The solubility of carbon dioxide in rhyolitic melts; a quantitative FTIR study. American Mineralogist, 75(11-12): 1311-1326.

Folch, A. and Marti, J., 1998. The generation of overpressure in felsic magma chambers by replenishment Earth and Planetary Science Letters 163(1-4): 301-314.

Fontes, J.C. and Matray, J.M., 1993. Geochemistry and origin of formation brines from the Paris Basin, France Chemical Geology 109(1-4): 149-175.

Foster, D. and Rubenach, M., 2006. Isograd pattern and regional low-pressure, high-temperature metamorphism of pelitic, mafic and calc-silicate rocks along an east-west section through the Mt Isa Inlier. Australian Journal of Earth Sciences, 53(1): 167-186.

Foster, D.R.W. and Austin, J.R., 2007. The 1800 to 1610 Ma stratigraphic and magmatic history of the Eastern Succession, Mount Isa Inlier, and correlations with adjacent paleoproterozoic terranes. Precambrian Research, accepted manuscript.

Frantz, J.D. Frantz, J. D., Mao, H. K., Zhang, Y.G., Wu, Y., Thompson, A. C., Underwood, J. H. Giauque, R. D., Jones, K. W., Rivers, M. L., 1988. Analysis of fluid inclusions by X-ray fluorescence using synchrotron radiation. Chemical Geology, 69(3-4): 235-244.

Fu, B. Baker, T., Oliver, N.H.S., Williams, P.J., Ulrich, T., Mernagh, T.P., van Achterberg, E., Ryan, C.G., Marshall, L.J., Rubenach, M.J., Mark, G., Yardley, B.W.D., 2004a. Regional fluid compositions of the Mount Isa Eastern Succession, NW Queensland, Australia. In Barnicoat, A.C., and Korsch, R.J., (eds.). Predictive Mineral Discovery Cooperative Research Centre – Extended Abstracts from the June 2004 Conference. Geocience Australia, Record 2004/9, pp. 63-66.

Fu, B. Oliver, N.H.S., Baker, T., Williams, P.J., Marshall, L.J., Rubenach, M.J., Ulrich, T., van Achterberg, E., Ryan, C.G., and Yardley, B.W.D., 2004b. Microanalysis of regional fluids from the Eastern Succession of the Mount Isa Block, NW Queensland. Predictive mineral discovery under cover; SEG conference and exhibition; extended abstracts 33: 378-382.

Fu, B., Williams PJ, Oliver NHS, Dong G, Pollard PJ, Mark G., 2003. Fluid mixing versus unmixing as an ore-forming process in the Cloncurry Fe-oxide-Cu-Au district, NW Queensland, Australia; evidence from fluid inclusions. In Proceedings of Geofluids IV, Journal of Geochemical Exploration, 78-79, 617-622.

Garrels, R.M. and Mackenzie, F.T., 1967. Origin of the chemical compositions of some springs and lakes, [Chapter] 10. In equilibrium concepts in natural water systems-Am. Chem. Soc., 151st Ann. Mtg., Pittsburgh, 1966, Div. Water, Air and Waste Chemistry Symposium, pp. 222-242.

Garrels, R.M. and Thompson, M.E., 1962. A chemical model for sea water at 25 degrees C and one atmosphere total pressure American Journal of Science 260(1): 57-66.

Gauthier, L., Hall, G., Stein, H. and Schaltegger, U., 2001. The Osborne deposit, Cloncurry district: a 1595 Ma Cu–Au skarn deposit. In: Williams P. J. ed. A Hydrothermal Odyssey, New Developments in Metalliferous Hydrothermal Systems Research, James Cook EGRU, 59: pp. 58 – 59.

Giles, D. and Nutman, A.P., 2003. SHRIMP U-Pb zircon dating of the host rocks of the Cannington Ag-Pb-Zn deposit, southeastern Mt. Isa Block, Australia Australian Journal of Earth Sciences 50(3): 295-309.

Gleeson, S.A., 2003. Bulk analysis of electrolytes in fluid inclusions, In: Samson, I., Anderson A., and Marshall D., (Editors), Fluid Inclusions: Analysis and Interpretation, Mineralogical Association of Canada, Short Course Volume 32, pp. 233-246.

Gross, G.A., 1965. Geology of iron deposits in Canada; v. 1, General geology and evaluation of iron deposits. Economic Geology Report - Geological Survey of Canada, 181 pp.

Gunther, D., Audetat, A., Frischknecht, R. and Heinrich, C.A., 1998. Quantitative analysis of major, minor and trace elements in fluid inclusionsusing laser-ablation inductively-coupled-plasma mass-spectrometry. Journal of Analytical Atomic Spectometry, 13(4): 263-270.

Hagemann, S.G. and Brown, P.E., 1996. Geobarometry in Archean lode–gold deposits. Eur. J. Mineral., 8: 937–960.

Hanor, J.S., 1994. Origin of saline fluids in sedimentary basins. In: J. Parnell (Editor), Geofluids; origin, migration and evolution of fluids in sedimentary basins, Geological Society of London Special Publication, 78: 151-174.

Haptonstall, J.C., 1994. Bismark; Mexico's new major zinc mine. Mining Engineering, 46(4): 295-302.

Hatton, O.J. and Davidson, G.J., 2004. Soldiers Cap Group iron-formations, Mt Isa Inlier, Australia, as windows into the hydrothermal evolution of a base-metal-bearing Proterozoic rift basin. Australian Journal of Earth Sciences, 51: 85–106.

Heinrich, C.A., 1990. The chemistry of hydrothermal tin(-tungsten) ore deposition. Economic Geology, 85(3): 457-481.

Heinrich, C.A., 2005. The physical and chemical evolution of low-salinity magmatic fluids at the porphry to epithermal transition; a thermodynamic study. Mineralium Deposita, 39(8): 864-889.

Heinrich, C.A., Driesner, T., Stefansson, A. and Seward, T.M., 2004. Magmatic vapor contraction and the transport of gold from the porphyry environment to epithermal ore deposits. Geology, 32(9): 761-764.

Heinrich, C.A. Pettke, T., Halter, W.E., Aigner-Torres, M., Audétat, A., Günther, D., Hattendorf, B., Bleiner, D., Guillong, M., and Horn, I., 2003. Quantitative multi-element analysis of minerals, fluid and melt inclusions by laser-ablation inductively-coupled-plasma mass-spectrometry. Geochimica et Cosmochimica Acta, 67(18): 3473-3497.

Heinrich, C.A., Ryan, C.G., Mernagh, T.P. and Eadington, P.J., 1992. Segregation of ore metals between magmatic brine and vapor; a fluid inclusion study using PIXE microanalysis. Economic Geology and the Bulletin of the Society of Economic Geologists, 87(6): 1566-1583.

Helgeson, H.C., 1968. Evaluation of irreversible reactions in geochemical processes involving minerals and aqueous solutions; I, Thermodynamic relations Geochimica et Cosmochimica Acta 32(8): 853-877.

Helgeson, H.C., 1969. Thermodynamics of hydrothermal systems at elevated temperatures and pressures American Journal of Science 267(7): 729-804.

Helgeson, H.C. and Kirkham, D.H., 1974a. Theoretical prediction of the thermodynamic behavior of aqueous electrolytes at high pressures and temperatures; I, Summary of the thermodynamic/electrostatic properties of the solvent. American Journal of Science, 274(10): 1089-1198.

Helgeson, H.C. and Kirkham, D.H., 1974b. Theoretical prediction of the thermodynamic behavior of aqueous electrolytes at high pressures and temperatures; II, Debye-Huckel parameters for activity coefficients and relative partial molal properties. American Journal of Science, 274(10): 1199-1261.

Helgeson, H.C., Kirkham, D.H. and Flowers, G.C., 1981. Theoretical prediction of the thermodynamic behavior of aqueous electrolytes by high pressures and temperatures; IV, Calculation of activity coefficients, osmotic coefficients, and apparent molal and standard and relative partial molal properties to 600 degrees C and 5kb. American Journal of Science, 281(10): 1249-1516.

Hemley, J.J., Cygan, G.L., Fein, J.B., Robinson, G.R. and d'Angelo, W.M., 1992. Hydrothermal ore-forming processes in the light of studies in rock-buffered systems; I, Iron-copper-zinc-lead sulfide solubility relations. Economic Geology, 87(1): 1-22.

Hitzman, M.W., Oreskes, N. and Einaudi, M.T., 1992. Geological characteristics and tectonic setting of Proterozoic iron oxide (Cu-U-Au-REE) deposits. Precambrian Research, 58(1-4): 241-287.

Hoadley, E., Rubenach, M., Coleborn, D., Sisois, I. and Fanning, C.M., 2001. Significance of an amphibolite facies shear zone event synchronous with the emplacement of the Sybella Batholith, Mount Isa. In 2001; a structural odyssey, Abstracts - Geological Society of Australia, 64-83.

Holloway, J.R., 1976. Fluids in the evolution of granitic magmas; consequences of finite CO_2 solubility. GSA Bulletin, 87(10): 1513-1518.

Holtz, F., Pichavant, M., Barbey, P. and Johannes, W., 1992. Effects of H 2 O on liquidus phase relations in the haplogranite system at 2 and 5 kbar. American Mineralogist, 77(11-12): 1223-1241.

Iiyama, J.T., 1965. Influence des anions sur les equilibres d'echange d'ions Na-K dans les feldspaths alcalins a 600 degrees C sous une pression de 1 000 bars Bulletin de la Societe Francaise de Mineralogie et de Cristallographie 88(4): 618-622.

Jackson, M.J., Scott, D.L. and Rawlings, D.J., 2000. Stratigraphic framework for the Leichhardt and Calvert superbasins; review and correlations of the pre-1700 Ma successions between Mt Isa and McArthur River. Australian Journal of Earth Sciences, 47(3): 381-403.

Jahns, R.H. and Tuttle, O.F., 1963a. Layered pegmatite-aplite. Special Paper - Mineralogical Society of America, 1: 78-92.

Jahns, R.H. and Tuttle, O.F., 1963b. Origin of igneous aplites. Special Paper - Geological Society of America, 177-178.

Jahns, R.H. and Burnham, C.W., 1969. Experimental studies of pegmatite genesis; [Part] 1, A model for the derivation and crystallization of granitic pegmatites. Economic Geology, 64(8): 843-864.

Johnson, J.W. and Norton, D., 1991. Critical phenomena in hydrothermal systems; state, thermodynamic, electrostatic, and transport properties of H_2O in the critical region. American Journal of Science, 291(6): 541-648.

Johnson, J.W., Oelkers, E.H. and Helgeson, H.C., 1992. SUPCRT92; a software package for calculating the standard molal thermodynamic properties of minerals, gases, aqueous species, and reactions from 1 to 5000 bar and 0 to 1000 degrees C Computers & Geosciences 18(7): 899-947.

Johnson, L.H., Burgess, R., Turner, G., Milledge, H.J. and Harris, J.W., 2000. Noble gas and halogen geochemistry of mantle fluids: comparison of African and Canadian diamonds. Geochimica et Cosmochimica Acta, 64(4): 717-732.

Kendrick, M.A., Baker, T., Fu, B., Phillips, D. and Williams, P.J., 2007a. Noble gas and halogen constraints on regionally extensive midcrustal Na-Ca metasomatism, the Proterozoic Eastern Mount Isa Block, Australia. Precambrian Research, in press.

Kendrick, M.A., Burgess, R., Leach, D. and Pattrick, R.A.D., 2002a. Hydrothermal Fluid Origins in Mississippi Valley-Type Ore Districts: Combined Noble Gas (He, Ar, Kr) and Halogen (Cl, Br, I) Analysis of Fluid Inclusions from the Illinois-Kentucky Fluorspar District, Viburnum Trend, and Tri-State Districts, Midcontinent United States. Economic Geology, 97(3): 453-469.

Kendrick, M.A., Burgess, R., Pattrick, R.A.D. and Turner, G., 2001. Fluid inclusion noble gas and halogen evidence on the origin of Cu-Porphyry mineralising fluids. Geochimica et Cosmochimica Acta, 65(16): 2651-2668.

Kendrick, M.A., Burgess, R., Pattrick, R.A.D. and Turner, G., 2002b. Hydrothermal Fluid Origins in a Fluorite-Rich Mississippi Valley-Type District: Combined Noble Gas (He, Ar, Kr) and Halogen (Cl, Br, I) Analysis of Fluid Inclusions from the South Pennine Ore Field, United Kingdom. Economic Geology, 97(3): 435-451.

Kendrick, M.A., Mark, G. and Phillips, D., 2007b. Mid-crustal fluid mixing in a Proterozoic Fe oxide-Cu-Au deposit, Ernest Henry, Australia: Evidence from Ar, Kr, Xe, Cl, Br, I. Earth and Planetary Science Letters, 256(3-4): 328-343.

Kendrick, M.A., Phillips, D. and Miller, J.M., 2006. Part I. Decrepitation and degassing behaviour of quartz up to 1560°C: Analysis of noble gases and halogens in complex fluid inclusion assemblages. Geochimica et Cosmochimica Acta, 70(10): 2540-2561.

Keppler, H., 1989. The influence of the fluid phase composition on the solidus temperatures in the haplogranite system $NaAlSi_3O_8$-$KAlSi_3O_8$-SiO_2-H_2O-CO_2. Contributions to Mineralogy and Petrology, 102(3): 321-327.

Kharaka, Y.K. and Barnes, I., 1973. SOLMNEQ; solution-mineral equilibrium computations. U.S. Geolological Survey Computer Contributions Report PB-215-899.

Kretz, R., 1983. Symbols for rock-forming minerals. American Mineralogist, 68(1-2): 277-279.

Komninou, A. and Sverjensky, D.A., 1995. Hydrothermal alteration and the chemistry of ore-forming fluids in an unconformity-type uranium deposit. Geochimica et Cosmochimica Acta, 59(13): 2709-2723.

Komninou, A. and Sverjensky, D.A., 1996. Geochemical modeling of the formation of an unconformity-type uranium deposit. Economic Geology and the Bulletin of the Society of Economic Geologists, 91(3): 590-606.

Lattanzi, P., 1991. Applications of fluid inclusions in the study and exploration of mineral deposits. European Journal of Mineralogy, 3(4): 689-701.

Lattanzi, P., 1994. Fluids in ore deposits. In: B. De Vivo and Frezzotti, M.L., (Editors), Fluid inclusions in Minerals: Methods and Applications. Short Course Volume, Virginia Polytechnic Institute and State University, pp. 297-307.

Little, G.A., 1997. Structural evolution and paragenesis of alteration and mineralisation at Mount Elliot Cu –Au mine, Northwest Queensland. BSc (Honours) thesis (unpublished). James Cook University, Townsville, 155 p.

Lofgren, G.E. and Donaldson, C.H., 1975. Curved branching crystals and differentiation in comb-layered rocks. Contributions to Mineralogy and Petrology, 49(4): 309-319.

London, D., 1992. The application of experimental petrology to the genesis and crystallization of granitic pegmatites. Canadian Mineralogist, 30: 499-540.

London, D., 2005. Granitic pegmatites: an assessment of current concepts and directions for the future. Lithos, 80(1-4): 281-303.

Loosveld, R.J.H., 1989. The intra-cratonic evolution of the central eastern Mount Isa Inlier, northwest Queensland, Australia. Precambrian Research, 44(3-4): 243-276.

Lowenstern, J.B., 2000. A review of the contrasting behavior of two magmatic volatiles; chlorine and carbon dioxide. Journal of Geochemical Exploration, 69–70: 287-290.

Lowenstern, J.B., 2001. Carbon dioxide in magmas and implications for hydrothermal systems Mineralium Deposita 36(6): 490-502.

Lu, C., Reed, M.H. and Misra, K.C., 1992. Zinc-lead skarn mineralization at Tin Creek, Alaska: Fluid inclusions and skarn-forming reactions. Geochimica et Cosmochimica Acta, 56(1): 109-119.

Maas, R., McCulloch, M.T., Campbell, I.H. and Page, R.W., 1987. Sm-Nd isotope systematics in uranium rare-earth element mineralization at the Mary Kathleen uranium mine, Queensland. Economic Geology, 82(7): 1805-1826.

Mark, G., 1998. Albitite formation by selective pervasive sodic alteration of tonalite plutons in the Cloncurry District, Queensland Australian Journal of Earth Sciences 45(5): 765-774.

Mark, G., 1999. Petrogenesis of Mesoproterozoic K-rich granitoids, southern Mt. Angelay igneous complex, Cloncurry District, northwest Queensland Australian Journal of Earth Sciences 46(6): 933-949.

Mark, G., 2001. Nd isotope and petrogenetic constraints for the origin of the Mount Angelay igneous complex; implications for the origin of intrusions in the Cloncurry District, NE Australia Precambrian Research 105(1): 17-35.

Mark, G. and Foster, D.R.W., 2000. Magmatic-hydrothermal albite-actinolite-apatite-rich rocks from the Cloncurry District, NW Queensland, Australia Lithos, 51(3): 223-245.

Mark, G., Darvall, M., Tolman, J., Foster, D. R. W., Williams, P. J. and Pollard, P. J., 1999. Magmas and regional Na-Ca alteration, Cloncurry Distric, Australia. In Proceedings of the Fifth biennial SGA meeting and the Tenth quadrennial IAGOD symposium, Mineral deposits; processes to processing, Society for Geology Applied to Mineral Deposits, 5: 385-388.

Mark, G., Baker, T., Williams, P.J., Mustard, R., Ryan, C., and Mernagh, T.P., 2004. The geochemistry of magmatic fluids, Cloncurry district, Australia: relations to IOCG systems. In Barnicoat, A.C., and Korsch, R.J., (Editors.). Predictive Mineral Discovery Cooperative Research Centre – Extended Abstracts from the June 2004 Conference. Geocience Australia, Record 2004/9, p. 123-126.

Mark, G., Oliver, N. and Carew, M., 2006a. Insights into the genesis and diversity of epigenetic Cu-Au mineralisation in the Cloncurry district, Mt Isa Inlier, northwest Queensland. Australian Journal of Earth Sciences, 53(1): 109-124.

Mark, G., Oliver, N. and Williams, P., 2006b. Mineralogical and chemical evolution of the Ernest Henry Fe oxide-Cu-Au ore system, Cloncurry district, northwest Queensland, Australia. Mineralium Deposita, 40(8): 769-801.

Mark, G., Oliver, N.H.S., Williams, P.J., Valenta, R.K. and Crookes, R.A., 2000. The evolution of the Ernest Henry Fe-oxide-(Cu-Au) hydrothermal system In: T.M. Porter (Editor), Hydrothermal iron oxide copper-gold and related deposits; a global perspective, Australian Mineral Foundation, Glenside, South Aust., Vol. 1, pp. 123-136.

Mark, G., Williams, P., Ryan, C.G. and Mernagh, T., 2001. Fluid chemistry and ore-forming processes at the Ernest Henry Fe oxide-copper-gold deposit, NW Queensland. In P.J. Williams (Editor), A hydrothermal odyssey, New Developments in Metalliferous Hydrothermal Systems Research, James Cook University EGRU Contribution, 59 pp. 124-125.

Marshall, L.J., 2003. Brecciation within the Mary Kathleen Group of the Eastern Succession, MT Isa Block, Australia: implication of district-scale structural and metasomatic processes for FE-oxide-Cu-Au mineralization. PhD thesis (Unpublished). James Cook University, Townsville, 323 p.

Marshall, L.J. and Oliver, N.H.S., 2006. Monitoring fluid chemistry in iron oxide–copper–gold-related metasomatic processes, eastern Mt Isa Block, Australia. Geofluids(6): 45–66.

Mavrogenes, J.A., Bodnar, R. J., Anderson, A. J., Bait, S., Sutton, S. R., and Rivers, M. L., 1995. Assessment of the uncertainties and limitations of quantitative elemental analysis of individual fluid inclusions using synchrotron X-ray fluorescence (SXRF). Geochimica et Cosmochimica Acta, 59(19): 3987-3995.

McCallum, M.E., 1985. Experimental evidence for fluidization processes in breccia pipe formation. Economic Geology, 80(6): 1523-1543.

McClellan, G.H. and Van Kauwenbergh, S.J., 1991. Mineralogical and chemical variation of francolites with geological time. Journal of the Geological Society, 148(5): 809-812.

McCreery, R.L., 2000. Raman Spectroscopy for Chemical Analysis, 157, 420 pp.

Meinert, L.D., 1982. Skarn, manto, and breccia pipe formation in sedimentary rocks of the Cananea mining district, Sonora, Mexico. Economic Geology, 77(4): 919-949.

Meinert, L.D., Hedenquist, J.W., Satoh, H. and Matsuhisa, Y., 2003. Formation of Anhydrous and Hydrous Skarn in Cu-Au Ore Deposits by Magmatic Fluids. Economic Geology, 98(1): 147-156.

Menez, B., Philippot, P., Bonnin-Mosbah, M., Simionovici, A. and Gibert, F., 2002. Analysis of individual fluid inclusions using synchrotron X-ray fluorescence microprobe: progress toward calibration for trace elements. Geochimica et Cosmochimica Acta, 66(4): 561-576.

Menez, B., Simionovici, A., Philippot, P., Bohic, S., Gibert, F., and Chukalina, M., 2001. X-ray fluorescence micro-tomography of an individual fluid inclusion using a third generation synchrotron light source. Nuclear Instruments and Methods in Physics Research Section B: Beam Interactions with Materials and Atoms, 181(1-4): 749-754.

Mitchell, L.C., 1993. Geology and geochemistry of the Wiley igneous complex, eastern fold belt, Mt. Isa inlier. BSc (Honours) thesis (Unpublished). James Cook University, Townsville, 136 p.

Mustard, R., Baker, T., Williams, P. J., Mernagh, T. P., Ryan, C. G., van Achterbergh, E., and Adshead, N. D., 2004. The role of unmixing in magnetite ± copper deposition in Fe-oxide Cu-Au systems. In Barnicoat, A.C., and Korsch, R.J., (eds.). Predictive Mineral Discovery Cooperative Research Centre – Extended Abstracts from the June 2004 Conference. Geocience Australia, Record 2004/9, p. 155-160.

Nabelek, P.I. and Ternes, K., 1997. Fluid inclusions in the Harney Peak Granite, Black Hills, South Dakota, USA: Implications for solubility and evolution of magmatic volatiles and crystallization of leucogranite magmas. Geochimica et Cosmochimica Acta, 61(7): 1447-1465.

Naden, J., 1996. CalcicBrine; a Microsoft Excel 5.0 add-in for calculating salinities from microthermometric data in the system NaCl-CaCl2-H2O. PACROFI VI; Sixth biennial Pan-American conference on Research on fluid inclusions; program and abstracts, 6: 97-98.

Newberry, S.P., Carswell, J.T., Allnutt, S.L. and Mutton, A.J., 1993. The Dugald River zinc-lead-silver deposit; an example of a tectonised Proterozoic stratabound sulphide deposit. World zinc '93; proceedings of the International symposium on Zinc, Hobart 1993, Australasian Institute of Mining and Metallurgy, 7/93: 7-21.

Oliver, N.H.S., 1995. Hydrothermal history of the Mary Kathleen Fold Belt, Mt. Isa Block, Queensland. Australian Journal of Earth Sciences, 42(3): pp. 267–280.

Oliver, N.H.S., Cleverley JS, Mark G, Pollard PJ, Fu B, Marshall LJ,Rubenach MJ, Williams PJ, Baker T., 2004. Modeling the Role of Sodic Alteration in the Genesis of Iron Oxide-Copper-Gold Deposits, Eastern Mount Isa Block, Australia. Economic Geology, 99(6): 1145-1176.

Oliver, N.H.S., Ord, A., Valenta, R.K. and Upton, P., 2001. Deformation, fluid flow, and ore genesis in heterogeneous rocks, with examples and numerical models from the Mount Isa district, Australia. In Structural controls on ore genesis, Reviews in Economic Geology, 14: 51-73.

Oliver, N.H.S., Rawling, T.J., Cartwright, I. and Pearson, P.J., 1994. High-temperature fluid-rock interaction and scapolitization in an extension-related hydrothermal system, Mary Kathleen, Australia Journal of Petrology 35(6): 1455-1491.

Oliver, N. H. S., Rubenach, M. J., Fu, B., Baker, T., Blenkinsop, T. G., Cleverley, J. S., Marshall, L. R., Ridd, P. J., 2006. Granite-related overpressure and volatile release in the mid-crust: fluidized breccia from the Cloncurry Fe-oxide-Cu-Au district. Geofluids, 6: 346-358.

Oliver, N.H.S., Valenta, R.K. and Wall, V.J., 1990. The effect of heterogeneous stress and strain on metamorphic fluid flow, Mary Kathleen, Australia, and a model for large-scale fluid circulation Journal of Metamorphic Geology 8(3): 311-331.

Page, R.W., 1983. Chronology of magmatism, skarn formation, and uranium mineralization, Mary Kathleen, Queensland, Australia. Economic Geology, 78(5): 838-853.

Page, R.W., 1998. Links between eastern and western fold belts in the Mount Isa Inlier, 1485 based on SHRIMP U-Pb studies. Geological Society of Australia Abstracts, 49, 349.

Page, R.W. and Sun, S.S., 1998. Aspects of geochronology and crustal evolution in the Eastern Fold Belt, Mt Isa Inlier. Australian Journal of Earth Sciences, 45(3): 343-361.

Pan, Y. and Fleet, M.E., 2002. Compositions of the apatite group minerals; substitution mechanisms and controlling factors. In M. J. Kohn, J. Rakovan, J. M Hughes (Editors), Phosphates; geochemical, geobiological, and materials importance, Reviews in Mineralogy and Geochemistry, 48: 13-49.

Pasteris, J.D., Wopenka, B. and Seitz, J.C., 1988. Practical aspects of quantitative laser Raman microprobe spectroscopy for the study of fluid inclusions. Geochimica et Cosmochimica Acta, 52(5): 979-988.

Pattison, D.R.M., Spear, F.S., Debuhr, C.L., Cheney, J.T. and Guidotti, C.V., 2002. Thermodynamic modelling of the reaction muscovite + cordierite Al_2SiO_5 + biotite + quartz + H_2O; constraints from natural assemblages and implications for the metapelitic petrogenetic grid. Journal of Metamorphic Geology, 20(1): 99-118.

Pearson, P.J., Holcombe, R.J. and Page, R.W., 1992. Synkinematic emplacement of the Middle Proterozoic Wonga Batholith into a mid-crustal extensional shear zone, Mount Isa Inlier, Queensland, Australia. Detailed studies of the Mount Isa Inlier, AGSO Bulletin, pp. 289-328

Perkins, C. and Wyborn, L.A.I., 1998. Age of Cu-Au mineralisation, Cloncurry District, eastern Mt Isa Inlier, Queensland, as determined by $^{40}Ar/^{39}Ar$ dating. Australian Journal of Earth Sciences, 45(2): 233-246.

Perring, C.S., Pollard, P.J., Dong, G., Nunn, A.J. and Blake, K.L., 2000. The Lightning Creek sill complex, Cloncurry District, Northwest Queensland; a source of fluids for Fe oxide Cu-Au mineralization and sodic-calcic alteration. Economic Geology and the Bulletin of the Society of Economic Geologists, 95(5): 1067-1089.

Philippot, P., Ménez, B., Chevallier, P., Gibert, F., Legrand, F. and Populus, P., 1998. Absorption correction procedures for quantitative analysis of fluid inclusions using synchrotron radiation X-ray fluorescence. Chemical Geology, 144(1-2): 121-136.

Philippot, P. Ménez, B. Drakopoulos, M. Simionovici, A., Snigirev, A. and Snigireva, I., 2001. Mapping trace-metal (Cu, Zn, As) distribution in a single fluid inclusion using a third generation synchrotron light source. Chemical Geology, 173(1-3): 151-158.

Philippot, P., Ménez, B., Simionovici, A., Chabiron, A., Cuney, M., Snigirev A. and Snigireva, I., 2000. X-ray imaging of uranium in individual fluid inclusions. Terra Nova, 12(2): 84-89.

Pokrovskii, V., Harrold, B., Heinrich, C. and Liu, X., 1998. Release notes for THERMODATA AGSO/ANU/ETH (version 5.2). Australian Geological Survey Organisation, Canberra.

Pollard, P.J., 2001. Sodic (-calcic) alteration in Fe-oxide-Cu-Au district; an origin via unmixing of magmatic H_2O-CO_2-NaCl±$CaCl_2$-KCl fluids. Mineralium Deposita, 36(1): 93-100.

Pollard, P.J., Davis, B.K. and Williams, P.J., 1997. Structural and physiochemical controls on ore formation in Cloncurry Cu-Au deposits, eastern Mount Isa Inlier, Queensland. In Pollard, P. J., (Editor), AMIRA P438, Cloncurry Base Metals and Gold, Final Report: Townsville, Australian Institute of Mining and Metallurgy: p. 2.1-2.41.

Pollard, P.J., Mark, G. and Mitchell, L.C., 1998. Geochemistry of post-1540 Ma granites in the Cloncurry District, Northwest Queensland. Economic Geology, 93(8): 1330-1344.

Potma, W. and Betts, P., 2006. Extension-related structures in the Mitakoodi Culmination: Implications for the nature and timing of extension, and effect on later shortening in the eastern Mt Isa Inlier. Australian Journal of Earth Sciences, 53(1): 55-67.

Ramboz, C., Pichavant, M. and Weisbrod, A., 1982. Fluid immiscibility in natural processes; use and misuse of fluid inclusion data; II, Interpretation of fluid inclusion data in terms of immiscibility. Chemical Geology, 37(1-2): 29-48.

Rankin, A.H., Ramsey, M.H., Coles, B., Van Langevelde, F. and Thomas, C.R., 1992. The composition of hypersaline, iron-rich granitic fluids based on laser-ICP and Synchrotron-XRF microprobe analysis of individual fluid inclusions in topaz, Mole granite, eastern Australia. Geochimica et Cosmochimica Acta, 56(1): 67-79.

Reed, M.H., 1982. Calculation of multicomponent chemical equilibria and reaction processes in systems involving minerals, gases and an aqueous phase Geochimica et Cosmochimica Acta 46(4): 513-528.

Rickers, K., Thomas, R. and Heinrich, W., 2004. Trace-element analysis of individual synthetic and natural fluid inclusions with synchrotron radiation XRF using Monte Carlo simulations for quantification. European Journal of Mineralogy, 16: 23-35.

Roedder, E., 1967. Fluid inclusions as samples of ore fluids. In: H.L. Barnes (Editor), Geochemistry of hydrothermal ore deposits. Holt, Rinehart and Winston, New York, Toronto, and London, pp. 515-574.

Roedder, E., 1984. Fluid inclusions: an introduction to studies of all types of fluid inclusions, gas, liquid, or melt, trapped in materials from earth and space, and their application to the understanding of geologic processes. Mineralogical Society of America, Reviews in Mineralogy, 12, 644 pp.

Roedder, E., 1990. Fluid inclusion analysis; prologue and epilogue Current research on fluid inclusions. Geochimica et Cosmochimica Acta, 54(3): 495-507.

Roedder, E. and Bodnar, R.J., 1980. Geologic pressure determinations from fluid inclusion studies Annual Review of Earth and Planetary Sciences 8: 263-301.

Roedder, E. and Bodnar, R.J., 1997. Fluid inclusion studies of hydrothermal ore deposits In: H.L. Barnes (Editor), Geochemistry of hydrothermal ore deposits John Wiley & Sons New York, NY pp. 657-697.

Rotherham, J.F., 1997. A metasomatic origin for the iron-oxide Au-Cu Starra orebodies, Eastern Fold Belt, Mount Isa Inlier Mineralium Deposita 32(3): 205-218.

Rotherham, J.F., Blake, K.L., Cartwright, I. and Williams, P.J., 1998. Stable isotope evidence for the origin of the Mesoproterozoic Starra Au-Cu deposit, Cloncurry District, Northwest Queensland. Economic Geology, 93(8): 1435-1449.

Rubenach, M.J. and Barker, A.J., 1998. Metamorphic and metasomatic evolution of the Snake Creek Anticline, Eastern Succession, Mt Isa Inlier. Australian Journal of Earth Sciences, 45(3): 363-372.

Rubenach, M.J. and Lewthwaite, K.A., 2002. Metasomatic albitites and related biotite-rich schists from a low-pressure polymetamorphic terrane, Snake Creek Anticline, Mount Isa Inlier, north-eastern Australia; microstructures and P-T-d paths. Journal of Metamorphic Geology, 20(1): 191-202.

Rubenach, M.J. Adshead N. D., Oliver N. H. S., Tullemans F., Esser D. and Stein H., 2001. The Osborne Cu –Au deposit: geochronology, and genesis of mineralization in relation to host albitites and ironstones. In: Williams P. J. (Editor), A Hydrothermal Odyssey, New Developments in Metalliferous Hydrothermal Systems Research, James Cook University EGRU Contribution, 59:172 – 173.

Rubenach, M.J., Foster, D.R.W., Evins, P.M., Blake, K.L. and Fanning, C.M., 2007. Age constraints on the tectonothermal evolution of the Selwyn Zone, Eastern Fold Belt, Mount Isa Inlier. Precambrian Research, accepted manuscript.

Ryan, C.G. Cousens, D. R., Heinrich C. A., Griffin W. L., Sie, S. H., Mernagh T. P., 1991. Quantitative PIXE microanalysis of fluid inclusions based on a layered yield model. Nuclear Instruments and Methods in Physics Research Section B: Beam Interactions with Materials and Atoms, 54(1-3): 292-297.

Ryan, C.G., Heinrich, C.A. and Mernagh, T.P., 1993. PIXE microanalysis of fluid inclusions and its application to study of ore metal segregation between magmatic brine and vapor. Nuclear Instruments and Methods in Physics Research, v. B77: p. 463–471.

Ryan, C.G., Jamieson, D.N., Griffin, W.L., Cripps, G. and Szymanski, R., 2001. The new CSIRO-GEMOC nuclear microprobe: First results, performance and recent applications. Nuclear Instruments and Methods in Physics Research, v. B181:12–19.

Ryburn, R.J., Grimes, K.G. and others, 1988a. Cloncurry, Queensland. 1:100 000 scale map, Canberra, Bureau of Mineral Resources.

Ryburn, R.J., Wilson, I.H., Grimes, K.G. and Hill, R.M., 1988b. Cloncurry, Queensland. 1:100 000 Geological Map Commentary, Canberra, Bureau of Mineral Resources.

Scaillet, B., Pichavant, M. and Roux, J., 1995. Experimental crystallization of leucogranite magmas Journal of Petrology 36(3): 663-705.

Scherkenbach, D.A., Sawkins, F.J. and Seyfried, W.E., 1985. Geologic, fluid inclusion, and geochemical studies of the mineralized breccias at Cumobabi, Sonora, Mexico. Economic Geology, 80(6): 1566-1592.

Schmidt, C. and Bodnar, R.J., 2000. Synthetic fluid inclusions; XVI, PVTX properties in the system H_2O-NaCl-CO_2 at elevated temperatures, pressures, and salinities. Geochimica et Cosmochimica Acta, 64(22): 3853-3869.

Scott, D.L. Rawlings D. J., Page R. W., Tarlowski C. Z., Idnurm M., Jackson M. J. and Southgate P. N., 2000. Basement framework and geodynamic evolution of the Palaeoproterozoic superbasins of north-central Australia; an integrated review of geochemical, geochronological and geophysical data. Australian Journal of Earth Sciences, 47(3): 341-380.

Shepherd, T.J. and Rankin, A.H., 1998. Fluid inclusion techniques of analysis. In: J.P. Richards and P.B. Larson (Editors), Techniques in hydrothermal ore deposits geology, Reviews in Economic Geology, 10:125-149.

Shepherd, T.J., Rankin, A.H. and Alderton, D.H.M., 1985. A practical guide to fluid inclusion studies. Blackie & Son, Glasgow.

Shinohara, H., and Hedenquist, J.W., 1997. Constraints on magma degassing beneath the Far Southeast porphyry Cu-Au deposit, Philippines. Journal of Petrology, 38 (12), p. 1741-1752

Shock, E.L. and Helgeson, H.C., 1988. Calculation of the thermodynamic and transport properties of aqueous species at high pressures and temperatures; correlation algorithms for ionic species and equation of state predictions to 5 kb and 1000 degrees C Geochimica et Cosmochimica Acta 52(8): 2009-2036.

Shock, E.L. and Helgeson, H.C., 1990. Calculation of the thermodynamic and transport properties of aqueous species at high pressures and temperatures; standard partial molal properties of organic species Geochimica et Cosmochimica Acta 54(4): 915-945.

Shock, E.L., Helgeson, H.C. and Sverjensky, D., 1989. Calculation of the thermodynamic and transport properties of aqueous species at high pressures and temperatures; standard partial molal properties of inorganic neutral species Geochimica et Cosmochimica Acta 53(9): 2157-2183.

Shvarov, Y.V. and Bastrakov, E.N., 1999. HCh: a software package for geochemical equilibrium modeling. User's guide. Australian Geological Survey Organisation, Record 1999/25.

Sillitoe, R.H., 1985. Ore-related breccias in volcanoplutonic arcs. Economic Geology, 80(6): 1467-1514.

Sillitoe, R.H. and Sawkins, F.J., 1971. Geologic, Mineralogic and Fluid Inclusion Studies Relating to the Origin of Copper-bearing Tourmaline Breccia Pipes, Chile. Economic Geology, 66(7): 1028-1041.

Sorby, H.C., 1858. On the microscope structure of crystals, indicating the origin of minerals and rocks. Quarterly journal of the Geological Society of London, 14: 453-500.

Sparks, R.S.J. and Walker, G.P.L., 1977. The significance of vitric-enriched air-fall ashes associated with crystal-enriched ignimbrites Journal of Volcanology and Geothermal Research 2(4): 329-341.

Sterner, S.M., Hall, D.L. and Bodnar, R.J., 1988. Synthetic fluid inclusions. V. Solubility relations in the system NaCl-KCl-H2O under vapor-saturated conditions. Geochimica et Cosmochimica Acta, 52(5): 989-1005.

Stewart, C.A., 1994. Shear zone hosted copper-gold mineralisation associated with stratabound ironstones in the Corella Formation, Kalkadoon-Leichardt Belt, Estearn Succession, Mount Isa Inlier. MSc thesis (Unpublished), James Cook University, Townsville.

Sverjensky, D.A., 1987. The role of migrating oil field brines in the formation of sediment-hosted Cu-rich deposits. Economic Geology and the Bulletin of the Society of Economic Geologists, 82(5): 1130-1141.

Sverjensky, D.A., Shock, E.L. and Helgeson, H.C., 1997. Prediction of the thermodynamic properties of aqueous metal complexes to 1000°C and 5 kb. Geochimica et Cosmochimica Acta, 61(7): 1359-1412.

Swanson, S.E., 1979. The effect of CO_2 on phase equilibria and crystal growth in the system $KAlSi_3O_8$-$NaAlSi_3O_8$-$CaAl_2Si_2O_8$-SiO_2-H_2O-CO_2 to 8000 bars. American Journal of Science, 279(6): 703-720.

Swanson, S.E. and Fenn, P.M., 1986. Quartz crystallization in igneous rocks. American Mineralogist, 71(3-4): 331-342.

Tanger, J.C. and Helgeson, H.C., 1988. Calculation of the thermodynamic and transport properties of aqueous species at high pressures and temperatures; revised equations of state for the standard partial molal properties of ions and electrolytes American Journal of Science 288(1): 19-98.

Taylor, R.G. and Pollard, P.J., 1993. Mineralized breccia systems; methods of recognition and interpretation. James Cook University EGRU Contributions, 46, 31 pp.

Thompson, J.F.H., Sillitoe, R.H., Baker, T., Lang, J.R. and Mortensen, J.K., 1999. Intrusion-related gold deposits associated with tungsten-tin provinces Mineralium Deposita 34(4): 323-334.

Tolman, J.L., 1998. Origin and formation of complexly textured albite-, actinolite-, apatite-rich rocks within the Central Mount Angelay igneous complex, Cloncurry district, Northwest Queensland. BSc (Honours) thesis (Unpublished). James Cook University, Townsville, 143.

Touret, J.L.R., 1992. CO_2 transfer between the upper mantle and the atmosphere; temporary storage in the lower continental crust. Terra Nova, 4(1): 87-98.

Touret, J.L.R. and Huizenga, J.M., 1999. Precambrian intraplate magmatism: high temperature, low pressure crustal granulites. Journal of African Earth Sciences, 28(2): 367-382.

Truesdell, A.H. and Jones, B.F., 1974. WATEQ, a computer program for calculating chemical equilibria of natural waters. Journal of Research of the U. S. Geological Survey, 2(2): 233-248.

Tunks, A., 1987. Breccia and metasomatism in the Corella Formation, Cloncurry, Queensland. BSc (Honours) thesis (Unpublished). Monash University, Melbourne.

Turrell, G. and Corset, J., 1996. Raman Microscopy, Developments and Applications. Academic press, 463 pp.

Twyerould, S.C., 1997. The geology and genesis of the Ernest Henry Fe–Cu–Au deposit, northwest Queensland, Australia. PhD thesis (Unpublished). University of Oregon.

Ulrich, T., Guenther, D. and Heinrich, C.A., 1999. Gold concentrations of magmatic brines and the metal budget of porphyry copper deposits. Nature (London), 399(6737): 676-679.

Vanko, D.D. and Mavrogenes, J.A., 1998. Synchrotron-source X-ray fluorescence microprobe; analysis of fluid inclusions. Applications of microanalytical techniques to understanding mineralizing processes, 7: 251-263.

Vanko, D.A., Bodnar, R.J. and Sterner, S.M., 1988. Synthetic fluid inclusions: VIII. Vapor-saturated halite solubility in part of the system NaCl-CaCl2-H2O, with

application to fluid inclusions from oceanic hydrothermal systems. Geochimica et Cosmochimica Acta, 52(10): 2451-2456.

Vanko, D.A., Sutton, S.R., Rivers, M.L. and Bodnar, R.J., 1993. Major-element ratios in synthetic fluid inclusions by synchrotron X-ray fluorescence microprobe. Chemical Geology, 109(1-4): 125-134.

Vaughan, J.P. and Stanton, R.L., 1986. Sedimentary and metamorphic factors in the development of the Pegmont stratiform Pb-Zn deposit, Queensland, Australia Institution of Mining and Metallurgy, Transactions, Section B: Applied Earth Science 95, May: B94-B121.

Veiderma, M., Tonsuaadu, K., Knubovets, R. and Peld, M., 2005. Impact of anionic substitutions on apatite structure and properties. Journal of Organometallic Chemistry, 690(10): 2638-2643.

Wager, L.R., Brown, G.M. and Wadsworth, W.J., 1960. Types of Igneous Cumulates. J. Petrology, 1(1): 73-85.

Walters, S. and Bailey, A., 1998. Geology and mineralization of the Cannington Ag-Pb-Zn deposit; an example of Broken Hill-type mineralization in the eastern succession, Mount Isa Inlier, Australia. Economic Geology, 93(8): 1307-1329.

Wang, S. and Williams, P.J., 2001. Geochemistry and origin of Proterozoic skarns at the Mount Elliott Cu-Au(-Co-Ni) deposit, Cloncurry District, NW Queensland, Australia Mineralium Deposita 36(2): 109-124.

Webster, J.D. and Holloway, J.R., 1988. Experimental constraints on the partitioning of Cl between topaz rhyolite melt and H2O and H2O + CO2 fluids: New implications for granitic differentiation and ore deposition. Geochimica et Cosmochimica Acta, 52(8): 2091-2105.

Wen, S. and Nekvasil, H., 1994. Ideal associated solutions; application to the system albite-quartz-H 2 O. American Mineralogist, 79(3-4): 316-331.

Wilkinson, J.J., 2001. Fluid inclusions in hydrothermal ore deposits. Lithos, 55(1-4): 229-272.

Williams, P.J., 1998a. An introduction to the metallogeny of the McArthur River-Mount Isa-Cloncurry minerals province. Economic Geology, 93(8): 1120-1131.

Williams, P.J., 1998b. Metalliferous economic geology of the Mt Isa Eastern Succession, Queensland. Geological framework and mineralisation in the Mt Isa Eastern Succession, Northwest Queensland, Australian Journal of Earth Sciences, 45(3): 329-341.

Williams, P.J. and Heinemann, M., 1993. Maramungee; a Proterozoic Zn skarn in the Cloncurry District, Mount Isa Inlier, Queensland, Australia. Economic Geology, 88(5): 1114-1134.

Williams, P.J. and Pollard, P.J., 2001. Australian Proterozoic Iron Oxide-Cu-Au Deposits: An Overview with New Metallogenic and Exploration Data from the Cloncurry District, Northwest Queensland. Exploration and Mining Geology, 10(3): 191-213.

Williams, P.J. and Skirrow, R.G., 2000. Overview of iron oxide-copper-gold deposits in the Curnamona Province and Cloncurry District (eastern Mount Isa Block), Australia In: T.M. Porter (Editor), Hydrothermal iron oxide copper-gold and related deposits; a global perspective; Vol. 1 Australian Mineral Foundation Glenside, South Aust. , pp. 105-122.

Williams, P.J. Barton, M.D., Johnson, D.A., Fontboté, L., De Haller, A., Mark. G., Oliver, N. H. S., Marschik, R.., 2005. Iron Oxide Copper-Gold Deposits: Geology, Space-Time Distribution, and Possible Modes of Origin. Economic Geology, 100th Anniversary Volume: pp. 371-406.

Williams, P.J., Dong G., Ryan C. G., Pollard P. J., Rotherham J., Mernagh T. P. and Chapman L. H., 2001. Geochemistry of hypersaline fluid inclusions from the Starra (Fe oxide)–Cu–Au deposit, Cloncurry district, Queensland. Economic Geology, 96(4): 875-883.

Williams, P.J., Pendergast, W.J. and Dong, G., 1998. Late orogenic alteration in the wall rocks of the Pegmont Pb-Zn deposit, Cloncurry District, Queensland, Australia. Economic Geology, 93(8): 1180-1189.

Wilson, L. and Head, J.W., 2004. Diatremes and kimberlites, 2: an integrated model of the ascent and eruption of kimberlitic magmas and the production of crater, diatreme and hypabyssal facies. In: Lithos Proceedings of the 8th International Kimberlite Conference, Abstract 244.

Wolery, T. and Jarek, R., 2003. EQ3/6, Version 8.0, Software User's Manual. Software Document Number 10813-UM-8.0-00, U.S. Department of Energy, Office of Civilian Radioactive Waste Management, Office of Repository Development, 1261 Town Center Drive, Las Vegas, NV 89144.

Wyborn, L., 1998. Younger ca 1500 Ma granites of the Williams and Naraku batholiths, Cloncurry District, eastern Mt Isa Inlier; geochemistry, origin, metallogenic

significance and exploration indicators. Australian Journal of Earth Sciences, 45(3): 397-411.

Wyborn, L.A.I., Page, R.W. and McCulloch, M.T., 1988. Petrology, geochronology and isotope geochemistry of the post-1820 Ma granites of the Mount Isa Inlier; mechanisms for the generation of Proterozoic anorogenic granites. Precambrian Research, 40-41: 509-541.

Xu, G., 1997. Microstructural evidence for an epigenetic origin of a Proterozoic zinc-lead-silver deposit, Dugald River, Mount Isa Inlier, Australia Mineralium Deposita 32(1): 58-69.

Xu, G., 1998. A fluid inclusion study of syntectonic Zn-Pb-Ag mineralization at Dugald River, Northwest Queensland, Australia. Economic Geology, 93(8): 1165-1179.

Yardley, B.W.D., 2005. 100th Anniversary Special Paper: Metal Concentrations in Crustal Fluids and Their Relationship to Ore Formation. Economic Geology, 100(4): 613-632.

Yardley, B.W.D., Banks, D.A. and Barnicoat, A.C., 2000. The chemistry of crustal brines; tracking their origins In: T.M. Porter (Editor), Hydrothermal iron oxide copper-gold and related deposits; a global perspective, Australian Mineral Foundation, Glenside, South Aust., Vol. 1, pp. 61-70.

Yardley, B., Bennett, A. and Banks, D., 2003. Controls on the chemical composition of crustal brines. Journal of Geochemical Exploration, 78-79: 133-135.

Appendices

Appendix 2.1 - Mineral abbreviations used in the thesis (after Kretz 1983)

Ab	Albite	Hem	Hematite
Act	Actinolite	Kfs	K feldspar
Ap	Apatite	Ilm	Ilmenite
Bt	Biotite	Mag	Magnetite
Cpx	Ca clinopyroxene	Ms	Muscovite
Cal	Calcite	Py	Pyrite
Ccp	Chalcopyrite	Po	Pyrrhotite
Chl	Chlorite	Qtz	Quartz
Crd	Cordierite	Rt	Rutile
Di	Diopside	Scp	Scapolite
Dol	Dolomite	Sd	Siderite
Ep	Epidote	Sp	Sphalerite
Fl	Fluorite	St	Staurolite
Gn	Galena	Tlc	Talc
Grt	Garnet	Ttn	Titanite
Ged	Gedrite	Tr	Tremolite
Gr	Graphite		

Appendix 3.1 – Sample List

List of abbreviations

TS – Thin sections

MA – Microprobe analisis

FIP – Fluid inclusion paragenesis and classification

M – Microthermometry

CL – Cathodoluminescence analysis

LR – Laser Raman analysis

LA ICP MS – Laser ablation ion coupled plasma mass spectrometry

BCL – Bulk crush leach analysis

Appendix 3.1 Sample list												
JCU Ref. No	Sample	Rock Type	Location			Fluid inclusion analysis						Source
				TS	MA	FIP	M	CL	LR	LA ICP MS	BCL	
74051	MT11	Ab-Qtz clast of granite pegmatite	463394/7678307	√		√	√	√		√	√	This study
74052	MT12	Mag-Qtz-hem ironstone	463426/7678330	√		√	√	√		√	√	This study
74053	MT13A	Ab-Qtz clast of granite pegmatite	463522/7678397	√	√	√	√	√		√	√	This study
74054	MT19	Mag-Qtz-hem ironstone	463265/76784240	√	√	√	√	√		√	√	This study
74055	MT20	Ab-Qtz clast of granite pegmatite	463474/7678349	√	√	√	√	√	√	√	√	This study
74056	MT22	Ab-Qtz clast of granite pegmatite	463561/7678394	√	√						√	This study
74057	MT22v	Quartz vein cutting sample MT22	463561/7678394	√							√	This study
74058	MT23	Hem-Qtz -ironstone	463563/7678394	√								This study
74233	04Snk02	Breccia	463475/7678345	√								Oliver et al. (2006)
74234	04Snk 04	Breccia	463610/7678413									Oliver et al. (2006)
74235	04Snk38	Granite	962831/7678334	√								Oliver et al. (2006)
74236	04Snk39	Breccia	463178/7678019									Oliver et al. (2006)

Appendixes 4.1-4.9

List of abbreviations

$TmCO_2$	CO_2 melting temperature
Tfm	Temperature of first melting
Thm	Temperature of hydrohalite melting
TmCla	Temperature of clathrate melting
Tm	Final melting temperature of ice
ThCO2	CO_2 homogenization temperature
Thv	Temperature of vapor disappearance
TsNaCl	Halite dissolution temperature
Th	Homogenization temperature
Th_total	Total homogenization temperature
TDec	Decrepitation temperature
Sal TmCla (wt% NaCl eq.)	Salinity calculated from CO_2 - clathrate melting temperature using the software Q_2 (Bakker, 1997; Bakker and Brown, 2003)
Sal Tm (wt% NaCl eq.)	Salinity calculated from final melting temperature of ice using the equation of Bodnar (1993)
Sal Ts (wt% NaCl eq.)	Salinity calculated from halite dissolution temperature using the equation of Sterner (1998)
Sal NaCl + $CaCl_2$ (wt% NaCl + $CaCl_2$ eq.)	Salinity calculated from final ice melting temperature and halite dissolution temperature (halite-bearing fluid inclusions or from final ice melting temperature and hydrohalite melting (two phase fluid inclusions) temperature using the software Calcicbrine (Naden, 1996)
D_F	Degree of filling
D CO_2	Density of the CO_2 phase

Temperature in degree Celcius

Appendix 4.1 Thermometric data on Type Ia fluid inclusions

Appendix 4.1 Thermometric data on Type Ia fluid inclusions									
Sample	**Ref. No**	**fi_id**	**Phases**	**Origin**	**$TmCO_2$**	**$ThCO_2$**	**Mode**	**Th_total**	**Density**
MT11	MT11-2	f2_5	CO_2 (L)	P	-57.5	-10.9	V→L	-10.9	0.988
MT11	MT11-2	f2_6	CO_2 (L)	P	-57.5	-5.9	V→L	-5.9	0.962
MT11	MT11-2	f2_7	CO_2 (L)	P	-57.3	-3.9	V→L	-3.9	0.951
MT11	MT11-2	f2_8	CO_2 (L)	P	-57.3	-9.9	V→L	-9.9	0.983
MT11	MT11-2	f2_9	CO_2 (L)	P	-57.5	-9.1	V→L	-9.1	0.979
MT11	MT11-3	f3_1	CO_2 (L)	P	-57.3	-3.7	V→L	-3.7	0.95
MT11	MT11-3	f3_2	CO_2 (L)	P	-57.3	-14	V→L	-14	1.004
MT11	MT11-3	f3_3	CO_2 (L)	P	-57.3	-10.8	V→L	-10.8	0.988
MT20	MT11-3	f3_7	CO_2 (L)	P	-57.3	-5.2	V→L	-5.2	0.958
MT20	MT20-3	f3_23	CO_2 (L)	P	-56.8	-12.9	V→L	-12.9	0.998
MT20	MT20-3	f3_24	CO_2 (L)	P	-56.8	-13.1	V→L	-13.1	0.999
MT20	MT20-3	f3_27	CO_2 (L)	P	-56.8	-4.5	V→L	-4.5	0.954
MT20	MT20-3	f3_28	CO_2 (L)	P	-57	-12.4	V→L	-12.4	0.996
MT20	MT20-3	f3_30	CO_2 (L)	P	-56.9	-11.5	V→L	-11.5	0.991
MT20	MT20-3	f3_38	CO_2 (L)	P	-56.7	-7.4	V→L	-7.4	0.97
MT20	MT20-3	f3_39	CO_2 (L)	P	-56.7	-4.2	V→L	-4.2	0.952
MT20	MT20-4	f4-1	CO_2 (L)	P	-57.6	-0.5	V→L	-0.5	0.931
MT20	MT20-4	f4-2	CO_2 (L)	P	-57.5	-10.5	V→L	-10.5	0.986
MT20	MT20-4	f4-3	CO_2 (L)	P	-57.5	-14.2	V→L	-14.2	1.005
MT20	MT20-4	f4-4	CO_2 (L)	P	-57.3	-2.7	V→L	-2.7	0.944
MT20	MT20-4	f4-11	CO_2 (L)	P	-57.5	-9.6	V→L	-9.6	0.982
MT20	MT20-4	f4-12	CO_2 (L)	P	-57.5	-17.5	V→L	-17.5	1.021
MT20	MT20-4	f4-13	CO_2 (L)	P	-57.6	-15.8	V→L	-15.8	1.013
MT20	MT20-4	f4-14	CO_2 (L)	P	-57.7	-14	V→L	-14	1.004
Min					-57.7	-17.5		-17.5	0.931
Max					-56.7	-0.5		-0.5	1.021
Average					-57.3	-9.3		-9.3	0.979
Median					-57.3	-10.2		-10.2	0.985

Appendix 4.2 Thermometric data on Type Ib fluid inclusions

Appendix 4.2 Thermometric data on Type Ib fluid inclusions									
Sample	**Ref. No**	**fi_id**	**Phases**	**Origin**	**$TmCO_2$**	**ThCO2**	**Mode**	**Th_total**	**Density**
MT20	MT20-3	f3_3	CO_2 (L)	PS	-56.5	16.5	V→L	16.5	0.809
MT20	MT20-3	f3_4	CO_2 (L)	PS	-56.5	24.2	V→L	24.2	0.723
MT20	MT20-3	f3_5	CO_2 (L)	PS	-56.5	16.2	V→L	16.2	0.811
MT20	MT20-3	f3_6	CO_2 (L)	PS	-56.5	15	V→L	15	0.822
MT20	MT20-3	f3_11	CO_2 (L)	PS	-56.5	30.5	V→L	30.5	0.569
MT20	MT20-3	f3_12	CO_2 (L)	PS	-56.5	21.6	V→L	21.6	0.756
MT20	MT20-3	f3_13	CO_2 (L)	PS	-56.5	19	V→L	19	0.785
MT20	MT20-3	f3_14	CO_2 (L)	PS	-56.1	1.9	V→L	1.9	0.917
MT20	MT20-3	f3_21	CO_2 (L)	PS	-57.3	6.9	V→L	6.9	0.884
MT20	MT20-3	f3_22	CO_2 (L)	PS	-57.3	-1.1	V→L	-1.1	0.935
Min					-57.3	-1.1		-1.1	0.569
Max					-56.1	30.5		30.5	0.935
Average					-56.6	15.1		15.1	0.801
Median					-56.5	16.35		16.35	0.810

Appendix 4.3 Thermometric data on Type IIa fluid inclusions

Appendix 4.3 Thermometric data on Type IIa fluid inclusions

Sample	Ref. No	fi_id	Phases	Origin	$TmCO_2$	Tfm	TmCla	ThCO2	Mode	Th	Mode	TDec	Sal TmCla (wt%	D_F	D CO_2	Bulk Density	$x(H_2O)$	$x(CO_2)$	x(NaCl)
MT20	MT20_3	f3_33	CO_2 (L)+H_2O (L)	P?	-57	-57.3	-12.7	4	V→L				29.0	0.63	0.90	0.91	0.64	0.20	0.16
MT20	MT20_3	f3_34	CO_2 (L)+H_2O (L)	P?	-57.2	-57.3	-12.4	7.2	V→L				29.0	0.65	0.88	0.90	0.65	0.18	0.16
MT20	MT20_3	f3_35	CO_2 (L)+H_2O (L)	P?	-57.1	-56.7	-3.6	17	V→L				22.4	0.56	0.80	0.88	0.66	0.23	0.12
MT20	MT20_3	f3_36	CO_2 (L)+H_2O (L)	P?	-57.1	-56.7	-6	25.4	V→L	276.4	LCO2 --> Laq		25.7	0.64	0.71	0.85	0.69	0.16	0.15
MT20	MT20_3	f3_37	CO_2 (L)+H_2O (L)	P?	-56.7		-12.9	7	V→L			338.1	29.0	0.75	0.88	0.91	0.70	0.13	0.18
MT20	MT20_3	f3_17	CO_2 (L)+H_2O (L)	P?	-56.5	-54.1	-11.6	17.9	V→L				29.0	0.40	0.80	0.84	0.52	0.35	0.13
MT20	MT20_8	f8_2	CO_2 (L)+H_2O (L)	P?	-57.7		-10.3	-6	V→L			248.9	29.0	0.37	0.96	0.96	0.47	0.41	0.12
MT20	MT20_8	f8_3	CO_2 (L)+H_2O (L)	P?	-57.7		-11.1	21.2	V→L			290.5	29.0	0.96	0.76	0.89	0.74	0.07	0.19
MT20	MT20_8	f8_4	CO_2 (L)+H_2O (L)	P?	-57.7		-10.4	7.7	V→L			256-260	29.0	0.68	0.88	0.93	0.67	0.16	0.17
MT20	MT20_8	f8_5	CO_2 (L)+H_2O (L)	P?	-57.8		-11.1	21.1	V→L			462.1	29.0	0.60	0.76	0.86	0.65	0.19	0.16
MT20	MT20_8	f8_6	CO_2 (L)+H_2O (L)	P?	-56.2		-10.5	6.8	V→L			263.4	29.0	0.39	0.88	0.90	0.49	0.38	0.12
MT20	MT20_8	f8_8	CO_2 (L)+H_2O (L)	P?	-56.2		-11.4	-9.1	V→L				29.0	0.30	0.98	0.96	0.40	0.50	0.10
Min					-57.8	-57.3	-12.9	-9.1				248.9	22.4	0.30	0.71	0.84	0.40	0.07	0.10
Max					-56.2	-54.1	-3.6	25.4		276.4		462.1	29.0	0.96	0.98	0.96	0.74	0.50	0.19
Average					-57.1	-56.4	-10.3	10.0				320.6	28.2	0.58	0.85	0.90	0.61	0.25	0.15
Median					-57.1	-56.7	-11.1	7.45				290.5	29.0	0.62	0.88	0.90	0.65	0.20	0.15

Appendix 4.4 Thermometric data on Type IIb fluid inclusions

Appendix 4.4 Thermometric data on Type IIb fluid inclusions													
Sample	**Ref. No**	**fi_id**	**Phases**	**Origin**	**$TmCO_2$**	**Tfm**	**Thm**	**TmCla**	**ThCO2**	**Mode**	**TsNaCl**	**TDec**	**Sal Ts (wt% NaCl eq)**
MT20	MT20_3	f3_16	CO_2 (L)+H_2O (L)+H±S	P?	-56.5	-32.4	13.4	-12	12.1	V→L			
MT20	MT20-3	f3_25	CO_2 (L)+H_2O (L)+H±S	P?	-56.8	-56.6	11.4	-12.1	21.3	V→L	307	315.4	38.7
MT20	MT20-8	f8_1	CO_2 (L)+H_2O (L)+H±S	P?	-57.7		13.7	-12.3	13.7	V→L	255.7	290.1	35
MT20	MT20-8	f8_7	CO_2 (L)+H_2O (L)+H±S	P?	-56.2		14.4	-11.6	-0.7	V→L	186.3	255-260	31.2
Min					-57.7	-56.6	11.4	-12.3	-0.7		186.3	255-260	31.2
Max					-56.2	-32.4	14.4	-11.6	21.3		307	315.4	38.7
Average					-56.8		13.2	-12.0	11.6		249.7	302.8	35.0
Median					-56.65		13.6	-12.1	12.9		255.7	302.8	35.0

Appendix 4.5 Thermometric data on Type IIIa fluid inclusions

Sample	Ref. No	fi_id	Phases	Origin	Tfm	Thm	Tm	Thv	TsNaCl	Th	Mode	Sal NaCl +$CaCl_2$ (wt% NaCl + $CaCl_2$ eq.)	NaCl	CaCl2	NaCl/(NaCl +$CaCl_2$)	Bulk Density
MT11	MT11-1	f1-5	L+V+H	S	-59.1	5	-27.5	121.4	238.9	238.9	S(h)→L	37.9	26.7	11.2	0.7	1.13
MT11	MT11-1	f1-6	L+V+H	S	-58.3	14.8	-28.1	121.3	226.8	226.8	S(h)→L	37.4	25.3	12.1	0.7	1.13
MT11	MT11-1	f1-7	L+V+H	S		7.8	-27.5	127.1	230.7	230.7	S(h)→L	37.4	26.0	11.4	0.7	1.14
MT11	MT11-3	f3_4_bis	L+V+H	S	-58.4	32.2	-26.8		166.1	166.1	S(h)→L	33.6	21.4	12.2	0.6	1.16
MT11	MT11-3	f3_5	L+V+H	S	-57.5	13.6	-27.9	140	217.1	217.1	S(h)→L	36.8	24.6	12.2	0.7	1.15
MT11	MT11-3	f3_6_bis	L+V+H	S	-60.1	14.6	-29.4		231.4	231.4	S(h)→L	38.2	25.3	13.0	0.7	1.15
MT11	MT11-3	f3-4	L+V+H	S	-57.9	11.9	-26.7	140			S(h)→L					
MT11	MT11-3	f3-6	L+V+H	S	-54	16.2	-27.4	138.6			S(h)→L					
MT11	MT11-3	f3_8	L+V+H	S	-55.3	10.7	-27.9	139	217.5	217.5	S(h)→L	36.8	24.7	12.2	0.7	1.15
MT11	MT11-3	f3_9	L+V+H	S	-55.9	6.4	-23.9	156.2	211.6	211.6	S(h)→L	33.9	27.1	6.7	0.8	1.12
MT11	MT11-3	f3_10	L+V+H	S	-55.9	6.3	-26.1	143.4	231.9	231.9	S(h)→L	36.7	26.9	9.9	0.7	1.13
MT11	MT11-3	f3_11	L+V+H	S	-53.5	7.1	-24.8	166.2			S(h)→L					
MT11	MT11-3	f3_12	L+V+H	S	-54	15.6	-23.5	160	188.2	188.2	S(h)→L	32.1	26.0	6.1	0.8	1.13
MT11	MT11-3	f3_13	L+V+H	S	-58.1	5.5	-23.1	152.3	191.1	191.1	S(h)→L	31.8	26.7	5.2	0.8	1.13
MT11	MT11-3	f3_"14"	L+V+H	S					197.8	197.8	S(h)→L					
MT12	MT12-1	f1-1	L+V+H	S	-50.7	9.2	-24									
MT12	MT12-1	f1-2	L+V+H	S	-51.4	8.4	-25.4		203.7	203.7	S(h)→L	34.7	25.2	9.5	0.7	1.14
MT12	MT12-1	f1-3	L+V+H	S	-54.2	5.3	-27.4	198.3	238.7	238.7	S(h)→L	37.9	26.8	11.1	0.7	1.13
MT12	MT12-1	f1-4	L+V+H	S	-52.4	7.4	-26.5									
MT12	MT12-1	f1-6	L+V+H	S	-54	7.8	-24.4									
MT12	MT12-1	f1-7	L+V+H	S	-53.3	12.5	-27.7									
MT12	MT12-1	f1-8	L+V+H	S	-54.1	3.9	-25.8	238.2	204.9	204.9	V→L	35.1	25.1	10.0	0.7	1.14
MT12	MT12-1	f1-17	L+V+H	S	-49.6	6.3	-22.8		168.1	168.1	S(h)→L	30.3	25.7	4.6	0.8	1.14
MT12	MT12-1	f1-35	L+V+H	S	-56.3	8	-26.2									
MT12	MT12-1	f1-36	L+V+H	S	-52.7	6.2	-24.5									
MT12	MT12-3	f3-1	L+V+H	S	-53.9	0.2	-25.6									
MT12	MT12-3	f3-3	L+V+H	S	-58.2	7.5	-29.1		315	315	S(h)→L	43.5	33.6	9.9	0.8	1.07
MT12	MT12-3	f3-4	L+V+H	S	-59.5	7.4	-24.7		187	187	S(h)→L	33.3	24.7	8.6	0.7	1.14
MT12	MT12-3	f3-5	L+V+H	S	-59.6	-1.5	-25.9		187.8	187.8	S(h)→L	34.2	23.7	10.5	0.7	1.15
MT12	MT12-3	f3-6	L+V+H	S	-53.8	12.2	-26.5									
MT12	MT12-4	f4-1	L+V+H	S	-56.2	6.3	-25.5		226.7	226.7	S(h)→L	36.0	26.8	9.2	0.7	1.12
MT12	MT12-4	f4-2	L+V+H	S	-58.3	8.1	-26.4		217.5	217.5	S(h)→L	36.1	25.5	10.6	0.7	1.14
MT12	MT12-4	f4-3	L+V+H	S	-56.4	10.6	-26		231.7	231.7	S(h)→L	36.7	26.9	9.8	0.7	1.13
MT12	MT12-4	f4-4	L+V+H	S	-57.4	7.2	-26.2		239.9	239.9	S(h)→L	37.3	27.5	9.8	0.7	1.12
MT12	MT12-4	f4-5	L+V+H	S	-58.2	9	-26.7		203.4	203.4	S(h)→L	35.5	24.2	11.3	0.7	1.15
MT13A	MT13A-2	f2-1	L+V+H	S	-58.2	-11.6	-25.6	127.4	226.8	226.8	S(h)→L	36.1	26.8	9.3	0.7	1.12
MT13A	MT13A-2	f2-2	L+V+H	S	-51.2	5	-24.6	117								

Appendix 4.5 Thermometric data on Type IIIa fluid inclusions

Sample	Ref. No	fi_id	Phases	Origin	Tfm	Thm	Tm	Thv	TsNaCl	Th	Mode	Sal NaCl +$CaCl_2$ (wt% NaCl + $CaCl_2$ eq.)	NaCl	CaCl2	NaCl/(NaCl +$CaCl_2$)	Bulk Density
MT13A	MT13A-2	f2-3	L+V+H	S	-53.2	12.9	-24.6	121.1	199.3	199.3	S(h)→L	33.9	25.6	8.2	0.8	1.13
MT13A	MT13A-2	f2-4	L+V+H	S	-54.6	10.7	-25.2	121.5	202	202	S(h)→L	34.5	25.3	9.2	0.7	1.14
MT13A	MT13A-2	f2-5	L+V+H	S	-52.2	13.2	-25.6	125.1	205.3	205.3	S(h)→L	35.0	25.2	9.8	0.7	1.14
MT13A	MT13A-2	f2-6	L+V+H	S				121	213.9	213.9	S(h)→L					
MT13A	MT13A-6	f6-1	L+V+H	S	-58.8	5.5	-25.3		204.2	204.2	S(h)→L	34.6	25.3	9.4	0.7	1.14
MT13A	MT13A-6	f6-2	L+V+H	S	-58.8	13.9	-25.2	126.3	170.5	170.5	S(h)→L	32.9	23.2	9.8	0.7	1.15
MT13A	MT13A-6	f6-3	L+V+H	S	-58.7	15.3	-24.9	124.3	174.3	174.3	S(h)→L	32.9	23.7	9.2	0.7	1.15
MT13A	MT13A-6	f6-4	L+V+H	S	-58.8	15.5	-24.8	123.3	195.4	195.4	S(h)→L	33.8	25.1	8.7	0.7	1.14
MT13A	MT13A-6	f6-5	L+V+H	S	-60.2	6.1	-24.9		199.4	199.4	S(h)→L	34.1	25.3	8.8	0.7	1.14
MT19	MT19-2	f2-2	L+V+H	S	-64.2	15.3	-25.2		188.5	188.5	S(h)→L	33.9	24.4	9.4	0.7	1.14
MT19	MT19-2	f2-3	L+V+H	S	-67.2	6.1	-25.9		214.5	214.5	S(h)→L	35.6	25.6	10.0	0.7	1.13
MT20	MT20-2	f2_1	L+V+h	S	-51.8	12.4	-27.1		147.5	147.5	S(h)→L	33.0	20.0	12.9	0.6	1.17
MT20	MT20-3	f3_1	L+V+h	S	-54.1	8.8	-25.4	113.6	188	188	S(h)→L	33.9	24.1	9.8	0.7	1.14
MT20	MT20-3	f3_2	L+V+h	S	-56.3	9.9	-24.1									
MT20	MT20-3	f3_19	L+V+h	S	-54.8	17	-22.4	106.8								
MT20	MT20-3	f3_29	L+V+H	S	-56.7	5	-25.4		175.2	175.2	S(h)→L	33.2	23.2	10.0	0.7	1.15
MT20	MT20-3	f3_41	L+V+H	S	-53.4	13.2	-24		212.2	212.2	S(h)→L	34.0	27.0	6.9	0.8	1.12
MT20	MT20-3	f3_42	L+V+H	S	-53.1	15.1	-23.8		235.9	235.9	S(h)→L	35.1	28.9	6.2	0.8	1.10
MT20	MT20-4	f4-5	L+V+H	S	-44.6	11.4	-23.2									
MT20	MT20-4	f4-6	L+V+H	S	-44.2	10.7	-24.2									
MT20	MT20-4	f4-8	L+V+H	S	-54.3	9.5	-22.5		259.2	259.2		35.3	32.1	3.2	0.9	1.02
MT20	MT20-4	f4-9	L+V+H	S	-54	8.8	-24.8		360	360		45.4	40.3	5.1	0.9	0.94
MT20	MT20-4	f4-10	L+V+H	S	-53	11.6	-24.7		336	336		43.2	37.6	5.6	0.9	0.97
MT20	MT20-4	f4-11	L+V+H	S					302.8	302.8						
MT20	MT20-4	f4-12	L+V+H	S					360	360						
MT20	MT20-6	f6-1	L+V+H	S	-51.1	8.5	-23		210.3	210.3	S(h)→L	32.8	28.1	4.8	0.9	1.11
MT20	MT20-6	f6-3	L+V+H	S	-53.2	8.6	-22.9		170.9	170.9	S(h)→L	30.6	25.8	4.8	0.8	1.14
MT20	MT20-6	f6-4	L+V+H	S	-45.3	13	-21.7		214.5	214.5	S(h)→L	31.4	30.0	1.5	1.0	1.10
MT20	MT20-6	f6-5	L+V+H	S	-57.7	6.3	-24.8									
MT20	MT20-6	f6-6	L+V+H	S		5.8	-23.2									
MT20	MT20-6	f6-7	L+V+H	S					206.8	206.8	S(h)→L					
MT20	MT20-6	f6-8	L+V+H	S					244.9	244.9	S(h)→L					
Min					-67.2	-11.6	-29.4	106.8	147.5	147.5		30.3	20.0	1.5	0.6	0.94
Max					-44.2	32.2	-21.7	238.2	360.0	360.0		45.4	40.3	13.0	1.0	1.17
Average					-55.3	9.4	-25.3	138.8	219.4	219.4		35.3	26.4	8.9	0.7	1.12
Median					-54.8	8.8	-25.3	127.1	211.6	211.6		34.7	25.6	9.5	0.7	1.14

Appendix 4.6 Thermometric data on Type IIIb fluid inclusions

Sample	Ref. No	fi_id	Phases	Origin	Tfm	Thm	Tm	Th	Mode	Sal NaCl +$CaCl_2$	NaCl	CaCl2	Sal NaCl +$CaCl_2$ (wt% NaCl + $CaCl_2$ eq.)	D_F	Bulk Density
MT11	MT11-1	f1-4	L+V	S	-54	25	-24.2	117.8	V→L					0.92	
MT11	MT12-1	f1-9	L+V	S	-53.1	15.2	-23.5	136.4	V→L						
MT11	MT12-1	f1-27	L+V	S	-53.6	12.1	-24.1	132.9	V→L						
MT12	MT12-1	f1-34	L+V	S	-53.7	-7.1	-23.1	128	V→L	25.8	20.7	5.2	0.8	0.26	1.13
MT12	MT12-2	f2-1	L+V	S	-54.5	-25.4	-21.9	150.2	V→L	22.8	12.9	9.9	0.6	0.54	1.09
MT12	MT12-2	f2-2	L+V	S	-53.6	-25.2	-21.7	155.6	V→L	22.7	13.2	9.5	0.6	0.58	1.08
MT12	MT12-2	f2-3	L+V	S	-53.7	-25	-24	151.3	V→L	24.1	14.5	9.7	0.6	0.43	1.10
MT12	MT12-2	f2-4	L+V	S	-57.4	-24	-21.1	152.9	V→L	22.5	15.5	7.1	0.7	0.61	1.08
MT12	MT12-2	f2-5	L+V	S	-50.4		-20	149.7	V→L					0.50	
MT12	MT12-3	f3-2	L+V	S	-59.3	13.5	-27.2							0.46	
MT13A	MT13A-4	f4-1	L+V	S	-63	-34.2	-26.3			24.0	4.2	19.8	0.2	0.86	
MT13A	MT13A-4	f4-2	L+V	S	-61.3	-34.6	-26.5	183.4	V→L	24.0	4.0	20.0	0.2	0.53	1.10
MT13A	MT13A-4	f4-4	L+V	S	-60.5	-35.2	-30.3			25.7	4.0	21.6	0.2	0.48	
MT13A	MT13A-4	f4-5	L+V	S	-69.5	-33.2	-27	154.8	V→L	24.4	4.8	19.6	0.2	0.93	1.12
MT13A	MT13A-4	f4-6	L+V	S	-52.2	-42.4	-26.2	154	V→L	23.6	2.1	21.5	0.1	0.92	1.12
MT13A	MT13A-4	f4-7	L+V	S	-69.2	-42.3	-33.7	156.4	V→L	26.6	2.4	24.2	0.1	0.89	1.15
MT13A	MT13A-5	f5-1	L+V	S	-69.7	-36.5	-33.5	142.8	V→L	26.8	3.7	23.1	0.1	0.30	1.16
MT13A	MT13A-5	f5-2	L+V	S	-69.7	-36.4	-26.7	160.8	V→L	24.0	3.4	20.7	0.1		1.12
MT19	MT19-1	f1-1	L+V	S	-69.5	-28	-24.2	181	V→L	23.6	9.3	14.3	0.4	0.63	1.09
MT19	MT19-1	f1-2	L+V	S	-69.5	-28	-22.9	175	V→L	22.9	9.0	13.9	0.4	0.47	1.08
MT19	MT19-1	f1-3	L+V	S	-66.1	-27.9	-21.9	161.1	V→L	22.4	9.0	13.4	0.4	0.92	1.09
MT19	MT19-1	f1-4	L+V	S	-57.6	10.8	-25.4							0.45	
MT19	MT19-2	f1-5	L+V	S	-64.5	14.8	-25.1							0.70	
MT19	MT19-2	f2-1	L+V	S	-62.5	-3.7	-26.6	150.1	V→L	28.1	15.7	12.4	0.6	0.67	1.13
MT20	MT20-2	f2_2	L+V	S	-67.7	-37.3	-23.5	183.5	V→L	22.5	2.9	19.6	0.1	0.45	1.09
MT20	MT20-2	f2_3	L+V	S	-65.1	-30.7	-24.1	180.5	V→L	23.2	6.3	16.9	0.3	0.47	1.09
MT20	MT20-2	f2_4	L+V	S	-53.7	-23.5								0.65	
MT20	MT20-2	f2_5	L+V	S	-68.2	-37.3	-29.7			25.3	3.2	22.0	0.1	0.41	
MT20	MT20-3	f3_7	L+V	S	-58.3	21.9	-26.3	127.7	V→L					0.87	
MT20	MT20-3	f3_20	L+V	S	-57.8	2.8	-22.7	109.2	V→L					0.8	
MT20	MT20-3	f3_40	L+V	S	-56.1	22.7	-24.1	157.2	V→L					0.88	
MT20	MT20-4	f4-7	L+V	S	-58.8	11.3	-26.5							0.92	
Min					-69.7	-42.4	-33.7	109.2		22.4	2.1	5.2	0.1	0.26	1.08
Max					-50.4	25.0	-20.0	183.5		28.1	20.7	24.2	0.8	0.93	1.16
Average					-60.4	-15.1	-25.3	152.2		24.3	8.0	16.2	0.3	0.64	1.11
Median					-59.1	-25.2	-24.2	153.5		24.0	5.6	18.2	0.2	0.61	1.10

Appendix 4.7 Thermometric data on Type IVa fluid inclusions

Sample	Ref. No	fi_id	Phases	Origin	Tfm	Thm	Tm	Thv	TsNaCl	Th	Mode	Sal Ts (wt% NaCl eq)	Bulk Density
MT11	MT11-2	f2_4	L+V+H	S	-29.9	13.4	-23.2		209.4	209.4	S(h)→L	32.4	
MT12	MT12-1	f1-15	L+V+H	S	-27.9	7.8	-24.1	255.9	246.3	246.3	V→L	34.5	1.11
MT12	MT12-1	f1-16	L+V+H	S	-27.9	5.9	-24.2	248.2	256.7	256.7	S(h)→L	35.1	1.11
MT12	MT12-1	f1-22	L+V+H	S	-28.1	6.9	-23.6						
MT12	MT12-1	f1-23	L+V+H	S	-27.3	8.3	-23.6						
MT12	MT12-1	f1-29	L+V+H	S	-29.9	5.1	-23.7	179.9	239.4	239.4	S(h)→L	34.0	1.16
MT20	MT20-3	f3_18	L+V+h	S	-34.8	5.4	-19.1	118.1	217	217	S(h)→L	32.8	1.19
MT20	MT20-3	f3_31	L+V+H	S	-28.3	14.2	-23.6						
MT20	MT20-3	f3_32	L+V+H	S	-36.6	10.7	-24.4						
MT20	MT20-3	f-"32"	L+V+H	S	-27.1	15	-24.1		203.6	203.6	S(h)→L	32.1	
MT20	MT20-6	f6-2	L+V+H	S	-36.4	6	-22		242.8	242.8	S(h)→L	34.2	
Min					-36.6	5.1	-24.4	118.1	203.6	203.6		32.1	1.11
Max					-27.1	15	-19.1	255.9	256.7	256.7		35.1	1.19
Average					-30.4	9.0	-23.2	200.5	230.7	230.7		33.6	1.14
Median					-28.3	7.8	-23.6	214.05	239.4	239.4		34	1.14

Appendix 4.8 Thermometric data on Type IVb fluid inclusions

Sample	Ref. No	fi_id	Phases	Origin	Tfm	Thm	Tm	Th	Mode	D_F	Bulk Density
MT11	MT11-2	f2_1	L+V	S	-29.2	12.1	-22.1	176.7	V→L	0.53	1.06
MT11	MT11-2	f2_2	L+V	S	-29	12.3	-21.6	166.3	V→L	0.59	1.07
MT11	MT11-2	f2_3	L+V	S	-29.8	11.5	-22.1	176.8	V→L	0.84	1.06
MT11	MT11-2	f2_10	L+V	S	-29.9	14.6	-22.6	177	V→L		1.07
MT11	MT11-2	f2_11	L+V	S	-31.1	12.9	-22.7	180	V→L	0.64	1.06
MT12	MT12-1	f1-30	L+V	S	-33.3	9	-25.1	184.7	V→L	0.79	1.07
Min					-33.3	9	-25.1	166.3		0.53	1.06
Max					-29	14.6	-21.6	184.7		0.84	1.07
Average					-30.4	12.1	-22.7	176.9		0.68	1.07
Median					-29.85	12.2	-22.35	176.9		0.64	1.07

Appendix 4.9 Thermometric data on Type V fluid inclusions

Appendix 4.9 Thermometric data on Type V fluid inclusions													
Sample	**Ref. No**	**fi_id**	**Phases**	**Origin**	**Tfm**	**Thm**	**Tm**	**Thv**	**Mode**	**Th_total**	**Sal Tm %NaCl eq.)**	**D_F**	**Bulk Density**
MT12	MT12-1	f1-24	L+V	S	-31.3	-20.5	-7.2	144	V→L	144	10.7	0.77	0.99
MT12	MT12-1	f1-25	L+V	S	-30.1		-6.8	178.5	V→L	178.5	10.2	0.45	0.96
MT12	MT12-1	f1-26	L+V	S	-30.9		-8.3	165	V→L	165	12.0	0.92	0.98
MT12	MT12-1	f1-31	L+V	S	-35.9	-20.9	-5.7	152.6	V→L	152.6	8.8	0.63	0.97
MT12	MT12-1	f1-32	L+V	S	-37.1	-24.9	-6	172.1	V→L	172.1	9.2	0.48	0.96
MT12	MT12-1	f1-33	L+V	S	-37.2	-23.7	-6	157.6	V→L	157.6	9.2	0.76	0.97
MT12	MT12-1	f1-10	L+V	S	-24		-9	170	V→L	170	12.8	0.95	0.99
MT12	MT12-1	f1-5	L+V	S	-24.9		-8.3	190	V→L	190	12.0	0.57	0.97
MT12	MT12-1	f1-18	L+V	S	-24		-7.5	245.4	V→L	245.4	11.1	0.22	0.91
Min					-37.2	-24.9	-9	144		144	8.8	0.22	0.91
Max					-24	-20.5	-5.7	245.4		245.4	12.8	0.95	0.99
Average					-30.6	-22.5	-7.2	175		175	10.7	0.64	0.97
Median					-30.9	-22.3	-7.2	170		170	10.7	0.63	0.97

Appendix 4.10 Laser Raman data on Type I and II fluid inclusions

Appendix 4.10 Laser Raman data on Type I and II fluid inclusions										
Sample	**Ref. No**	**Flui inclusion type**	**Phases**	**CO_2 (mol%)**	**N_2 (mol%)**	**H_2S (mol%)**	**C_3H_2 (mol%)**	**CH_4 (mol%)**	**C_2H_6 (mol%)**	**NH_3 (mol%)**
MT20	MT20-z3	Type I	CO_2 (L)	100	0	0	0	0	0	0
MT20	MT20-z3	Type I	CO_2 (L)	100	0	0	0	0	0	0
MT20	MT20-z3	Type I	CO_2 (L)	100	0	0	0	0	0	0
MT20	MT20-z3	Type I	CO_2 (L)	100	0	0	0	0	0	0
MT20	MT20-z8	Type I	CO_2 (L)	100	0	0	0	0	0	0
MT20	MT20-z8	Type I	CO_2 (L)	100	0	0	0	0	0	0
MT20	MT20-z8	Type I	CO_2 (L)	100	0	0	0	0	0	0
MT20	MT20-z8	Type I	CO_2 (L)	100	0	0	0	0	0	0
MT20	MT20-z8	Type I	CO_2 (L)	100	0	0	0	0	0	0
MT20	MT20-z8	Type I	CO_2 (L)+H_2O (L)	100	0	0	0	0	0	0
MT20	MT20-z3	Type IIa	CO_2 (L)+H_2O (L)	100	0	0	0	0	0	0
MT20	MT20-z3	Type IIa	CO_2 (L)+H_2O (L)	100	0	0	0	0	0	0
MT20	MT20-z3	Type IIa	CO_2 (L)+H_2O (L)	100	0	0	0	0	0	0
MT20	MT20-z3	Type IIa	CO_2 (L)+H_2O (L)	100	0	0	0	0	0	0
MT20	MT20-z3	Type IIa	CO_2 (L)+H_2O (L)	100	0	0	0	0	0	0
MT20	MT20-z3	Type IIa	CO_2 (L)+H_2O (L)	100	0	0	0	0	0	0
MT20	MT20-z3	Type IIa	CO_2 (L)+H_2O (L)	100	0	0	0	0	0	0
MT20	MT20-z8	Type IIa	CO_2 (L)+H_2O (L)	100	0	0	0	0	0	0
MT20	MT20-z8	Type IIa	CO_2 (L)+H_2O (L)	100	0	0	0	0	0	0
MT20	MT20-z8	Type IIa	CO_2 (L)+H_2O (L)	100	0	0	0	0	0	0
MT20	MT20-z8	Type IIa	CO_2 (L)+H_2O (L)	100	0	0	0	0	0	0
MT20	MT20-z8	Type IIb	CO_2 (L)+H_2O (L)+H±S	100	0	0	0	0	0	0
MT20	MT20-z8	Type IIb	CO_2 (L)+H_2O (L)+H±S	100	0	0	0	0	0	0
MT20	MT20-z8	Type IIb	CO_2 (L)+H_2O (L)+H±S	100	0	0	0	0	0	0
MT20	MT20-z8	Type IIb	CO_2 (L)+H_2O (L)+H±S	100						

Appendix 5.1 LA ICP MS data on Type III and IV fluid inclusions from the SRBP

Appendix 5.1 LA ICP MS data on Type III and IV fluid inclusions from the SRBP														
			Concentration (ppm)						LOD (ppm)					
Sample	Inclusion Ref. No	Fluid inclusion type	Na	K	Ca	Mn	Fe	Sr	Na	K	Ca	Mn	Fe	Sr
MT11	25: MT11-3A.	Type III	1	0.4166	0.3451	0.0057	0.0119	0.0082	0.1384	0.1614	0.0157	0.0434	0.0116	0.0005
MT11	27: MT11-3B.	Type III	1	0.1371	0.1951	0.0012	0.0047	0.0033	0.0282	0.0384	0.0038	0.0124	0.0034	0.0003
MT11	28: MT11-3B.	Type III	1	0.2232	0.3942	-0.0104	0.0193	0.0065	0.1274	0.1734	0.0173	0.0560	0.0153	0.0014
MT11	35: MT11-3E.	Type III	1	0.1279	0.3013	0.0982	0.0297	0.0096	0.0506	0.0682	0.0071	0.0206	0.0056	0.0000
MT11	42: MT11-3SA	Type III	1	0.1073	0.2603	0.0119	0.5168	0.0051	0.0565	0.0654	0.0065	0.0182	0.0056	0.0002
MT11	43: MT11-3SA	Type III	1	0.1661	0.2649	0.0052	0.0328	0.0058	0.0194	0.0225	0.0022	0.0063	0.0019	0.0001
MT11	45: MT11-3SB	Type III	1	0.0879	0.1369	0.0017	0.0021	0.0015	0.0047	0.0053	0.0006	0.0017	0.0005	0
MT11	46: MT11-3SB	Type III	1	0.0836	0.1057	0.0040	0.0018	0.0027	0.0236	0.0271	0.0029	0.0085	0.0026	0
MT11	48: MT11-3SC	Type III	1	0.1809	0.3950	0.0127	0.0073	0.0075	0.0581	0.0790	0.0069	0.0219	0.0073	0
MT11	52: MT11-3SC	Type III	1	0.3611	0.4861	0.0067	0.0439	0.0097	0.0272	0.0370	0.0033	0.0103	0.0034	0.0002
MT13A	61: MT13A-6F	Type III	1	0.2746	0.2360	-0.0005	0.2362	0.0010	0.3348	0.2299	0.0376	0.4245	0.1238	0.0004
MT13A	64: MT13A-6g	Type III	1	0.2748	0.4035	0.0696	0.0809	0.0039	0.0911	0.0609	0.0096	0.1062	0.0304	0
MT13A	65: MT13A-6g	Type III	1	0.1362	0.1993	0.0580	0.1287	0.0023	0.0724	0.0484	0.0076	0.0844	0.0242	0
MT13A	69: MT13A-6i	Type III	1	0.2722	0.2265	0.0147	0.0389	0.0027	0.0808	0.0577	0.0086	0.0868	0.0284	0.0001
MT13A	72: MT13A-6i	Type III	1	0.4097	0.1354	0.0975	0.0927	0.0015	0.1979	0.1412	0.0210	0.2126	0.0694	0.0003
MT13A	75: MT13A-6l	Type III	1	0.1407	0.2298	0.0809	0.0026	0.0014	0.1294	0.0976	0.0135	0.1518	0.0473	0.0002
MT13A	76: MT13A-6l	Type III	1	0.2193	0.1144	0.0289	0.1525	0.0014	0.0414	0.0312	0.0043	0.0485	0.0151	0.0001
MT13A	79: MT13A-6m	Type III	1	0.1076	0.2663	0.0969	0.5016	0.0029	0.1024	0.0700	0.0103	0.1180	0.0336	0.0002
MT13A	82: MT13A-6n	Type III	1	0.1569	0.2118	-0.0160	0.0386	0.0019	0.1379	0.0808	0.0118	0.1499	0.0418	0.0003
MT13A	7: MT20-4d.	Type III	1	0.0894	0.1290	-0.0549	0.0448	0.0011	0.0876	0.0367	0.0068	0.1003	0.0323	0.0001
MT13A	15: MT20-4c.	Type III	1	0.1098	0.1582	-0.0809	0.0147	0.0012	0.1001	0.0468	0.0085	0.1328	0.0380	0.0001
MT13A	36: MT20-6c.	Type III	1	0.0871	0.1623	0.0240	0.0175	0.0018	0.0455	0.0240	0.0044	0.0430	0.0137	0
MT13A	37: MT20-6c.	Type III	1	0.1905	0.1382	0.0046	0.0140	0.0023	0.0485	0.0256	0.0047	0.0459	0.0147	0.0001
MT13A	43: MT20-6e.	Type III	1	0.3019	0.3089	0.0289	-0.0140	0.0023	0.1385	0.0813	0.0129	0.1485	0.0546	0.0001
MT20	70: MT20-5i.	Type III	1	0.2129	0.1772	0.0026	0.0082	0.0062	0.2189	0.1942	0.0096	0.0069	0.0036	0.0003
MT20	72: MT20-5i.	Type III	1	0.2437	0.1554	-0.0002	0.0003	0.0014	0.1442	0.1280	0.0063	0.0046	0.0024	0.0002
MT20	74: MT20-5i.	Type III	1	0.1864	0.1271	-0.0001	-0.0002	0.0011	0.0759	0.0674	0.0033	0.0024	0.0013	0.0001
MT20	75: MT20-5l.	Type III	1	0.2135	0.2105	0.0024	0.0078	0.0035	0.3253	0.2505	0.0148	0.0077	0.0043	0.0003
MT20	76: MT20-5l.	Type III	1	0.2469	0.2535	0.0041	0.0052	0.0022	0.2431	0.1872	0.0110	0.0057	0.0032	0.0002
MT20	77: MT20-5l.	Type III	1	0.1641	0.1282	0.0009	0.0028	0.0014	0.1139	0.0877	0.0052	0.0027	0.0015	0.0001
MT20	78: MT20-5l.	Type III	1	0.2760	0.2480	0.0012	0.0096	0.0034	0.1602	0.1233	0.0073	0.0038	0.0021	0.0001
MT20	79: MT20-5m.	Type III	1	0.0879	0.2048	0.0049	0.0101	0.0056	0.1833	0.1780	0.0076	0.0047	0.0034	0
MT20	82: MT20-5m.	Type III	1	0.1268	0.1751	0.0020	0.0056	0.0021	0.0825	0.0802	0.0034	0.0021	0.0015	0
MT20	84: MT20-5m.	Type III	1	0.1621	0.1862	0.0028	0.0089	0.0035	0.1224	0.1189	0.0051	0.0031	0.0023	0
MT20	94: MT20-5p.	Type III	1	0.3243	0.3004	0.0033	0.0060	0.0028	0.3364	0.2612	0.0132	0.0082	0.0038	0.0003
MT20	95: MT20-5p.	Type III	1	0.2593	0.1520	0.0025	0.0097	0.0022	0.1967	0.1527	0.0077	0.0048	0.0022	0.0002
MT12	10: MT12-4G.	Type III	1	0.1213	0.1675	0.0009	0.0309	0.0031	0.0155	0.0187	0.0018	0.0062	0.0015	0.0001
MT12	11: MT12-4G.	Type III	1	0.2751	0.2111	0.0061	6.3320	0.0067	0.0370	0.0444	0.0042	0.0148	0.0035	0.0002
MT12	12: MT12-3A.	Type III	1	0.1581	0.3975	0.0064	0.7380	0.0063	0.0162	0.0167	0.0014	0.0039	0.0013	0.0001
MT12	15: MT12-3B.	Type III	1	0.2306	0.2561	0.0080	0.5422	0.0066	0.1534	0.1620	0.0162	0.0404	0.0118	0
MT12	16: MT12-3C.	Type III	1	0.2701	0.2848	0.0162	0.0599	0.0058	0.1151	0.1387	0.0133	0.0319	0.0091	0
MT12	17: MT12-3C.	Type III	1	0.3323	0.2476	0.0269	0.0661	0.0048	0.1850	0.2229	0.0214	0.0513	0.0146	0
MT12	18: MT12-3D.	Type III	1	0.2801	0.3004	0.0027	0.0350	0.0086	0.0601	0.0735	0.0067	0.0171	0.0046	0
MT12	22: MT12-3F.	Type III	1	0.3368	0.1930	-0.0179	0.0664	0.0051	0.1499	0.2006	0.0184	0.0449	0.0129	0
MT19	2: MT19-1h.	Type III	1	0.1241	0.1322	0.0022	0.0107	0.0011	0.2290	0.1783	0.0101	0.0102	0.0038	0.0002
MT19	4: MT19-1h.	Type III	1	0.1996	0.1689	0.0105	0.0141	0.0012	0.3717	0.2894	0.0164	0.0165	0.0062	0.0004
MT19	5: MT19-1h.	Type III	1	0.2553	0.2744	0.0031	0.0529	0.0014	0.1447	0.1126	0.0064	0.0064	0.0024	0.0001
MT19	13: MT19-1l.	Type III	1	0.3809	0.2785	0.0007	0.0057	0.0019	0.1300	0.1095	0.0053	0.0056	0.0020	0.0002
MT19	14: MT19-1m.	Type III	1	0.2054	0.2661	0.0032	0.0202	0.0025	0.1911	0.1380	0.0087	0.0072	0.0035	0.0002
MT19	15: MT19-1m.	Type III	1	0.1099	0.3989	0.0071	0.0149	0.0027	0.2784	0.2010	0.0126	0.0104	0.0051	0.0003
MT19	17: MT19-1m.	Type III	1	0.2994	0.2767	0.0074	0.0778	0.0021	0.1560	0.1126	0.0071	0.0059	0.0028	0.0002
MT19	20: MT19-1n.	Type III	1	0.1751	0.2396	0.0041	0.0186	0.0014	0.5300	0.4867	0.0217	0.0234	0.0092	0.0006
MT19	26: MT19-1o.	Type III	1	0.2261	0.3471	0.0060	0.0354	0.0020	0.1431	0.1148	0.0058	0.0061	0.0025	0.0001
MT19	27: MT19-1o.	Type III	1	0.2342	0.5770	0.0062	0.0110	0.0029	0.1582	0.1269	0.0064	0.0068	0.0028	0.0001
MT19	30: MT19-2g.	Type III	1	0.2335	0.1953	0.0018	-0.0001	0.0018	0.1328	0.0975	0.0063	0.0054	0.0023	0
MT19	31: MT19-2g.	Type III	1	0.2927	0.1214	0.0007	0.0027	0.0011	0.1340	0.0983	0.0064	0.0054	0.0024	0
MT19	33: MT19-2h.	Type III	1	0.0975	0.4431	0.0028	0.0073	0.0016	0.5159	0.3855	0.0195	0.0213	0.0080	0.0004
MT19	34: MT19-2h.	Type III	1	0.2257	0.1494	-0.0017	0.0047	0.0013	0.3899	0.2913	0.0147	0.0161	0.0061	0.0003
MT11	98: MT11-2i.	Type IV	1	0.1513	0.2909	0.0500	0.1286	0.0033	0.1369	0.1092	0.0149	0.1241	0.0357	0.0002
MT11	99: MT11-2i.	Type IV	1	0.0451	0.1893	0.0338	0.0711	0.0022	0.1495	0.1193	0.0163	0.1356	0.0390	0.0002
MT11	106: MT11-2n	Type IV	1	0.3255	spike	spike	0.0789	0.0038	0.0761	0.0616	0.0074	0.0620	0.0179	0.0001
MT12	56: MT12-1c.	Type IV	1	0.7175	0.3551	-0.0034	0.0111	0.0013	0.2905	0.2257	0.0122	0.0138	0.0054	0
MT12	59: MT12-1e.	Type IV	1	0.2111	0.2940	0.0025	0.0161	0.0018	0.2224	0.1852	0.0102	0.0095	0.0043	0.0002
MT12	63: MT12-1f.	Type IV	1	0.1461	0.5887	0.0049	0.0112	0.0022	0.1016	0.0887	0.0051	0.0047	0.0018	0
MT12	64: MT12-1f.	Type IV	1	0.0885	0.3122	-0.0005	0.0041	0.0018	0.4604	0.4021	0.0229	0.0212	0.0081	0
MT12	65: MT12-1f.	Type IV	1	0.0978	0.5893	0.0010	0.0193	0.0023	0.3974	0.3470	0.0198	0.0183	0.0070	0
MT12	68: MT12-1g.	Type IV	1	0.1265	0.2493	0.0012	0.0060	0.0028	0.1528	0.1344	0.0072	0.0066	0.0029	0.0003

Appendix 5.1 LA ICP MS data on Type III and IV fluid inclusions from the SRBP														
			Concentration (ppm)						LOD (ppm)					
Sample	Inclusion Ref. No	Fluid inclusion type	Na	K	Cu	Zn	Ba	Pb	Na	K	Cu	Zn	Ba	Pb
MT11	27: MT11_3SF.	Type III	1	0.3593	0.0034	0.0149	spike	0.0007	0.0837	0.0758	0.0011	0.0025	0.0007	0.0003
MT11	53: MT11_3SL.	Type III	1	0.0316	0.0011	0.0051	0.0255	0.0019	0.0333	0.0301	0.0006	0.0019	0.0000	0.0002
MT11	55: MT11_3SL.	Type III	1	0.5122	0.0055	0.0178	spike	0.0016	0.2751	0.2489	0.0050	0.0153	0.0000	0.0016
MT11	59: MT11_4A.	Type III	1	0.1408	0.0019	0.0018	0.0005	0.0003	0.0467	0.0430	0.0009	0.0017	0.0005	0.0003
MT11	60: MT11_4A.	Type III	1	0.6687	0.0072	0.0132	0.0023	0.0013	0.2216	0.2039	0.0043	0.0080	0.0023	0.0013
MT11	61: MT11_4A.	Type III	1	0.7439	0.0038	0.0240	0.0289	0.0009	0.1613	0.1485	0.0031	0.0058	0.0017	0.0009
MT11	23: MT11_3I.	Type III	1	0.1096	0.0013	0.0056	0.0068	0.0007	0.0737	0.0688	0.0013	0.0033	0.0009	0.0003
MT11	39: MT11_3SI.	Type III	1	0.1876	0.0010	0.0028	0.0150	0.0002	0.0561	0.0471	0.0010	0.0026	0.0000	0.0002
MT11	46: MT11_3SJ.	Type III	1	0.4384	0.0029	0.0062	0.0259	0.0006	0.1312	0.1398	0.0029	0.0034	0.0000	0.0004
MT11	64: MT11_4B.	Type III	1	0.1896	0.0021	0.0012	0.0109	0.0006	0.1317	0.1142	0.0021	0.0055	0.0015	0.0006
MT11	66: MT11_4C.	Type III	1	0.3178	0.0063	0.0106	0.0349	0.0021	0.3486	0.2799	0.0063	0.0088	0.0033	0.0021
MT11	67: MT11_4C.	Type III	1	0.5186	0.0064	0.0147	0.0126	0.0021	0.3531	0.2835	0.0064	0.0089	0.0033	0.0021
MT11	68: MT11_4C.	Type III	1	0.1540	0.0027	0.0070	0.0092	0.0009	0.1495	0.1201	0.0027	0.0038	0.0014	0.0009
MT11	71: MT11_4E.	Type III	1	0.1601	0.0016	0.0018	0.0034	0.0002	0.0383	0.0332	0.0006	0.0018	0.0000	0.0002
MT11	26: MT11_3SE.	Type III	1	0.2957	0.0031	0.0059	0.0130	0.0025	0.1301	0.1357	0.0031	0.0059	0.0000	0.0006
MT11	47: MT11_3SK.	Type III	1	0.1501	0.0023	0.0062	0.0115	0.0006	0.1130	0.1047	0.0023	0.0062	0.0010	0.0005
MT13A	100: MT13A_6	Type III	1	0.2777	0.0035	0.0122	0.0057	0.0008	0.1948	0.1822	0.0035	0.0060	0.0047	0.0008
MT13A	102: MT13A_6	Type III	1	0.3118	0.0082	0.0069	0.0081	0.0009	0.2147	0.2007	0.0039	0.0066	0.0052	0.0009
MT13A	103: MT13A_6	Type III	1	0.3052	0.0049	0.0104	0.0074	0.0014	0.2679	0.2505	0.0049	0.0083	0.0064	0.0012
MT13A	105: MT13A_6	Type III	1	0.3965	0.0117	0.0082	0.0158	0.0053	0.1711	0.1574	0.0028	0.0082	0.0000	0.0007
MT13A	107: MT13A_6	Type III	1	0.3296	0.0123	0.0097	0.0408	0.0021	0.1901	0.1748	0.0031	0.0091	0.0000	0.0008
MT13A	109: MT13A_6	Type III	1	0.1053	0.0012	0.0015	0.0039	0.0010	0.0617	0.0524	0.0009	0.0013	0.0006	0.0003
MT13A	110: MT13A_6	Type III	1	0.3448	0.0023	0.0042	spike	0.0006	0.1519	0.1288	0.0023	0.0031	0.0014	0.0006
MT13A	112: MT13A_6	Type III	1	0.2035	0.0024	0.0038	spike	0.0006	0.1575	0.1336	0.0024	0.0033	0.0015	0.0006
MT20	3: MT20-6o.	Type III	1	0.1254	0.0026	0.0000	0.0050	0.0011	0.1230	0.0564	0.0026	0.0035	0.0020	0.0004
MT20	4: MT20-6o.	Type III	1	0.1263	0.0021	0.0000	0.0020	0.0004	0.0982	0.0451	0.0021	0.0028	0.0016	0.0003
MT20	5: MT20-6o.	Type III	1	0.0981	0.0004	0.0018	0.0053	0.0003	0.0182	0.0084	0.0004	0.0005	0.0003	0.0001
MT20	41: MT20-5g.	Type III	1	0.0965	0.0017	0.0054	0.0235	0.0007	0.0895	0.0494	0.0017	0.0033	0.0007	0.0004
MT20	42: MT20-5g.	Type III	1	0.0780	0.0008	0.0025	spike	0.0003	0.0431	0.0238	0.0008	0.0016	0.0003	0.0002
MT20	8: MT20-6p.	Type III	1	0.0923	0.0054	0.0000	0.0061	0.0008	0.0966	0.0481	0.0026	0.0042	0.0009	0.0006
MT20	10: MT20-6r.	Type III	1	0.4385	0.0044	0.0000	0.0010	0.0014	0.2037	0.0818	0.0032	0.0062	0.0000	0.0014
MT20	12: MT20-6r.	Type III	1	0.0433	0.0015	0.0032	0.0032	0.0006	0.0822	0.0330	0.0013	0.0025	0.0000	0.0006
MT20	43: MT20-5g.	Type III	1	0.1465	0.0052	0.0000	0.0044	0.0014	0.2548	0.1407	0.0048	0.0093	0.0020	0.0012
MT12	1: MT12_3G.	Type III	1	0.1577	0.0015	0.0035	0.0042	0.0003	0.0612	0.0566	0.0007	0.0035	0.0000	0.0003
MT12	3: MT12_3I.	Type III	1	0.2079	0.0065	0.0110	0.0032	0.0009	0.1997	0.2040	0.0038	0.0110	0.0022	0.0009
MT12	5: MT12_3J.	Type III	1	0.2489	0.0019	0.0040	0.0083	0.0004	0.0909	0.0744	0.0014	0.0032	0.0000	0.0004
MT12	6: MT12_3J.	Type III	1	0.1555	0.0013	0.0029	0.0086	0.0004	0.0819	0.0670	0.0013	0.0029	0.0000	0.0004
MT19	47: MT19-1a.	Type III	1	0.0865	0.0034	0.0106	0.0030	0.0036	0.1145	0.0797	0.0019	0.0057	0.0009	0.0004
MT19	48: MT19-1a.	Type III	1	0.1185	0.0069	0.0070	0.0016	0.0012	0.1398	0.0973	0.0023	0.0070	0.0012	0.0005
MT19	61: MT19-1f.	Type III	1	0.0471	0.0008	0.0030	0.0009	0.0002	0.0345	0.0247	0.0008	0.0011	0.0000	0.0002
MT19	54: MT19-2a	Type III	1	0.1998	0.0044	0.0234	0.0048	0.0064	0.2001	0.1619	0.0044	0.0069	0.0015	0.0009
MT19	55: MT19-2a	Type III	1	0.1128	0.0024	0.0179	0.0052	0.0030	0.1071	0.0867	0.0024	0.0037	0.0008	0.0005
MT19	56: MT19-2c	Type III	1	0.1102	0.0021	0.0084	0.0024	0.0005	0.1046	0.0803	0.0021	0.0021	0.0010	0.0003
MT19	66: MT19-2e	Type III	1	0.2745	0.0009	0.0205	0.0121	0.0049	0.0463	0.0400	0.0009	0.0017	0.0000	0.0002
MT19	57: MT19-2d	Type III	1	0.0831	0.0013	0.0052	0.0019	0.0009	0.0649	0.0577	0.0011	0.0014	0.0007	0.0003
MT19	59: MT19-2d	Type III	1	0.1114	0.0002	0.0065	0.0031	0.0009	0.0122	0.0109	0.0002	0.0003	0.0001	0.0001
MT19	71: MT19-2f	Type III	1	0.0382	0.0012	0.0117	0.0007	0.0019	0.0388	0.0382	0.0008	0.0016	0.0004	0.0002
MT19	72: MT19-2f	Type III	1	0.1034	0.0013	0.0210	0.0028	0.0059	0.0475	0.0467	0.0010	0.0020	0.0005	0.0002
MT11	77: MT11_2A.	Type IV	1	0.3708	0.0048	0.0143	0.0793	0.0012	0.2266	0.2338	0.0048	0.0130	0.0000	0.0012
MT11	83: MT11_2C.	Type IV	1	0.4013	0.0164	0.0121	0.0017	0.0016	0.3671	0.3405	0.0060	0.0121	0.0000	0.0015
MT11	85: MT11_2C.	Type IV	1	0.1584	0.0017	0.0057	0.0046	0.0004	0.1029	0.0954	0.0017	0.0034	0.0000	0.0004
MT12	89: MT12_1A.	Type IV	1	0.0000	0.0121	0.0207	0.0092	0.0009	0.1234	0.1143	0.0024	0.0071	0.0011	0.0007
MT12	90: MT12_1A.	Type IV	1	0.1717	0.0016	0.0157	0.0012	0.0031	0.0420	0.0389	0.0008	0.0024	0.0004	0.0002
MT12	91: MT12_1B.	Type IV	1	0.0410	0.0012	0.0163	0.0029	0.0009	0.0330	0.0334	0.0008	0.0013	0.0007	0.0001
MT12	92: MT12_1B.	Type IV	1	0.6972	0.0366	0.1117	0.0031	0.0024	0.1280	0.1296	0.0030	0.0051	0.0027	0.0005
MT12	93: MT12_1B.	Type IV	1	0.1223	0.0022	0.0307	0.0022	0.0004	0.0933	0.0944	0.0022	0.0037	0.0020	0.0004
MT12	94: MT12_1B.	Type IV	1	0.2132	0.0038	0.0134	0.0034	0.0008	0.1603	0.1623	0.0038	0.0064	0.0034	0.0007

Appendix 5.2 Microprobe analysis of apatite

Appendix 5.2 Microprobe analysis of apatites

		Oxide weight %												Number of atoms per formula units													
Sample	Analysis Ref. No	P2O5	SO3	SiO2	As2O5	Ce2O3	FeO	CaO	Na2O	MnO	SrO	F	Cl	Total	P	S	Si	As	Ce	Fe	Ca	Na	Mn	Sr	F	Cl
MT13A	MT13A-ap1	40.3	0.000	0.000	0.000	0.171	0.065	54.0	0.109	0.032	0.040	4.5	0.512	97.7	5.9	0.000	0.000	0.000	0.011	0.009	9.9	0.036	0.005	0.004	2.5	0.149
MT13A	MT13A-ap2	40.5	0.004	0.026	0.000	0.214	0.085	54.0	0.095	0.015	0.056	4.0	0.635	97.8	5.9	0.001	0.004	0.000	0.013	0.012	9.9	0.032	0.002	0.006	2.2	0.185
MT13A	MT13A-ap3a	40.8	0.001	0.000	0.005	0.119	0.051	53.6	0.098	0.017	0.052	4.2	0.442	97.6	6.0	0.000	0.000	0.000	0.008	0.007	9.9	0.033	0.002	0.005	2.3	0.130
MT13A	MT13A-ap3b	41.0	0.000	0.008	0.014	0.298	0.084	53.8	0.093	0.000	0.000	3.9	0.460	97.9	6.0	0.000	0.001	0.001	0.019	0.012	9.9	0.031	0.000	0.000	2.1	0.135
MT13A	MT13A-ap3c	40.9	0.005	0.033	0.000	0.226	0.129	53.8	0.082	0.013	0.020	3.9	0.390	97.9	6.0	0.001	0.006	0.000	0.014	0.019	9.9	0.027	0.002	0.002	2.1	0.114
MT13A	MT13A-ap4a	40.7	0.009	0.019	0.000	0.131	0.029	53.9	0.110	0.000	0.000	3.5	0.442	97.3	5.9	0.001	0.003	0.000	0.008	0.004	10.0	0.037	0.000	0.000	1.9	0.129
MT13A	MT13A-ap4b	40.9	0.000	0.007	0.000	0.286	0.035	53.9	0.087	0.062	0.009	3.5	0.442	97.6	6.0	0.000	0.001	0.000	0.018	0.005	9.9	0.029	0.009	0.001	1.9	0.129
MT13A	MT13A-ap4c	40.7	0.014	0.000	0.006	0.292	0.007	53.7	0.076	0.043	0.025	3.5	0.452	97.2	5.9	0.002	0.000	0.001	0.018	0.001	9.9	0.025	0.006	0.003	1.9	0.132
MT13A	MT13A-ap4d	41.1	0.000	0.020	0.021	0.048	0.001	53.9	0.080	0.055	0.039	3.5	0.465	97.6	6.0	0.000	0.003	0.002	0.003	0.000	10.0	0.027	0.008	0.004	1.9	0.136
MT13A	MT13A-ap2c	40.7	0.006	0.000	0.027	0.083	0.052	54.0	0.088	0.043	0.024	3.4	0.585	97.4	5.9	0.001	0.000	0.002	0.005	0.007	9.9	0.029	0.006	0.002	1.9	0.171
MT13A	MT13A-ap2d	40.7	0.007	0.000	0.004	0.256	0.039	53.9	0.076	0.005	0.000	3.4	0.588	97.4	5.9	0.001	0.000	0.000	0.016	0.006	10.0	0.025	0.001	0.000	1.9	0.172
MT13A	MT13A-ap5a	40.9	0.000	0.000	0.000	0.137	0.035	54.0	0.058	0.035	0.038	3.5	0.504	97.7	6.0	0.000	0.000	0.000	0.009	0.005	10.0	0.019	0.005	0.004	1.9	0.147
MT13A	MT13A-ap5b	40.7	0.001	0.000	0.000	0.184	0.028	53.9	0.061	0.025	0.041	3.5	0.525	97.4	5.9	0.000	0.00	0.00	0.011608	0.004035	10.0	0.02038	0.003649	0.004097	1.9	0.153335
MT13A	MT13A-ap5c	40.6	0.016	0.000	0.000	0.143	0.087	53.9	0.077	0.017	0.017	3.6	0.511	97.2	5.9	0.002	0.000	0.000	0.009	0.013	9.9	0.026	0.002	0.002	1.9	0.149
MT13A	MT13A-ap5d	40.7	0.013	0.019	0.000	0.167	0.110	54.0	0.094	0.014	0.013	3.5	0.529	97.6	5.9	0.002	0.003	0.000	0.011	0.016	9.9	0.031	0.002	0.001	1.9	0.154
MT19	MT19ap1_1	40.3	0.171	0.058	0.606	0.326	0.218	54.2	0.166	0.105	0.149	3.7	0.656	99.0	5.8	0.022	0.010	0.054	0.020	0.031	9.9	0.055	0.015	0.015	2.0	0.189
MT19	MT19ap1_2	40.5	0.177	0.118	0.318	0.232	0.189	54.1	0.123	0.140	0.140	3.8	0.609	98.7	5.8	0.023	0.020	0.028	0.014	0.027	9.9	0.041	0.020	0.014	2.1	0.176
MT19	MT19ap2_1	40.9	0.064	0.162	0.080	0.626	0.159	54.7	0.237	0.067	0.058	3.2	0.625	99.4	5.8	0.008	0.027	0.007	0.039	0.022	9.8	0.077	0.010	0.006	1.7	0.178
MT19	MT19ap2_2	40.9	0.062	0.157	0.003	0.626	0.175	54.5	0.221	0.049	0.126	5.1	0.580	100.2	5.8	0.008	0.026	0.000	0.039	0.025	9.8	0.072	0.007	0.012	2.7	0.166
MT19	MT19ap4_1	40.2	0.078	0.082	0.049	0.394	0.238	54.7	0.158	0.121	0.059	3.8	0.917	99.1	5.7	0.010	0.014	0.004	0.024	0.034	9.9	0.052	0.017	0.006	2.0	0.262
MT19	MT19ap4_2	41.0	0.101	0.152	0.024	0.551	0.256	54.6	0.160	0.056	0.041	3.3	0.862	99.5	5.8	0.013	0.026	0.002	0.034	0.036	9.9	0.052	0.008	0.004	1.8	0.246
MT19	MT19ap4_3	40.5	0.205	0.086	0.133	0.544	0.170	54.2	0.156	0.103	0.057	4.7	0.975	99.7	5.8	0.026	0.015	0.012	0.034	0.024	9.9	0.051	0.015	0.006	2.5	0.281
MT20	MT20-ap1a	41.3	0.000	0.000	0.000	0.208	0.086	54.6	0.084	0.397	0.022	3.9	0.578	99.4	5.9	0.000	0.000	0.000	0.013	0.012	9.9	0.028	0.057	0.002	2.1	0.166
MT20	MT20ap3_1	41.9	0.011	0.005	0.009	0.115	0.085	56.1	0.052	0.167	0.014	2.7	0.731	100.6	5.9	0.001	0.001	0.001	0.007	0.012	9.9	0.017	0.023	0.001	1.4	0.205
MT20	MT20ap3_2	41.3	0.009	0.000	0.003	0.184	0.085	56.1	0.050	0.175	0.076	3.9	0.689	100.8	5.8	0.001	0.000	0.000	0.011	0.012	9.9	0.016	0.024	0.007	2.0	0.193
MT20	MT20ap3_3	41.7	0.007	0.000	0.000	0.103	0.026	56.1	0.051	0.186	0.018	4.1	0.708	101.2	5.8	0.001	0.000	0.000	0.006	0.004	9.9	0.016	0.026	0.002	2.1	0.198
MT20	MT20ap3_4	41.9	0.007	0.010	0.000	0.092	0.072	56.2	0.038	0.119	0.033	3.6	0.661	101.1	5.9	0.001	0.002	0.000	0.006	0.010	10.0	0.012	0.017	0.003	1.9	0.185
MT20	MT20ap3_5	41.9	0.057	0.059	0.042	0.115	0.060	56.4	0.052	0.159	0.036	3.9	0.625	101.6	5.8	0.007	0.010	0.004	0.007	0.008	9.9	0.017	0.022	0.003	2.0	0.174
MT20	MT20ap3_6	42.0	0.051	0.013	0.029	0.235	0.037	56.2	0.066	0.187	0.034	4.4	0.686	102.0	5.9	0.006	0.002	0.002	0.014	0.005	9.9	0.021	0.026	0.003	2.3	0.192
MT20	MT20ap3_7	42.0	0.013	0.000	0.008	0.149	0.071	56.3	0.046	0.152	0.045	3.4	0.709	101.3	5.9	0.002	0.000	0.001	0.009	0.010	9.9	0.015	0.021	0.004	1.8	0.198

Appendix 5.2 Microprobe analysis of apatites

		Oxide weight %												Number of atoms per formula units												
Sample	Analysis Ref. No	P2O5	SO3	SiO2	As2O5	Ce2O3	FeO	CaO	Na2O	MnO	SrO	F	Cl	Total	P	S	Si	As	Ce	Fe	Ca	Na	Mn	Sr	F	Cl
MT20	MT20ap3_8	41.6	0.011	0.012	0.009	0.086	0.031	55.6	0.051	0.182	0.031	3.9	0.848	100.5	5.9	0.001	0.002	0.001	0.005	0.004	9.9	0.017	0.026	0.003	2.1	0.240
MT20	MT20ap3_9	41.3	0.017	0.000	0.000	0.121	0.078	55.4	0.061	0.202	0.063	4.1	0.800	100.2	5.9	0.002	0.000	0.000	0.007	0.011	9.9	0.020	0.029	0.006	2.2	0.227
MT20	MT20ap3_10	41.9	0.003	0.000	0.012	0.189	0.065	55.5	0.042	0.171	0.053	4.8	0.678	101.2	5.9	0.000	0.000	0.001	0.012	0.009	9.9	0.014	0.024	0.005	2.6	0.192
MT20	MT20ap3_11	41.8	0.011	0.000	0.023	0.057	0.086	55.7	0.041	0.267	0.000	4.6	0.540	101.1	5.9	0.001	0.000	0.002	0.003	0.012	9.9	0.013	0.038	0.000	2.4	0.152
MT20	MT20ap4_2	41.7	0.007	0.029	0.000	0.103	0.078	55.5	0.043	0.317	0.051	4.3	0.584	100.8	5.9	0.001	0.005	0.000	0.006	0.011	9.9	0.014	0.045	0.005	2.2	0.165
MT20	MT20ap4_3	41.8	0.010	0.000	0.000	0.161	0.185	55.8	0.045	0.314	0.029	3.5	0.567	100.9	5.9	0.001	0.000	0.000	0.010	0.026	9.9	0.014	0.044	0.003	1.8	0.159
MT22	MT22-1	40.6	0.003	0.000	0.000	0.110	0.190	53.3	0.050	0.695	0.046	3.3	0.574	97.3	5.9	0.000	0.000	0.000	0.007	0.027	9.8	0.017	0.101	0.005	1.8	0.168
mt22	MT22-1b	40.7	0.010	0.000	0.000	0.049	0.206	53.5	0.057	0.641	0.007	3.2	0.563	97.4	5.9	0.001	0.000	0.000	0.003	0.030	9.9	0.019	0.093	0.001	1.7	0.164
mt22	MT22-1c	40.5	0.007	0.000	0.008	0.147	0.175	53.6	0.056	0.639	0.010	3.3	0.558	97.5	5.9	0.001	0.000	0.001	0.009	0.025	9.9	0.019	0.093	0.001	1.8	0.162
mt22	MT22-2a	40.7	0.010	0.005	0.000	0.000	0.297	53.4	0.045	0.511	0.018	3.9	0.499	97.6	5.9	0.001	0.001	0.000	0.000	0.043	9.9	0.015	0.075	0.002	2.1	0.146
mt22	MT22-2b	40.6	0.017	0.000	0.000	0.079	0.404	53.3	0.021	0.585	0.002	4.1	0.447	97.8	5.9	0.002	0.000	0.000	0.005	0.058	9.8	0.007	0.085	0.000	2.2	0.131
mt22	MT22-2d	40.6	0.019	0.000	0.000	0.128	0.264	53.6	0.029	0.549	0.037	4.3	0.452	98.0	5.9	0.002	0.000	0.000	0.008	0.038	9.9	0.010	0.080	0.004	2.3	0.132
mt22	MT22-2c	40.7	0.010	0.011	0.000	0.000	0.351	53.2	0.030	0.530	0.000	4.2	0.548	97.6	6.0	0.001	0.002	0.000	0.000	0.051	9.9	0.010	0.078	0.000	2.3	0.161
mt22	MT22-3a	41.0	0.003	0.000	0.000	0.000	0.269	53.5	0.037	0.496	0.014	3.9	0.560	98.0	6.0	0.000	0.000	0.000	0.000	0.039	9.9	0.012	0.072	0.001	2.1	0.164
mt22	MT22-3b	41.0	0.010	0.003	0.000	0.085	0.340	53.5	0.030	0.491	0.046	3.8	0.562	98.2	6.0	0.001	0.001	0.000	0.005	0.049	9.9	0.010	0.071	0.005	2.1	0.164
mt22	MT22-3d	40.6	0.005	0.000	0.000	0.085	0.278	53.2	0.035	0.512	0.002	3.8	0.625	97.5	6.0	0.001	0.000	0.000	0.005	0.040	9.9	0.012	0.075	0.000	2.1	0.183
mt22	MT22-3d	40.7	0.011	0.000	0.000	0.097	0.265	53.6	0.066	0.430	0.000	3.8	0.555	97.8	5.9	0.001	0.000	0.000	0.006	0.038	9.9	0.022	0.063	0.000	2.1	0.162

Appendix 6.1 LA ICP MS data on L+V+nS and L+V+H fluid inclusions from the Eloise Cu-Au deposit

All fluid inclusion samples are from Baker (1996).

JCU Ref No	Fluid inclusions type	Inclusion Ref No.	Concentration (ppm)								LOD (ppm)							
			Na	K	Ca	Mn	Fe	Cu	Zn	Pb	Na	K	Ca	Mn	Fe	Cu	Zn	Pb
48164	L+V+nS	B8	1	0.2285	spike	0.0707	0.0170	0.0076	0.0234	0.0278	0.0749	0.0886	0.0128	0.0148	0.0043	0.0076	0.0044	0.0051
48164	L+V+nS	B12	1	0.3103	0.6437	0.3630	spike	0.0199	0.0214	0.0118	0.2081	0.2724	0.0465	0.0512	0.0134	0.0199	0.0157	0.0090
48164	L+V+nS	B13	1	0.1172	0.1773	0.1818	0.3693	0.0075	0.0077	0.0054	0.0971	0.1172	0.0223	0.0214	0.0059	0.0075	0.0048	0.0054
48164	L+V+nS	B17	1	0.3253	spike	0.1298	0.3934	0.0252	0.0320	spike	0.0716	0.0895	0.0135	0.0139	0.0043	0.0063	0.0029	0.0032
48164	L+V+nS	B18	1	0.1433	0.4861	0.1340	0.1492	spike	0.0146	0.0047	0.0503	0.0558	0.0092	0.0089	0.0026	0.0046	0.0013	0.0014
48164	L+V+nS	B19	1	0.0349	0.1055	0.0187	0.0108	0.0017	0.0021	0.0006	0.0185	0.0219	0.0035	0.0034	0.0009	0.0017	0.0005	0
48164	L+V+nS	B20	1	0.2740	0.7033	0.3036	spike	spike	0.0266	0.0090	0.1642	0.1963	0.0310	0.0316	0.0092	0.0130	0.0102	0
48164	L+V+nS	B22	1	0.1526	0.2071	0.1557	0.4730	0.0109	0.0153	0.0035	0.1275	0.1526	0.0241	0.0249	0.0074	0.0109	0.0075	0
48170	L+V+nS	E1	1	0.0944	0.1112	0.0281	0.5988	0.0006	0.0010	0.0012	0.0055	0.0077	0.0012	0.0018	0.0005	0.0006	0.0003	0.0012
48170	L+V+nS	E2	1	0.6109	0.2821	0.0846	0.4047	0.0071	0.0152	0.0099	0.0530	0.0818	0.0124	0.0181	0.0050	0.0071	0.0038	0.0099
48170	L+V+nS	E3	1	0.1516	0.2139	0.0496	0.4926	0.0034	0.0050	0.0067	0.0349	0.0364	0.0067	0.0093	0.0025	0.0034	0.0021	0.0067
48170	L+V+nS	E4	1	0.4092	0.6333	0.0451	0.1068	0.0282	0.0131	0.0297	0.1753	0.1888	0.0334	0.0451	0.0122	0.0165	0.0095	0.0297
48170	L+V+nS	E5	1	0.0463	0.0370	0.0097	0.0766	0.0030	0.0054	0.0022	0.0364	0.0463	0.0064	0.0097	0.0028	0.0030	0.0017	0.0000
48170	L+V+nS	E8	1	0.3768	0.5907	0.0991	0.5001	0.0265	0.0232	0.0178	0.1918	0.2302	0.0359	0.0448	0.0162	0.0265	0.0082	0
48170	L+V+nS	E9	1	0.5441	0.3160	0.0617	0.1715	0.0372	0.0514	0.0121	0.1380	0.1638	0.0258	0.0324	0.0116	0.0202	0.0058	0
48170	L+V+nS	E11	1	1.1971	0.9653	0.2525	0.3788	0.0624	0.0579	0.0430	0.9165	1.1971	0.1643	0.2525	0.0731	0.0624	0.0443	0
48170	L+V+nS	E13	1	spike	0.6892	0.2162	0.4062	0.0446	0.0906	0.0469	0.4476	0.5388	0.0865	0.1297	0.0396	0.0446	0.0204	0.0469
48170	L+V+nS	E14	1	0.4539	0.1515	0.0302	0.1329	0.0085	0.0302	0.0139	0.0879	0.1063	0.0166	0.0248	0.0072	0.0085	0.0050	0.0114
48170	L+V+nS	E15	1	0.2213	0.7402	0.1368	0.4441	0.0151	0.0163	0.0190	0.1471	0.1896	0.0272	0.0438	0.0128	0.0151	0.0069	0.0190

Appendix 6.1 LA ICP MS data on L+V+nS and L+V+H fluid inclusions from the Eloise Cu-Au deposit

			Concentration (ppm)						LOD (ppm)					
JCU Ref No	Fluid inclusions type	Inclusion Ref No.	Na	K	Rb	Sr	Cs	Ba	Na	K	Rb	Sr	Cs	Ba
48164	L+V+nS	A8	1	0.2732	0.0023	0.0054	0.0008	0.0647	0.0434	0.0243	0.0009	0	0.0003	0.0010
48164	L+V+nS	A2	1	0.3138	0.0102	0.0136	0.0047	0.1029	0.4039	0.2152	0.0102	0	0.0047	0.0151
48164	L+V+nS	A9	1	0.4179	0.0041	0.0092	0.0014	0.0691	0.0720	0.0397	0.0018	0	0.0009	0.0026
48164	L+V+nS	A10	1	0.1320	0.0047	0.0038	0.0017	0.0263	0.2464	0.1320	0.0047	0.0007	0.0017	0.0086
48164	L+V+nS	A12	1	0.0525	0.0024	0.0090	0.0022	0.0343	0.0758	0.0525	0.0016	0	0.0008	0.0027
48164	L+V+nS	A13	1	0.0064	0.0002	0.0019	0.0002	0.0118	0.0099	0.0064	0.0002	0	9E-05	0.0003
48164	L+V+nS	A14	1	0.2606	0.0054	0.0109	0.0010	0.0612	0.1041	0.0603	0.0020	0	0.0008	0.0039
48164	L+V+nS	A16	1	0.7020	0.0095	0.0154	0.0026	0.0736	0.2412	0.1361	0.0049	0	0.0026	0.0053
48164	L+V+nS	A17	1	0.7762	0.0049	0.0137	0.0021	0.1015	0.2240	0.1185	0.0014	0.0006	0.0021	0
48164	L+V+nS	A19	1	0.3803	0.0033	0.0115	0.0016	0.1002	0.1905	0.1107	0.0013	0	0.0016	0
48170	L+V+nS	D10	1	0.4210	0.0043	0.0027	0.0031	0.0172	0.0537	0.0378	0.0015	0.0004	0.0008	0.0026
48170	L+V+nS	A18	1	0.1854	0.0027	0.0004	0.0004	0.0029	0.0034	0.0025	6.8E-05	1.2E-05	3.6E-05	0.0001
48170	L+V+nS	A17	1	0.1358	0.0018	0.0004	0.0003	0.0030	0.0039	0.0030	7.6E-05	1.2E-05	4.2E-05	0.0002
48170	L+V+nS	D12	1	0.0212	0.0003	0.0001	0.0001	0.0006	0.0043	0.0029	0.0001	2.8E-05	4.4E-05	0.0001
48170	L+V+nS	D13	1	0.0463	0.0004	0.0001	0.0001	0.0011	0.0125	0.0094	0.0004	0	0.0001	0.0004
48170	L+V+nS	D14	1	0.2403	0.0102	0.0024	0.0036	0.0095	0.3484	0.2403	0.0102	0	0.0036	0.0095
48170	L+V+nS	D16	1	0.1834	0.0032	0.0098	0.0011	0.0076	0.1022	0.0761	0.0022	0.0010	0.0011	0.0076

Appendix 6.1 LA ICP MS data on L+V+nS and L+V+H fluid inclusions from the Eloise Cu-Au deposit

			Concentration (ppm)								LOD (ppm)							
JCU Ref No	Fluid inclusions type	Inclusion Ref No.	Na	K	Ca	Mn	Fe	Cu	Zn	Pb	Na	K	Ca	Mn	Fe	Cu	Zn	Pb
48178	L+V+H	C1	1	0.1816	0.9091	0.1224	0.1450	0.0059	0.0114	0.0175	0.0255	0.0263	0.0043	0.0055	0.0018	0.0039	0.0017	0.0023
48178	L+V+H	C2	1	0.2148	0.8722	0.1239	0.1195	0.0064	0.0242	0.0181	0.0384	0.0451	0.0074	0.0080	0.0027	0.0064	0.0027	0.0053
48178	L+V+H	C3	1	0.2242	0.8468	0.0388	0.0549	0.0085	0.0128	0.0117	0.0526	0.0589	0.0098	0.0109	0.0036	0.0085	0.0036	0.0057
48178	L+V+H	C4	1	0.7906	spike	0.1894	0.1601	0.0259	0.0524	0.0744	0.1073	0.1233	0.0212	0.0222	0.0075	0.0131	0.0057	0.0126
48178	L+V+H	C5	1	0.7049	spike	0.1701	0.0864	0.0101	0.0386	0.0577	0.0847	0.0963	0.0167	0.0185	0.0062	0.0101	0.0049	0.0107
48178	L+V+H	C7	1	0.3189	1.5683	0.0654	0.1099	0.0238	0.0183	0.0272	0.2217	0.2613	0.0366	0.0428	0.0118	0.0217	0	0.0272
48178	L+V+H	C9	1	0.3383	spike	0.0839	0.0970	0.0318	0.0224	0.0292	0.2469	0.2974	0.0462	0.0546	0.0178	0.0318	0.0136	0.0278
48178	L+V+H	C13	1	1.0465	spike	0.1498	0.1283	0.0193	0.0260	0.0420	0.1151	0.1365	0.0191	0.0233	0.0086	0.0193	0.0098	0.0125
48178	L+V+H	C14	1	0.4650	spike	0.1105	0.1645	0.0312	0.0188	0.0333	0.1753	0.2174	0.0289	0.0367	0.0135	0.0312	0.0158	0.0164
48076	L+V+H	C1	1	0.6425	spike	0.1391	0.1274	0.0465	0.0298	0.0247	0.4690	0.5911	0.0882	0.1107	0.0291	0.0465	0.0187	0.0247
48076	L+V+H	C2	1	0.4952	1.1506	0.0522	0.0587	0.0213	0.0142	0.0158	0.2238	0.2863	0.0433	0.0522	0.0142	0.0213	0.0086	0.0158
48076	L+V+H	C5	1	0.3999	0.6278	0.0500	0.0985	0.0206	0.0139	0.0164	0.2191	0.2697	0.0396	0.0500	0.0138	0.0206	0.0090	0.0164
48076	L+V+H	C23	1	0.8329	0.9504	0.1042	0.0582	0.0414	0.0024	0.0016	0.6450	0.8329	0.1054	0.1042	0.0322	0.0414	0	0
EDW6	L+V+H	A1	1	0.0551	0.7856	0.0159	0.0100	0.0034	0.0022	0.0039	0.0393	0.0543	0.0084	0.0082	0.0025	0.0034	0	0.0039
EDW6	L+V+H	A2	1	0.1130	0.3231	0.0156	0.0053	0.0057	0.0070	0.0024	0.0865	0.1130	0.0169	0.0156	0.0047	0.0057	0.0070	0
EDW6	L+V+H	A3	1	0.4215	1.1620	0.0540	0.0236	0.0219	0.0271	0.0059	0.3010	0.4215	0.0623	0.0540	0.0177	0.0219	0.0271	0
EDW6	L+V+H	A16	1	0.1096	0.4199	0.0173	0.0138	0.0079	0.0113	0.0081	0.0943	0.1096	0.0165	0.0173	0.0050	0.0079	0.0028	0.0040
EDW6	L+V+H	A17	1	0.0791	0.1455	0.0138	0.0817	0.0063	0.0123	0.0035	0.0628	0.0791	0.0102	0.0107	0.0033	0.0063	0.0029	0.0030

Appendix 6.1 LA ICP MS data on L+V+nS and L+V+H fluid inclusions from the Eloise Cu-Au deposit

			Concentration (ppm)						LOD (ppm)					
JCU Ref. No	**Fluid inclusions type**	**Inclusion Ref No.**	**Na**	**K**	**Rb**	**Sr**	**Cs**	**Ba**	**Na**	**K**	**Rb**	**Sr**	**Cs**	**Ba**
48178	L+V+H	A1	1	0.4141	0.0132	0.0200	0.0035	0.0101	0.1984	0.1016	0.0041	0.0005	0.0019	0.0031
48178	L+V+H	A4	1	0.0869	0.0014	0.0017	0.0006	0.0035	0.0542	0.0280	0.0014	0.0001	0.0006	0.0013
48178	L+V+H	A3	1	0.0198	0.0005	0.0008	0.0002	0.0007	0.0149	0.0079	0.0003	0	0.0002	0
48178	L+V+H	A6	1	0.4218	0.0141	0.0204	0.0047	0.0237	0.0713	0.0336	0.0020	0.0002	0.0007	0.0029
48178	L+V+H	A7	1	0.1757	0.0068	0.0124	0.0023	0.0107	0.1787	0.0799	0.0041	0.0004	0.0016	0.0055
48178	L+V+H	B1	1	0.0208	0.0006	0.0008	0.0002	0.0005	0.0144	0.0064	0.0005	0	0.0001	0.0003
48178	L+V+H	B2	1	0.1616	0.0066	0.0104	0.0018	0.0132	0.3278	0.1503	0.0049	0	0.0037	0.0073
48178	L+V+H	B3	1	0.1769	0.0073	0.0169	0.0023	0.0104	0.1972	0.0996	0.0043	0.0004	0.0023	0.0043
48178	L+V+H	B4	1	0.2605	0.0090	0.0157	0.0032	0.0212	0.2655	0.1231	0.0055	0	0.0028	0.0058
48076	L+V+H	D1	1	0.0969	0.0038	0.0038	0.0018	0.0019	0.1670	0.0987	0.0038	0	0.0018	0.0049
48076	L+V+H	D2	1	0.1235	0.0059	0.0031	0.0024	0.0044	0.2376	0.1273	0.0059	0	0.0024	0.0044
48076	L+V+H	D4	1	0.0204	0.0016	0.0015	0.0008	0.0006	0.0945	0.0507	0.0016	0.0002	0.0008	0
48076	L+V+H	D6	1	0.1889	0.0037	0.0050	0.0019	0.0015	0.2010	0.1164	0.0037	0.0005	0.0019	0
48076	L+V+H	D7	1	0.2233	0.0060	0.0037	0.0029	0.0053	0.3320	0.1988	0.0060	0.0008	0.0029	0
48076	L+V+H	D9	1	0.1895	0.0027	0.0052	0.0006	0.0118	0.0784	0.0475	0.0010	0	0.0005	0.0017
48076	L+V+H	D10	1	0.0519	0.0017	0.0056	0.0012	0.0030	0.1254	0.0741	0.0017	0	0.0012	0.0030
48076	L+V+H	D11	1	0.0704	0.0024	0.0017	0.0012	0.0045	0.1295	0.0682	0.0024	0.0003	0.0012	0.0045
48076	L+V+H	D13	1	0.0868	0.0102	0.0027	0.0053	0.0162	0.5700	0.2787	0.0102	0.0015	0.0053	0.0162
EDW6	L+V+H	B9	1	0.0102	0.0003	0.0003	0.0001	0.0005	0.0175	0.0102	0.0003	0	0.0001	0.0005
EDW6	L+V+H	B10	1	0.1967	0.0080	0.0052	0.0024	0.0068	0.3871	0.1967	0.0080	0.0010	0.0024	0.0068
EDW6	L+V+H	B12	1	0.2459	0.0079	0.0258	0.0033	0.0099	0.3109	0.1595	0.0060	0.0008	0.0019	0.0057
EDW6	L+V+H	B13	1	0.0290	0.0006	0.0004	0.0003	0.0012	0.0538	0.0290	0.0006	0.0002	0.0003	0.0012
EDW6	L+V+H	B14	1	0.0421	0.0009	0.0017	0.0005	0.0014	0.0753	0.0421	0.0009	0.0004	0.0005	0.0014
EDW6	L+V+H	B16	1	0.0051	0.0001	0.0004	0.0001	0.0003	0.0082	0.0049	0.0001	2.5E-05	5.2E-05	0.0003
EDW6	L+V+H	B17	1	0.2526	0.0053	0.0161	0.0013	0.0035	0.1955	0.1039	0.0029	0	0.001	0.0028